

Philipps



Universität  
Marburg

# Gilbert-Taylor cones and multi-phase Electrospinning

Dissertation  
zur  
Erlangung des Doktorgrades  
der Naturwissenschaften  
(Dr. rer. nat.)

dem

Fachbereich Physik  
der Philipps-Universität Marburg

vorgelegt von

**Florian Großmann**

aus

Hamburg

Marburg/Lahn, (2009)

Vom Fachbereich Physik der Philipps-Universität

als Dissertation angenommen am: 2009-07-16

Erstgutachter: Prof. Dr. Bruno Eckhardt, Marburg

Zweitgutachter: Prof. Dr. Hans-Jürgen Stöckmann, Marburg

Tag der mündlichen Prüfung: 2009-07-17

Midway upon the journey of our life  
I found myself within a forest dark,  
For the straightforward pathway had been lost.

Ah me! how hard a thing it is to say  
What was this forest savage, rough, and stern,  
Which in the very thought renews the fear.

So bitter is it, death is little more;  
But of the good to treat, which there I found,  
Speak will I of the other things I saw there.

Excerpted from *The Divine Comedy*  
[Dante Alighieri, 1307]



# Zusammenfassung

## Einführung

Das Elektrospinning ist von großer Bedeutung für die Nanotechnologie. Hierbei handelt es sich um eine elektrohydrodynamische Strömung, welche durch ein externes elektrisches Feld und einer, auf einer freien Flüssigkeitsoberfläche, induzierten elektrischen Ladungsverteilung angetrieben wird. Eine klassische Elektrospinning Apparatur besteht aus einem Plattenkondensator von dessen oberer Platte eine Kanüle einen Flüssigkeitstropfen endlicher Leitfähigkeit dem homogenen elektrischen Feld aussetzt. Aufgrund der endlichen Leitfähigkeit der Flüssigkeit bewegen sich die Ladungsträger bzw. Ionen der Flüssigkeit so lange, bis sie kräftefrei sind. Dies bedeutet, dass die Flüssigkeit nach hinreichend langen Zeiten auf einem Equipotential liegt und die Ladungen zu Oberflächenladungen werden. Aufgrund der Selbstabstoßung der Oberflächenladungen wird die Flüssigkeitsoberfläche des Tropfens durch den resultierenden Maxwell Druck deformiert. Unter gewissen Umständen kann sich die Flüssigkeitsoberfläche in einen Gilbert-Taylor Konus verformen, welcher nach überschreiten eines kritischen elektrischen Feldes instabil wird und einen Flüssigkeitsstrahl von seiner Kegelspitze emittiert. Je nach Beschaffenheit der Flüssigkeit zerfällt dieser dünne Strahl in kleine Tropfen, was mit Elektrospraying bezeichnet wird und zahlreiche technische Anwendungen hat. Bleibt der Strahl strahlförmig, so verdünnt er sich zunehmend unter der durch das elektrische Feld hervorgerufenen Beschleunigung und erreicht nach diversen Instabilitäten, wild schlagend, die untere Platte des Plattenkondensators. Ist die verwendete Flüssigkeit eine Polymerlösung, so verdunstet das Lösungsmittel während des Prozesses und es resultieren feste Fasern, die sich auf der unteren Kondensatorplatte kontinuierlich ansammeln. Der Flüssigkeitsstrahl wird während des Elektrosinnings so stark gestreckt, dass der Durchmesser der Fasern im Submikrometer Bereich liegt und er in besonderen Fällen nur wenige Nanometer aufweist. Durch die Wahl der Polymere lassen sich die Eigenschaften der Nanofasern festlegen, womit das Elektrosinning in Bezug auf die Herstellung von Nanofasern bereits zu einer bedeutenden Fertigungsmethode der Werkstoffwissenschaft geworden ist.

Der Gilbert-Taylor Konus ist der Ausgangspunkt des Elektrosinnings und daher von entscheidender Bedeutung für das Verständnis des gesamten Prozesses. Konische Flüssigkeitsoberflächen fanden zum ersten Mal in Sir William Gilberts berühmten Buch 'De Magnete' Erwähnung, welches bereits im Jahre 1600nChr. veröffentlicht wurde. Erst 1964

lieferte Sir William Taylor eine theoretische Erklärung asymptotischer Natur, welche den Öffnungswinkel des Taylor Konus von  $\vartheta_c = 49.3^\circ$  theoretisch vorhersagt und durch gezielte Experimente eindrucksvoll verifiziert werden konnte. Ferner liefert Taylors Erklärung auch eine erste Abschätzung über eine kritische Potentialdifferenz oberhalb derer der Konus instabil wird. Spätere Studien Taylors beschäftigten sich mit Strahlemissionen aus elektrisch aufgeladenen konischen Flüssigkeitsoberflächen.

## Ziel der Arbeit

Aufgrund der vielen beim Elektrospinning beteiligten physikalischen Prozesse ist es bisher nicht gelungen eine geschlossene Theorie zu entwickeln, welche zuverlässige Vorhersagen über das zu erwartende Endprodukt bei gegebenen Anfangsbedingungen ermöglicht. Aus Sicht der Produktentwicklung wäre eine Theorie wünschenswert, welche zu gegebenen experimentellen Größen und Materialparametern relativ zuverlässig vorhersagen könnte, welches Endprodukt zu erwarten ist, so dass Experimente zuverlässiger geplant werden können, um die Entwicklungszeit von speziell designten Nanofasern verkürzen zu können.

Eine solche Theorie ist derzeit noch nicht greifbar. Zunächst müssen erst einzelne Teilaspekte besser verstanden werden, welche aus physikalischer Sicht ebenso interessant wie reichhaltig sind. So beschäftigen sich etablierte theoretische Arbeiten typischerweise mit dem Tropfen vor der Entstehung des Strahls oder aber setzen seine Existenz ab initio voraus. Der eigentliche Mechanismus hinter der Strahl Emission, welcher unter anderem auch den initialen Radius des emittierten Strahls festlegt, ist noch nicht verstanden.

Ferner haben experimentelle Arbeiten zum Elektrospinning und zu aufgeladenen Tropfen gezeigt, dass durchaus Tropfen mit kleineren Öffnungswinkeln als dem von Taylor vorhergesagten beobachtet werden. Taylors theoretische Erklärung ist ein asymptotischer Grenzfall, welcher zwei divergente Drücke, den Laplace Druck und den Maxwell Druck, balanciert und den im wesentlichen konstanten hydrostatischen Druck vernachlässigt, wodurch ein Öffnungswinkel des Taylor cones von  $\vartheta = 49.3^\circ$  vorhergesagt werden kann.

Um das Elektrospinning besser verstehen zu können, ist es notwendig den Entstehungsprozess des emittierten Strahls näher zu untersuchen. Aus diesem Grund wird in dieser Arbeit das Problem einer sich im mechanischen und elektrischen Gleichgewicht befindlichen freien Flüssigkeitsoberfläche eines leitfähigen Fluids in einem externen elektrischen Feld näher untersucht.

Obwohl dieses Problem statischer Natur ist, tritt eine große Schwierigkeit auf, da die freie Flüssigkeitsoberfläche eines Tropfens auf einem Equipotential in einem elektrischen Feld ein Dirichlet Problem darstellt, welches leicht mit etablierten Methoden zu lösen ist und dessen Lösung die Feldverteilung um den Tropfen darstellt. Diese Feldverteilung bedingt

eine Oberflächenladungsdichte auf dem leitfähigen Tropfen, welche diesen dann durch den Maxwell Druck verformt, wodurch die Randbedingungen des zuvor gelösten Dirichlet Problems geändert werden. Diese Kopplung von mechanischem und elektrischem Gleichgewicht stellt eine starke Nichtlinearität dar, welche zudem von nicht lokaler Natur ist. Diese Nichtlokalität stammt von der Ladungsgesamtheit auf dem Tropfen, welche an jedem Punkt des Tropfens zu einem konstanten Potential führen muss. Aus diesem Grund wird die Equipotentialbedingung durch eine nichtlineare Integralgleichung erster Art beschrieben, welche das Inverse Problem beschreibt, aus einem vorgegebenen Potential eine geeignete Ladungsdichte zu bestimmen.

Da exakte analytische Ansätze zur selbstkonsistenten Lösung des mechanischen und elektrischen Gleichgewichts nicht aussichtsreich erscheinen, ist es unabdingbar einen geeigneten numerischen Ansatz zur Lösung dieses Problems zu verfolgen.

## Methodischer Ansatz

Die mathematische Theorie zu nichtlinearen Integralgleichungen erster Art ist nur sehr spärlich entwickelt. Dennoch ist es gelungen einen numerischen Algorithmus zu entwickeln, welcher zunächst einmal die Existenz mindestens einer Lösung des Problems voraussetzt und versucht die Differentialgleichung für die Beschreibung des mechanischen Gleichgewichts unter Berücksichtigung der Integralgleichung für das elektrische Gleichgewicht iterativ in der oben beschriebenen Weise zu lösen. Von zentraler Bedeutung ist hierbei die Diskretisierung eines kontinuierlichen Integraloperators, welcher einen nicht trivialen Nullraum aufweist. Der diskretisierte Integraloperator ist eine im allgemeinen nicht singuläre Matrix, weshalb sie einen trivialen Nullraum besitzt. Folglich wird durch die Diskretisierung des Integraloperators die Lösung in systematischer Weise unvermeidbar verfälscht, indem durch die Diskretisierung ein Element des nicht trivialen Nullraumes des kontinuierlichen Integraloperators ausgewählt wird, welches die tatsächliche Lösung additiv überlagert. Dies ist eine Konsequenz des Faktums, dass Integralgleichungen erster Art mathematisch schlecht gestellte Probleme darstellen und nicht ohne weiteres lösbar sind.

Schlecht gestellte inverse Probleme lassen sich mitunter durch die Anwendung zusätzlich zur Verfügung stehender Informationen über das spezielle Problem lösen. Im vorliegenden Fall ist eine räumlich stark oszillierende Oberflächenladungsdichte unphysikalisch, so dass die zusätzliche Forderung einer glatten Oberflächenladungsdichte das Problem beherrschbar macht und den iterativen numerischen Algorithmus gegen physikalisch sinnvoll erscheinende Lösungen konvergieren lässt.

Der analytisch bekannte lineare Grenzfall einer leitfähigen Kugel in einem elektrischen Feld lässt sich auf diese Weise reproduzieren. Ferner gehen die Lösungen geladener Tropfen im Grenzfall verschwindenden hydrostatischen Druckes in einen abgerundeten Kegel über, welcher den Öffnungswinkel des Taylor Konus aufweist. Die Reproduktion dieser Grenzfälle ist ein starker Hinweis auf die Funktionstüchtigkeit des entwickelten Verfahrens.

## Wichtige Resultate

Der entwickelte Algorithmus zur Berechnung von Flüssigkeitsoberflächen in mechanischem und elektrischem Gleichgewicht ist zur Berechnung von Tropfenformen an Kanülen konstanten Radius im homogenen elektrischen Feld eines Plattenkondensators verwendet worden. Hierbei konnte durch adiabatisches Aufladen ursprünglich ungeladener Kanülen-tropfen festgestellt werden, dass Tropfen der Fuchikami Moden 1 und 2 unter isobaren Bedingungen durch Aufladen in einem geeignet gesteuerten elektrischen Feld stetig ineinander überführt werden können. Ferner konnten Tropfenformen aufgefunden werden, welche als intermediäre Tropfen und konische Tropfen bezeichnet werden. Intermediäre Tropfen sind elongierte Tropfen die eine runde Tropfenspitze aber schon einen leicht kegeligen Schaft aufweisen. Konische Tropfen sind Tropfen, die sich durch eine sehr ausgeprägte kegelige Spitze auszeichnen, wie sie beispielsweise in Taylors Experimenten auftreten. Die Rechnungen zeigen, dass ein solches Vorgehen nur für spezielle Kanülenradien möglich ist. Im Fall zu großer Kanülenradien, treten nur geladene Fuchikami Tropfen der Moden 1 und 2 auf ohne dass Gilbert-Taylor Konen auftreten. Für zu gering dimensionierte Kanülenradien gibt es unter den gleichen isobaren Bedingungen intermediäre und konische Tropfen, allerdings ist eine stetige Überführung geladener Tropfen der Fuchikami Moden 1 und 2 dann nicht mehr möglich, da die Lösungsmenge geladener Tropfen in diesem Fall durch eine Bifurkation im Kanülenradius nicht mehr einfach zusammenhängend ist.

Ferner konnten noch nicht bekannte überladene Tropfen aufgefunden werden. Das Überladen äußert sich durch einen sehr kleinen runden Tropfen, welcher sich an der Spitze des kegeligen Tropfenschaftes abzuschneiden beginnt. Diese Überladenen Tropfen sind eine Konsequenz der Equipotentialbedingung bei zu großen elektrischen Feldern. Der Radius der Abschnürung folgt hierbei direkt aus den Gleichungen und unterscheidet sich im Wesentlichen dadurch, ob ein intermediärer oder konischer Tropfen überladen wurde. Konische Tropfen weisen kleinere Abschnürradien auf als intermediäre Tropfen.

Weiterhin konnte auf Basis der dielektrischen Zeitskala und hydrodynamischer Zeitskalen ein Verfahren vorgeschlagen werden, durch welches die gezielt ausgelöste Strahlemission, durch präzise gesteuerte Störungen im elektrischen Feld, realisierbar erscheint.

Es konnte nachgewiesen werden, dass der hydrostatische Druck in Verbindung mit der Equipotentialbedingung den Winkel der Gilbert-Taylor Konen festlegt und dass sich die Strahlemission an endlich ausgedehnten konischen Flüssigkeitsoberflächen signifikant von der idealer Taylor Konen unterscheidet.

Da sich das entwickelte Verfahren auch dazu eignet geschlossene Tropfen in der Abwesenheit von Gravitation zu studieren, konnte ein Tropfen konstanten Volumens aufgeladen werden. Hierbei stellt sich der Druck im Innern des Tropfens passend ein. Es konnte gezeigt werden,



dass ab einem gewissen elektrischen Feld zwei und sogar drei mögliche elektrohydrostatische Lösungen koexistieren, welche sich in ihrer Zustandsenergie nicht signifikant unterscheiden. Ferner gibt es ein maximales elektrisches Feld, oberhalb dessen keine elektrohydrostatische Lösung für einen Tropfen dieses Volumens mehr existiert. Größere elektrische Felder setzen das Fluid des Tropfens unweigerlich in Bewegung und werden den Tropfen zerreißen.

Eine geringfügig überladene konische Lösung dieses Tropfens hat eine Abschätzungen über die Eigenschaften kleiner Tropfen ermöglicht, die aus einer Strahlemission aus der konischen Tropfenspitze hervorgehen können. Derartige Prozesse sind für die Gewitterforschung im Zusammenhang mit der Entstehung von Blitzentladungen von Interesse.

In einem weiteren Kapitel ist das Multi-Phasen Elektrosinning modelliert worden. Beim Multi-Phasen Elektrosinning werden kinetisch stabilisierte monodisperse Kolloide in einer wässrigen Polymerlösung im Elektrosinning Verfahren versponnen. Es resultieren kolloidale Nanofasern, welche von einer Polymerschicht überzogen sind. Auch nach dem chemischen Entfernen des verbliebenen Polymerfilms bleiben die kolloidalen Fasern mechanisch stabil. Ein geeignetes Modell zur Simulation der Strukturbildung im Multi-Phasen Elektrosinning hat quantitative Aussagen über die auftretenden Strukturen ermöglicht und konnte sie mit der Existenz eindimensionaler Kristalle in Verbindung bringen, welche einen ordnenden Einfluss auf die beobachteten Strukturen der amorphen kolloidalen Nanofasern haben. Das Multi-Phasen Elektrosinning ist ein Verfahren, welches ermöglicht, wasserunlösliche Nanofasern aus einer wässrigen Lösung herzustellen, ohne dabei organische Lösungsmittel verwenden zu müssen, was dieses Verfahren sehr wertvoll für zukünftige technologische Anwendungen macht.

## Ausblick

Der Autor hält gezielte Experimente zur Bestätigung der berechneten Strukturen im Parameterraum, die in Abbildungen 3.25 und 3.26 auf den Seiten 73 und 74 dargestellt sind, für ausgesprochen interessant. Ferner ist die kontrollierte Auslösung von Strahlemissionen, die in Abschnitt 3.3.6 ab Seite 83 beschrieben wird, von großem Interesse. Sollten sich die vorliegenden Ergebnisse dieser Arbeit als zutreffend erweisen, erwachse hieraus ein echter Fortschritt hinsichtlich der Steuerungsmöglichkeiten des Elektrosinningprozesses. Kanülentropfen könnten über geeignete Parameterkurven  $\mathcal{K}(\Delta p_1(t), \Pi_3(t))$  kontrolliert in Zuständen intermediärer Tropfen oder konischer Tropfen präpariert werden und dann durch Überführung in Parameterbereiche nicht existenter elektrohydrostatischer Lösungen destabilisiert werden, so dass der initiale Radius des Strahls gezielt eingestellt bzw. ausgewählt werden könnte.

Hinsichtlich der elektrohydrodynamischen Stabilität der berechneten aufgeladenen Tropfen wäre es aus theoretischer Sicht sehr erstrebenswert, dezidierte Stabilitätsaussagen über die berechneten Tropfenformen tätigen zu können, was in weiteren theoretischen Arbeiten verfolgt werden könnte.



# Contents

<b>1</b>	<b>Introduction</b>	<b>1</b>
<b>2</b>	<b>Conical fluid interfaces</b>	<b>7</b>
2.1	The classical Taylor explanation . . . . .	8
2.1.1	Application to electrospaying experiments . . . . .	10
2.2	Critical voltage for ideal Taylor cones . . . . .	10
2.2.1	Taylor's critical voltage . . . . .	11
2.2.2	The electrical Weber number on ideal Taylor cones . . . . .	12
2.2.3	Upshot on the critical voltage . . . . .	13
2.3	The onset of jetting from ideal Taylor cones . . . . .	13
<b>3</b>	<b>Charged and compound droplets</b>	<b>19</b>
3.1	The modified Fuchikami equations . . . . .	22
3.1.1	Solving Fuchikami equations . . . . .	25
3.1.2	Simple droplets . . . . .	29
3.1.3	Compound droplets . . . . .	34
3.1.4	In anticipation of coaxial electrospaying . . . . .	38
3.2	Charged droplets . . . . .	41
3.2.1	The inverse source problem . . . . .	41
3.2.2	Integral equations of the first kind & ill-posedness . . . . .	47
3.2.3	Discretization & validation . . . . .	49
3.2.4	Smoothing . . . . .	51
3.2.5	Regularization . . . . .	52
3.2.6	The impact of resolution and first numerical solutions . . . . .	61
3.2.7	The properties of charged droplets . . . . .	63
3.3	Droplets hanging from a nozzle . . . . .	67
3.3.1	Equilibrium shapes of charged droplets . . . . .	68
3.3.2	Charged mode 3 solutions . . . . .	75
3.3.3	About stability analysis . . . . .	78
3.3.4	Gilbert-Taylor cone angles . . . . .	79
3.3.5	Overcharged droplets . . . . .	83
3.3.6	Controlling the directed Coulomb instability . . . . .	83
3.4	Closed droplets . . . . .	86

3.4.1	Charged droplets of constant volume . . . . .	89
3.4.2	Emission of tiny droplets . . . . .	96
<b>4</b>	<b>Modelling of multi-phase Electrospinning</b>	<b>101</b>
4.1	Electrified colloidal dispersions . . . . .	103
4.2	The model . . . . .	105
4.3	Solving the model . . . . .	109
4.4	Numerical results . . . . .	112
4.5	Conclusions on multi-phase electrospinning . . . . .	119
<b>5</b>	<b>Conclusion &amp; outlook</b>	<b>123</b>
5.1	Conclusion . . . . .	123
5.2	Outlook . . . . .	126
<b>A</b>	<b>Definitions, supplements and derivations</b>	<b>127</b>
A.1	List of symbols . . . . .	127
A.2	List of scales . . . . .	128
A.3	Definition of functions . . . . .	128
A.4	Singular value decomposition and condition . . . . .	130
A.5	Discretized integral equations . . . . .	132
A.6	The potential of a charged ring . . . . .	134
A.7	Ideal conducting sphere in a homogeneous field . . . . .	136
A.8	Experimental determination of the particle density . . . . .	138

# Chapter 1

## Introduction

Electrospinning is a method to produce polymeric fibers from electrified liquids featuring diameters on the micro- and nanometer scale. In industries related to nanotechnology electrospinning is already an established technique of production. Applications range from dust filters for mining vehicles [Grafe and Graham, 2003] of the *Donaldson Company, Inc. (Minneapolis)*<sup>1</sup> to the production of well designed scaffolds in medical tissue engineering [Boudriot et al., 2006]. Some authors envision the production of protective clothing for military applications [Adams, 2001] or the direct application of wound dressing material [Doshi and Reneker, 1995]. At least the ideas about wound dressing are at the threshold to commercialization as this subject is pursued for example by *The Electrospinning company Ltd.*<sup>2</sup> Furthermore, electrified liquids are under consideration as *colloidal thruster* for the propulsion of satellites or spacecrafts [Castro and Bocanegra, 2006, Bartoli et al., 1984, Carretero-Benignos, 2005].

The history of the development of electrospinning begins in the year 1600. In this year Sir William Gilbert published his famous book 'De Magnete' [Gilbert, 1600]. One of his major achievements is the discrimination between electrical and magnetic forces when he investigated attracting forces between materials. Therewith, he was most probably the first person to distinguish between these effects. It follows an excerpt of his argumentation:

“Hence it is probable that amber exhales something peculiar that attracts the bodies themselves, and not the air. It plainly attracts the body itself in the case of a spherical drop of water standing on a dry surface; for a piece of amber held at suitable distance pulls towards itself the nearest particles and draws them up into a cone.“

Sir William Gilbert

By the way, he mentions a conical fluid interface, which nowadays is denominated the Gilbert-Taylor cone that still is a subject of intense research. Conical fluid interfaces due

---

<sup>1</sup>Have a look at <http://www.donaldson.com>.

<sup>2</sup>Have a look at <http://www.nanocentral.eu/ourproviders/the-electrospinnig-company>.

to electrical forces are denominated Gilbert-Taylor cones throughout this thesis, while the term Taylor cone is used to indicate the special properties of conical fluid interfaces related to Taylor's asymptotic explanation, which followed more than three centuries after the discovery by Gilbert. In case the Gilbert-Taylor cone emits a jet from its apex, the process is either called electrospaying or electrospinning, depending on the situation.

The first electrospinning has been mentioned by Rayleigh in 1897 [Burger et al., 2006] followed by the pioneering experiments of Zeleny [Zeleny, 1917], who studied jet emission from electrified droplets hanging from a nozzle. It followed the first patent by Formhals [Formhals, 1934], who already envisioned the production and industrial use of fibers drawn from electrified liquids. In 1964 Sir Geoffrey Taylor explained the observed conical shape of droplets theoretically and performed carefully designed experiments, which validated the theoretical value  $\vartheta_c = 49.3^\circ$  [Taylor, 1964] for the Taylor cone opening angle. Further studies of Taylor emphasized jet emission from Gilbert-Taylor cones [Taylor, 1969]. Inspired by the works of Zeleny and Taylor electrospinning has been introduced to material science by Larrondo and Manley [Larrondo and Manley, 1981], who studied electrified polymer melts that undergo electrospinning and solidify prior to decaying into droplets via the Rayleigh Plateau instability. The liquids typically used are polymeric solutions or polymeric melts [Larrondo and Manley, 1981]. The polymers make the fluid non-Newtonian and suppress the Rayleigh Plateau instability sufficiently long [Clasen et al., 2005] such that the liquid jet solidifies into a fiber of the desired material prior to decomposition into tiny droplets. In case the liquid decomposes into tiny droplets the process is known as electrospaying. In industry this process is used to produce fine sprays for climate machines, medical inhalation, the distribution of paint or applications in mass spectrometry of biomolecules by Fenn et al. [Fenn et al., 1989], who has been awarded the noble price for chemistry in 2002 [Burger et al., 2006].

Although electrospinning is intensively studied experimentally as well as theoretically since the publication by Doshi and Reneker [Doshi and Reneker, 1995], there still is demand for further research. Because of the many physical processes involved predictions on the outcome of an experiment sometimes appear to be a game of pure chance. Consequently, the utilization of electrospinning is still based on trial and error to great extend. From the engineering point of view a good theory is desired to allow useful and reliable predictions on the outcome of a conceivable experiment. This reduces costs, time of development and might allow to control production processes in real time, which is of importance especially for the coaxial electrospinning.

Unfortunately, the many physical processes involved make the development of a theory of electrospinning a challenging task. Figure 1.1 illustrates a classical electrospinning setup with the involved processes:

- Electrospinning is a process far from equilibrium.
- The Navier Stokes equation is a highly nonlinear equation of motion.

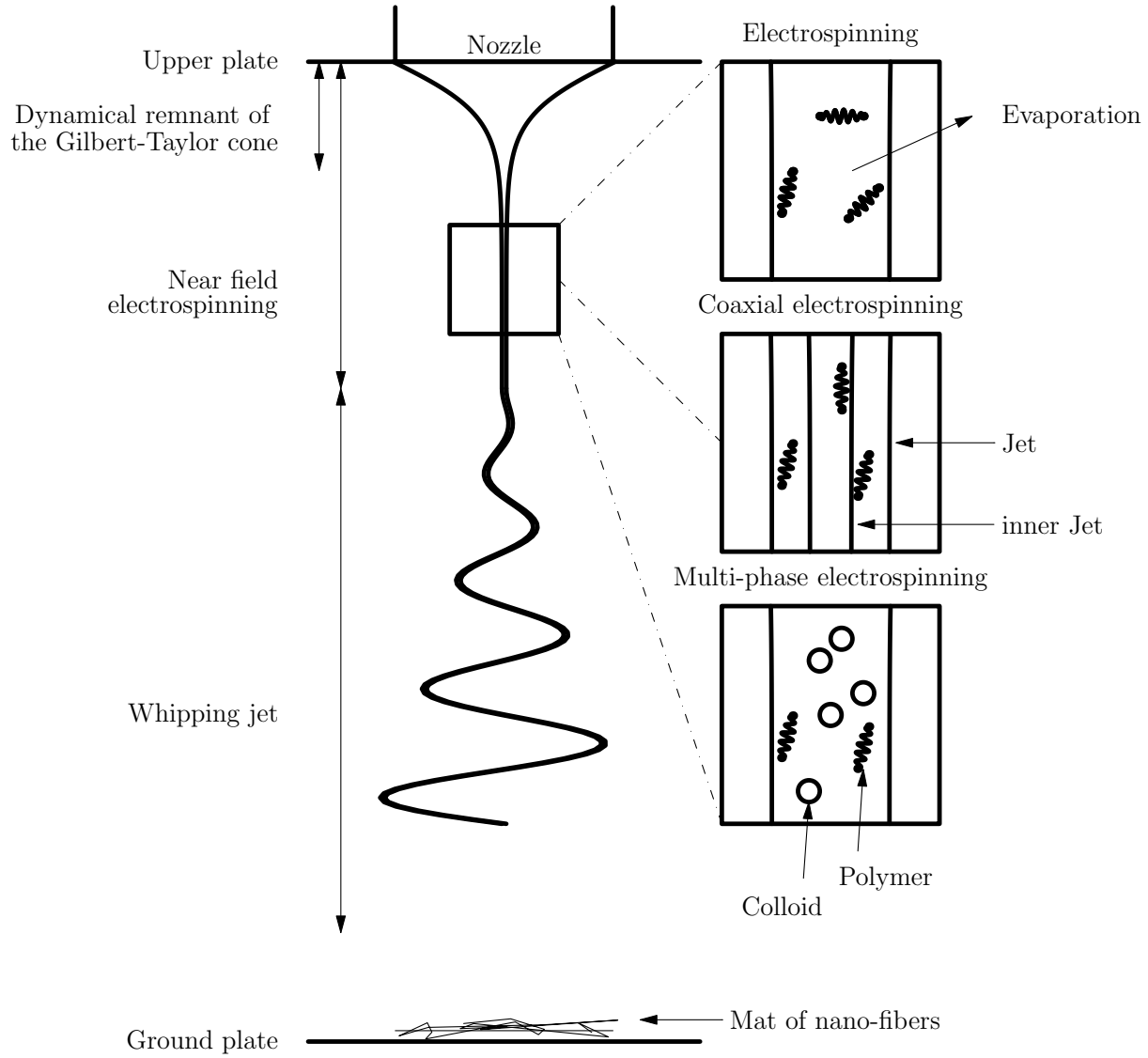


**Figure 1.1:** The classical electrospinning setup consists of a nozzle placed into a plate capacitor, which is charged to a high voltage. The nozzle emits a droplet of a sufficiently conducting fluid consisting of a polymeric solution or melt. The highly charged droplet may eventually result in a Gilbert-Taylor cone that can be destabilized to a *dynamical remnant of the Gilbert-Taylor cone* in order to emit a jet in the so called cone-jet regime. This jet is accelerated and stretched by the electrical field. After a certain distance the *whipping instability* [Hohman et al., 2001a] causes the jet to undergo rampant oscillations. At the ground plate mats of non-woven polymeric nano-fibers are collected. If the jet is conditioned appropriately, an inner jet may be entrained into the outer jet giving rise to *coaxial electrospinning*. In case the fluid consists of a polymeric colloidal dispersion the process is denominated *multi-phase electrospinning*.

- A free surface flow introduces a discontinuous pressure field.
- Surface charges lead to an additional pressure term at the surface, which couples each point of the surface to the shape of the entire jet due to Coulomb interaction. Hence, the presence of charges require a non-local integral description.
- Polymers make the fluid non-Newtonian.
- Evaporation of the solvent introduces sink terms to the balance equations and changes material parameters drastically:
  - Evaporation: Up to 97 per cent of mass evaporates.
  - Density  $\rho$ : Factor of order one.
  - Surface tension  $\gamma$ : Factor of two.
  - Conductivity  $K$ : Orders of magnitude.
  - Viscosity  $\eta$ : Limit process:  $\eta \rightarrow \infty$ .

Variations of the electrospinning process make the system even more complicated:

- Coaxial electrospinning: An inner jet introduces another free surface and changes the flow topology of the outer jet.
- Multi-phase electrospinning: Particles are driven by the flow and feed back to it.

Existing theories aimed at an understanding of the whipping instability of the jet [Hohman et al., 2001a, Hohman et al., 2001b], who extended the earlier works on stability of electrified jets by Saville [Saville, 1970, Saville, 1971b, Saville, 1971a] and Mestel [Mestel, 1994, Mestel, 1995] to the situation of a whipping jet. This whipping instability has been made responsible for the rapid thinning of the jet [Hohman et al., 2001a], but recent developments of the near field electrospinning show that nano-fibers can be produced using electrospinning without the onset of whipping [Sun et al., 2006].

Other theoretical works aimed at finding appropriate scalings for the process variables in a systematic way [Ganan-Calvo, 2004] or studied flow, pressure and electrical field distributions of jet emitting Gilbert-Taylor cones using matched solutions of the cone-jet regime [Cherney, 1999]. Similarly, Higuera investigated the scaling of the electrical current with the flow rate of electrified jets emitted from Gilbert-Taylor cones [Higuera, 2003]. Most of the works published on electrospinning are experimental studies. The many physical effects give theoretical approaches a hard time keeping up with the fast growing amount of experimental findings [Greiner and Wendorff, 2007].

The gateway to the electrospinning process is given by the Gilbert-Taylor cone and its destabilization. An understanding of the onset of jet emission will help improve the control over the entire process and the resulting product. Very interesting contributions to



Gilbert-Taylor cones have been published from the community of liquid metal ion sources (LMIS). These ion sources consist of electrified metallic liquids of very large conductivity that result in very sharp Gilbert-Taylor cones, which emit jets of diameters as small as three nanometers [Forbes, 1997]. Already in 1935 the conical shape has been interpreted by an early version of a self-similarity solution method [Tonks, 1935]. A more advanced study on self-similarity has been performed by Suvorov and Zubarev [Suvorov and Zubarev, 2004], who demonstrated that the equations of electrohydrodynamics possess a self-similar solution with a finite time singularity, which makes electrocapillary waves collapse into a cone that asymptotically is an ideal Taylor cone.

The onset of jet emission has scarcely been studied as typical approaches either stop at the conical singularity or already assume the presence of a jet. This thesis mainly deals with numerically obtained electrohydrostatical solutions of droplets in simultaneous mechanical and electrical equilibrium that develop conical tips. Special emphasis is laid on situations that precede the onset of jet emission.

The outline of the thesis is as follows. Chapter 2 is essentially intended to familiarize the reader with the established insights about Gilbert-Taylor cones, introduces the electrical Weber number  $W_{eE}$  and closes with a short treatise on the onset of jet emission from ideal Taylor cones.

In this thesis two subjects of the electrospinning process illustrated in Figure 1.1 are investigated. The first subject is studied in Chapter 3 and considers quite a universal approach to electrified droplets starting from first principles in order to gain an understanding of the onset of jet emission from Gilbert-Taylor cones. The equations of electrohydrostatics solved, apply to any axisymmetric free surface of an electrified liquid of finite conductivity, whether the fluid is Newtonian, non-Newtonian, features an inner core fluid or carries colloidal particles. This is the key advantage compared to electrohydrodynamical simulations that depend on the rheological properties of the chosen fluid in any case. The method is developed for droplets hanging from a nozzle into a plate capacitor field. In the absence of gravity it also allows to study closed spherical droplets exposed to a homogeneous electrical field. The electrical field enhancement at the conical tips of the latter droplets is interesting in connection with research on lightning discharges in thunderstorms [Ebert, 2008].

The second subject is studied in Chapter 4 and deals with the structures found in the self assembly of colloidal nano wires during multi-phase electrospinning, which is studied using an appropriate modelling approach and statistical analysis. In Chapter 5 conclusions are drawn and an outlook is presented.



# Chapter 2

## Conical fluid interfaces

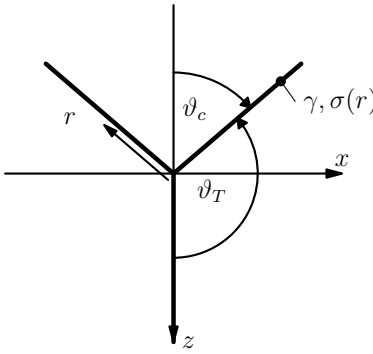
Inspired by the work of Zeleny [Zeleny, 1917] on electrified liquid droplets hanging from a nozzle Sir G.I. Taylor derived the value of the famous Taylor cone angle [Taylor, 1964] from the balance of electrical stress and surface tension namely the balance between Maxwell and Laplace pressure. His carefully designed experiment proved his theoretical finding.

Figure 2.1 illustrates that spherical coordinates are well suited coordinates to describe functions on a conical surface. By choosing spherical coordinates Taylor obtained an impressive asymptotic solution of the governing equations that explains the Taylor cone angle very well. The shortcomings are singularities of physical quantities like the electrical field, the surface charge density and the curvature at the apex of the cone. Even Taylor's photographs of electrified liquid cones reveal that the cone is not arbitrarily sharp at the apex hinting that the curvature and the charge density at the apex stay finite. Charge carriers in positively charged liquids are positively charged ions of finite charge and finite size. Consequently the concentration of charge carriers cannot diverge at the apex of the cone and delimitates the singularity.

In this chapter some fundamentals of conical fluid interfaces are surveyed in order to refer to them throughout this thesis. As the Taylor cone angle plays an important role, Taylor's classical explanation is reviewed briefly, followed by a discussion of the underlying assumptions and the resulting implications. The critical voltage is estimated using the concept of the electrical Weber number  $W_{eE}$ , which renders the entire cone unstable. Estimates on timescales of electrical, viscous and inertial effects reveal jet emission as a directed *Coulomb explosion*<sup>1</sup> [Achtzehn et al., 2005].

---

<sup>1</sup>*Coulomb explosions* [de la Mora, 2007] of droplets are sometimes also referred to as *Coulomb instability* [Achtzehn et al., 2005]. In general it is meant that charge repulsion overcomes surface tension and disintegrates the fluid interface, bursting the droplet into many tiny droplets.



**Figure 2.1:** Spherical coordinates are suitable to consider conical surfaces. The angle  $\vartheta_T$  is the Taylor cone angle,  $\vartheta_c$  the Taylor cone opening angle,  $\gamma$  the surface tension, and  $\sigma$  the surface charge density.

## 2.1 The classical Taylor explanation

Mechanical equilibrium of a charged liquid surface is found by demanding a balance between the Laplace pressure and the Maxwell pressure  $p^L = p^M$  at the surface. The Laplace pressure is given by  $p^L = \gamma\kappa$  with  $\gamma$  the surface tension and  $\kappa = -\cot\vartheta_T/r$  the mean curvature on the cone [Bronstein et al., 1999]. The Maxwell pressure is given by  $p^M = \frac{1}{2}\vec{E} \cdot \vec{D}$ , with  $\vec{E}$  the electrical field and  $\vec{D}$  the dielectrical displacement. For isotropic fluids the dielectric displacement satisfies  $\vec{D} = \epsilon\epsilon_0\vec{E}$  with  $\epsilon$  the relative permittivity of the outer medium. The electrical field is given by  $\vec{E} = -\nabla\phi$  due to the static situation. From these definitions the pressure balance condition is found to be

$$0 = (\nabla\phi(r, \vartheta))^2|_{\vartheta=\vartheta_T} + \frac{2\gamma \cot \vartheta_T}{\epsilon\epsilon_0} \frac{1}{r} \quad (2.1)$$

on a cone in terms of the electrostatic potential  $\phi(r, \vartheta)$ . Obviously the potential satisfies  $(\nabla\phi)^2(r, \vartheta_T) \sim r^{-1}$  on a cone which implies  $\phi(r, \vartheta) \sim r^{\frac{1}{2}}$ . Hence, the ansatz of separation

$$\phi(r, \vartheta) = r^{\frac{1}{2}}f(\cos(x)) \quad (2.2)$$

is reasonable for solving Laplace's equation  $\Delta\phi(r, \vartheta) = 0$  in the region outside of the cone. Using spherical coordinates it follows

$$0 = \left[ \frac{1}{r^2} \frac{\partial}{\partial r} r^2 \frac{\partial}{\partial r} + \frac{1}{r^2 \sin \vartheta} \frac{\partial}{\partial \vartheta} \sin \vartheta \frac{\partial}{\partial \vartheta} + \frac{1}{r^2 \sin \vartheta} \frac{\partial^2}{\partial \varphi^2} \right] r^{\frac{1}{2}} f(\cos \vartheta) \quad (2.3)$$

where the last term of the Laplacian vanishes, as the problem is axisymmetric and therefore independent of  $\varphi$ . Making the substitutions

$$\cos \vartheta = x \quad \Longrightarrow \quad \sin \vartheta = \sqrt{1-x^2}, \quad \frac{\partial}{\partial \vartheta} = -\sqrt{1-x^2} \frac{\partial}{\partial x} \quad (2.4)$$

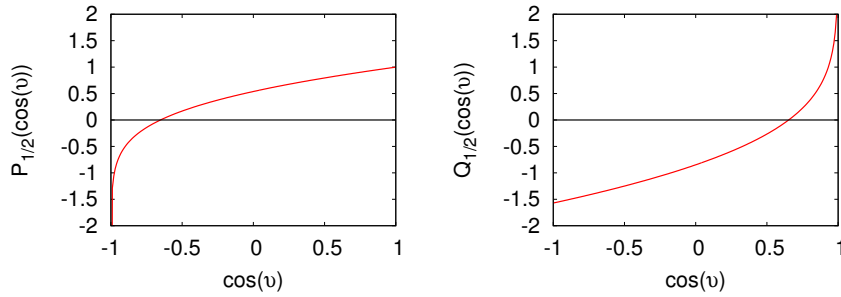


**Figure 2.2:** The Legendre function of the first kind  $P_{\frac{1}{2}}(\cos \vartheta)$  is singular at  $\cos \vartheta = -1$  and possesses one root at  $\vartheta = 130.7^\circ$ . The Legendre function of the second kind  $Q_{\frac{1}{2}}(\cos \vartheta)$  is singular at  $\cos \vartheta = 1$ . Analytical expressions are given in appendix A.3.

equation 2.3 results in

$$0 = (1 - x^2)f''(x) - 2xf'(x) + \frac{1}{2} \left( \frac{1}{2} + 1 \right) f(x) \quad (2.5)$$

which is Legendre's ODE of parameter  $\nu = \frac{1}{2}$ . Hence, the electrostatic potential is given by

$$\phi(r, \theta) = A r^{\frac{1}{2}} \left( P_{\frac{1}{2}}(\cos \vartheta) + \lambda Q_{\frac{1}{2}}(\cos \vartheta) \right) + \phi_0 \quad (2.6)$$

in terms of Legendre functions of the first  $P_\nu(x)$  and second kind  $Q_\nu(x)$  and is uniquely determined up to a constant  $\phi_0$ . As the Legendre function of the second kind  $Q_{\frac{1}{2}}(\cos \vartheta)$  is singular at  $\vartheta = 0$  it is reasonable to set  $\lambda = 0$ . Demanding the equipotential  $\phi_0 = \phi(r, \vartheta_T)$  on a conical surface the potential has to be independent of  $r$ . This implies  $0 = P_{\frac{1}{2}}(\cos \vartheta)$  and therewith selects the unique root of  $P_{\frac{1}{2}}(\cos \vartheta)$  illustrated in Figure 2.2, which determines the Taylor cone angle  $\vartheta_T$ . At that angle  $\vartheta_T = 130.7^\circ$  the pressure balance condition and the equipotential condition are both satisfied consistently. Despite the fact that Taylor computed the angle  $\vartheta_T$  in the literature the complementary angle  $\vartheta_c = 180^\circ - \vartheta_T = 49.3^\circ$  is typically called Taylor cone angle. In the following it will always be made clear in the context if angle  $\vartheta_T$  or  $\vartheta_c$  is of concern.

At this point the underlying assumptions to Taylor's explanation should be discussed as they are subject of justified criticism [Forbes, 1997]. In the derivation only Maxwell and Laplace pressure have been balanced and therefore the hydrostatic pressure has been utterly ignored. Doing so may be considered reasonable as both pressures diverge at the apex, such that the constant hydrostatic pressure can be neglected. However, far from the apex the Maxwell pressure vanishes and a constant hydrostatic pressure will lead to a constant curvature of the surface of the fluid, finally squeezing the cone into a rounded droplet. In Subsection 3.3.4 it is shown that it is the hydrostatic pressure, which influences

the opening angle of the observed cones.

If a closed droplet of given volume is exposed to a large electrical field, the hydrostatic pressure inside the droplet adapts itself such that the surface of the droplet is continuously differentiable at the center. In Section 3.4 it is shown that the resulting opening angle of the conical apex of the droplet is smaller than Taylor's opening angle  $\vartheta_c = 49.3^\circ$  as well, which is ascribed to the larger hydrostatic pressure inside the droplet.

Furthermore, in the classical Taylor explanation the cone is infinitely extended and the surface tension is constant everywhere. This is not necessarily the case, because a large charge density at the apex of the cone goes along with a large concentration of ions that might be responsible for altering the surface tension due to their different chemical nature alone.

Finally, the counter electrode in Taylor's experiment was of the same family of equipotential surfaces as the cone parameterized by

$$R(\vartheta) = R_0 P_{\frac{1}{2}}(\cos \vartheta) \quad (2.7)$$

where  $R(\vartheta)$  is the distance from the apex of the cone to the counter electrode. These are very special electrodes and it can not be taken for granted that the Taylor explanation holds for other types of electrodes without modification [Forbes, 1997].

### 2.1.1 Application to electrospaying experiments

In electrospaying experiments fluid is emitted from Gilbert-Taylor cones in a fine spray that sometimes features a conical shape [de la Mora, 1992]. In these situations the so called space charge effect changes the Taylor cone angle slightly. As the spray cloud of tiny droplets looks like an inverted cone, touching the Gilbert-Taylor cone apex to apex Fernandez de la Mora [de la Mora, 1992] (page 564) or [de la Mora, 2007] (page 227) matches an inverted cone to the angular part of the potential by

$$\phi(r, \vartheta) = r^{\frac{1}{2}} \left[ m P_{\frac{1}{2}}(\cos \vartheta) + n P_{\frac{1}{2}}(\cos(\pi - \vartheta)) \right]. \quad (2.8)$$

It should be noted that the full solution 2.6 already includes an inverted cone, which follows from the identity  $P_{\frac{1}{2}}(x) = -\frac{\pi}{2} Q_{\frac{1}{2}}(-x)$  [Abramowitz and Stegun, 1972] (page 337). Determining an appropriate  $\lambda < 0$  in equation 2.6 yields essentially the same result. Figure 2.3 shows such a plot for  $\lambda = -0.1$ . The left root moves slightly to the left, corresponding to a slightly smaller Taylor cone opening angle  $\vartheta_c$  in case a conical spray is present.

## 2.2 Critical voltage for ideal Taylor cones

Having solved the electrostatical problem of a cone at an equipotential helps predict the voltage necessary to make the fluid collapse into the expected conical surface. In the

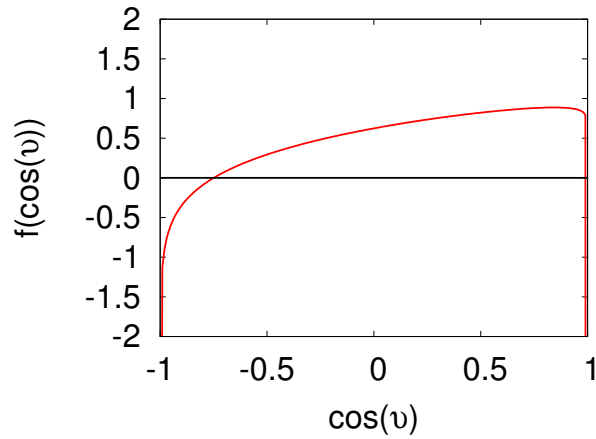


**Figure 2.3:** By choosing  $\lambda < 0$  in equation 2.6 another root appears corresponding to another equipotential conical surface.

following Taylor's estimation of the critical voltage will be reviewed, which relies on the special geometry of his experiment and follows from his solution of the Laplace equation. After that, the electrical Weber number is introduced, which in general measures the ratio between Maxwell and Laplace pressure. Complementary to Taylor's estimate the critical electrical Weber number is considered for an infinitely extended cone. The critical voltage resulting from the electrical Weber number approach is shown to be equivalent to Taylor's estimate apart from a geometric factor, which is  $\approx 1.02$ . The complementary approach via the electrical Weber number elucidates that the entire conical surface is destabilized in case the electrical field increases beyond the critical voltage.

### 2.2.1 Taylor's critical voltage

Taylor estimates a critical voltage for a conical point from the solution of the Laplace equation given by equation 2.6 with  $\lambda = 0$ . The gradient of this potential is found to be

$$\nabla\phi(r, \vartheta)\Big|_{\vartheta=\vartheta_T} = \frac{1}{r} \frac{\partial\phi}{\partial\vartheta}\Big|_{\vartheta=\vartheta_T} = A r^{-\frac{1}{2}} \frac{d}{d\vartheta} P_{\frac{1}{2}}(\cos\vartheta)\Big|_{\vartheta=\vartheta_T} \quad (2.9)$$

which is inserted into the pressure balance condition 2.1 in order to determine the coefficient

$$A = \sqrt{-\frac{2\gamma \cot\vartheta_T}{\epsilon\epsilon_0}} \frac{1}{P'_{\frac{1}{2}}(\cos\vartheta_T)} \quad (2.10)$$

where  $P'_{\frac{1}{2}}(\cos\vartheta_T) = 0.974$ . Taylor used a water / oil interface [Taylor, 1964] with  $\gamma = 0.037 J/m^2$ ,  $\epsilon = 2.2$  and an electrode distance of  $R = 0.0125m$ , which allows to calculate

the critical potential difference from equation 2.6 by using the coefficient 2.10 and  $\phi_0 = 0$  such that the critical voltage is found to be

$$\delta\phi^{crit} = \phi(r, \vartheta = 0) = \sqrt{-\frac{2\gamma \cot \vartheta_T}{\epsilon\epsilon_0}} \frac{1}{P'_{\frac{1}{2}}(\cos \vartheta_T)} R^{\frac{1}{2}} \underbrace{P_{\frac{1}{2}}(\cos \vartheta)}_{=1} \quad (2.11)$$

which is evaluated as  $\delta\phi = 6.5kV$  and has been found to be  $\delta\phi = 7.2kV$  in his experiments.

### 2.2.2 The electrical Weber number on ideal Taylor cones

The electrical Weber number measures the ratio between Maxwell and Laplace pressure according to

$$W_{eE} \stackrel{\text{def}}{=} 2 \frac{p^M}{p^L} = 2 \frac{\frac{1}{2}\epsilon\epsilon_0 E^2}{\gamma\kappa} = \frac{\epsilon\epsilon_0 E^2}{\gamma\kappa} \quad (2.12)$$

where  $E$  is the value of the electrical field at the surface of the conducting fluid,  $\gamma$  the surface tension,  $\kappa$  the mean curvature and  $\epsilon$  the relative permittivity of the surrounding fluid. In case the Maxwell pressure is as large as the Laplace pressure the critical Weber number  $W_{eE}^{crit} = 2$  is obtained. Consequently, no larger electrical Weber number can be found at a static fluid interface. If the Maxwell pressure were larger than the Laplace pressure either the fluid deforms its interface such that a larger mean curvature is provided in order to increase  $p^L$ , or the fluid cannot withstand the electrical forcing anymore and starts moving.

Evaluating the electrical Weber number on an infinitely extended ideal Taylor cone, the electrical field on the surface is given by  $E_{\perp} = A(\delta\phi)/\sqrt{r}$ , where the dependence on the potential difference is hidden in the unknown function  $A(\delta\phi)$ . The mean curvature of the cone again is  $\kappa = -\cot \vartheta_T/r$  such that we obtain

$$W_{eE}(\delta\phi) = -\frac{\epsilon\epsilon_0(A(\delta\phi))^2}{\gamma \cot \vartheta_T} \quad (2.13)$$

which is a function of the applied potential difference  $\delta\phi$ . As the surface charge and normal electric field  $E_{\perp}$  scale linearly with the potential difference it follows  $A^2(\delta\phi) \sim (\delta\phi)^2/R$  for dimensional reasons, where  $R$  is a length scale for the distance between the electrodes, which is chosen to be the same  $R$  as in Taylor's explanation for compatibility. This gives an approximation of the electrical Weber number

$$W_{eE}(\delta\phi) \approx -\frac{\epsilon\epsilon_0(\delta\phi)^2}{\gamma R \cot \vartheta_T}. \quad (2.14)$$

Asking for the critical voltage by setting  $W_{eE}(\delta\phi^{crit}) \stackrel{\text{def}}{=} 2$  yields

$$\delta\phi^{crit} = \sqrt{-\frac{2\gamma R \cot \vartheta_T}{\epsilon\epsilon_0}} \quad (2.15)$$

which is apart from the factor  $1/P'_{\frac{1}{2}}(\cos \vartheta_T) \approx 1.02$  identical to Taylor's critical voltage 2.11.



### 2.2.3 Upshot on the critical voltage

Summarizing the above approaches to the critical voltages of conical fluid interfaces Taylor solved the Laplace equation for a conical fluid interface and derived a critical potential difference for a given adequate experimental setup that has explicitly been designed to satisfy the theoretical assumptions. The complementary approach uses the electrical Weber number that represents a more general approach to any fluid interface independent of a special geometry. Evaluating the electrical Weber number for the special case of Taylor's conical fluid interface the same formula is obtained lacking only the geometry factor related to Taylor's well chosen counter electrode. As this factor is essentially one, there is no considerable difference at all.

The advantage of the electrical Weber number approach becomes obvious from equation 2.13 as it is no longer a function of the spacial coordinates  $r$ ,  $\varphi$ ,  $\vartheta = \vartheta_T$  despite the fact that it has been derived as a spatially resolved property. Hence, the electrical Weber number is constant on the entire cone. In case the critical electrical Weber number is reached, the conical fluid interface is destabilized on the entire surface of the cone.

In the following section a dimensional analysis quantifies the effects that lead to jet emission from a destabilized ideal Taylor cone. In Subsection 3.3.6 to the contrary it will be shown that jet emission from a finite size Gilbert-Taylor cone differs qualitatively from jet emission from an ideal Taylor cone, because a finite size Gilbert-Taylor cone is not destabilized on its entire surface simultaneously, but only in the vicinity of its apex. Once jet emission has started the full electrohydrodynamical problem has to be addressed as is done in [Collins et al., 2007, Carretero-Benignos, 2005, Cherney, 1999, Higuera, 2003].

## 2.3 The onset of jetting from ideal Taylor cones

A destabilized ideal Taylor cone emits a jet from its apex and it is of fundamental interest to explain the emission of a jet that evidently is preferred to a disintegration via an undirected *Coulomb explosion*. In the following an analysis of non-dimensional numbers is performed and two critical length scales are studied with respect to an ideal Taylor cone at the threshold of destabilization.

In the previous two subsections it has been shown that Taylor cones are not stable beyond a critical potential difference i.e. an associated critical electrical field. Furthermore, an infinitely extended ideal Taylor cone is destabilized on its entire surface simultaneously in case the electrical field increases beyond the critical electrical field. The experimental observation is that the almost ideal Taylor cone emits a small jet from its apex in case it is destabilized by the application of too large a voltage difference [Taylor, 1969] Figures 6c, 8b and 10b. In Taylor's experiment a liquid surface is located on top of a large conical electrode, such that the liquid cone appears much larger than it actually is from the point of electrostatics. For this reason these Taylor cones are identified with the experimental realization of ideal Taylor cones in the following.

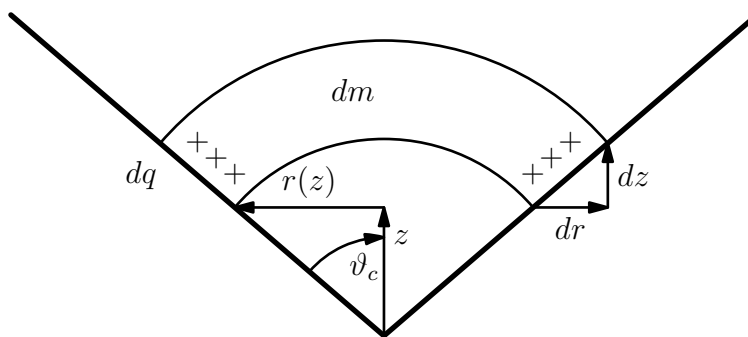


**Figure 2.4:** The cone is sliced in infinitesimal spherical caps of mass  $dm$  and charge  $dq$ .

Regarding the onset of jet emission it will be worked out in Chapter 3 that it makes a difference, whether an infinitely extended Taylor cone is considered or a droplet of finite size that features a conical apex. The difference is that the infinitely extended Taylor cone is destabilized on its entire surface, whereas a closed droplet or a droplet hanging from a nozzle within the homogeneous electrical field of a plate capacitor is just destabilized in the vicinity of its apex as will be shown in Subsection 3.3.5.

In Taylor's study on electrified jets [Taylor, 1969] he mentions that the agreement between theory and experiment is better in case the two plate apparatus is used, which essentially is a plate capacitor with a nozzle and a conical droplet that is considerably smaller than the conical equipotential surface consisting of the Taylor cone on top of the conical electrode of the previous experiments. The following calculation aims at explaining jet emission from the infinitely extended cone that is destabilized on its entire surface.

Many electrospinning or electrospinning experiments involve destabilized Gilbert-Taylor cones and are often based on the application of a constant volume flow rate  $\dot{V}_{ol}$  that has an effect on perturbing the nozzle pressure [de la Mora, 1992, Ganan-Calvo, 1997, Higuera, 2003, Carretero-Benignos, 2005]. From the results that will be presented in Section 3.3 it will be seen that a perturbation in the nozzle pressure can render the droplet unstable, such that the hydrostatic pressure should not be neglected<sup>2</sup>.

The destabilized Taylor cone cannot withstand the electrical forces anymore and fluid is set into motion in order to decrease the electrical Weber number locally. As the charge on the surface is a locally<sup>3</sup> conserved quantity the electrical Weber number can only be lowered

<sup>2</sup>Some authors use ultrasound vibrations to increase the electrospinnability of polymer solutions. The vibrations lower the voltages needed, reduce the viscosity via shear thinning and finally results in finer fibers [Wan et al., 2006].

<sup>3</sup>The infinitely extended Taylor cone is an open system providing any amount of charge necessary to satisfy the electrical boundary conditions from a source located at infinity.

by an increase in curvature or by lowering the surface charge density i.e. by increasing the surface. Decomposing the cone into infinitesimal spherical caps as displayed in Figure 2.4 of infinitesimal  $dz$  the mass and charge associated with the cap are given by

$$dm(z) = 2\pi \rho (1 - \cos \vartheta_c) z^2 dz \quad dq(z) = 2\pi r(z) \sqrt{1 + r'^2(z)} \sigma(z) dz \quad (2.16)$$

with  $r(z) = z \tan \vartheta_c$  and  $r'(z) = \tan \vartheta_c$ . From equations 2.9 and 2.10 of Taylor's solution follows the normal electrical field

$$E_{\perp}(z) = \sqrt{\frac{2\gamma}{\epsilon\epsilon_0}} \frac{1}{\tan \vartheta_c} \frac{1}{\sqrt{z}} \quad (2.17)$$

on the conducting cone, such that  $\sigma(z) = \epsilon\epsilon_0 E_{\perp}$  in equations 2.16 results in

$$\frac{dq(z)}{dm(z)} = \frac{\sqrt{2\gamma\epsilon\epsilon_0}}{\rho} f(\vartheta_c) z^{-\frac{3}{2}} \quad (2.18)$$

with the geometry factor

$$f(\vartheta_c) = \frac{\sqrt{1 + \tan^2 \vartheta_c}}{1 - \cos \vartheta_c} \approx 4.41. \quad (2.19)$$

From Newton's law an estimate for the acceleration and hence the velocity of the fluid surface

$$\ddot{x}(z, t) = \frac{dq(z)}{dm(z)} E_{\perp} \quad \implies \quad v(z, t) \stackrel{\text{def}}{=} \dot{x}(z, t) = \frac{dq(z)}{dm(z)} E_{\perp} t \quad (2.20)$$

can be derived. This estimate holds for times  $t$  satisfying  $0 \leq t \ll \tau_{\epsilon}$  under the assumption that surface tension forces vanish due to the imminent destabilization of the liquid's surface. The velocity  $v(z, t)$  describes the onset of motion of the surface at position  $z$  on the cone shortly after the entire ideal Taylor cone has been destabilized by the application of too large an electrical field. The leaky dielectric timescale  $\tau_{\epsilon} = \frac{\epsilon\epsilon_0}{K}$  is the characteristic timescale for charges to respond to a change in electrical boundary conditions [Saville, 1997] with  $K$  the electrical conductivity and  $\epsilon$  the relative permittivity of the fluid. In order to investigate the behavior of the destabilized cone, the non-dimensional numbers

$$W_e = \frac{\rho v^2 R}{\gamma} \quad W_{eE} = \frac{\epsilon\epsilon_0 E_{\perp}^2 R}{\gamma} \quad C_a = \frac{\eta v}{\gamma} \quad R_e = \frac{W_e}{C_a} \quad (2.21)$$

are the Weber number, the electrical Weber number, the Capillary number and the Reynolds number respectively<sup>4</sup>. These numbers are similarity parameters used to compare different experimental situations of characteristic size  $R$  with a characteristic velocity  $v$ . As an infinitely extended cone at rest does not provide a characteristic length or velocity scale, identifying  $R = z$  and  $v = v(z, t)$  according to 2.20 makes these numbers spatially resolved

---

<sup>4</sup> $W_e$  relates forces of inertia to surface tension forces,  $W_{eE}$  relates electrical forces to surface tension forces,  $C_a$  relates viscous forces to surface tension forces and  $R_e$  relates forces of inertia to viscous forces.

quantities, which measure the relationship of the forces involved, locally. Some algebra reveals the ratios

$$\frac{W_e}{W_{eE}} = \frac{2\gamma}{\rho} \frac{t^2}{z^3} f(\vartheta_c) = \frac{\text{inertial forces}}{\text{electrical forces}} \quad (2.22)$$

$$\frac{C_a}{W_{eE}} = \nu \frac{t}{z^2} \tan \vartheta_c f(\vartheta_c) = \frac{\text{viscous forces}}{\text{electrical forces}} \quad (2.23)$$

$$R_e = \frac{2\gamma}{\rho\nu} \frac{t}{z} \frac{1}{\tan \vartheta_c} \quad (2.24)$$

of these numbers. They conveniently give information about the change of the relative importance of different forces on the cone at position  $z > 0$  shortly after the destabilization. By definition, destabilization occurs at the critical electrical Weber number  $W_{eE}^{crit} = 2$ , such that electrical and surface tension forces stop balancing each other. As the fluid starts moving, the above ratios reveal, which effect grows fastest instantly after the event of destabilization. Obviously, the ratio of viscous forces to electrical forces  $C_a/W_{eE}$  grows linearly in time and hence viscous forces dominate at least for infinitesimal  $t = \delta t$  over forces of inertia. Extracting the timescales

$$\tau_i = \sqrt{\frac{\rho z^3}{2\gamma}} \quad \tau_\nu = \frac{z^2}{\nu} \quad \tau_R = \frac{z\rho\nu}{2\gamma} \quad (2.25)$$

of inertia, viscosity and the growth of the Reynolds number from the ratios 2.22, 2.23 and equation 2.24, quantitative estimates about the initial growth are straightforward.

After time  $t = \tau_R$  has passed the forces of inertia have grown beyond the viscous forces as the Reynolds number increases beyond one. As  $\tau_R$  vanishes in the limit of  $z \rightarrow 0$  it becomes obvious that very close to the apex the electrical forces overcome the initial resistance of the viscous forces quickly in order to mainly work against forces of inertia.

Because the Reynolds number and its time derivative  $\dot{R}_e = 1/\tau_R \tan \vartheta_T$  diverge for  $z \rightarrow 0$  the destabilized cone changes into a free surface flow, where the velocity starts from zero and increases at the apex with a diverging rate. From the definition of the Reynolds number

$$R_e \stackrel{\text{def}}{=} \frac{zv}{\nu} \stackrel{\text{eqn.2.24}}{\sim} \frac{t}{z} \implies v \sim \frac{t}{z^2} \quad (2.26)$$

follows the divergence of the velocity at the ideally sharp apex of the Taylor cone. At the beginning of this chapter it has been reasoned that experimentally observed Gilbert-Taylor cones cannot be ideally sharp at the apex due to the finite charge and finite size of the ions inside the fluid. Consequently, the concentration of ions at the apex is finite. Based on this argument there is no diverging charge density, no diverging curvature and

no diverging electrical field respectively and hence this singularity in  $v$  will also be inhibited.

In conclusion, it is no surprise that the destabilized ideal Taylor cone emits a jet from its apex. The fact that the cone-jet mode is sometimes observed to be a steady state is an indication for the existence of an attractive fixed point in the phase space, which has to be found by solving the full electrohydrodynamics problem [Collins et al., 2007, Carretero-Benignos, 2005, Cherney, 1999, Higuera, 2003, Hohman et al., 2001a].

From the timescales of viscous effects, effects of inertia and charge relaxation

$$\tau_\nu = \frac{l_\nu^2}{\nu} \quad \tau_i = \sqrt{\frac{l_i^3 \rho}{2\gamma}} \quad \tau_\epsilon = \frac{\epsilon\epsilon_0}{K} \quad (2.27)$$

critical length scales  $l_\nu^{crit}$  and  $l_i^{crit}$  can be defined according to the following calculation. The viscous timescale is the time it takes the viscous effects to diffuse imposed momentum up to the viscous length scale  $l_\nu$ . The timescale of inertia is the time it takes a forcing to accelerate fluid visibly up to the length scale  $l_i$  of the flow. Charge relaxation is independent of any length scale. The non-dimensional numbers

$$\Pi_{\nu\epsilon} = \frac{\tau_\nu}{\tau_\epsilon} = \frac{l_\nu^2}{\nu} \frac{K}{\epsilon\epsilon_0} \quad \Pi_{i\epsilon} = \frac{\tau_i}{\tau_\epsilon} = \frac{K}{\epsilon\epsilon_0} \sqrt{\frac{l_i^3 \rho}{2\gamma}} \quad (2.28)$$

relate these timescales and lead to the critical length scales

$$l_\nu^{crit} = \sqrt{\frac{\nu\epsilon\epsilon_0}{K}} = \sqrt{\nu\tau_\epsilon} \quad l_i^{crit} = \sqrt[3]{\frac{2\gamma}{\rho} \left(\frac{\epsilon\epsilon_0}{K}\right)^2} = \sqrt[3]{\frac{2\gamma}{\rho} \tau_\epsilon^2} \quad (2.29)$$

where viscous effects and effects of inertia are as fast as charge relaxation respectively. This is done by setting  $\Pi_{\nu\epsilon} = \Pi_{i\epsilon} = 1$  and solving for  $l_\nu$  and  $l_i$  respectively. These critical length scales are material parameters as they directly depend on the properties of the fluid.

At distances  $l_\nu < l_\nu^{crit}$  from the apex of the destabilized Taylor cone the viscous timescale is smaller than the leaky dielectric timescale. In this situation the charge carriers may be considered more or less fixed inside the moving fluid as they do not have the necessary time to relax. At larger distances  $l_\nu > l_\nu^{crit}$  the situation is the other way around and the charge carriers equilibrate rather quickly compared to a change in electrical boundary conditions while the diffusion of momentum of the impressed momentum on the charge carriers is not sufficient to spread to full extend to the size of the cone  $r(z)$ .

The same argument holds for the critical length of inertia  $l_i^{crit}$ . For small distances  $l_i < l_i^{crit}$  the impressed momentum on the charge carriers changes the velocity of the flow significantly within the time it takes the charge carriers to equilibrate to the changed electrical boundary conditions. For larger distances  $l_i > l_i^{crit}$  the charges equilibrate fast enough

**Table 2.1:** Material parameters of distilled water H<sub>2</sub>O and PLA i.e. Polylactic acid solved in Dichloromethane [Zeng, 2003].

Fluid	$\epsilon$	$\frac{K}{S}$ $\frac{m}{m}$	$\frac{\nu}{m^2}$ $\frac{s}{s}$	$\frac{\rho}{kg}$ $\frac{m^3}{m^3}$	$\frac{\gamma}{J}$ $\frac{m^2}{m^2}$	$\frac{l_{\nu}^{crit}}{m}$	$\frac{l_i^{crit}}{m}$	$\frac{\tau_{\epsilon}}{s}$
H <sub>2</sub> O	$\approx 80$	$\approx 5.5 \cdot 10^{-6}$	$\approx 10^{-6}$	1000	0.072	$1.13 \cdot 10^{-5}$	$1.34 \cdot 10^{-4}$	$1.29 \cdot 10^{-4}$
PLA	$\approx 2$	$\approx 10^{-4}$	$\approx 10^{-5}$	1300	0.028	$1.33 \cdot 10^{-6}$	$1.11 \cdot 10^{-6}$	$1.77 \cdot 10^{-7}$

such that the changes of the flow due to the electrical forcing do not extend to the dimensions of the cone  $z$  and  $r(z)$ .

In conclusion, small scale flows are initiated in shorter times than large scale flows and the initial flow has a lower bound for its small scales given by  $l_{\nu}^{crit}$ . From the material data the time derivative of the Reynolds number and the Reynolds number itself are evaluated using the critical length  $l_{\nu}^{crit}$  from the apex of the cone and at time  $t = \tau_{\epsilon}$  yielding

$$\dot{R}_e(z = l_{\nu}^{crit}) = 1.10 \cdot 10^7 \frac{1}{s} \quad \text{and} \quad R_e(z = l_{\nu}^{crit}, t = \tau_{\epsilon}) = 1414. \quad (2.30)$$

Integrating the velocity over the time interval  $\Delta t = \tau_{\epsilon}$  yields

$$x(z = l_{\nu}^{crit}, t = \tau_{\epsilon}) = 1.5 \cdot 10^{-2} m = 1.5 cm. \quad (2.31)$$

These numbers show that directly after the destabilization the fluid initially located at the critical length  $l_{\nu}^{crit}$  already has traveled large distances compared to the critical length during the time  $t = \tau_{\epsilon}$  it takes the charge carriers to relax according to the electrical boundary conditions that are changed all the time by the flowing charged fluid.

Therefore, it can be stated that the conical fluid interfaces undergoes a *Coulomb explosion* directed along the axis of symmetry. For  $t < \min(\tau_{\nu}, \tau_i)$  viscous forces dominate such that the length scale of the radius of the emerging protrusion will be of the order of the critical viscous length  $l_{\nu}^{crit}$ , which is determined by the material properties of the fluid.

After the protrusion emerged the full electrohydrodynamical problem has to be addressed and for sure effects of inertia will become more important in later phases of the flow. Then, the full electrohydrodynamics problem has to be addressed including electrical forces, viscous forces as in [Eggers and Dupont, 1994], surface tension forces, and perhaps elastical forces originating from polymeric fluids will contribute [Clasen et al., 2005, Feng, 2002].

The qualitative dependence of the critical length  $l_{\nu}^{crit} \sim \sqrt{\nu/K}$  on the kinematic viscosity  $\nu$  and the conductivity  $K$  is in agreement with experimental observations of smaller fibers obtained from electrospinning experiments with decreasing viscosity [Zeng, 2003] (Table 3.1 on page 26) and increasing conductivity [Zeng, 2003] (Table 3.2 on page 28, Figure 3.6 on page 29).

# Chapter 3

## Charged and compound droplets

In physics, technology and daily live, droplets are a physical phenomenon of paramount interest as they are present everywhere. Existing solely due to the attractive van der Waals forces between individual molecules droplets are a subject of classical physics.

In phenomenological thermodynamics the energy of macroscopic physical systems like droplets are described by thermodynamical potentials. Such a thermodynamical potential is Helmholtz's free energy  $F(T, V, A)$ , whose change is described by the total differential

$$dF = -S dT - p dV + \gamma dA. \quad (3.1)$$

The surface tension is a partial derivative of this thermodynamical potential

$$\gamma = \left. \frac{\partial F}{\partial A} \right|_{T,V} \quad (3.2)$$

and measures the amount of free energy contributed to a thermodynamical state by an infinitesimal change of the surface of the interface. This allows a quantitative energetical description of interfaces between phases of molecules in different states of aggregation or phases of molecules of different species.

In case the system is driven out of equilibrium e.g. by exposing droplets to a flow, the interfaces are local storages of energy. If temperature gradients exist or surface active molecules are involved in a two phase flow the interface dynamics get more complicated as the Marangoni effect [Marangoni, 1871] becomes important or tip streaming [Eggleton et al., 2001] sets in. Rigorous fluid dynamics of thermodynamical systems involving multiple phases still represents a challenge.

Gradients in surface energy give rise to forces on the interfaces described by the Laplace pressure  $p^L = \gamma\kappa$  at curved fluid interfaces, which connects the discontinuity in pressure at a fluid interface with the mean curvature  $\kappa$  of the interface. In thermodynamical equilibrium this  $\gamma$  is the same as the one defined by equation 3.2 and just a coefficient for the

pressure otherwise.

Pressure boundary conditions on free surface flows are much less convenient than the classical no slip boundary condition applicable for flows in solid geometries. Reasons for this is the non-vanishing velocity field at the boundary, which is not necessarily continuous at the free surface [Batchelor, 2002] (page 150). Despite the development of numerical techniques<sup>1</sup> the interplay of a moving fluid interface and its feedback on the discontinuous pressure field of the flow causes fundamental problems related to discretization<sup>2</sup> [Scardovelli and Zaleski, 1999]. Nevertheless, in special cases the Navier-Stokes equation can be solved asymptotically using approximations like the slender body theory<sup>3</sup> [Eggers, 1997], which has been used successfully in explaining the pinch off of droplets [Eggers and Dupont, 1994].

In case droplets consisting of a conducting fluid are electrified, electrical charges accumulate on the surface of the droplets and electrostatical effects come into play causing an additional pressure, namely the Maxwell pressure to arise at the fluid interface. Charges located on the surface of a free surface flow are both carried by the flow and conducted within the flow. These two mechanisms are of separate origin as the flow originates from fluid dynamics and the conduction originates from electrodynamics. The charges on the surface of the free surface flow feed back on the fluid dynamics via Maxwell's pressure that is introduced to the pressure balance. These effects introduce a lot of very different timescales to the physical problem and it still is an unsolved problem to reliably predict the motion of electrohydrodynamical free surface flows [Melcher and Taylor, 1969], although some progress has been made on the numerical treatment of electrically induced droplet pinch off [Collins et al., 2007]. Droplets exposed to a homogeneous electrical field have been studied before using different techniques and different limiting cases. Harris et al. studied shape deformations of a perfect dielectric liquid hanging from a rod electrode within a conducting liquid [Harris and Basaran, 1995]. Basaran et al. studied a conducting droplet of constant volume placed on the lower plate of a plate capacitor using a finite element numerical approach [Basaran and Scriven, 1990]. Stone et al. studied a droplet consisting of a perfect dielectric liquid in the presence of a strong electrical field and the absence of gravity. The arising integral equation is a Fredholm integral equation of the second kind that is transformed into a boundary value problem using the slender body approximation. Their integral equations resembles a Fredholm integral equation of the first kind in the limit of a perfectly conducting fluid [Stone et al., 1999].

The coupling of the unknown shape of the droplet and the unknown spatial variation of the electric field has inhibited the development of any exact description of even this static configuration.

Howard Stone et al.

---

<sup>1</sup>Examples are the Volume of fluid method (VOF) or level set methods etc.

<sup>2</sup>For example in the VOF method the solution depends on the method of interpolation used.

<sup>3</sup>The slender body theory is also known as radial expansion method.



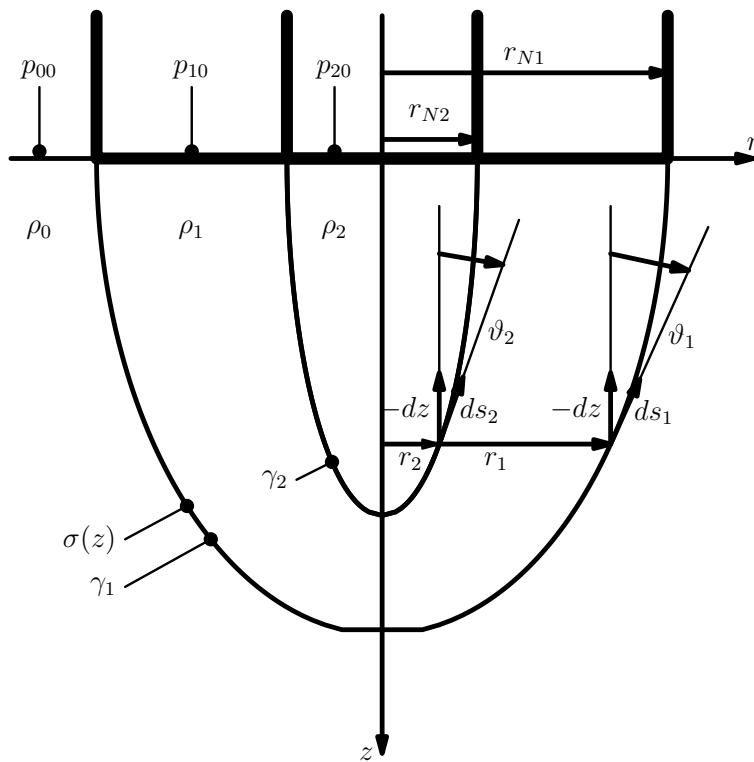


**Figure 3.1:** Two coaxial nozzles emit droplets of different fluids into the surrounding fluid.

The methods developed in this chapter aim at making progress to the solution of the above posed problem from the numerical point of view. At first a method to compute the shapes of droplets hanging from a nozzle in mechanical equilibrium is developed in Section 3.1. This method allows to study compound coaxial droplets, which are studied in Section 3.1.3 briefly. In Section 3.2 the problem of charging an electrostatically neutral droplet by exposure to a static electrical field is discussed. The underlying Fredholm equation of the first kind is derived from first principles and an iterative method of solution is developed in order to solve the equations of electrohydrodynamics numerically. Special focus lies on the exclusion of unphysical solutions to the ill posed Fredholm integral equation of the first kind [Phillips, 1962]. The computed shapes of droplets satisfying mechanical equilibrium and electrical equilibrium simultaneously are presented and discussed in Sections 3.3 and 3.4. Two cases of boundary conditions are considered. A droplet hanging from a nozzle and a closed droplet in the absence of gravity. The Taylor cone angle  $\vartheta_c = 49.3^\circ$  is reproduced in the asymptotic regime of Taylor's calculation, while the presence of a non-vanishing hydrostatic pressure decreases  $\vartheta_c$ .

### 3.1 The modified Fuchikami equations

Fuchikami et al. [Fuchikami et al., 1999] developed a method to compute the shapes of droplets in mechanical equilibrium. The main idea of Fuchikami et al. was to investigate a chaotically dripping faucet starting from rigorous hydrodynamics and determined exact shapes of droplets in mechanical equilibrium hanging from a nozzle. Later Couillet et al. [Couillet et al., 2005] adapted the method for further work on the chaotically dripping faucet. In the following the Fuchikami equations will be derived under three major modifications to the original. In the first place the surrounding fluid is allowed to have a non-zero density in order to take buoyancy effects into consideration. Secondly, the equations are extended in order to allow another fluid interface to be studied inside the droplet, such that the resulting droplets are coaxial compound droplets. Finally, the Fuchikami equations are extended to include an additional Maxwell pressure originating from an externally specified surface charge density  $\sigma(z)$ .

Considering a compound droplet as illustrated in Figure 3.1 with fluid densities  $\rho_i$ , surface tensions  $\gamma_i$  and nozzle pressures  $p_{i0} \stackrel{\text{def}}{=} p_i(z=0)$  the hydrostatic pressure in the fluid is given by

$$p_i(z) = \rho_i g z + p_{i0} \quad i \in \{0, 1, 2\} \quad (3.3)$$

with  $g$  the acceleration due to gravity. The pressure differences at the fluid interfaces are given by the Laplace pressures at interfaces  $i$

$$p_i^L = \gamma_i \kappa_i = p_i - p_{i-1} = \Delta P_i \quad i \in \{1, 2\} \quad (3.4)$$

which is determined by the surface tension  $\gamma$  and the mean curvature

$$\kappa_i = \left( \frac{1}{R_{i1}} + \frac{1}{R_{i2}} \right) \quad (3.5)$$

of the fluid interface  $i$ . The main radii of curvature at interface  $i$  are given by

$$\frac{1}{R_{i1}} = -\frac{d\vartheta_i}{ds_i} \quad \frac{1}{R_{i2}} = \frac{\cos \vartheta_i}{r_i} \quad (3.6)$$

according to the situation on interface  $i$  sketched in Figure 3.2. A fluid of finite conductivity  $K$  charged to a potential  $\phi > \phi_{ground} \stackrel{\text{def}}{=} 0$  provides a non zero ion concentration sensitive to electrical fields  $\vec{E}$ . If external electrical fields penetrate the fluid, the ions will swim along the electrical field lines in order to minimize their potential energy until they are free of unbalanced forces. For charged static droplets, this implies that the electrical field inside the drop will vanish and hence the charges will be localized at the fluid interfaces. From the point of electrostatics conducting fluids behave like liquid metals, which mainly differ in the much larger timescales necessary for the ionic charge carriers to equilibrate. Applying a voltage to a droplet results in an effective surface charge density  $\sigma$ . As illustrated in

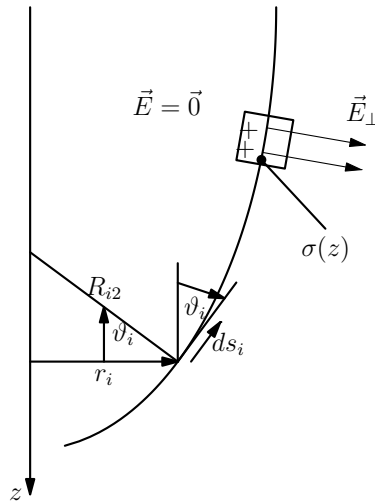


**Figure 3.2:** The variables  $r_i$  and  $\vartheta_i$  are used to describe the Laplace pressure due to curvature. The Maxwell pressure is due to the surface charge  $\sigma(z)$ .

Figure 3.2 the relationship between normal electrical field  $E_{\perp}$  at the surface of the fluid and the associated surface charge density

$$E_{\perp} = \vec{E} \cdot \vec{n} = \frac{\sigma}{\epsilon\epsilon_0} \quad (3.7)$$

is found from Gauss' Law easily. The Maxwell pressure acting on the fluid interface is equivalent to the electrical energy density directly at the surface and originates from the surface charge density via

$$p^M = \frac{1}{2} \vec{E} \cdot \vec{D} = \frac{1}{2} \epsilon\epsilon_0 \vec{E}^2 = \frac{\sigma^2}{2\epsilon\epsilon_0} \quad (3.8)$$

for an electrically isotropic outer fluid satisfying  $\vec{E} = \epsilon\epsilon_0 \vec{D}$ .

The pressure difference  $\Delta p_i$  in equation 3.4 may either arise from a difference in the hydrostatic pressure or from Maxwell's pressure. Therefore, the pressure balance 3.4 has to be extended to include electrical contributions

$$p_1^L = p_1^M + \Delta P_1 \quad (3.9)$$

where  $\Delta P_1 = p_1 - p_0$  is the difference of the hydrostatic pressure at the outer fluid interface. Evaluating equation 3.9 for the outer fluid interface in Figure 3.1 using 3.5 leads to an ordinary differential equation for  $\vartheta_1$

$$\frac{d\vartheta_1}{ds_1} = \frac{\cos \vartheta_1}{r_1} - \frac{(\rho_1 - \rho_0)g}{\gamma_1} z - \frac{p_{10} - p_{00}}{\gamma_1} - \frac{1}{2\gamma_1\epsilon\epsilon_0} \sigma^2. \quad (3.10)$$

From Figure 3.1 the relationship

$$-dz = \cos \vartheta_1 ds_1 = \cos \vartheta_2 ds_2 \quad (3.11)$$

is obvious and results in the identities

$$ds_2 = \frac{\cos \vartheta_1}{\cos \vartheta_2} ds_1 \quad \Longrightarrow \quad \frac{d}{ds_2} = \frac{\cos \vartheta_2}{\cos \vartheta_1} \frac{d}{ds_1} \quad (3.12)$$

allowing to express  $ds_2$  by  $ds_1$  and an ordinary differential equation for  $z$

$$\frac{dz}{ds_1} = -\cos \vartheta_1. \quad (3.13)$$

Furthermore, Figure 3.1 gives way to

$$\frac{dr_1}{ds_1} = \sin \vartheta_1 \quad (3.14)$$

and

$$\frac{dr_2}{ds_2} = \sin \vartheta_2 \quad \xrightarrow{\text{eqn 3.12}} \quad \frac{dr_2}{ds_1} = \cos \vartheta_1 \tan \vartheta_2. \quad (3.15)$$

Proceeding in the same way as in the derivation of equation 3.10 under the use of identity 3.12 and the assumption of an uncharged inner fluid interface the ordinary differential equation

$$\frac{d\vartheta_2}{ds_1} = \frac{\cos \vartheta_1}{\cos \vartheta_2} \left[ \frac{\cos \vartheta_2}{r_2} - \frac{(\rho_2 - \rho_1)g}{\gamma_2} z - \frac{p_{20} - p_{10}}{\gamma_2} \right] \quad (3.16)$$

is derived for  $\vartheta_2$ . Nondimensionalizing equations 3.10, 3.13, 3.14, 3.15 and 3.16 by using the scales

$$\begin{aligned} l_0 &= \sqrt{\frac{\gamma_1}{(\rho_1 - \rho_0)g}} & P_0 &= \sqrt{\gamma_1(\rho_1 - \rho_0)g} = \frac{\gamma_1}{l_0} \\ m_0 &= \rho_1 l_0^3 & \sigma_0 &= \sqrt{\frac{\gamma_1 \epsilon \epsilon_0}{l_0}} \end{aligned} \quad (3.17)$$

for the length, the pressure, mass and the surface charges, respectively, as well as the non-dimensional parameters

$$\begin{aligned} \Pi_1 &= \frac{\gamma_1}{\gamma_2} & \Pi_2 &= \frac{p_{20} - p_{10}}{\rho_1 - \rho_0} \\ \Delta p_1 &= \frac{p_{10} - p_{00}}{P_0} & \Delta p_2 &= \frac{p_{20} - p_{10}}{P_0} \end{aligned} \quad (3.18)$$

results in the non-dimensional system of ordinary differential equations

$$\begin{aligned}
\frac{d\vartheta_1}{ds_1} &= \frac{\cos \vartheta_1}{r_1} - z - \Delta p_1 - \frac{1}{2}\sigma(z)^2 \\
\frac{d\vartheta_2}{ds_1} &= \left\{ \frac{\cos \vartheta_2}{r_2} - \frac{\cos \vartheta_1}{\cos \vartheta_2} \Pi_1 [\Pi_2 z + \Delta p_2] \right\} \Theta(h_0 - z) \\
\frac{dz}{ds_1} &= -\cos \vartheta_1 \\
\frac{dr_1}{ds_1} &= \sin \vartheta_1 \\
\frac{dr_2}{ds_1} &= \cos \vartheta_1 \tan \vartheta_2 \Theta(h_0 - z)
\end{aligned} \tag{3.19}$$

with  $\Theta(x)$  the Heaviside step function, which allows to start integrating the inner droplet at a specified  $z$  coordinate. The modified Fuchikami equations 3.19 describe the hydrostatic shape of a compound droplet satisfying a force balance at the fluid interfaces when integrated from reasonable initial conditions. The system of equations depends on four physical parameters, where  $\Pi_1$  and  $\Pi_2$  are fixed numbers for chosen fluids describing the influence of the surfaces and that of buoyancy, respectively. The parameters  $\Delta p_1$  and  $\Delta p_2$  are operational parameters, which can be adjusted in experiments by controlling the pressure at the nozzles. These equations are an extension of the system of equations originally derived by Fuchikami et al. [Fuchikami et al., 1999], which is reproduced by setting  $\sigma(z) \equiv 0$ ,  $\Delta p_1 = 0$  and by skipping the equations for  $r_2$  and  $\vartheta_2$ .

It should be noted that Fuchikami et al. assumed a constant pressure in the outer fluid, which corresponds to the case without buoyancy that is reproduced by setting  $\Delta p_1 = 0$  in equations 3.19. Their approach is a good approximation for their study of water droplets in air. As electrohydrodynamics experiments often consider droplets of fluid of type 1 emerged within fluid of type 2 [Melcher and Taylor, 1969], parameter  $\Delta p_1$  is not dropped here and will turn out to be important in Subsections 3.3 and 3.4. The modified Fuchikami equations 3.19 allow to study the shapes of different kinds of droplets that will be addressed in the following sections.

### 3.1.1 Solving Fuchikami equations

Before the modified Fuchikami equations are used in order to study shapes of droplets, a method of integration has to be chosen, as the modified Fuchikami equations are stiff sometimes due to the singularities of the  $1/r_1$  and  $1/r_2$  terms. These singularities have to be dealt with by posing an adequate initial condition to the initial value problem. The convergence behavior with respect to the initial condition is of interest and is studied in the

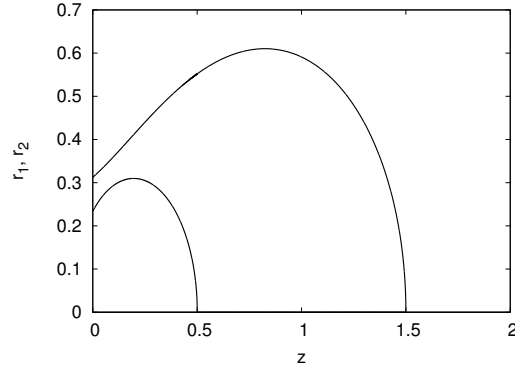


**Figure 3.3:** A compound *s/w/a* droplet is integrated from  $z_0 = 1.5$  and  $h_0 = 0.5$  with  $\Delta p_1 = 2$  and  $\Delta p_2 = 1.5$  with  $\epsilon = 10^{-3}$ .

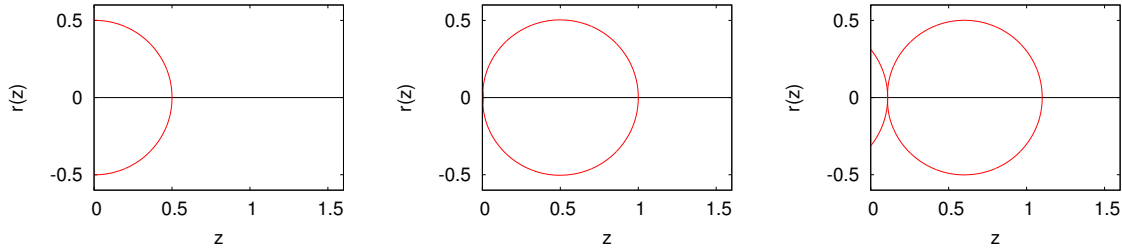


**Figure 3.4:** Integration of a single droplet free of gravity with parameters  $\Delta p_1 = 4$  and  $z_0 \in \{0.5, 1.0, 1.1\}$  respectively yields spherical droplets and shows droplet detachment.

following. The stiffness of the Fuchikami equations is more or less significantly depending on the values of  $\Pi_1$ ,  $\Pi_2$  and  $\Delta p_1$  used. The method of choice for the integration of the Fuchikami equation is a Rosenbrock 4 method, which is very reliable and quite fast for systems of ordinary differential equations of moderate size [Press et al., 1992]. Integrating the Fuchikami equations with parameters  $\Delta p_1 = 2$ ,  $\Delta p_2 = 1.5$ ,  $\Pi_1 = 4.3$  and  $\Pi_2 = -0.16$  from the initial condition  $z_0 = 1.5$ ,  $h_0 = 0.5$ ,  $r_1 = r_2 = \epsilon = 10^{-3}$ ,  $\vartheta_1 = \vartheta_2 = \frac{\pi}{2} - \epsilon$  results in the compound droplet shown in Figure 3.3. The values of  $\Pi_1$  and  $\Pi_2$  used here can be found in Table 3.2 on page 35 and correspond to a compound *s/w/a* droplet that is a droplet of sunflower oil emitted from the inner nozzle and water emitted from the outer nozzle in ambient air.

Unfortunately, the Fuchikami equations 3.19 are singular for the initial condition  $r_1 = r_2 = \epsilon \rightarrow 0$ . By choice of the initial conditions as specified above the limits in the singular terms are well behaved

$$\lim_{\substack{\vartheta \rightarrow \frac{\pi}{2} \\ r \rightarrow 0}} \frac{\cos \vartheta}{r} \stackrel{\text{def}}{=} \lim_{\epsilon \rightarrow 0} \frac{\cos\left(\frac{\pi}{2} - \epsilon\right)}{\epsilon} = \lim_{\epsilon \rightarrow 0} \frac{\sin(\epsilon)}{\epsilon} = 1 \quad (3.20)$$

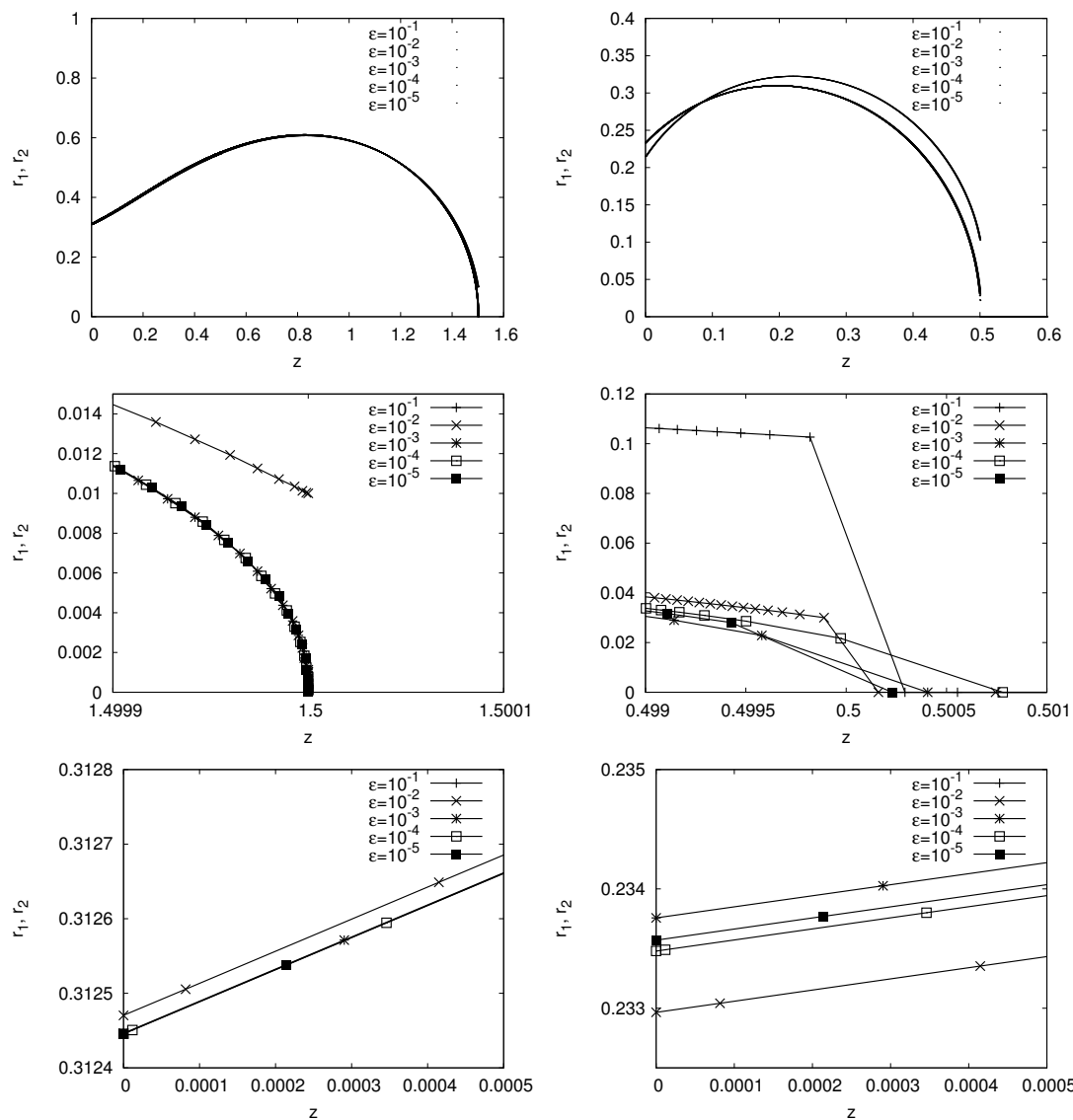
and hence a sequence of decreasing  $\epsilon$  towards zero yields a sequence of solutions that converge to the true solution naturally satisfying  $r_1(z_0) = r_2(h_0) = 0$  and  $\vartheta_1(z_0) = \vartheta_2(h_0) = \frac{\pi}{2}$ .

Figure 3.5 shows the converging sequence of droplets for decreasing  $\epsilon$ . The individual solutions of the sequence of solutions are closely located and can hardly be distinguished in the surveys. The details show that the sequence of solutions of the outer droplet converges rapidly to a single curve and might be considered converged for  $\epsilon \leq 10^{-3}$ . The detail of the inner droplet shows slightly worse a convergence than the outer droplet, but with  $\epsilon \leq 10^{-3}$  the inner nozzle radius  $r_2(z = 0)$  is identical up to one tenth of a percent. A reasonable choice is  $\epsilon = 10^{-3}$ , which gives  $\cos(\frac{\pi}{2} - \epsilon)/\epsilon = 1 - 1.67 \cdot 10^{-7}$  that is considered close enough to one. Unless otherwise mentioned  $\epsilon = 10^{-3}$  will be used whenever the Fuchikami equations are integrated.

In order to validate the correctness of the Fuchikami equations and their implementation the limiting case of a spherical droplet in the absence of gravity may be checked against analytical results. The Laplace pressure within a spherical droplet is given by  $p^L = \gamma\kappa$  with  $\kappa = 2/R$  where  $R$  is the radius of the spherical droplet. Using the scales 3.18 results in the non-dimensional Laplace pressure

$$p^L = \frac{2}{R}. \quad (3.21)$$

In order to obtain a droplet of radius  $R = 0.5$  a non-dimensional Laplace pressure  $\Delta p_1 \stackrel{\text{def}}{=} p^L = 4$  acts within the droplet. A droplet integrated using this pressure under the neglect of gravity is displayed in Figure 3.4 being an evidence for the physical correctness of the Fuchikami equations. The last droplet shows droplet detachment, where the numerical method of integration of the Fuchikami equations inevitably struggle with the vanishing of the radius  $r_1$  due to the singularity  $1/r_1$  in the first of the Fuchikami equations 3.19. In order to overcome this problem the initial condition are restored  $r(z_s) \stackrel{\text{def}}{=} \epsilon$  and  $\vartheta(z_s) \stackrel{\text{def}}{=} \frac{\pi}{2} - \epsilon$  at positions  $z_s$ , where singularities are detected by condition  $r(z_s) < \epsilon$ .



**Figure 3.5:** A sequence of solutions of the same droplet as the one in Figure 3.3 for decreasing  $\epsilon$ . From top to bottom a survey of the sequence of solutions, a detail of the beginning of the integration and a detail of the end of the integration is given, where the left and the right column show the outer and inner droplet, respectively.



### 3.1.2 Simple droplets

In this section the modified Fuchikami equations 3.19 are considered for the study of simple droplets. This is a measure to establish the understanding and the terminology of Fuchikami et al. as a basis for further studies of coaxial droplets in Section 3.1.3 and charged droplets that are considered in Subsections 3.3 and 3.4.

The modified Fuchikami equations 3.19 can be studied in the limit of the original Fuchikami equations

$$\begin{aligned} \frac{d\vartheta_1}{ds_1} &= \frac{\cos \vartheta_1}{r_1} - z - \underbrace{\Delta p_1}_{=0} - \underbrace{\frac{1}{2}\sigma(z)^2}_{\stackrel{\text{def}}{=}0\forall z} \\ \frac{dz}{ds_1} &= -\cos \vartheta_1 \\ \frac{dr_1}{ds_1} &= \sin \vartheta_1 \end{aligned} \tag{3.22}$$

by dropping the equations for the inner droplet and setting  $\sigma(z) \equiv 0$ . The parameters  $\Pi_1$  and  $\Pi_2$  do not occur anymore as they have been dropped together with the equations for the inner droplet. The material parameters like surface tension  $\gamma$  or density  $\rho$  and gravity  $g$  as well have been absorbed in the capillary pressure  $P_0$  and the capillary length  $l_0$ , which still are the appropriate scalings summarized in Appendix A.2.

Integrating these equations from specified initial conditions as outlined in the last section still demands 2 parameters  $z_0$  and  $\Delta p_1$  to be specified. In experiments a nozzle has to be chosen that provides a fixed nozzle radius  $r_n = \text{const}$  giving rise to a boundary value problem that could for example be solved using a shooting method. Taking advantage of the substitution  $\tilde{z} = z - z_0 + \Delta p_1$  reduces equations 3.22 to the original Fuchikami equations. This way the boundary value problem is transformed into an initial value problem that can be integrated starting from  $\tilde{z} = 0$  and resulting in  $r(\tilde{z})$ . Whenever  $r(\tilde{z}) = r_n$  is satisfied a valid solution of a droplet in mechanical equilibrium has been found for the specified nozzle radius. As Fuchikami et al. neglected buoyancy due to the presence of the outer fluid, which is equivalent to setting  $\Delta p_1 = 0$ , the length of the droplet  $z_0 = -\tilde{z}(r = r_n)$  is obtained by integrating the Fuchikami equations. The length of the droplet  $z_0$  is most often multivalued or non-existent in case the nozzle radius is too large as can be seen in Figure 3.6.

Unfortunately, this substitution does not hold in the case of charged droplets as the surface charge density  $\sigma(z) \neq 0$  breaks the symmetry that made this substitution possible. As this study is devoted to the adiabatic charging of primarily uncharged droplets the substitution mentioned above is not used in the following, leaving both parameters  $z_0$  and  $\Delta p_1$  in the

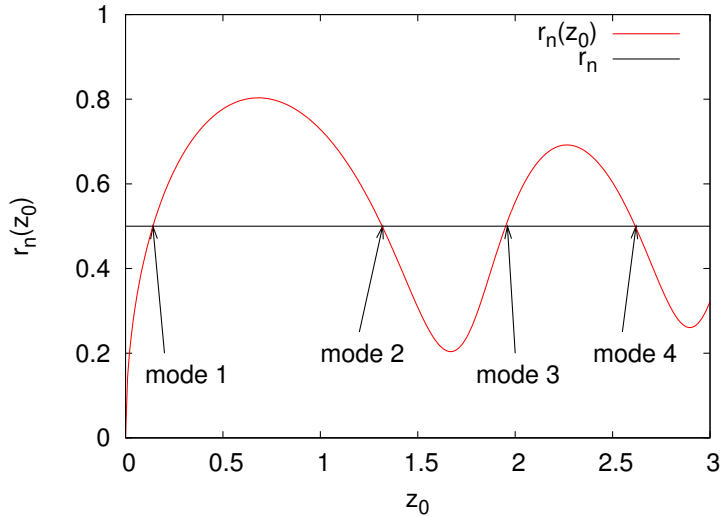


**Figure 3.6:** The nozzle radius  $r_n$  necessary to make the droplet at pressure  $\Delta p_1 = 2.0$  a valid solution can be considered a function of the droplet length  $z_0$ . Choosing a nozzle radius  $r_n \stackrel{\text{def}}{=} 0.5$  shows that there exist several solutions with different  $z_0$ . These solutions are the modes of a droplet hanging from a specified nozzle. For nozzle radii larger than  $\max(r_n(z_0)) \approx 0.8$  there exists no hydrostatic solution.

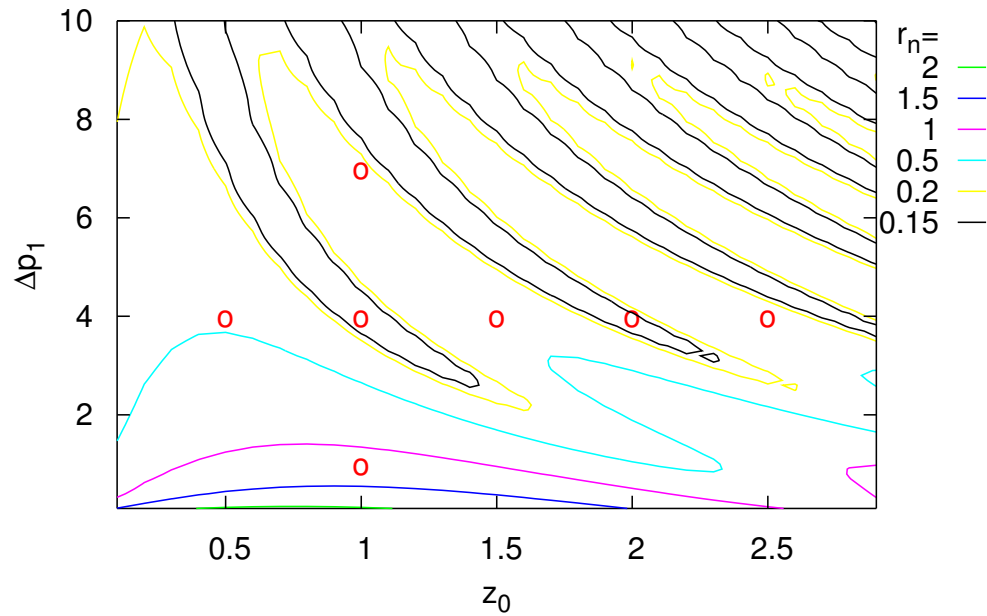
Fuchikami equations and hence keeping it being a boundary value problem.

Integrating the droplets from  $z = z_0$  to  $z = 0$  for the parameters of the two-dimensional parameter space  $(\Delta p_1, z_0) \in \mathbb{R}^+ \times \mathbb{R}^+$  results in a nozzle radius  $r_n = r(z = 0)$  for which the droplet obtained is a valid solution to the problem of a droplet in mechanical equilibrium.

Figure 3.7 shows a contour plot of the nozzle radius  $r_n(\Delta p_1, z_0)$  as a function of the two-dimensional parameter space. The lines in the contour plot are lines of equal nozzle radius  $r_n = \text{const}$ . In the lower part of the figure the qualitative shapes of the droplets are sketched according to the red dots in the contour plot. The more pressure  $\Delta p_1$  is applied from the nozzle for  $z_0 = \text{const}$  the more curved the droplet is, resulting in more and more undulations of the droplet's shape  $r(z)$ . The longer the droplet is i.e. the larger  $z_0$  at constant pressure  $\Delta p_1 = \text{const}$ , the more undulations are found either.

The cyan line of the contour plot is the line associated with  $r_n = 0.5$  and shows how the solutions or modes indicated in Figure 3.6 develop under the variation of the nozzle pressure  $\Delta p_1$ . Figure 3.8 follows the obtained solutions  $r(z)$  of droplets along the cyan line of the contour plot starting at  $z_0 = 0$ . Displayed are solutions that have been computed using a shooting method based on bisectioning in order to achieve a very precise agreement with the selected nozzle radius. First, the solutions  $r(z)$  are mode 1 droplets, whose volume increases for increasing pressure. After the maximum in pressure has been passed, the

a)



b)

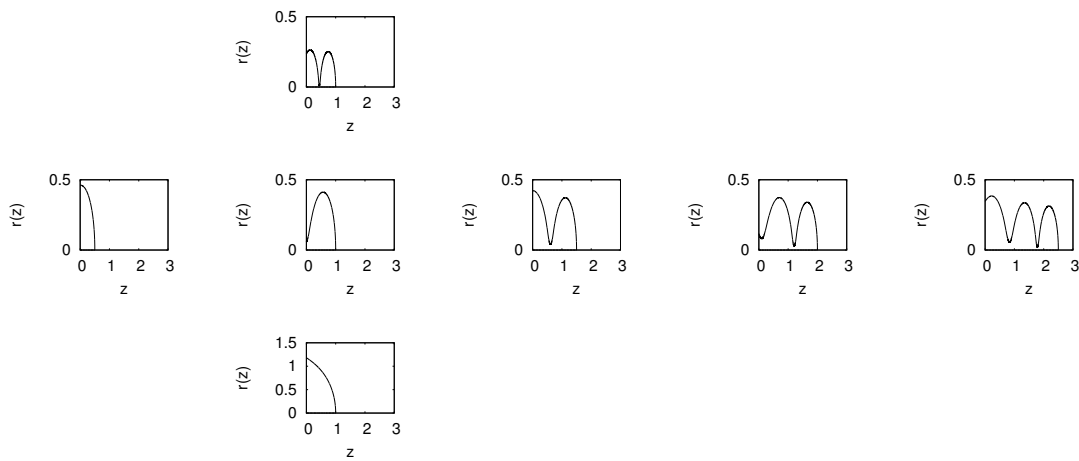


**Figure 3.7:** a) A contour plot of the color coded nozzle radius  $r_n$  as a function of the parameters  $z_0$  and  $\Delta p_1$ . b) Specific points in the parameter space have been marked in the contour plot by red circles, whose solutions are visualized explicitly. Increasing  $z_0$  at constant pressure  $\Delta p_1$  modulates the corresponding nozzle radius. Increasing  $\Delta p_1$  for constant  $z_0$  also modulates the nozzle radius and decreases it.

solutions are mode 2 solutions, where a decrease in pressure results in an increase of  $z_0$  and therewith an increase in volume as well. This might be counterintuitive to the reader as decreasing the pressure at the nozzle results in droplets of larger volume<sup>4</sup>. The correct interpretation is quite simple as larger pressures go along with larger curvatures on the entire droplet that are provided by droplets of smaller volume.

Going further along the cyan line in the contour plot the pressure decreases to a minimum and the last mode 2 droplet that is displayed in Figure 3.8 with  $\Delta p_1 = 1.0$  is so close to the minimum that it almost is a mode 3 droplet as it is not convex anymore. Increasing the pressure from the minimum may by chance lead to a mode 3 droplet that corresponds to the upper branch of the cyan line. The mode 3 droplets are valid solutions up to the next maximum in pressure followed by mode 4 droplets and so forth.

The integration of the Fuchikami equations 3.19 from given initial condition results in droplets in mechanical equilibrium. This means that the pressure balance between forces of gravity i.e. buoyancy and the Laplace pressure are balanced at every point of the surface of the droplets. Whether these solutions are stable with respect to perturbations of the shape is not always obvious from the solutions obtained. The Fuchikami equations arise from a hydrostatical problem and thus cannot describe the stability of a dynamical problem, where the development of perturbations superposed to the static solutions are to be investigated. Therefore dynamical equations are demanded. Fuchikami et al. investigated the stability of the solutions obtained using Lagrangian dynamics [Fuchikami et al., 1999]. It turned out that mode 1 and mode 2 droplets are stable, while all higher modes are unstable such that tiny perturbations in the shape are amplified by the equations of motion in time and give rise to dynamics leading away from the static solution.

From a thermodynamical point of view this outcome is not astonishing at all, as the surface of the droplets contributes to the free energy according to

$$dF = -S dT - p dV + \gamma dA.$$

such that any change in shape that decreases the surface  $dA < 0$  will essentially decrease the free energy and will be energetically more favorable for an incompressible fluid  $dV = 0$  at constant temperature  $dT = 0$ . For any convex droplet an infinitesimal change in shape  $\delta r(z)$  will increase the surface. As mode 1 and mode 2 droplets are found to be convex, it is no surprise that they are stable, while all other modes are neither convex nor stable.

In case of electrified liquid droplets in mechanical and electrical equilibrium statements about the stability of solutions are not obtained easily. The problems associated with this stability analysis will be discussed in Section 3.3.3.

---

<sup>4</sup>By mistake, it might be thought that a larger pressure results in droplets of larger volume as more fluid is pushed out. This interpretation is misleading as this problem is of hydrostatic origin.

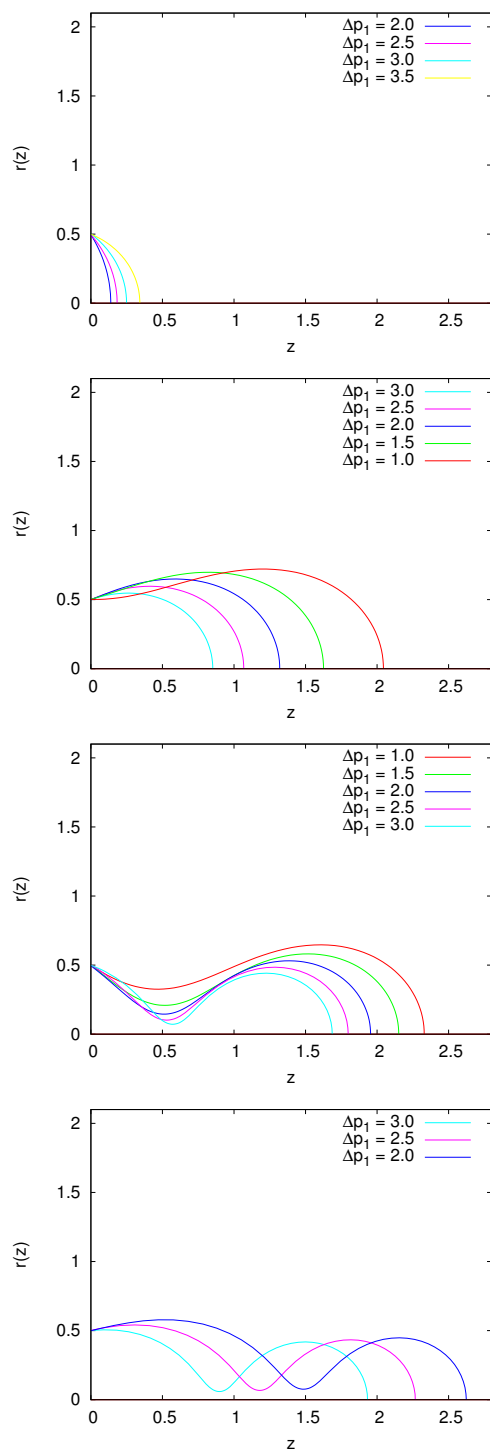


**Figure 3.8:** From top to bottom mode 1, mode 2, mode 3 and mode 4 are illustrated using droplets of nozzle radius  $r_n = 0.5$ . These droplets are found for different color-coded pressures along the cyan contour line of Figure 3.7 (a), which if traversed from left to right corresponds to the keys of the plots read from top to bottom. Mode 1 and 2 are generally stable while modes 3, 4 and higher are all unstable [Fuchikami et al., 1999]. The axes are scaled appropriately, such that the true aspect ratios of the droplets are maintained.

### 3.1.3 Compound droplets

The encapsulation of an inner fluid by an outer fluid is denominated a compound droplet. Compound droplets hanging from a nozzle can be processed by the method of coaxial electrospinning. The inner and the outer fluid form a coaxial jet that undergoes a Rayleigh instability and results in specifically designed microcapsules [Loscertales et al., 2002]. Among applications in material science these microcapsules are also of special interest in pharmacology for the purpose of long term drug delivery [Reithmeier et al., 2001]<sup>5</sup>.

There exist various methods to produce compound droplets like double emulsion processes [Utada et al., 2005], selective withdrawal [Cohen et al., 2001], vapor explosions [Shepherd and Sturtevant, 1982] and electrospinning [Larsen et al., 2003]. They allow to produce compound droplets from a wide variety of fluids for different types of applications. As most of these methods produce microcapsules down to several micrometers, the advantage of the electrospinning method is the accessibility of the sub-micrometer range in capsule diameter.

The modified Fuchikami equations 3.19 allow to study the hydrostatic shapes of compound coaxial droplets hanging from a nozzle. Charging these droplets electrically may eventually result in coaxial electrospinning [Lopez-Herrera et al., 2003, Dror et al., 2007]. The study of the onset of coaxial electrospinning is more complicated than the onset of simple electrospinning. That is because the Gilbert-Taylor cone starts to emit a more complicated compound coaxial jet from its apex. This is a complicated situation as it has to be ensured that the outer fluid entrains the inner fluid appropriately. The outer fluid might undergo single phase electrospinning, while the inner fluid is just accumulated inside the outer droplet.

A vortex of recirculation has been observed in the dynamical remnants<sup>6</sup> of Gilbert-Taylor cones operating in cone-jet mode using tracer particles and long time exposure photographs [Barrero et al., 1998]. This vortex of circulation is in agreement with theory and the presence of a stagnation point inside the dynamical remnant of the Gilbert-Taylor cone [Cherney, 1999]. For this reason the inner syringe sometimes has to be stucked out into the outer droplet by some distance in order to provide that the inner droplet extends beyond the stagnation point as for example in [Lopez-Herrera et al., 2003]. If all these conditions are met, the inner droplet may be entrained into the outer jet if the inner flow rate  $\dot{V}_2$  is large enough and the ratio of viscosities  $\eta_2/\eta_1 \approx 10$  is appropriately tuned [Reznik et al., 2006]. Unfortunately, the latter publication only covers short times after the onset of motion of the compound droplet. Therefore true coaxial electrospinning could not be studied in detail.

---

<sup>5</sup>Microparticles have been used to deliver hormones for medical treatment over a time span of several days and up to two months.

<sup>6</sup>The flow of a jet issuing from the apex of the cone is denominated Taylor cone in the cone-jet mode in the literature. This description is misleading, as the conical shape is no longer the solution of the hydrostatical equations. For this reason the flow will be termed dynamical remnant of the Gilbert-Taylor cone.

**Table 3.1:** The material parameters density  $\rho$ , electrical conductivity  $K$ , relative permittivity  $\epsilon$ , kinematic viscosity  $\nu$  and the resulting dielectric timescale  $\tau_\epsilon$  for sunflower oil, water and air [Lopez-Herrera et al., 2003]. The surface tensions  $\gamma_{ij}$  are symmetric with respect to their indices  $i, j \in \{a, s, w\}$ .

Material	Acronym	$\frac{\rho}{\frac{kg}{m^3}}$	$\frac{K}{\frac{S}{m}}$	$\frac{\epsilon}{1}$	$\frac{\nu}{\frac{m^2}{s}}$	$\frac{\tau_\epsilon}{s}$		$\frac{\gamma_{ij}}{\frac{J}{m^2}}$
Sunflower oil	$s$	840	$8.0 \cdot 10^{-8}$	3.4	$5.1 \cdot 10^{-5}$	$3.76 \cdot 10^{-4}$	$\gamma_{sa}$	$32.8 \times 10^{-3}$
Water	$w$	$10^3$	$1.4 \cdot 10^{-4}$	80	$10^{-6}$	$5.06 \cdot 10^{-6}$	$\gamma_{ws}$	$16.6 \times 10^{-3}$
Air	$a$	1.29	—	1	$1.4 \cdot 10^{-5}$	-	$\gamma_{aw}$	$72.0 \times 10^{-3}$

**Table 3.2:** The resulting non-dimensional parameters occurring in the Fuchikami equations of the three phase systems consisting of sunflower oil, water and air according to their definition summarized in Appendix A.2.

	$s/w/a$	$w/s/a$	$a/w/s$	$a/s/w$	$s/a/w$	$w/a/s$
$\Pi_1$	4.3	2.0	0.23	0.51	2.2	0.46
$\Pi_2$	-0.16	0.19	-6.2	5.2	-0.84	-1.2
	no engulfing	engulfing	no engulfing	engulfing	no engulfing	no engulfing

As any starting point for the electrohydrodynamics problem is a hydrostatical one, it is considered worthwhile to study the shapes of compound droplets in mechanical equilibrium. Charging the droplets then adiabatically may lead to a better understanding of the onset of coaxial electrospinning. For this reason the modified Fuchikami equations are used in order to determine the hydrostatic shapes of droplets in mechanical equilibrium. The equilibrium shapes of these droplets can be studied using the modified Fuchikami equations derived in Section 3.1.

The material parameters of a three phase system successfully used for coaxial electrospinning [Lopez-Herrera et al., 2003] is given in Table 3.1. This system of fluids is well suited for the study of compound droplets or compound jets because of the wetting coefficients

$$S_i = \gamma_{jk} - (\gamma_{ij} - \gamma_{ik}) \quad i, j, k \in \{a, w, s\} \quad (3.23)$$

of this three phase system

$$\begin{aligned} S_a &= -0.0882 J/m^2 < 0 \\ S_w &= -0.0558 J/m^2 < 0 \\ S_s &= +0.0226 J/m^2 > 0. \end{aligned} \quad (3.24)$$

These wetting coefficients indicate that three phase boundaries are energetically unfavorable for this system and will not be observed according to the insights of Torza and Mason [Torza and Mason, 1970, Johnson and Sadhal, 1985]. Instead, complete engulfing and no engulfing will be preferred. A water droplet will be engulfed droplet of sunflower oil surrounded by air  $w/s/a$  and an air bubble will be engulfed by a droplet of sunflower oil surrounded by water  $a/s/w$ , while all other combinations will prefer no engulfing.

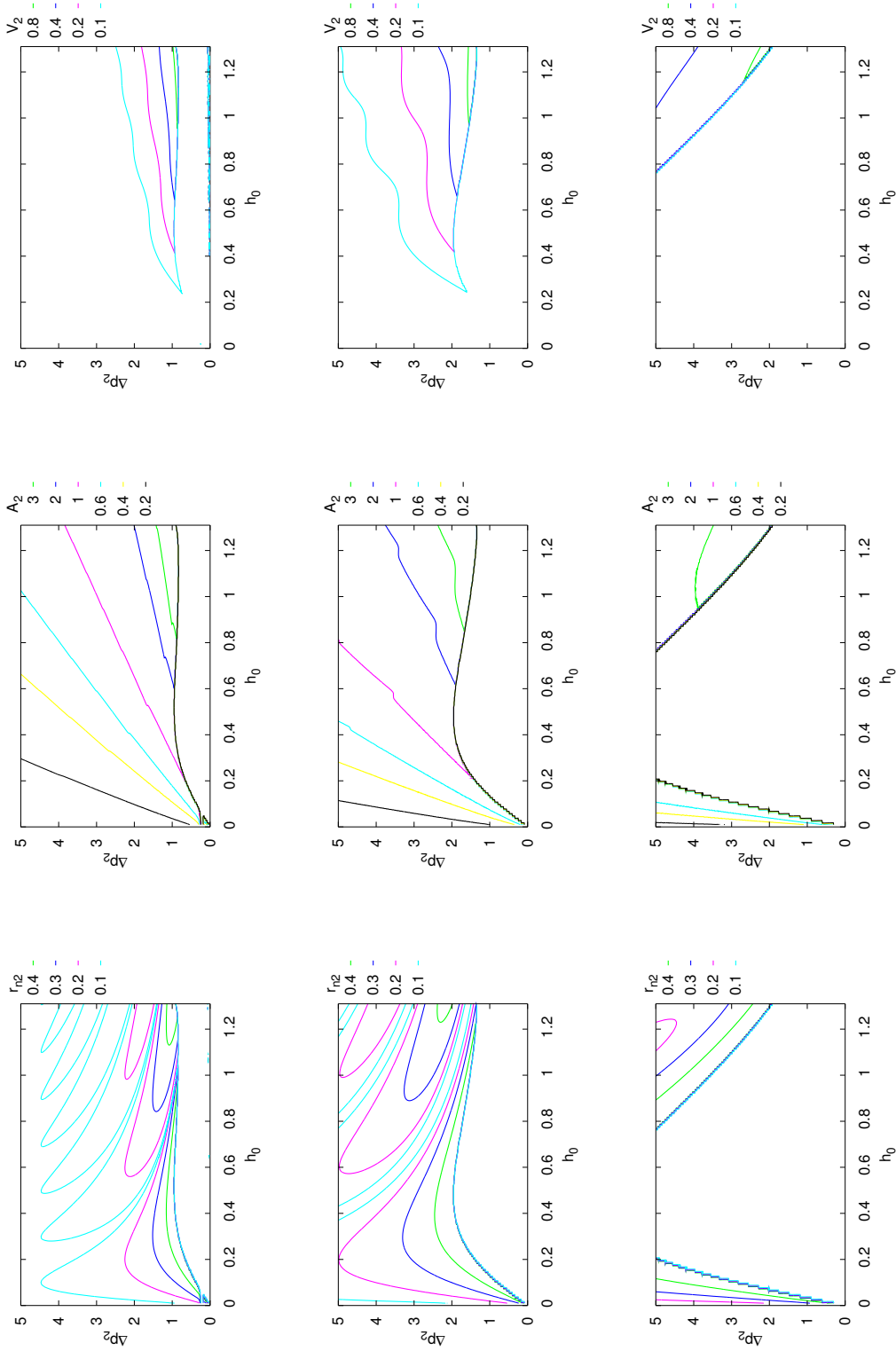


**Figure 3.9:** For a fixed outer droplet with nozzle radius  $r_{n1} = 0.5$  obtained from  $\Delta p_1 = 2$ ,  $z_0 = 1.32$  the resulting properties of the inner droplet are investigated for different combinations of fluids under variation of the parameter  $\Delta p_2$  and  $h_0$ . From top to bottom data plots are shown for compound droplets of types  $s/w/a$ ,  $w/s/a$  and  $a/s/w$ . From left to right the contour plots of inner nozzle radius  $r_{n2}$ , the surface  $A_2$  and the volume  $V_2$  of the inner droplet are displayed, respectively.



From the modified Fuchikami equations 3.19 it can be seen that the equations for the outer droplet i.e. equations 3.22 do not depend on the variables describing the inner droplet  $\vartheta_2$  and  $r_2$ . This means that the outer droplet's surface does not feel a difference arising from the presence of an inner droplet. Consequently, the shapes of the outer droplets are in any case identical to the simple droplets studied in Section 3.1.2, whether an inner droplet is present or not. On the other hand, the inner droplet feels the presence of the outer fluid via the non-dimensional parameters  $\Pi_1$  and  $\Pi_2$ . As long as the outer droplet completely encapsulates the inner droplet the specific shape of the outer droplet  $r_1(z)$  does not have an impact on the hydrostatic shape of the inner droplet  $r_2(z)$ . The reason for this is obvious from Figure 3.1. The curvature at any point of the fluid interfaces is determined by the local pressure balance at that point, which is given by the hydrostatic pressures according to Bernoulli's law. Hence, it makes no difference for the inner droplet, whether it is completely encapsulated inside an outer droplet or a surrounding ocean.

In order to study the inner droplet that is more or less independent of the outer droplet all inner droplets are investigated inside a sufficiently large outer mode 2 droplet. It hits the outer nozzle radius  $r_{n1} = 0.5$  and follows from the parameters  $\Delta p_1 = 2$  and  $z_0 = 1.32$ . This droplet is stable, because it is a mode 2 droplet. In Figure 3.9 the inner nozzle radius  $r_{n2}$ , the inner droplet's surface  $A_2$ , and the volume of the inner droplet  $V_2$  are visualized using contour plots as functions of the parameters  $\Delta p_2$  and  $h_0$ , which determine the shape of the inner droplet  $r_2(z)$ . This figure shows results on three interesting situations:

1.  $s/w/a$ : An inner sunflower oil droplet encapsulated by an outer water droplet in air.
2.  $w/s/a$ : An inner water droplet encapsulated by an outer sunflower oil droplet in air.
3.  $a/s/w$ : An inner air bubble encapsulated by a sunflower oil droplet in water.

The compound  $a/w/s$  droplet turned out to yield no interesting results as the inner droplet just exists as mode 1 droplet. Furthermore, the compound  $s/a/w$  and  $w/a/s$  droplets are not so interesting for the outlined applications as the outer fluid is volatile air.

The lines in the contour plot of the nozzle radius  $r_{n2}$  are similarly shaped as those for the simple droplets in Figure 3.7. The branches between the extrema of these lines have exactly the same meaning as each branch is associated with the corresponding mode of the inner droplet. The differences to the contour plot of the simple droplet lies within the deformations of these contour lines as the minimum between the branches of mode 2 and mode 3 is almost irresolvable in the  $s/w/a$  and not existent  $w/s/a$  plot. This means that a droplet showing necking is not easily found in the parameter space of the compound  $s/w/a$  droplet. The minimum in the  $w/s/a$  droplet is found for values of  $h_0$  where the inner droplet extends far beyond the outer droplet, which is unphysical. Furthermore, at too low pressure differences  $\Delta p_2$  the inner droplet is not curved enough, such that the solutions violate  $r_2(z) < r_1(z) \forall z \in [0, h_0]$  i.e. the fluid interfaces of the inner and outer droplet intersect, which results in an invalid solution. Points in parameter space  $\Delta p_2 \times h_0$

located below the contour line  $r_{n2} = 0.1$  associated with low pressure  $\Delta p_2$  lead to such invalid solutions.

The choice of the outer droplet i.e. the choice of  $\Delta p_1$  and  $r_{n1}$  restricts the obtainable solutions of the inner droplet. The contour lines of the surface  $A_2$  of the inner droplet show that the surface of the droplet may be kept constant in case the pressure  $\Delta p_2$  is increased more or less monotonically with the length  $h_0$  of the droplet. Just in case a mode switch occurs the growth in surface is slowed down. The volume  $V_2$  of these droplets indicates mode switches more sensitively in regions where  $\Delta p_2(h_0)|_{V_2 \stackrel{\text{def}}{=} \text{const}} \approx \text{const}$ .

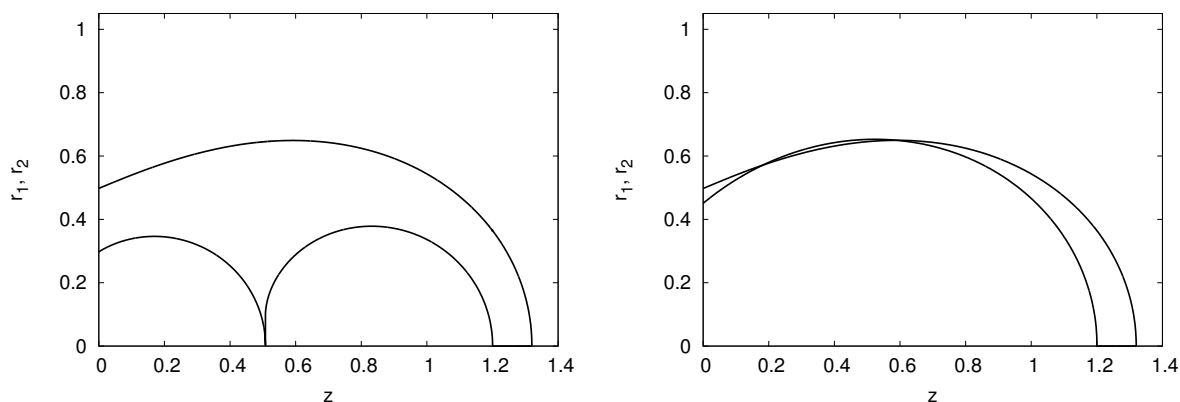
Figure 3.10 displays some example solutions that illustrate the new features of the inner droplets due to the additional inclusion of buoyancy to the Fuchikami equations. As buoyancy is present a lighter inner fluid like sunflower oil submerged into a water droplet is exposed to buoyancy and swims up. Due to this fact, the unstable mode 4 droplet displayed in Figure 3.10 a) shows a very short neck, such that the mode 4 droplet more or less decayed into two droplets. As the mode 4 droplets are not stable, the neck is practically not present resulting in two isolated inner droplets; one droplet being something like a mode 2 droplet and the other about to float away freely. Due to the upward buoyancy the free floating droplet is pushed up. The buoyancy is indicated by a decrease of  $r_2(z)$  in the lower part and an increase in the upper part of a droplet that would be spherical in case it is free of gravity. In Figure 3.10 b) the droplet's fluids have been swapped to a compound  $w/s/a$  droplet. A comparable inner mode 4 droplet only exists for a much larger pressure. The effect of buoyancy is reversed, as the inner water droplet is about to fall right through the sunflower oil. The deformations of the droplets towards the ground is much less characteristic as the inner pressure is much larger and diminishes the effect of deformation. The neck of the unstable inner mode 4 droplet is well resolved. The  $a/s/w$  droplet in Figure 3.10 b) (right) shows an inner droplet that extends very far into the outer droplet. As the inner and the outer droplet are both mode 2 droplets this configuration is stable. The outer fluid is a well behaved liquid shell of the encapsulated inner fluid that forces the outer fluid to flow around the inner droplet in case dynamics sets in by e.g. the application of an electrical field. Hence, an inner droplet of this kind is considered expedient for the entrainment into an outer jet if the droplet is electrified for the purpose of electrospinning or electrospraying.

### 3.1.4 In anticipation of coaxial electrospraying

Figure 3.11 shows two examples of compound  $w/s/a$  droplets that are considered unsuitable and suitable for electrospraying applications, respectively. In case the outer droplet is exposed to a large electrical field, it will be deformed into a conical droplet like the droplets shown in Figure 3.24 in Subsection 3.3.1.

After a sufficiently long time, all charge carriers inside the droplet will be located at the surface of the outer droplet and maintain the droplet in mechanical and electrical equilib-

a)



b)

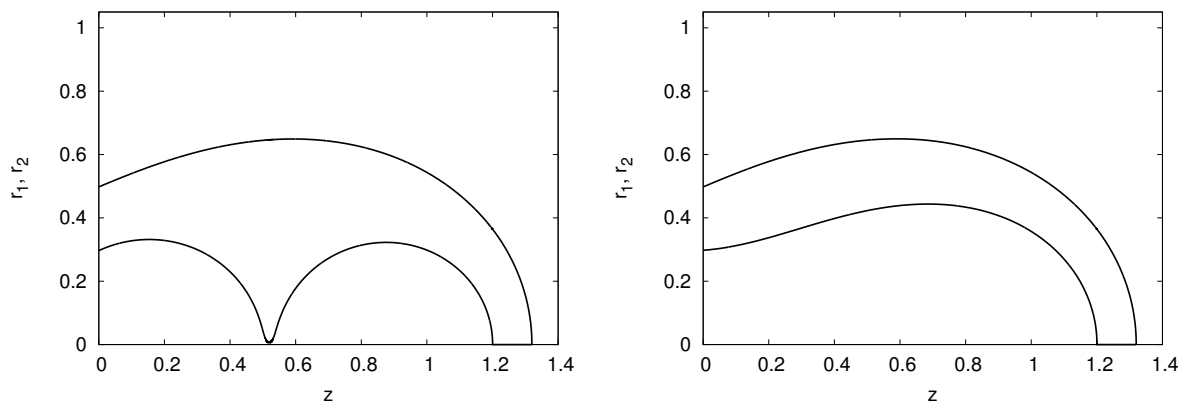


**Figure 3.10:** Compound droplets for the outer and inner nozzle radii  $r_{n1} = 0.5$  and  $r_{n2} = 0.3$ , respectively. a) For parameters  $\Delta p_2 = 1.35$  and  $h_2 = 1.2$  an  $s/w/a$  droplet (left) is a valid solution for these nozzle radii. Buoyancy pushes up the inner sunflower oil towards the nozzles causing an asymmetric shape  $r_2(z)$ . At the neck  $z \approx 0.5$ , the Fuchikami equations are stiff. If the inner droplet detaches and floats to outer droplet's interface, it will leave the outer droplet, as the  $s/w/a$  system prefers no engulfing. For the same parameters an  $w/s/a$  droplet (right) is an invalid solution as the droplet's surfaces interpenetrate. b) The  $w/s/a$  droplet (left) hits the nozzles for a larger pressure  $\Delta p_2 = 2.9$  and shows a slightly asymmetric shape towards the ground due to lack of buoyancy. At the neck  $z \approx 0.5$  the Fuchikami equations are well behaved. The  $a/s/w$  droplet (right) at  $\Delta p_2 = 3.65$  reveals a shape appropriate for entrainment in a coaxial jet, as it extends sufficiently far to the apex of the outer fluid in a stable mode 2 bubble. The compound  $w/s/a$  and  $a/s/w$  droplets prefer engulfing such that a detached inner droplet will stay inside the outer droplet.

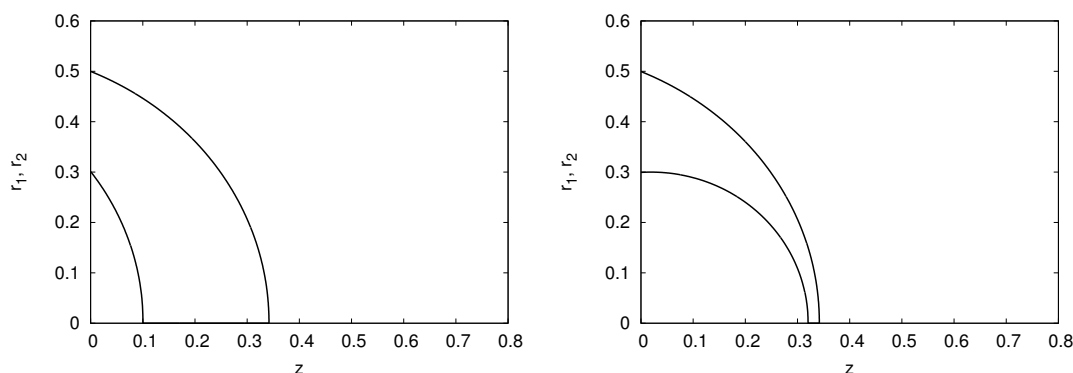


**Figure 3.11:** Two examples of compound  $w/s/a$  mode 1,1 droplets similar to those in [Lopez-Herrera et al., 2003] at nozzles  $r_{n1} = 0.5$  and  $r_{n2} = 0.3$  that are unsuitable and suitable for coaxial compound electrospinning, respectively. In the first case the inner droplet is not extended far enough into the outer droplet to be readily entrained by viscous forces in case the outer fluid starts jet emission by being subjected to sufficiently large an electrical field. The parameters are  $\Delta p_1 = 3.5$ ,  $z_0 = 0.3$  with  $\Delta p_2 = 2.0$ ,  $h_0 = 0.1$  and  $\Delta p_2 = 3.5$ ,  $h_0 = 0.32$ , respectively.

rium at the same time. This means that the inner droplet does not feel any difference to the hydrostatic problem as long as its solution stays valid with respect to the encapsulation inside the outer fluid  $r_2(z) < r_1(z) \forall z \in [0, h_0]$ . If this condition is satisfied in the static case, but violated in the charged case, there exists no solution to this electrohydrostatical problem inevitably giving rise to the onset of fluid motion. Thus, in this case the coaxial jet emission can only be understood from the full dynamical problem. If the condition is satisfied for the static and the charged droplet, the inner droplet may be encapsulated by an electrified conical droplet, which might cover the inner droplet with a similar thickness as the uncharged droplet in Figure 3.11. The inner water droplet provides a shorter electrical relaxation time than sunflower oil (see Table 3.1). An increase in the electrical field causes charge carriers to approach the droplet from the nozzle such that the charge carriers are quickly located at the inner fluid interface as has been argued by Lopez-Herrera et al. [Lopez-Herrera et al., 2003]. It takes the charge carriers much longer to relax in the outer fluid as its charge relaxation time is much larger. This way the outer fluid may be *driven*<sup>7</sup> by the inner fluid as the inner fluid is deformed accordingly, *driving* the outer fluid to jet emission.

Compound coaxial electrospinning and electrospinning are poorly understood in detail, but the results of this section in combination with the results of Section 3.2 on charged droplets may help focus research on the onset of jet emission.

<sup>7</sup>Making a not sufficiently conducting fluid electrospinnable by coupling it to a conducting fluid for coaxial electrospinning is denominated *driving* in the literature on coaxial electrospinning.

## 3.2 Charged droplets

In this section a method is developed that allows to compute the shapes of electrostatically charged liquid surfaces.

The liquid surfaces under consideration either are shapes of droplets of conducting fluids hanging from a nozzle or surfaces of spherical droplets of conducting fluid in the absence of gravity. These droplets are exposed to an external electrical field and change their shape accordingly. Both situations are interesting for applications and have to be treated separately as the corresponding boundary conditions differ. The first situation is realized in the Taylor experiments, which also affect electrospinning or electrospinning experiments while the second situation applies to free falling droplets exposed to an electrical field. The latter case is a clinical idealization of what might happen to droplets within a thunderstorm. These two situations differ in the underlying Fuchikami equations, the control parameters and the boundary conditions.

In the first situation the droplet hanging from the nozzle is exposed to gravity and the Fuchikami equations are given exactly by equations 3.19. The pressure  $\Delta p_1$  is an operational control parameter to be controlled by the experimentalist. Furthermore, the droplet is treated as an open system, which is supplied with arbitrary amounts of fluid and charge from the nozzle such that the radius  $r(z)$  hits the nozzle radius  $r(z=0) \stackrel{\text{def}}{=} r_n = \text{const}$  while the derivative  $r'(z=0)$  is unrestrained.

In the second situation the droplet is falling such that gravity is switched off in the Fuchikami equations, which corresponds to dropping the two explicit  $z$  terms on the right hand side of equations 3.19. The fluid volume  $V_{ol} \stackrel{\text{def}}{=} \text{const}$  is a physical control parameter for a given spherical droplet, which is to be charged. The derivative  $r'(z=0) \stackrel{\text{def}}{=} 0$  is fixed, while the radius  $r(z=0) \in \mathbb{R}^+$  is formally unrestrained and will implicitly be determined by the electrical field and the constant volume of the droplet. The pressure  $\Delta p_1$  becomes a dependent variable, which is implicitly determined by the control parameters volume  $V_{ol}$  and electrical field  $E^{pc}$ . Table 3.3 summarizes the relationships between the variables in both situations.

### 3.2.1 The inverse source problem

The iterative algorithm to solve for charge densities and droplet shapes, which simultaneously satisfy mechanical and electrical equilibrium at the droplet's surface is illustrated in Figure 3.12. The Fuchikami equations have been derived under the inclusion of a specified surface charge  $\sigma(z)$ . Given a surface charge  $\sigma(z)$ , the integration of the Fuchikami equations results in the shape  $r(z)$  of the droplet. Using  $r(z)$  and  $\sigma(z)$  i.e. a charge density of

**Table 3.3:** Two different situations of electrified droplets differ in boundary conditions (b.c.), parameterization and observables. The role of  $\Delta p_1$  and  $V_{ol}$  are interchanged and the radius  $r(z=0)$  behaves differently. For the nozzle droplet  $q$  is the amount of monopole charge on the droplet. The closed droplet is uncharged such that  $q$  is the monopole charge on a semi-droplet due to polarization.

Type of variable	Nozzle droplet	Closed droplet	Description
Boundary condition:	$\phi(r(z), z) \stackrel{\text{def}}{=} \phi_0 \stackrel{\text{def}}{=} 0$ $r(z=0) \stackrel{\text{def}}{=} r_n$	$\phi(r(z), z) \stackrel{\text{def}}{=} \phi_0 \stackrel{\text{def}}{=} 0$ $r'(z=0) \stackrel{\text{def}}{=} 0$	equipotential b.c. radius b.c.
Parameters:	$E^{pc}$ $\Delta p_1$	$E^{pc}$ $V_{ol}$	plate capacitor field pressure, volume
Observables:	$r(z)$ $\sigma(z)$ $V_{ol}$ $A$ $q$ $\vec{p}$ $E$	$r(z)$ $\sigma(z)$ $\Delta p_1$ $A$ $q$ $\vec{p}$ $E$	radius charge density volume, pressure surface monopole charge dipole moment energy of state

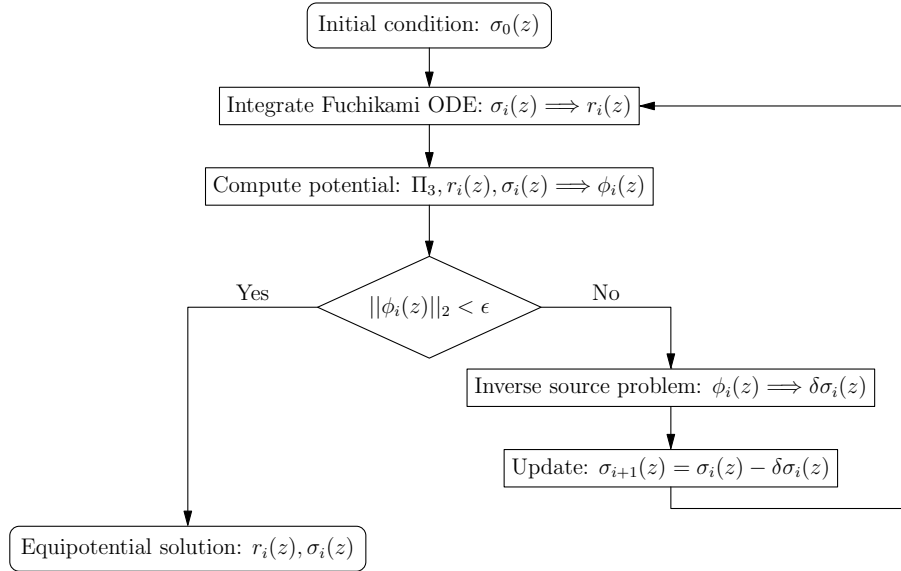


**Figure 3.12:** The algorithm to approach the solution of a charged equipotential droplet in simultaneous mechanical and electrical equilibrium. After the solution  $r(z)$ ,  $\sigma(z)$  has been obtained, the electrical field  $\Pi_3 \rightarrow \Pi_3 + \Delta\Pi_3$  may be increased slightly. Restarting the algorithm with  $\sigma_0(z) \stackrel{\text{def}}{=} \sigma(z)$  then adiabatically charges a droplet. Convergence may not be achieved for large fields without appropriate initial charge density  $\sigma_0(z)$ .

the form  $\rho(\vec{x}) = \sigma(z) \sqrt{1 + r'^2(z)} \delta(r - r(z))$  the potential is given by

$$\phi(\vec{x}) = -E^{pc} \vec{x} \cdot \vec{e}_z + \frac{1}{4\pi\epsilon\epsilon_0} \int_{\mathbb{R}^3} \frac{\rho(\vec{x}')}{|\vec{x} - \vec{x}'|} d^3\tilde{x}. \quad (3.25)$$

The first term originates from the plate capacitor boundary condition and the second term from the Newtonian potential arising from the charge density  $\rho(\vec{x})$  distributed on the droplet. This potential has been gauged to the equipotential  $\phi_0 = 0$  on the droplet.

The problem of finding the charge density  $\rho(\vec{x})$  for a specified potential is an inverse source problem. In general these problems suffer from non-uniqueness [Kirsch, 1996]. A well-known example of an inverse source problem is the Coulomb potential, which may originate from of a point charge or from any other bound charge distribution of spherical symmetry. These charge distributions provide the same Coulomb potential in the outside of their domain. Determining the charge density from such a given potential there exist many solutions to the problem and additional knowledge is needed in order to choose the specific solution that is of interest.

Fortunately, the situation is not that bad as physical restrictions to the problem exist. The restriction to axisymmetric charge densities located on the axisymmetric surface of the droplet provides a lot of additional information that reduces the amount of possible solutions drastically. These restrictions allow to reformulate equation 3.25 in terms of the Green's function of charged rings, which is derived in appendix A.6 according to Zhu [Zhu, 2005] for the sake of completeness.

Due to the restriction to an axisymmetric problem, the potential on the surface of the droplet

$$\phi(z) \stackrel{\text{def}}{=} \phi(\vec{x}) \Big|_{\vec{x}=r(z)\vec{e}_r+z\vec{e}_z} \quad (3.26)$$

may be written as a function of  $z$  defined on the entire droplet and its image charge. The deviation from the equipotential  $\phi_0 = \phi(z = 0) = 0$  is measured using the 2-norm  $\|\phi(z)\|_2$ . If this norm falls below  $\epsilon > 0$  the pair  $r(z)$ ,  $\sigma(z)$  is considered a solution to the problem of determining a droplet in mechanical and electrical equilibrium. If the norm is larger than  $\epsilon$  the inverse source problem

$$\phi(\vec{x}) = \frac{1}{4\pi\epsilon\epsilon_0} \int_{\mathbb{R}^3} \frac{\delta\rho(\vec{x}')}{|\vec{x} - \vec{x}'|} d^3\tilde{x} \quad (3.27)$$

has to be solved in order to obtain a new charge density  $\rho_{i+1}(\vec{x}) = \rho_i(\vec{x}) - \delta\rho_i(\vec{x})$  that hopefully decreases  $\|\phi(z)\|_2$ . Expecting a change in surface charge, the expectation on the charge density is  $\delta\rho(\vec{x}) = \delta\sigma(z) \sqrt{1 + r'^2(z)} \delta(r - r(z))$  such that the inversion of the above equation yields a suggested change  $\delta\sigma(z)$  under the assumption that  $r(z)$  does not change too much. It is noteworthy that the algorithm converges to the equipotential

solution within a single step if  $r(z)$  does not change at all, which might be achieved by freezing the droplet. This is a consequence of the linearity of the electrostatic equations. The nonlinearity, which makes the convergence of the algorithm a subtle task, lies in the impact of the solution to the Dirichlet problem on its boundary conditions. Updating  $\sigma(z) \stackrel{\text{def}}{=} \sigma(z) - \delta\sigma(z)$  yields a modified surface charge density that results in a new droplet  $r(z)$  and a new potential  $\phi(z)$  on the surface of the droplet. If the iterative algorithm converges,  $\|\phi(z)\|_2 < \epsilon$  indicates that the pair  $r(z)$ ,  $\sigma(z)$  is the solution of a droplet in mechanical and electrical equilibrium.

In the following the governing integral equation will be derived for the inverse source problem given by equation 3.25 under the assumptions outlined above. This integral equation is of the form

$$0 = f(z) + \int_{\tilde{z}=a}^b \tilde{K}(z, \tilde{z}, \sigma(z)) d\tilde{z}. \quad (3.28)$$

The kernel  $\tilde{K}(z, \tilde{z}, \sigma(z))$  of the integral equation depends nonlinearly on the unknown function  $\sigma(z)$ , which is the solution of the integral equation. The natural form of this integral equation appears as Fredholm integral equation of the first kind, whose kernel is implicitly dependent on the solution  $\sigma(z)$ . This allows an iterative method of solution to be constructed. The dependence of the kernel on the solution  $\sigma(z)$  makes the problem a highly nonlinear one. The theory of nonlinear integral equations of this form is poorly developed as even the linear Fredholm integral equations of the first kind already cause severe difficulties [Wing and Zahrt, 1991].

After the derivation of the governing integral equation a method of solution will be developed that takes into account additional physical information allowing to solve this equation iteratively. This method of solution is validated against an exact analytical result for the special linear case  $\tilde{K}(z, \tilde{z}, f(z)) = K(z, \tilde{z})f(z)$  and is studied for the nonlinear case extensively in Sections 3.3 and 3.4. The solutions are physically useful and reproduce experimental results such as a finite size droplet rounded at the apex that approaches Taylor's cone asymptotically. Droplets with conical ends of different opening angles are found, which have also been observed in experiments [Yarin et al., 2001, Achtzehn et al., 2005].

Consider a droplet of shape  $r(z)$  hanging from a nozzle i.e. a hole in the upper plate of a plate capacitor as illustrated in Figure 3.13. The droplet is exposed to the electrical field  $E^{pc}$  of the plate capacitor giving rise to the surface charge  $\sigma = \sigma(z)$  on the droplet. In order to satisfy the equipotential boundary condition at the upper plate of the plate capacitor the method of image charges is used as illustrated in Figure 3.13, with  $\sigma(z) = -\sigma(-z)$  an odd and  $r(z) = r(-z)$  an even function. Obviously, the resulting potential  $\phi(z) = -\phi(-z)$  is an odd function as well.

As the charges are expected to be surface charges, the charged axisymmetric droplet may be decomposed into a continuous set of charged rings of radius  $r(z)$  located at position



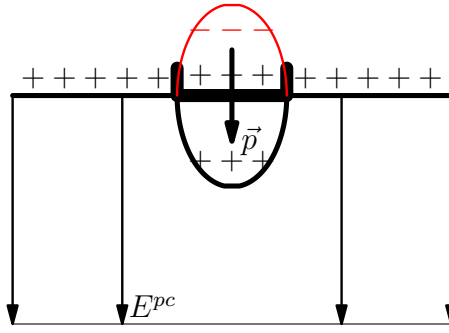


**Figure 3.13:** A charged droplet hanging from a nozzle inside a plate capacitor. Its image charge ensures the equipotential at the upper plate and gives rise to a dipole moment  $\vec{p}$ , which is always aligned collinear with the electrical field  $E^{pc}$ . If the lower plate is moved to infinity, this is the only image charge.

$z$ . The potential of a ring is given by equation A.39 and is the Green's function to be used in the Newtonian potential, which is the general solution to the Poisson equation [Jackson, 1998]. Using this Green's function the electrostatical potential is composed using the surface charge density defined on the axisymmetric cylindrical surfaces.

**Lemma 1.** *The surface charge density  $\sigma(z)$  on a protrusion  $r(z)$  at equipotential inside a plate capacitor is the solution to the Fredholm integral equation of the first kind*

$$0 = -\Pi_3 z + \int_{\tilde{z}=-z_0}^{z_0} f_r(z, \tilde{z}) \sigma(\tilde{z}) d\tilde{z} \quad (3.29)$$

in non-dimensional variables with the non-dimensional electrical field  $\Pi_3 = \frac{\sigma_0}{4\pi^2 \epsilon \epsilon_0} E^{pc}$  and the integral kernel

$$f_r(z, \tilde{z}) = 2\pi \sqrt{\frac{r(\tilde{z})}{r(z)}} k K(k) \sqrt{1 + r'^2(z)} \quad (3.30)$$

where

$$k \stackrel{\text{def}}{=} k(r(z), z, r(\tilde{z}), \tilde{z}) = 2 \sqrt{\frac{r(\tilde{z})r(z)}{(z - \tilde{z})^2 + (r(\tilde{z}) + r(z))^2}}. \quad (3.31)$$

$K(x)$  is the complete elliptic integral of the first kind as defined by equation A.8.

*Proof.* Starting in dimensional variables, the electrostatical potential inside the plate capacitor disturbed by a protrusion at equipotential is given by

$$\phi(\tilde{r}, z) = \phi^{pc}(z) + \int_{\tilde{z}=-z_0}^{z_0} d\phi^{ring}(\tilde{r}, \tilde{z}, r, z) \quad (3.32)$$

where  $\phi(\tilde{r}, z = 0) \stackrel{\text{def}}{=} 0$  and  $z, \tilde{r} \in \mathbb{R}_0^+$  with the ring potential  $\phi^{ring}$  from equation A.39. In fact  $z$  should be bound by the width of the plate capacitor, but as it is sufficient to

consider electrical fields, the lower plate may be thought of as being located at  $z \rightarrow \infty$ . From the plate capacitor potential  $\phi^{pc}(z) = -E^{pc}z$ , the relationship between line charge  $\tau(\tilde{z})$  of the ring at position  $\tilde{z}$  and surface charge  $\sigma(\tilde{z})$  on the protrusion

$$\tau(\tilde{z}) = \sigma(\tilde{z}) \sqrt{1 + r'^2(\tilde{z})} d\tilde{z} \quad r'(\tilde{z}) = \frac{dr}{dz}(\tilde{z}) \quad (3.33)$$

and the ring potential A.39 the resulting potential

$$\phi(\tilde{r}, z) = -E^{pc}z + \frac{1}{2\pi\epsilon\epsilon_0} \int_{\tilde{z}=-z_0}^{z_0} \sigma(\tilde{z}) \sqrt{\frac{r(\tilde{z})}{\tilde{r}}} k K(k) \sqrt{1 + r'^2(\tilde{z})} d\tilde{z} \quad (3.34)$$

is obtained. It is defined for  $\tilde{r} \in \mathbb{R}^+$ ,  $z \in \mathbb{R}$  and

$$k \stackrel{\text{def}}{=} k(\tilde{r}, z, r(\tilde{z}), \tilde{z}) = 2 \sqrt{\frac{r(\tilde{z})\tilde{r}}{(z - \tilde{z})^2 + (r(\tilde{z}) + \tilde{r})^2}} \quad (3.35)$$

is inherited from Lemma 5 (page 134). Nondimensionalizing equation 3.34 using the common scales listed in appendix A.2 (page 128) with the newly introduced non-dimensional electrical field  $\Pi_3 = \frac{\sigma_0}{4\pi^2\epsilon\epsilon_0} E^{pc}$  results in the Fredholm integral equation of the second kind

$$\Pi_3 \phi(\tilde{r}, z) = -\Pi_3 z + 2\pi \int_{\tilde{z}=z_0}^{z_0} \sqrt{\frac{r(\tilde{z})}{\tilde{r}}} k K(k) \sqrt{1 + r'^2(\tilde{z})} \sigma(\tilde{z}) d\tilde{z}. \quad (3.36)$$

in non-dimensional variables. Performing the limit

$$\tilde{r} \rightarrow r(z) \quad \text{and hence} \quad \lim_{\tilde{r} \rightarrow r(z)} \phi(\tilde{r}, z) \stackrel{\text{def}}{=} \phi_0 = 0 \quad (3.37)$$

the equipotential boundary condition at the droplet results in the Fredholm integral equation of the first kind

$$0 = -\Pi_3 z + \int_{\tilde{z}=-z_0}^{z_0} f_r(z, \tilde{z}) \sigma(\tilde{z}) d\tilde{z} \quad (3.38)$$

with kernel

$$f_r(z, \tilde{z}) = 2\pi \sqrt{\frac{r(\tilde{z})}{r(z)}} k K(k) \sqrt{1 + r'^2(z)} \quad (3.39)$$

and  $k = k(r(z), z, r(\tilde{z}), z)$  as defined in equation 3.31, which is already non-dimensional.  $\square$

The index  $r$  at the kernel  $f_r(z, \tilde{z})$  indicates that  $f$  implicitly depends on the shape of the droplet  $r(z)$  despite the fact that it only appears to be explicitly dependent on  $z$  and  $\tilde{z}$ .

**Corollary 2.** *Rewriting the integral in equation 3.29 by using the symmetry  $\sigma(\tilde{z}) = -\sigma(-\tilde{z})$  with  $f_r(z, \tilde{z})$  as defined before in equation 3.30 results in*

$$0 = -\Pi_3 z + \int_{\tilde{z}=0}^{z_0} [f_r(z, \tilde{z}) - f_r(z, -\tilde{z})] \sigma(\tilde{z}) d\tilde{z}, \quad (3.40)$$

which is more convenient for later discretization. The new integral kernel is non-zero as its symmetry is broken by  $k$ . Additional differentiation of the above equation with respect to  $z$  yields

$$0 = -\Pi_3 + \int_{\tilde{z}=0}^{z_0} \left[ \left( \frac{\partial f_r}{\partial z} \right) (z, \tilde{z}) - \left( \frac{\partial f_r}{\partial z} \right) (z, -\tilde{z}) \right] \sigma(\tilde{z}) d\tilde{z}. \quad (3.41)$$

Multiplying the above equation with  $\lambda \in \mathbb{R}$  and adding it to equation 3.40 results in the modified Fredholm integral equation of the first kind

$$0 = -\Pi_3(z + \lambda) + \int_{\tilde{z}=0}^{z_0} \left[ f_r(z, \tilde{z}) - f_r(z, -\tilde{z}) + \lambda \left( \frac{\partial f_r}{\partial z} \right) (z, \tilde{z}) - \lambda \left( \frac{\partial f_r}{\partial z} \right) (z, -\tilde{z}) \right] \sigma(\tilde{z}) d\tilde{z}. \quad (3.42)$$

This equation is important for later use.

In order to establish electrical equilibrium on a given droplet  $r(z)$ , the surface charge density  $\sigma(z)$  has to be located on the surface of the droplet, which is the solution to the Fredholm integral equation of the first kind 3.40.

### 3.2.2 Integral equations of the first kind & ill-posedness

Fredholm integral equations arise from different origins [Wazwaz, 1997], where the most commonly known is the formal integration of a boundary value problem. In most cases it is easier to solve the differential equation directly. Unfortunately, Fredholm integral equations of the first kind cannot be replaced by differential equations in every case, as is possible for other types of integral equations of the second kind in a systematic way<sup>8</sup>. As the kernel of integral equation 3.40 is a highly nonlinear function of  $z$  and  $\tilde{z}$  that will continuously be altered during the iteration of the algorithm visualized in Figure 3.12, an analytical approach appears to be hopeless. Hence, the Fredholm integral equation of the first kind 3.40 has to be solved numerically, which unfortunately is a very difficult though still tractable problem. The difficulty of the problem arises from the fact that Fredholm integral equations of the first kind are ill-posed. This means they do not satisfy the demands of well-posedness of Hadamard.

**Definition 3** (Hadamard). *A problem is well posed if*

1. *A solution exists.*
2. *The solution is unique.*
3. *The solution depends continuously on the problem parameters.*

---

<sup>8</sup>For example Volterra integral equations of the second kind can often be reformulated into an equivalent ordinary differential equation [Wazwaz, 1997]. Integral equations arising from the calculus of variation can often be reformulated into an equivalent Euler-Lagrange partial differential equation as for example in classical mechanics [Herbert Goldstein and Safko, 2006].

otherwise it is considered ill-posed [V.K. Ivanov and Tanana, 2002].

From the Lemma of Riemann-Lebesgue [Heuser, 2004]

$$\lim_{n \rightarrow \infty} \int_a^b f(x) \sin(nx) dx = 0 \quad (3.43)$$

with  $f \in L^2$  follows that the Fredholm integral equation of the first kind in general violates the 3rd point of Hadamard's demand of well-posedness. The solution  $u(z)$  of

$$0 = f(z) + \epsilon + \int_{\tilde{z}=a}^b K(z, \tilde{z}) \underbrace{[\sigma(\tilde{z}) + \delta \sin(n\tilde{z})]}_{=u(\tilde{z})} d\tilde{z}. \quad (3.44)$$

does not depend continuously on the inhomogeneity as  $\epsilon \rightarrow 0$  for finite  $\delta > M \gg 0$  and sufficiently large  $n$ . Consequently, tiny deviations in the inhomogeneity may spoil the solution

$$u(z) \stackrel{\text{def}}{=} \sigma(z) + \delta g(z) \neq \sigma(z) \quad (3.45)$$

with large oscillations  $\delta g(z)$  [Phillips, 1962]. This is a common problem in case  $f(x)$  is obtained from measured data with  $\epsilon > 0$  for example in inverse source problems arising from applications in tomography [Kirsch, 1996, Wing and Zahrt, 1991].

In the numerical approach aimed at finding the equipotential droplet in mechanical equilibrium, the inhomogeneity  $f(z)$  of the Fredholm integral equation is known analytically. Therewith, the inhomogeneity is exact to machine precision and is not the cause for problems in this approach. The true cause for problems lies in the ill-posedness itself and the necessary discretization of the Fredholm integral equation. From the functional analysis point of view it is obvious that function  $\delta g(z)$  of equation 3.45 belongs to the null space of the Fredholm operator<sup>9</sup> [Werner, 2002] of equation 3.44. Consequently, the solutions to the Fredholm integral equation of the first kind are given by the sum of the *fixed solution*  $\sigma(z)$  plus an arbitrary element of the null space of the Fredholm operator.

Discretizing the Fredholm integral equation for numerical treatment replaces the infinite-dimensional integral operator by a finite-dimensional one, which differ in domain, codomain and null space. Unless the matrix representing the discretized Fredholm operator is singular by coincidence, its null space is trivial and the discretized analogon of function  $u(z)$  is uniquely determined then, being a discretization of a solution  $u(z)$  consisting of the *fixed solution*  $\sigma(z)$  and the spoiling null space element  $\delta g(z)$ , which has implicitly been chosen by the discretization.

The discretized analogon of function  $\delta g(z)$  is strongly dependent on the resolution as an increasing resolution more and more approximates the infinite-dimensional integral operator leading to larger and larger frequencies of  $\delta g(z)$ . Nevertheless, the limit towards the

---

<sup>9</sup>The integral operator  $T_k(s) \stackrel{\text{def}}{=} \int_{t=a}^b k(s, t) \cdot dt$  is known as Fredholm operator.

infinite-dimensional operator leads to arbitrary large frequencies with finite amplitudes as demonstrated by equation 3.44. The limit towards the infinite-dimensional problem cannot be performed numerically, but fortunately the solution converges towards the fixed solution by *average convergence* [Heuser, 2004]. Hence, an increase in resolution is useful until the frequencies of the null space element are significantly larger than the frequencies of the *fixed solution* such that the frequencies of the *fixed solution* and the null space element separate.

In conclusion, the discretization of the Fredholm integral equation of the first kind introduces errors of discretization that will ultimately lead to the solution  $u(z) = \sigma(z) + \delta g(z)$ , where  $\delta g(z)$  is a function oscillating with high frequency.

### 3.2.3 Discretization & validation

The dimension of the finite-dimensional integral operator is the number of sample points, which will also be called modes in the following. When solving the discretized Fredholm integral equation by methods of linear algebra in praxis the number of modes and the distribution of the sample points have a dramatic effect on the amplitude  $\delta$  and the frequency of oscillation of  $g(z)$ . Too low a resolution results in large errors of discretization, but the errors do not vanish with increasing resolution for the reasons discussed in the previous subsection. This means that an adequate number of sample points has to be found such that the occurring errors do not originate from the lack of resolution<sup>10</sup> and keep the numerical effort tractable. Concerning the distribution of sample points,

$$z_\nu = z_0 \left[ 1 - \left( \frac{\nu}{n-1} \right)^s \right] \quad \nu \in \{0, 1, 2, \dots, n-1\} \quad (3.46)$$

is used to discretize the  $z$  coordinate into the sample points  $z_\nu$ . Here,  $n$  is the number of modes,  $\nu$  is the index of the mode and  $z_0$  is the length of the droplet under consideration just as in Section 3.1.1. The exponent  $s$  controls the distribution of sample points, which are equidistant for  $s = 1$  and may be concentrated at the apex of the droplet by increasing  $s$ . Equidistant sample points unfortunately lead to *very* large discretization errors. This behavior is understandable as the almost periodic spoiling oscillations  $\delta g(z)$  are sampled by periodically located sample points. This results in an effectively reduced resolution. Breaking this periodicity by using a quadratic distribution of the sample points  $s = 2$  leads to the best results obtained so far, which additionally emphasizes the apex of the droplet, where most of the charge is located. Therefore, all following results are obtained by using a quadratic distribution of sample points.

The discretized versions of the Fredholm integral equations of the first kind 3.40 and 3.42, which are used for the numerics are given in appendix A.5 without further proof as they are

---

<sup>10</sup>Finding an appropriate resolution is a common struggle in the field of inverse source problems and is often a matter of experience as well as trial and error [Kaipio and Erkki, 2005].

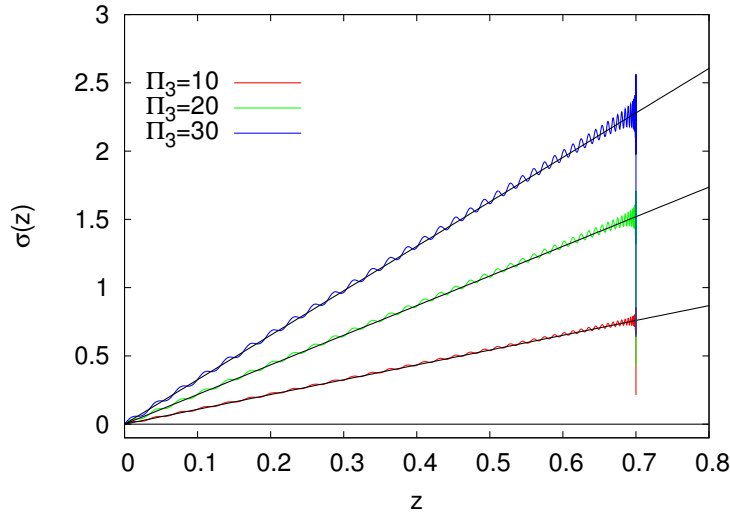


**Figure 3.14:** Comparison between the numerical and the exact analytical solution of the charge density  $\sigma(z)$  of a conducting sphere in a homogeneous electrical field. The numerical solutions are colored and have been obtained using  $n = 800$  modes. The analytical solutions are displayed by black lines. The spoiling oscillations due to the discretization and the ill-posedness of the inverse source problem are relatively small.

found by straight forward discretization of the continuous equations. In order to validate the numerical implementation of the Fredholm integral equation, the algorithm illustrated in Figure 3.12 is tested against the exact analytical result of a conducting sphere in a homogeneous electrical field. To do so, only the integration of the Fuchikami equation has to be short-circuited in order to keep the spherical shape  $r(z)$  independent of the Maxwell pressure. The radius of a sphere and the exact analytical expression of the charge density on a conducting sphere are given by

$$r(z) = \sqrt{z_0^2 - z^2} \quad \sigma^{an}(z) = \frac{3}{4\pi^2} \Pi_3 \frac{z}{z_0}. \quad (3.47)$$

The expression for  $\sigma^{an}(z)$  is derived in appendix A.7 for the sake of completeness as it commonly is a textbook exercise [Fliessbach, 2000, Jackson, 1998].

Figure 3.14 illustrates the comparison of the charge densities obtained from the numerical solution to the discretized Fredholm integral equation of the first kind  $\sigma(z)$  and the exact analytical solution  $\sigma^{an}(z)$  of a conducting sphere in a homogeneous electrical field. The numerical solution oscillates around the analytical solution with *moderate* amplitude and shows a peak at the apex of the droplet. The resolution has been chosen to  $n = 800$  modes such that the resolution is large enough to eliminate resolution-dependent errors to great extend, while keeping the numerical effort bounded. In this way, the discretized Fredholm integral equation is solvable within a few seconds on contemporary PCs. As the

Dirichlet problem is linear and the shape of the conducting sphere  $r(z)$  does not depend on the solution of the Dirichlet problem in this special case, the iteration converges within a single step corresponding to a direct deterministic solution.

In conclusion, the algorithm for solving the equipotential boundary condition shown in Figure 3.12 works and has been validated against an exact analytical result.

### 3.2.4 Smoothing

The problem of charging a droplet held at an equipotential takes a lot more iterations to converge compared to the deterministic solution of a solid protrusion located at the plate capacitor. In case  $r(z)$  does not change with  $\sigma(z)$  the problem is linear and algorithmically equivalent to the problem of a conducting sphere in a homogeneous electrical field studied in the previous subsection. The rate of convergence of the iteration depends on the impact of the change in charge density on the shape of the droplet. For small electrical fields the algorithm converges within a few iterations, whereas large electrical fields may take the algorithm a large amount of iterations<sup>11</sup> to converge.

The prolonged iteration results from the stronger coupling between the shape  $r(z)$  and the charge density  $\sigma(z)$  for larger fields via the algorithm displayed in Figure 3.12. Even in case the spoiled solution as those in Figure 3.14 could be tolerated aesthetically, the impact of the oscillations itself on the iteration demands additional remedial measures in order to suppress the oscillations. This is of special importance for large electrical fields  $\Pi_3 \gtrsim 5$  as the impact of the charge density on the shape gets stronger such that oscillations in  $\sigma(z)$  cause undulations in  $r(z)$  that are fed back to  $\sigma(z)$ . This feedback sometimes leads to a numerical resonance, which is followed by a divergence of the iteration from time to time. Because of the *average convergence* of the spoiled solution towards the physically relevant *fixed solution*, the quandary of high frequency oscillations can be remedied by smoothing the solutions by local averaging. Such a procedure allows to get rid of the spoiling null space elements to great extend in order to determine the *fixed solution*, which is physically meaningful. In the theory of inverse source problems this action corresponds to the application of additional knowledge of the problem [Press et al., 1992]. The method of choice is *moving window averaging* [Press et al., 1992] realized by a convolution of the spoiled solution  $u(z)$  with a box function

$$\sigma(z) \approx \int_{\tilde{z}=0}^{z_0} f_\epsilon(z - \tilde{z}) u(\tilde{z}) d\tilde{z} \quad \text{with} \quad f_\epsilon(z - \tilde{z}) = \begin{cases} 0 & |z - \tilde{z}| > \epsilon \\ \frac{1}{2\epsilon} & |z - \tilde{z}| < \epsilon \end{cases} \quad (3.48)$$

where  $\epsilon$  is chosen such that it approximately coincides with half the period of the oscillations. In case the resolution is large, the spoiling solution features high frequencies while

---

<sup>11</sup>For a droplet  $z_0 = 0.7$  and small electrical fields  $\Pi_3 \lesssim 5$  it takes the algorithm only three to four iterations to converge to the equipotential solution satisfying  $\|\phi\|_2 < 10^{-20}$ . For very large electrical fields  $\Pi_3 \approx 30$  and the same  $z_0$  even a small increase in  $\Pi_3$  takes the algorithm up to  $\approx 100$  iterations to converge with respect to the same bound.

the *fixed solution* only varies slowly. Hence, the moving window averaging acts as a low pass filter and results in a much better approximation of the charge density because of  $u(z) = \sigma(z) + \delta g(z)$  and

$$\int_{\tilde{z}=a}^b f_\epsilon(z - \tilde{z}) u(\tilde{z}) d\tilde{z} = \int_{\tilde{z}=a}^b \underbrace{f_\epsilon(z - \tilde{z})}_{\approx \delta(z - \tilde{z})} \sigma(\tilde{z}) d\tilde{z} + \underbrace{\int_{\tilde{z}=a}^b f_\epsilon(z - \tilde{z}) \delta g(\tilde{z}) d\tilde{z}}_{\rightarrow 0} \approx \sigma(z). \quad (3.49)$$

The above statement holds as  $\sigma(\tilde{z})$  varies slowly in the interval  $[\tilde{z} - \epsilon, \tilde{z} + \epsilon]$  such that

$$\int_{\tilde{z}=a}^b f_\epsilon(z - \tilde{z}) \sigma(\tilde{z}) d\tilde{z} = \bar{\sigma}(z) \frac{1}{2\epsilon} \int_{\tilde{z}=z-\epsilon}^{z+\epsilon} d\tilde{z} = \bar{\sigma}(z) \approx \sigma(z). \quad (3.50)$$

Hence,  $f_\epsilon(z - \tilde{z})$  approximately acts like Dirac's delta distribution.

In conclusion it has been shown that appropriate smoothing of the numerically obtained solution helps getting rid of the spoiling null space element, which is inevitably introduced to the numerical solution by the discretization of the integral equation.

### 3.2.5 Regularization

A common problem in solving inverse source problems are ill-conditioned matrices arising from ill-conditioned problems. The definition of an ill-conditioned matrix is found in appendix A.4. In the following, the mapping of a charged droplet  $r_i(z)$ ,  $\sigma_i(z)$  to another one  $r_{i+1}(z)$ ,  $\sigma_{i+1}(z)$  performed during a single loop in the iterative algorithm displayed in Figure 3.12 will be referred to as *iterated map* of the algorithm.

When solving the Fredholm integral equation 3.40 i.e. its discrete analogon given by equation A.30, the numerically obtained solution is spoiled by the spoiling null space element  $\delta g(z)$  as discussed in Subsection 3.2.2. The *moving window averaging* removes spoiling oscillations to great extend and the iteration of the algorithm most often converges towards the equipotential solution of interest for small electrical fields  $\Pi_3$ . Restarting the algorithm with the previous charge density as initial condition after a slight increase of the electrical field, charges the droplet adiabatically. In case the electrical field is already large, the mutual feedback between the shape  $r(z)$  and the surface charge density  $\sigma(z)$  gets stronger. This sometimes leads to a numerical resonance that utterly destroys the convergence of the iterated map towards the fixed point, which represents the equipotential solution.

The matrix  $\mathbf{M}$  representing the discretized Fredholm integral operator A.31 typically features a condition  $\text{cond}(\mathbf{M}) \approx 10^{-7}$  for the resolution of choice  $n = 800$  modes. This condition is still small enough to obtain a vector of solution that is reliable to approximately 8 digits, which typically is sufficient to make the algorithm converge. Due to the iteration of the algorithm, all entries of the matrix  $\mathbf{M}$  change at each step of the iteration. By coincidence, the matrix may become ill-conditioned from time to time in case of larger



electrical fields that provide strong enough a coupling between shape and surface charge density. As will be shown in the following, the matrix becomes ill-conditioned due to the smallest singular value, which almost vanishes in these cases. Reasonably, the eigenvector corresponding to the smallest eigenvalue is the discrete eigenfunction featuring the largest frequency of oscillation possible for the discretized Fredholm integral operator as it is closest to the null space of the infinite-dimensional Fredholm operator.

Whenever there is no useful alternative to solving an ill-conditioned problem, methods of regularization such as *truncated singular value decomposition* (TSVD) or the *Tikhonov regularization* for example have to be employed [Kaipio and Erkki, 2005]. By using these methods, additional information is applied to the ill-posed problem leading to much better a result<sup>12</sup> than obtained otherwise. The single vanishing singular value of the matrix representing the discretized Fredholm integral operator A.31 suggests that the TSVD appears to be the method of choice as the almost vanishing singular value has to be set to zero<sup>13</sup>. Appendix A.4 compiles the properties of SVD, TSVD and the condition of a matrix. Performing a TSVD, the dimension of the problem is essentially reduced by one. This is because the vector representing the solution  $\vec{\sigma}$  may be thought of as being expanded in the basis of the left singular vectors<sup>14</sup>  $\vec{e}_\nu$  of matrix  $\mathbf{M}$

$$\vec{\sigma} = \sum_{\nu=1}^n a_\nu \vec{e}_\nu. \quad (3.51)$$

Ignoring the smallest singular value  $s_n$  implies setting  $a_n = 0$ . This prevents large expansions of the vector of solution in the direction of  $\vec{e}_n$ . As  $\vec{e}_n$  almost lies in the null space its presence in the solution  $\vec{\sigma}$  does not have a significant impact on the validity of the algebraic equation.

The TSVD has been used as a method of regularization, but failed to improve the convergence of the iterative algorithm. The most probable reason for this is that the vectors  $\vec{e}_n$  of the previous iterations have not been null space elements at all. As the vanishing of  $s_n$  brings vector  $\vec{e}_n$  closer to the null space, its vanishing and the subsequent removal by the TSVD also removes the contribution to the averaged charge density that has been present in the iterations before. Hence, speaking in the abstract picture of dynamical systems, the lack of contribution of vector  $\vec{e}_n$  to the solution redirects the itinerary of the iteration in the *configuration space* spanned by the modes. It is not surprising that such an impact by the TSVD on the iteration destroys the convergence of the algorithm<sup>15</sup>.

---

<sup>12</sup>From the mathematics point of view, ill-conditioned problems suffer from a more or less incurable defect, but from the physics or technology point of view, additional information often is available helping to find solutions that solve physical or technological problems [Kirsch, 1996].

<sup>13</sup>When solving a linear algebraic equation with ill-conditioned matrix, setting an almost vanishing singular value to exactly zero, tells the SVD algorithm to ignore this direction of expansion. This is equivalent to solving the equation by a multiplication with the pseudoinverse matrix, which results in a regularized solution to the problem.

<sup>14</sup>The left singular vectors of matrix  $\mathbf{M}$  are the column vectors of the unitary matrix  $\mathbf{U}$  of the singular value decomposition. Thus, the left singular vectors are an orthogonal basis [Stoer and Burlisch, 2005].

<sup>15</sup>The iteration rather looks Lyapunov stable and never converges.

Speaking vividly, the contribution of  $\vec{e}_n$  to the averaged solution  $\sigma(z)$  is located directly at the apex as an edge effect, where  $u(z)$  oscillates most heavily. At this position, a change in charge density impacts the droplet at most as the Fuchikami equations are integrated from the apex to the nozzle. Decreasing the curvature at the apex due to the reduced surface charge density the droplet gets wider, which has a strong nonlinear effect on the kernel of the integral equation. This is the best interpretation available, why the TSVD does not work for this problem.

The method of Tikhonov regularization [Wing and Zahrt, 1991] can be used to solve a Fredholm integral equation of the first kind

$$0 = f(z) - (\mathbf{T}_k \sigma)(z) \quad (3.52)$$

with  $\mathbf{T}_k$  the Fredholm integral operator by minimizing the functional

$$F_\lambda = \|f - \mathbf{T}\sigma\| + \lambda\|\mathbf{L}\sigma\|. \quad (3.53)$$

The operator  $\mathbf{L}$  is the stabilizing functional and applies additional information to the system like smoothness or boundedness with  $\mathbf{L} = \mathbf{id}$ . The disadvantage of this method of regularization with respect to the charging of equipotential droplets is that there is a large freedom in the choice of operator  $\mathbf{L}$  and the parameter of minimization  $\lambda$ . In order to make the iteration converge, all these parameters would have to be considered at every iteration of the *iterated map* of the algorithm shown in Figure 3.12 as operator  $\mathbf{T}_k$  changes at each step of the iteration, which is considered too complicated.

The discrete Fredholm integral operator is altered permanently during the iteration of the algorithm displayed in Figure 3.12. This demands a method that takes into account this property and justifies a special approach of regularization. In corollary 2 the Fredholm integral equation of the first kind 3.40 has been used in order to derive the modified Fredholm integral equation of the first kind 3.42 that is satisfied by any solution of the previous equation. Independent of that, a free parameter  $\lambda \in \mathbb{R}$  is introduced where the limit  $\lambda \rightarrow 0$  reproduces the original equation. By selecting a vanishingly small parameter  $\lambda$ , essentially the original problem is solved with the same trouble as before. In case  $\lambda$  is large, this problem changes to a totally different one that is not of interest.

The idea of solving an equation, which is only slightly different from the equation of interest in a tunable way is an approach of regularization. Choosing an appropriately small parameter  $\lambda$  allows to manipulate the equation in a systematic way as the  $z$  derivative of the Fredholm integral equation 3.41 originates from the Fredholm integral equation itself and is added to the original Fredholm integral equation 3.40. In case a singular value vanishes, the corresponding singular vector begins to dominate the charge densities obtained during the iteration and the algorithm starts diverging. This divergence is detected and the  $\lambda$  is changed in sign or to another value.

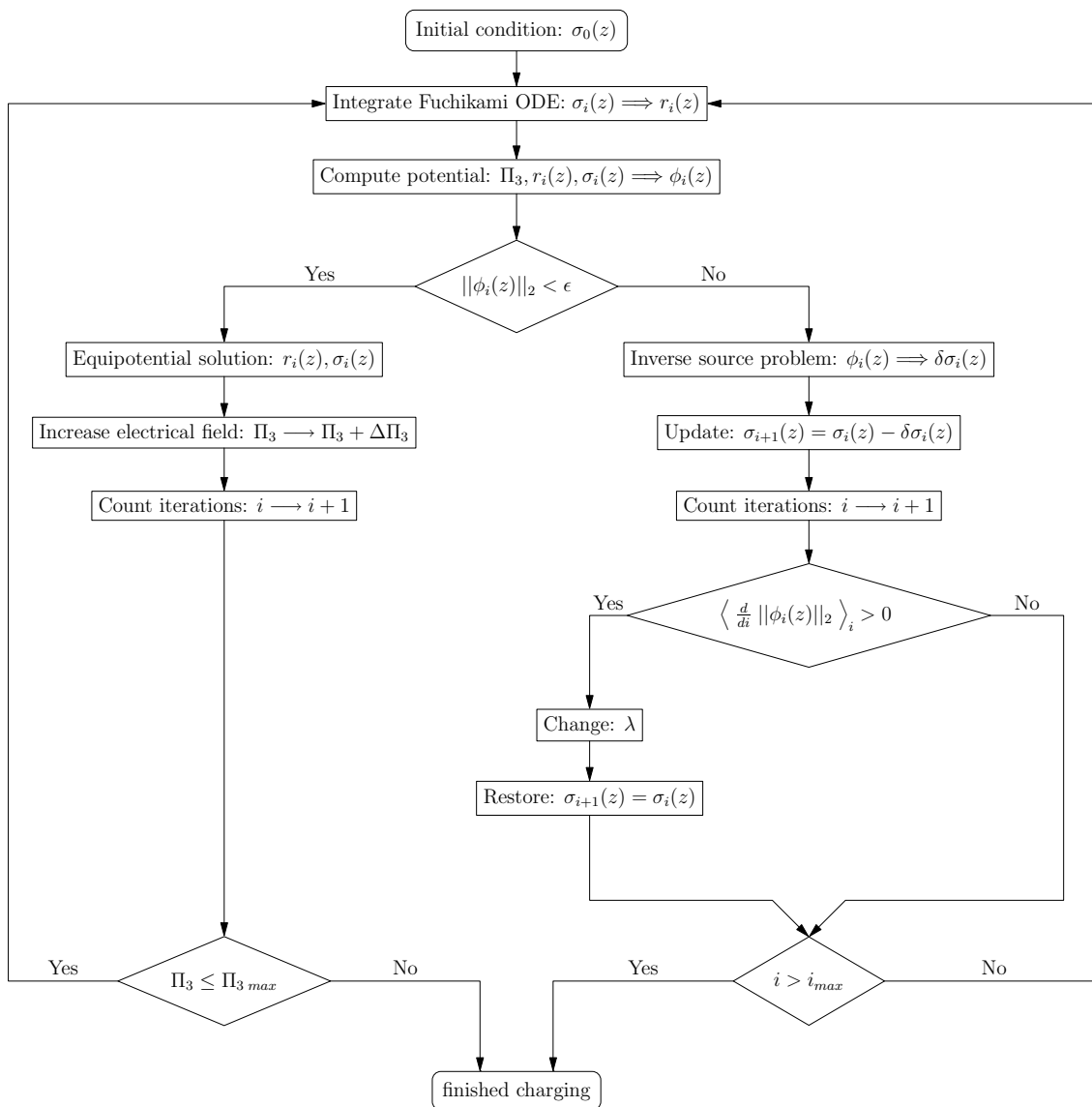


**Figure 3.15:** The modified algorithm used for charging droplets via the modified Fredholm integral equation 3.42.

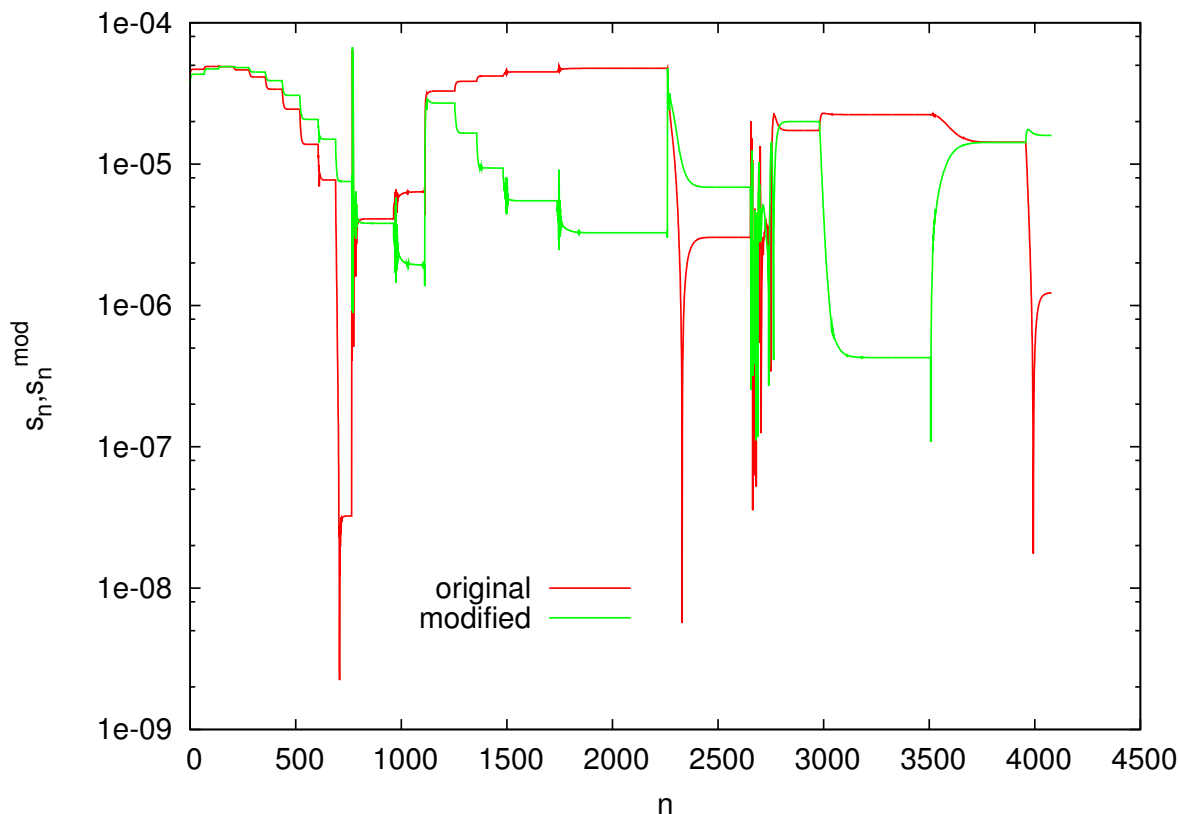


**Figure 3.16:** The values of the smallest singular values  $s_n$  and  $s_n^{mod}$  of matrices  $\mathbf{M}$  and  $\mathbf{M}_\lambda^{mod}$ , respectively, as a function of the iteration  $n$ . The negative peak of  $s_n$  at  $n = 708$  causes iterations using just matrix  $\mathbf{M}$  to diverge at these events, while the iteration of the regularized matrix  $\mathbf{M}_\lambda^{mod}$  still converges. From  $n = 0 \dots 500$  each step indicates a converged iteration and an increase of the electrical field  $\Pi_3$  by 0.1 starting from  $\Pi_3 = 28.1$  at  $n = 0$ . At the jumps of  $s_n^{mod}$  at  $n = 1112$  and  $n = 2261$ , parameter  $\lambda$  had to be changed due to lack of convergence going along with a larger jump of the smallest singular value. At  $n \approx 2700$  parameter  $\lambda$  had to be changed several times. It is clearly seen that the modified matrix does not show such vanishing singular values as the original matrix does.

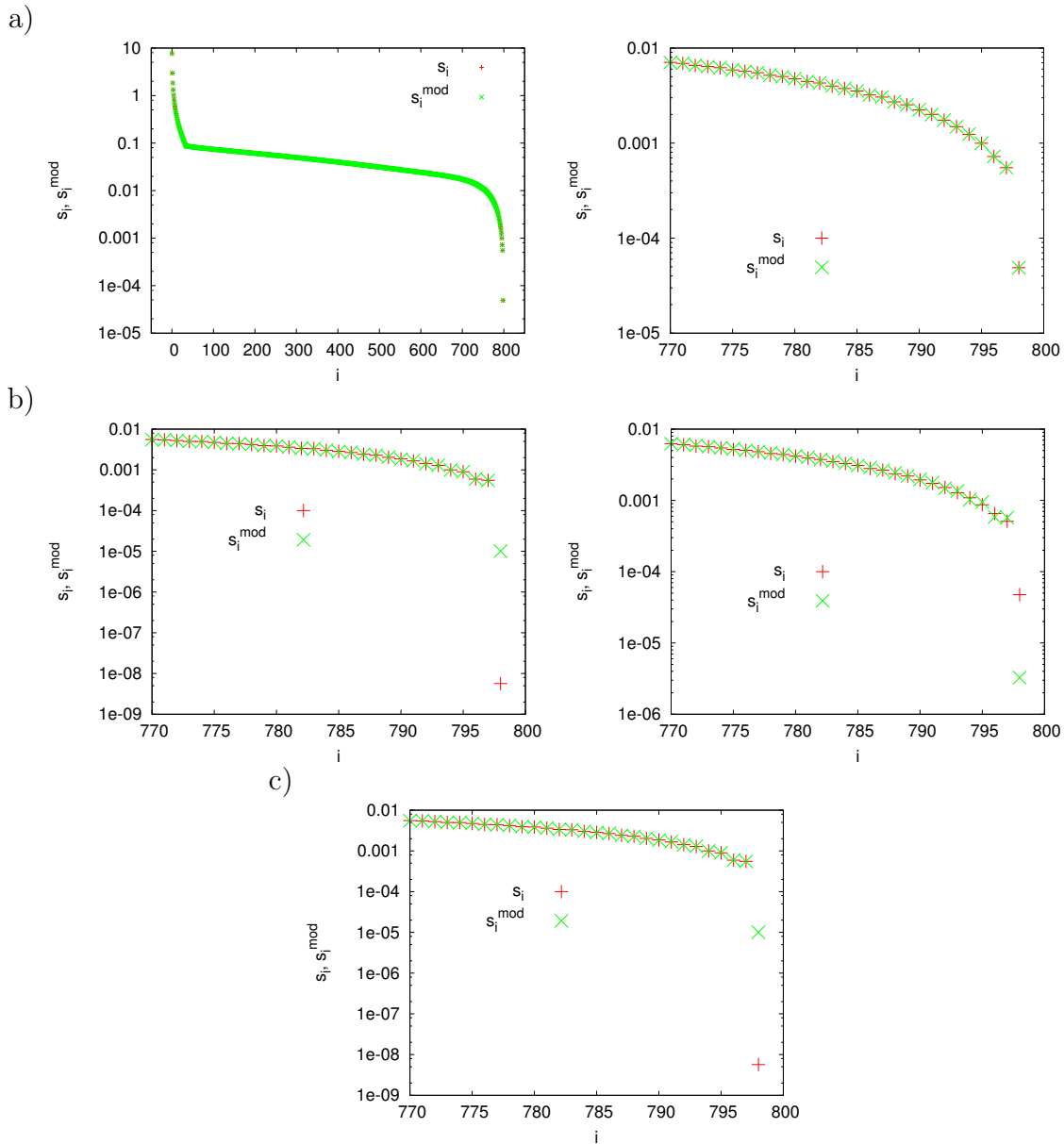


**Figure 3.17:** Details to the singular values at special events of Figure 3.16. a) The singular values of the matrices  $\mathbf{M}$  and  $\mathbf{M}_\lambda^{mod}$  are almost identical at iteration  $n = 200$  in a survey (left) and a detail (right). The condition approximately is  $\text{cond}(\mathbf{M}) \approx 10^6$ . b) At  $n = 708$  the singular value  $s_{799}$  starts to vanish (left), while  $s_{799}^{mod}$  does not. The conditions yield  $\text{cond}(\mathbf{M}) \approx 10^9$  and  $\text{cond}(\mathbf{M}_\lambda^{mod}) \approx 10^6$ . The modified equation is regularized. The regularization practically only influences the smallest few singular values e.g. at  $n = 2000$  (right). c) Another vanishing event at  $n = 2330$  shows again that just the smallest few singular values differ.

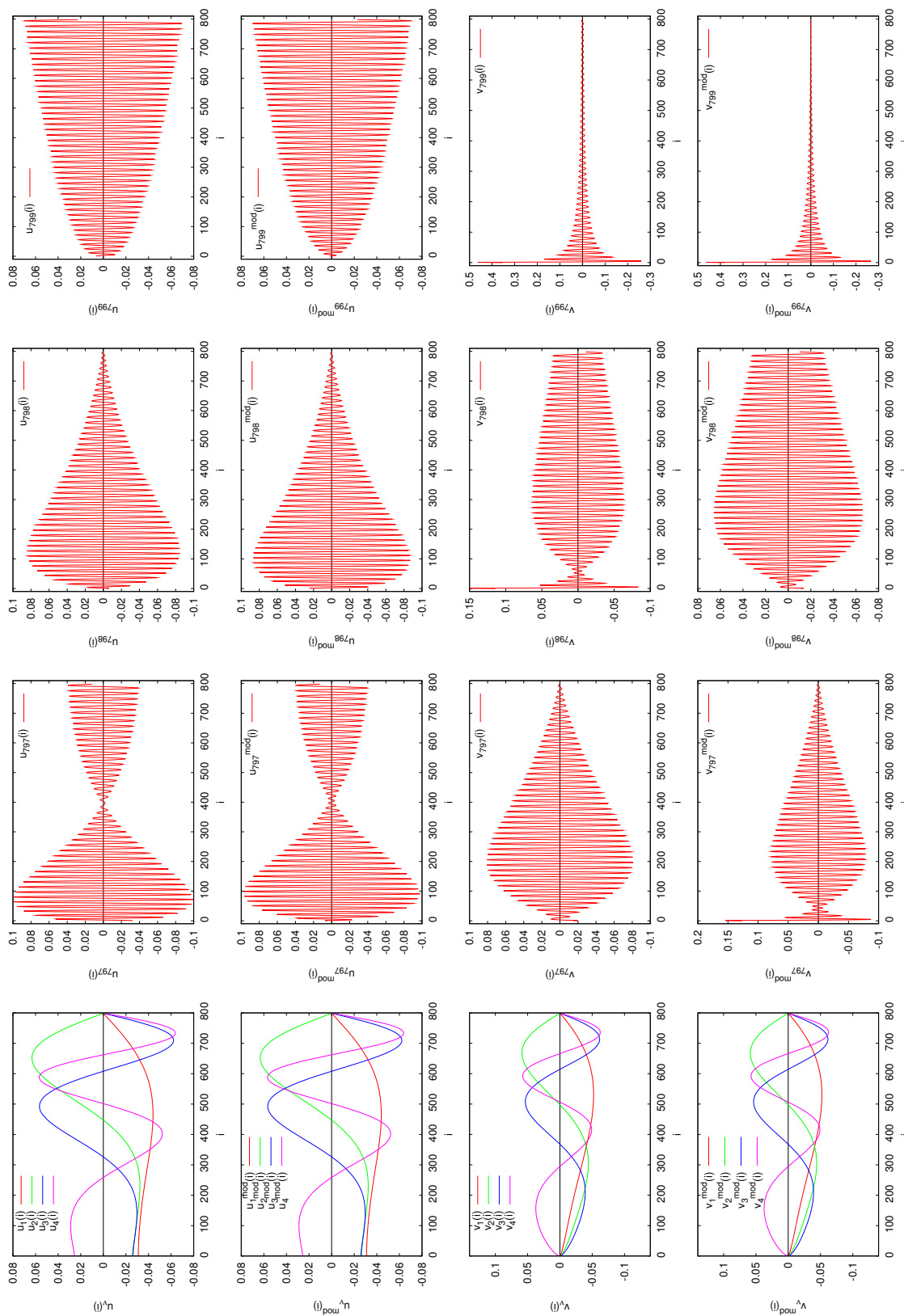


**Figure 3.18:** Selected left and right singular vectors  $\tilde{u}_\nu$ ,  $\tilde{u}_\nu^{mod}$ ,  $\tilde{v}_\nu$  and  $\tilde{v}_\nu^{mod}$  of matrices  $\mathbf{M}$  and  $\mathbf{M}_\lambda^{mod}$ , respectively.

Figures 3.16, 3.17, 3.18 and 3.19 show the results of the iteration of the modified algorithm displayed in Figure 3.15 at step  $n = 708$ , where the regularization takes effect. In this approach, the discretized equation A.38 of the modified Fredholm integral equation of the first kind 3.42 is used with a set of small parameters  $\lambda \in \{7 \cdot 10^{-10}, 1 \cdot 10^{-9}, 4 \cdot 10^{-9}, 1 \cdot 10^{-8}, 1 \cdot 10^{-7}\}$  and a randomly chosen sign.

Figure 3.16 shows the smallest singular value of the discrete Fredholm integral operator  $\mathbf{M}$  as well as its modified analog  $\mathbf{M}_\lambda^{mod}$  as a function of the iteration of the *iterated map* of the algorithm. In this study, the modified Fredholm integral operator is used for the iteration, while the ordinary Fredholm integral operator is just evaluated from the actual state of the iteration. The figure reveals that the discretized original Fredholm integral operator sometimes shows a vanishing singular value that would lead the iteration astray. The modified Fredholm equation does not show such drastic peaks, but if it does  $\lambda$  is changed in order to try again. Figure 3.17 shows the singular values of both discretized Fredholm integral operators  $\mathbf{M}$  and  $\mathbf{M}_\lambda^{mod}$  in different situations that occurred in Figure 3.16 and reveals that the singular values of both operators are almost identical apart from the smallest ones. The idea behind this regularization is to prevent the vanishing of the smallest singular value by modifying the matrix of the discretized Fredholm operator by tuning the free parameter  $\lambda$  appropriately.

In Figure 3.18 the left and right singular vectors of matrices  $\mathbf{M}$  and  $\mathbf{M}_\lambda^{mod}$  have been plotted. First of all, the left and right singular values differ as the discrete Fredholm integral operators are non-symmetric. The singular vectors  $\vec{u}_\nu$  and  $\vec{u}_\nu^{mod}$  do not differ for small indices  $\nu$ . Without illustration, slight deviations in the amplitude of peaks have been observed. For large  $i \lesssim n$  the singular values differ in envelope, which can be seen from the comparison shown in Figure 3.19.

In conclusion it has been demonstrated that by the choice of  $\lambda$  the modified discrete Fredholm integral operator is almost the same matrix as the original discrete Fredholm integral operator that possesses almost the same singular values and almost the same left and right singular vectors. These singular vectors have been altered due to the regularization such that the envelopes of these functions have changed or phase shifts occurred. The only considerable differences occurred in the highly oscillating singular vectors corresponding to the smallest singular values. Hence, this regularization essentially manipulates the singular values belonging to the singular vectors, which are very close to the null space of the matrix. The oscillations due to these vectors are removed by smoothing, while their residual contribution allows the algorithm to converge. Whenever vanishing singular values occur, a change in  $\lambda$  allows to suppress these singular events, which destroy convergence otherwise.

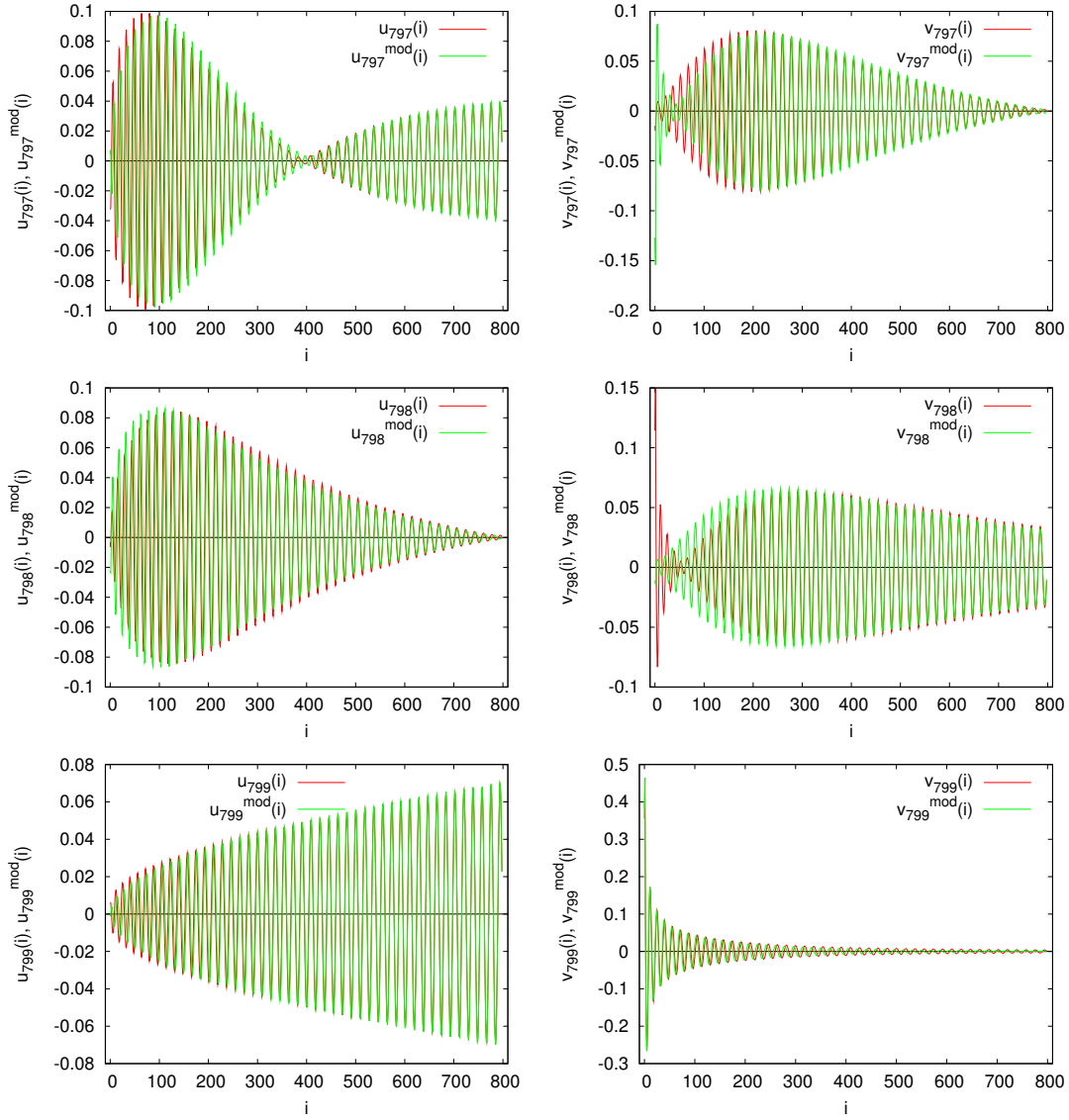


**Figure 3.19:** A direct comparison of the left singular vectors  $\vec{u}_{\nu}$  and  $\vec{u}_{\nu}^{mod}$  on the left and the right singular values,  $\vec{v}_{\nu}$  and  $\vec{v}_{\nu}^{mod}$  on the right for indices  $\nu \in \{797, 798, 799\}$  from top to bottom, respectively. It can be seen that the regularization shifts phases, slightly changes the envelopes of the functions and removes an oscillating peak from  $\vec{v}_{798}$ , but introduces one to  $\vec{v}_{797}^{mod}$ . Singular vector  $\vec{v}_{799}$  is flattened out for larger  $i$  in  $\vec{v}_{799}^{mod}$ .



### 3.2.6 The impact of resolution and first numerical solutions

In Subsections 3.2.2 and 3.2.3, it has been discussed that the resolution should be fine enough to increase the frequency of the oscillations of the spoiled solution in order to be able to smooth them by moving window averaging. Therefore, it is of interest, which number of modes is necessary to prevent errors due to a lack of resolution. The number of modes should be kept as small as possible in order to save time of computation when solving<sup>16</sup> the matrix equation representing the discretized integral equation. Unfortunately, the algorithms available for solving matrix equations for the occurring non-sparse and non-symmetric matrices generally are  $n^3$  processes.

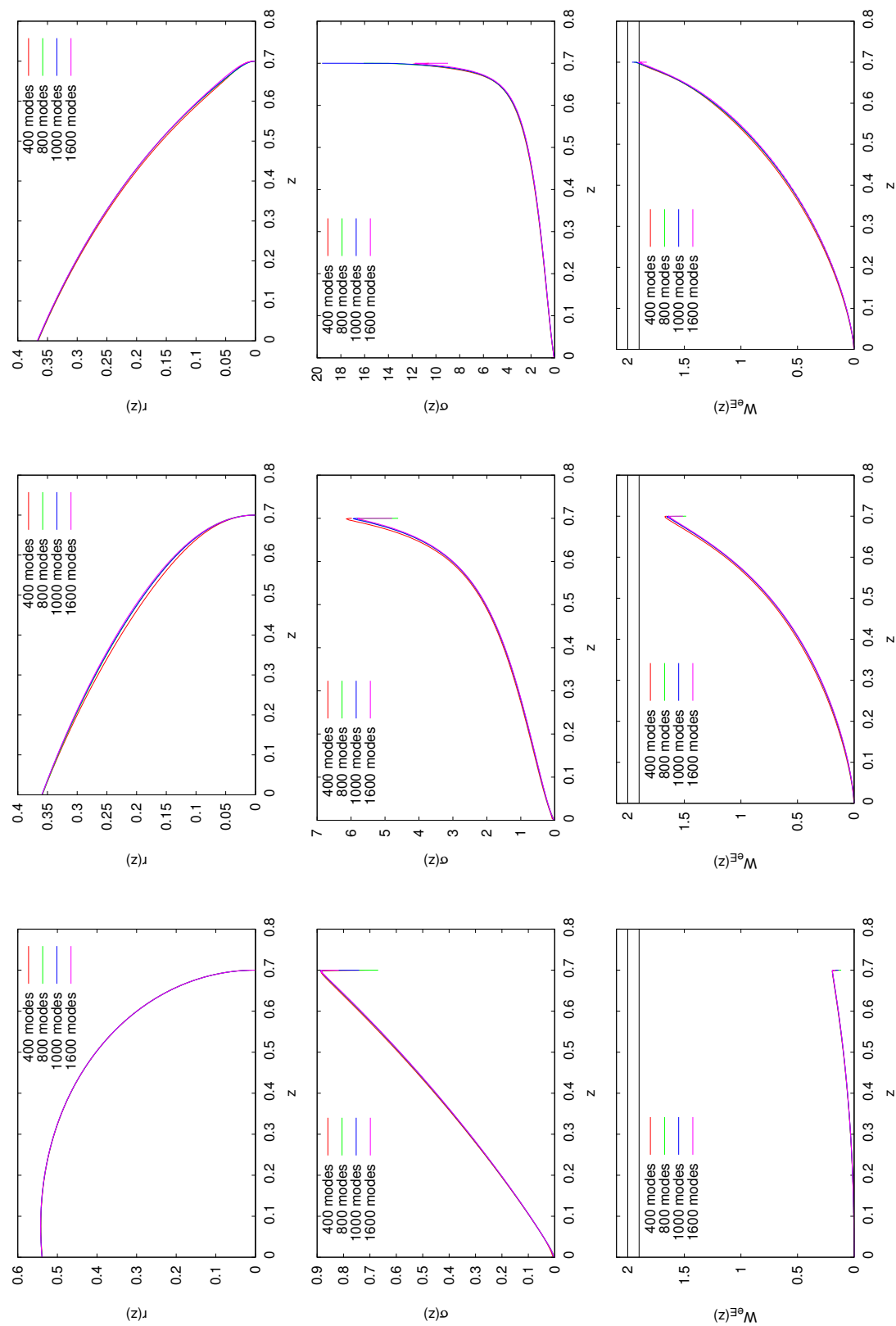
In order to choose such a resolution, parameters  $z_0 = 0.7$ ,  $\Delta p_1 = 3$  are used for charging a droplet under the use of the resolutions  $n \in \{400, 800, 1000, 1600\}$ . Figure 3.20 illustrates the results obtained from the charging of these droplets. Smaller resolutions such as  $n = \{50, \dots, 300\}$  have also been investigated but lead to considerable deviations to the results displayed, which shows that for  $n \gtrsim 400$  modes the resolution is large enough to fully charge the droplets until a conical droplet is reached. The lower resolutions also work for small electrical fields but start having convergence problems in case the surface charge density increases at the apex for the larger fields. As the solution is not improved anymore by using more than  $n > 800$  modes, all following droplets charged throughout this work have been obtained by using  $n = 800$  modes unless otherwise mentioned.

Figure 3.20 reveals that for relatively small electrical fields like  $\Pi_3 = 10$  the droplet qualitatively still looks like an uncharged droplet. For an electrical field of  $\Pi_3 = 29$  the droplet is considerably deformed due to the additional Maxwell stress, which yet strongly increases the curvature at the apex. The slight increase to  $\Pi_3 = 30$  then dramatically changes the shape of the droplet as the surface charge heavily increases the Maxwell pressure at the apex and hence also strongly increases the curvature there such that the droplet deforms into a highly curved almost conical shape. Figure 3.21 additionally shows the spoiled solutions  $u(z) = \sigma(z) + \delta g(z)$  to the discretized integral equation before window averaging is performed in comparison to the window averaged charge density  $\sigma(z)$  for different resolutions corresponding to the results displayed in Figure 3.20. Apparently, the oscillations do not vanish for increasing resolution as expected.

Despite the relatively fast change of the curvature as a function of the applied electrical field  $\Pi_3$ , the transition from solutions of  $\Pi_3 = 29$  to the solutions of  $\Pi_3 = 30$  is continuous. For the droplets of interest the electrical Weber number  $W_{eE}$ , which is the ratio of Maxwell and Laplace pressure, becomes a function of  $z$  and follows directly from the computed droplet and the control parameters used. This will be shown in Lemma 4 in Subsection 3.2.7. The lower plots of Figure 3.20 show an increase in the electrical Weber number  $W_{eE}$  directly at the apex from  $\approx 1.7$  to  $\approx 1.95$  which shows that almost the electrical forces alone determine the curvature there. The hydrostatic pressure is of negligible importance where the electrical Weber number is close to the critical electrical Weber number  $W_{eE}^{crit} = 2$  while it dominates where the electrical Weber number is small.

---

<sup>16</sup>Matrix equations are solved using either the fast QR or the insightful SVD methods of the linear algebra package of the Gnu Scientific Library (GSL) that is based on LAPACK.



**Figure 3-20:** From top to bottom: Charged droplets  $r(z)$ , their corresponding charge density  $\sigma(z)$  and the electrical Weber number  $W_{eE}(z)$  for the electrical fields  $\Pi_3 \in \{10, 29, 30\}$  from left to right, respectively. Each plot shows the result obtained for the resolutions  $n \in \{400, 800, 1000, 1600\}$ . For  $n > 400$  the results are practically resolution independent.

For  $\Pi_3 = 30$  the obtained charge densities  $\sigma(z)$  show considerable differences between the different resolutions directly at the apex of the droplet. This phenomenon is owed to the fact that the droplet is already highly charged and the system of equations is close to a point of a bifurcation with respect to control parameter  $\Pi_3$ . Increasing the field  $\Pi_3$  beyond a critical value  $\Pi_3^{crit}$  of bifurcation a solution of simultaneous mechanical and electrical equilibrium  $r(z)$ ,  $\sigma(z)$  no longer seems to exist as expected from previous works [Taylor, 1964].

For a better illustration of the charging process, a sequence of adiabatically charged droplets is visualized in Figure 3.22 where the electrical field  $\Pi_3$  increases from solution to solution by  $\Delta\Pi_3 = 5$ . For convenience the control parameters are  $z_0 = 0.7$  and  $\Delta p_1 = 3$  as before and it is expected that the nozzle located at  $z = 0$  always possesses the adequate nozzle radius  $r_n = r(z = 0)$  needed to supply the droplet.

### 3.2.7 The properties of charged droplets

In the previous subsections methods to charge droplets adiabatically have been developed, allowing to compute the shapes and charge densities of charged equipotential droplets that satisfy mechanical and electrical equilibrium simultaneously. These droplets have physical properties that follow directly from the solution obtained. Quantities like surface  $A$ , Volume  $V_{ol}$ , monopole charge  $q$  on a droplet and the dipole moment  $p$  of the droplet are given by

$$V_{ol} = \pi \int_{z=0}^{z_0} r(z)^2 dz \quad (3.54)$$

$$A = 2\pi \int_{z=0}^{z_0} r(z) \sqrt{1 + r'(z)^2} dz \quad (3.55)$$

$$q = 2\pi \int_{z=0}^{z_0} r(z) \sqrt{1 + r'(z)^2} \sigma(z) dz \quad (3.56)$$

$$\vec{p} = 4\pi \vec{e}_z \int_{z=0}^{z_0} r(z) \sqrt{1 + r'(z)^2} \sigma(z) z dz \quad (3.57)$$

$$(3.58)$$

without the demand for a proof. Lemma 4 asserts explicit expressions for physical quantities that also follow from charged equipotential droplets.

**Lemma 4.** *For a charged droplet given by  $r(z)$ ,  $\sigma(z)$ , the spatially resolved electrical Weber number is given by*

1)

$$W_{eE}(z) = \frac{\sigma(z)^2}{z + \Delta p_1 + \frac{1}{2}\sigma(z)^2}. \quad (3.59)$$

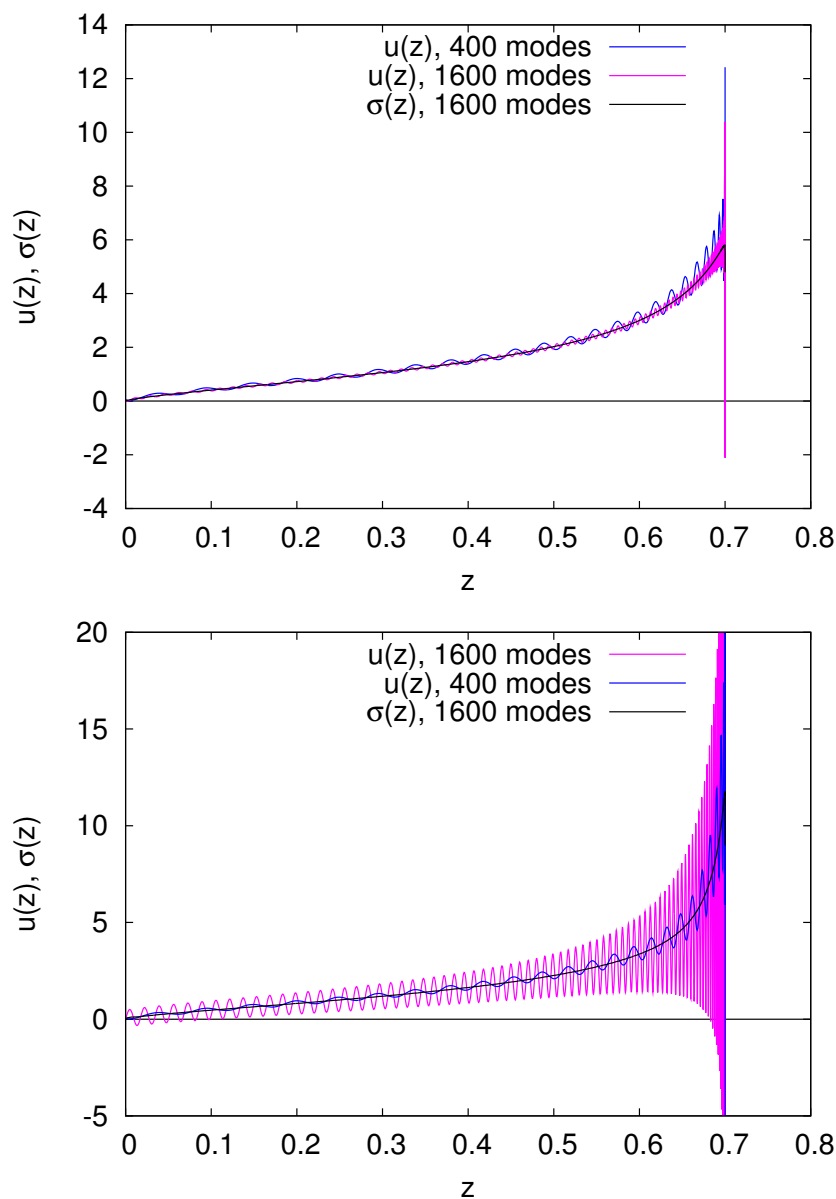
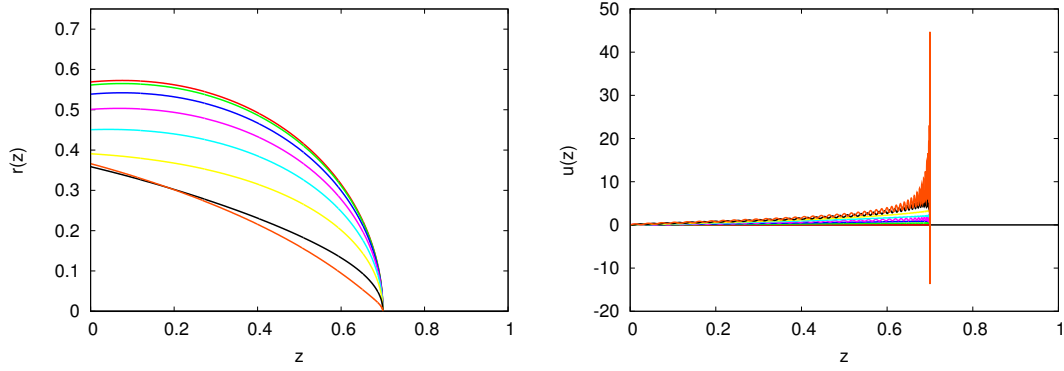


**Figure 3.21:** From top to bottom the numerically obtained oscillating charge densities before window averaging  $u(z) = \sigma(z) + \delta g(z)$  are displayed for  $\Pi_3 \in \{29, 30\}$ , respectively, belonging to the results presented in Figure 3.20. For  $\Pi_3 = 29$  the spoiling oscillations  $\delta g(z)$  increase in frequency and reduce in amplitude for increased resolution while for  $\Pi_3 = 30$  the frequency and the amplitude increase with increasing resolution. The window averaged solution is an approximation to the desired resolution independent *fixed solution*  $\sigma(z)$  of the continuous Fredholm integral equation 3.40. The iteration takes  $\mathcal{O}(100)$  steps to converge after an increase in the electrical field  $\Pi_3 \rightarrow \Pi_3 + 0.1$ . It is important to note that these oscillations are not just due to a single singular vector but are composed of a lot of singular vectors belonging to a whole set of singular values. Similar spoiling problems of Fredholm integral equations have been encountered in [Phillips, 1962] and are a common problem.

a)



b)

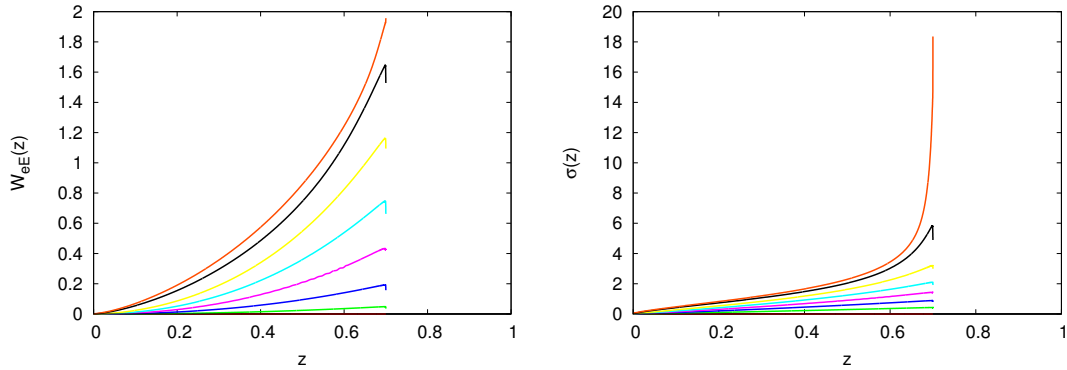


**Figure 3.22:** a) A sequence of charged droplets  $r(z)$  at different electrical fields  $\Pi_3 \in \{5, 10, 15, 20, 25, 30\}$  (left) with the numerically obtained charge density solutions  $u(z) = \sigma(z) + \delta g(z)$  (right). b) The corresponding electrical Weber numbers  $W_{eE}(z)$  indicate the growing influence of the Maxwell pressure (left) and the charge densities  $\sigma(z)$  obtained after the spoiling oscillations have been averaged out. The orange droplet reveals a conical apex, but due to the presence of the hydrostatical pressure its electrical Weber number always satisfies  $W_{eE}(z) < W_{eE}^{crit} = 2 \forall z$ , which is a fundamental difference to ideal Taylor cones with  $W_{eE}(z) = W_{eE}^{crit} = 2 \forall z$ .

In the absence of gravity the energy of state of an equipotential droplet is obtained from  
2)

$$E = A - \frac{p}{8\pi^2} \Pi_3 \quad p = |\vec{p}| \quad (3.60)$$

where  $A$  is the surface of the droplet and  $\vec{p}$  is the dipole moment.

*Proof.* 1) From the definition of the electrical Weber number

$$W_{eE} = \frac{\epsilon\epsilon_0 E^2}{\gamma\kappa} = \frac{\sigma^2}{\epsilon\epsilon_0\gamma\kappa} \quad (3.61)$$

in dimensional form, nondimensionalization via the common scalings A.2 results in

$$W_{eE}(z) = \frac{\sigma(z)^2}{\kappa(z)} \quad (3.62)$$

in non-dimensional formulation, which is spatially resolved as in Section 2.3. From equations 3.5, 3.6 and 3.19 follows

$$\kappa(z) = z + \Delta p_1 + \frac{1}{2}\sigma(z)^2 \quad (3.63)$$

and hence the proof of equation 3.59.

2) The electrostatic energy of a charge density  $\rho(\vec{r})$  exposed to an external electrostatic potential  $\phi(\vec{r})^{ext}$  is given by

$$E^{el} = E^{ext} + E^\rho \quad (3.64)$$

where  $E^{ext}$  and  $E^\rho$  are the energy of the charge density  $\rho(\vec{r})$  due to an external electrostatic potential and the eigenenergy, respectively, given by

$$E^{ext} = \int \rho(\vec{r})\phi(\vec{r})^{ext} d^3r \quad E^\rho = \frac{1}{2} \int \rho(\vec{r})\phi(\vec{r})^\rho d^3r. \quad (3.65)$$

These expressions are well-known from standard textbooks [Jackson, 1998]. From the plate capacitor potential  $\phi^{pc} = -E^{pc} z$  the equipotential boundary condition leads to

$$0 \stackrel{\text{def}}{=} \phi_0 = \phi(\vec{r})^{ext} + \phi(\vec{r})^\rho \Big|_{\vec{r} \in V_{ol}} \implies \phi(\vec{r})^\rho \Big|_{\vec{r} \in V_{ol}} = E^{pc} z \quad (3.66)$$

and therewith

$$E^{el} = \int \rho(\vec{r}) \phi(\vec{r})^{ext} d^3r + \frac{1}{2} \int \rho(\vec{r}) \phi(\vec{r})^\rho d^3r = -\frac{1}{2} E^{pc} \underbrace{\int \rho(\vec{r}) z d^3r}_{=|\vec{p}|} = -\frac{1}{2} |\vec{p}| |\vec{E}^{pc}| \quad (3.67)$$

with  $\vec{p}$  the dipole moment aligned with the field as shown in Figure 3.13 such that

$$E^{el} = -\frac{1}{2} \vec{p} \cdot \vec{E}^{pc}. \quad (3.68)$$

The energy of the droplet in the absence of gravity is composed from the surface energy  $E^{sf} = \int_{\partial V_{ol}} \gamma dA$  and the electrostatical energy  $E^{el}$  yielding

$$E = \gamma A - \frac{1}{2} |\vec{p}| |\vec{E}^{pc}| \quad (3.69)$$

which becomes

$$E = A - \frac{p}{8\pi^2} \Pi_3 \quad p = |\vec{p}|. \quad (3.70)$$

in non-dimensional formulation from the common scales defined in appendix A.2.  $\square$

An immediate consequence of Lemma 4 is that the electrical Weber number is a function of the axial coordinate  $z$  and hence varies along the charged droplet. At  $z = 0$  the electrical Weber number is  $W_{eE} = 0$  as  $\sigma(z)$  is an odd function. Consequently, the droplet cannot be destabilized on the entire surface as is the case for the ideal Taylor cone discussed in Section 2.2. Furthermore, a droplet resulting from the integration of the Fuchikami equations cannot exceed the critical electrical Weber number  $W_{eE}^{crit} = 2$  no matter how large the surface charge density is as the curvature increases accordingly in order to balance Maxwell and Laplace pressure with each other. From the energy of the droplet 3.60 it is obvious that only the dipole moment determines the loss of energy of the system by forming a charged droplet compared to a plate capacitor without a droplet. The monopole charge on the droplet does not contribute to the energy as the monopole charge on the image charge is located at the same potential cancelling the monopole contribution. This means that an isolated, charged, ideal plate capacitor does not change its voltage in case a droplet is pushed out from a nozzle at a plate of the plate capacitor.

The energy of the droplet increases with increasing surface of the droplet as is the case for an uncharged droplet. An applied electrical field causes an accumulation of charge carriers at the surface of the droplet, giving rise to a dipole moment  $\vec{p}$ , which is always aligned with the electrical field in the minimal energy configuration. Hence, the energy of a large elongated droplet increases due the increase of surface  $A$  but decreases with the induced dipole moment and the electrical field.

### 3.3 Droplets hanging from a nozzle

The method to solve the problem of a conducting liquid droplet exposed to a homogeneous electrical field in mechanical and electrical equilibrium has been developed in Section 3.2. By using this method, the physical properties of charged droplets hanging from a nozzle are studied in the following. From the point of thermodynamics these droplets are open systems as fluid mass and charge are supplied from the nozzle to any amount necessary to

form such a droplet.

By construction these solutions of a droplet in electrical and mechanical equilibrium are fixed points of the dynamical system of a droplet or jet issuing from the nozzle under the given parameters i.e. the pressure  $\Delta p_1$  and the plate capacitor field  $\Pi_3$ . Hence, the solutions of the considered electrohydrostatical problem are a subset of the solutions to the full and more complex electrohydrodynamics problem. Hence, from this dynamical systems point of view, it is worthwhile to study the fixed points as they reveal a lot of information about the phase space in which the dynamics takes place. Therefore, the solutions to the electrohydrostatical problem are studied in Subsection 3.3.1.

Unfortunately, it is non-trivial to perform a stability analysis on this electrohydrostatical problem. Therefore, the stability of the obtained solutions is not investigated in a rigorous way as might be expected as for a hydrostatical problem. Sometimes it is possible to guess about the stability of solutions e.g. a concave solution is certainly unstable, while a charged mode 1 like droplet is most probably stable. In Subsection 3.3.3 the difficulties of a reliable stability analysis are worked out in detail. Subsection 3.3.4 deals with the dependency of the observed opening angle of electrified droplets with conical ends due to the hydrostatical pressure. Overcharged droplets and the impact of an instantaneous switching of the electrical field on the charged droplet are investigated in Subsections 3.3.5 and 3.3.6, respectively, in order to gain an understanding about the onset of jet emission.

### 3.3.1 Equilibrium shapes of charged droplets

The experimental situation of a droplet hanging from a nozzle is fully characterized for a given nozzle of radius  $r_n$ , a pressure difference  $\Delta p_1$  and an applied electrical field  $\Pi_3$  as already outlined in Table 3.3 on page 42. It will turn out that the solution set to these parameters is either empty, contains a single or up to an indefinite number of elements in case  $\Pi_3 = 0$ . The numerical parameters are not identical to the operational parameters of the experiment, because the modified Fuchikami equations are integrated from the apex of the droplet at  $z_0$  to the nozzle located at  $z = 0$ . The obtained solution  $r(z)$ ,  $\sigma(z)$  then results in the nozzle radius  $r_n = r(z = 0)$  for which the droplet  $r(z)$ ,  $\sigma(z)$  is a valid solution for the parameters  $\Delta p_1$  and  $\Pi_3$ . Setting the nozzle radius  $r_n$  to a specific constant value, as is done in experiments, gives rise to a boundary value problem posed on the modified Fuchikami equations, which are of course additionally constraint by the equipotential boundary condition.

As has been demonstrated in Section 3.1.2 for uncharged droplets, the nozzle radius depends on both parameters  $z_0$  and  $\Delta p_1$ . In case of a charged droplet the nozzle radius also depends on the electrical field  $\Pi_3$ , which is illustrated in Figure 3.23. The nozzle radius  $r_n = r_n(\Delta p_1, z_0, \Pi_3)$  resulting from the numerically obtained solutions is a function of the three-dimensional parameter space<sup>17</sup>  $(\Delta p_1, z_0, \Pi_3) \in \mathbb{R} \times \mathbb{R}^+ \times \mathbb{R}^+$ . As the adiabatic

---

<sup>17</sup>Negative pressures  $\Delta p_1 < 0$  are conceivable in case the droplet is already highly charged  $\Pi_3 \gg 0$  and



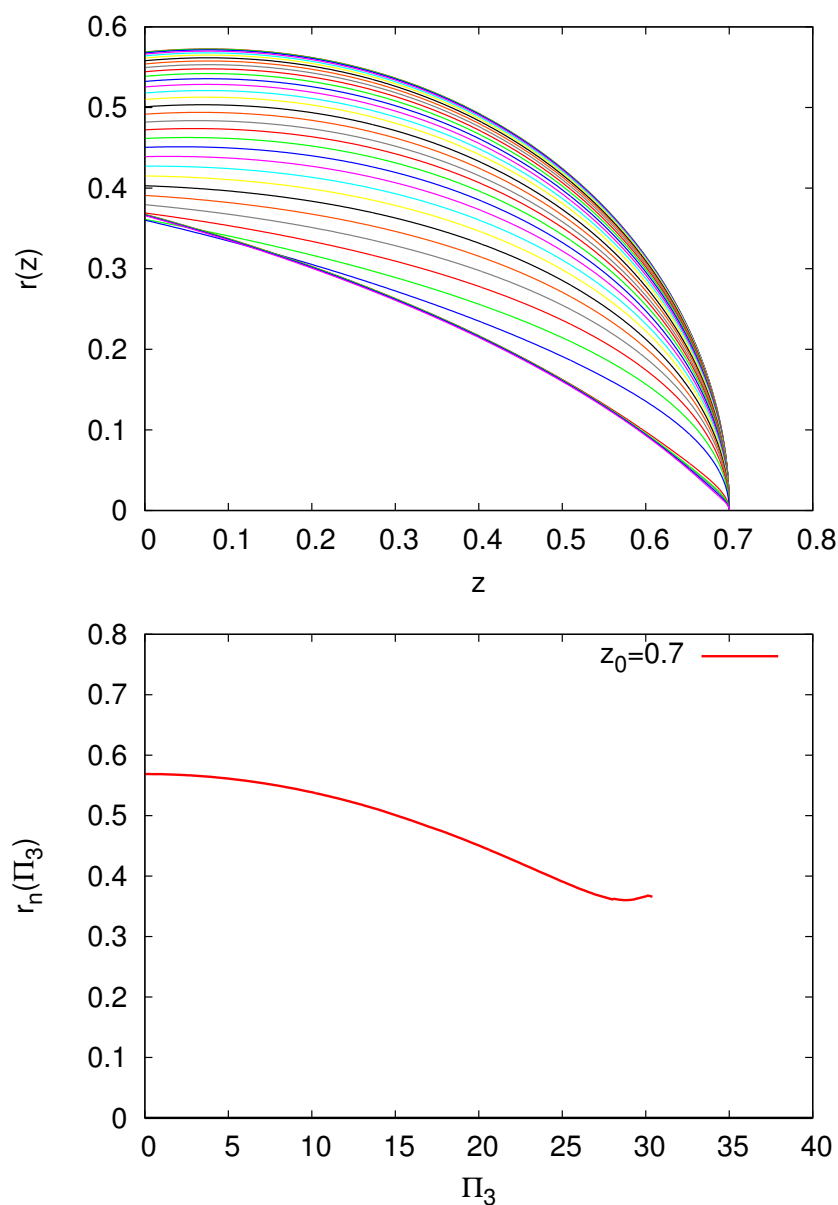


**Figure 3.23:** A droplet at nozzle pressure  $\Delta p_1 = 3$  hanging down to  $z_0 = 0.7$  is charged to electrical fields  $\Pi_3 \in \{0, 1, \dots, 29, 30, 30.1, \dots, 30.4\}$  respectively. With increasing field the radius  $r(z)$  typically becomes smaller. Each computed solution is an experimentally valid solution only, in case it hangs down from a nozzle of appropriate nozzle radius  $r_n = r(z = 0)$ . The nozzle radius  $r_n(\Pi_3)$  necessary for the solutions to be valid is a function of the electrical field. With increasing electrical field  $\Pi_3$  the function  $r_n(\Pi_3)$  is decreasing to a minimum  $r_n(\Pi_3) = 0.360$  at  $\Pi_3 = 28.8$ , increasing to a maximum at  $\Pi_3 = 30.1$  and just starts decreasing again before the algorithm stops converging at all. Hence, given a nozzle radius  $r_n$  in an experiment, there are either none, one or up to three discrete values of the electrical field at which a droplet featuring  $z_0 = 0.7$  at  $\Delta p_1 = 3$  is a solution of simultaneous electrical and mechanical equilibrium.

charging of a droplet is a tedious numerical procedure, which consumes a lot of computer time in case the droplets are highly charged, a shooting method in the three-dimensional parameter space based on some kind of bisectioning is not useful as it has been for the simple droplets. Instead, it is much simpler to scan the parameter space and refine the resolution, wherever interesting features occur. The algorithm displayed in Figure 3.15 has been used to compute solutions for the discrete subspace of control parameters

$$\Delta p_1 \times z_0 = \{1.4, 1.6, \dots, 2.8, 3.0\} \times \{0.2, 0.22, 0.24, \dots, 0.78, 0.8\} \quad (3.71)$$

and sometimes also for larger  $z_0$ . Generally the algorithm is started from the uncharged droplet with the electrical field  $\Pi_3 = 0$ . After a solution has been found, the electrical field is updated via  $\Pi_3 \rightarrow \Pi_3 + \Delta\Pi_3$  with  $\Delta\Pi_3 \in \{0.1, 1\}$  depending on the behavior of convergence of the algorithm.

Figure 3.24 shows a contour plot of the nozzle radius  $r_n(\Delta p_1, z_0, \Pi_3)$  at constant pressure  $\Delta p_1 = 3$  as a function of  $z_0$  and the electrical field  $\Pi_3$ . There are three contour lines, each corresponds to a constant nozzle radius. All contour lines visualized hit the abscissa at  $\Pi_3 = 0$  twice corresponding to the uncharged case. These two uncharged solutions are the mode 1 and mode 2 solutions that have been introduced in Section 3.1.2. In the following, the left and right branch of the contour lines will be referred to as charged mode 1 and charged mode 2 solutions, respectively. It can be seen that the uncharged mode 1 corresponds to the smallest value of  $z_0$  and the uncharged mode 2 to the largest  $z_0$  for each of the contour lines. Furthermore, an increase in the electrical field  $\Pi_3$  makes modes 1 and 2 of  $r_n = \text{const}$  approach each other with respect to  $z_0$ . Eventually, both modes collapse at a critical electrical field  $\Pi_3^{\text{max}}$  into a single solution for the given nozzle radius  $r_n$  of interest. For electrical fields larger than this maximal electrical field there exists no solution for the chosen nozzle radius anymore. This implies that for too large an electrical field the onset of fluid motion is unavoidable for a droplet initially hanging from a nozzle at constant pressure  $\Delta p_1$ .

In the lower part of Figure 3.24 the plots of all numerically obtained solutions along the contour lines are displayed for the three nozzle radii  $r_n = 0.5$ ,  $r_n = 0.36$  and  $r_n = 0.35$ , respectively. The solutions are parameterized by equidistant values of  $z_0$ .

For the large nozzle  $r_n = 0.5$  all solutions are rounded droplets. The contour plot in Figure 3.24 suggests that it is at least theoretically possible to convert a mode 2 droplet into a mode 1 droplet and vice versa by charging and uncharging of the droplet<sup>18</sup>. This conversion may be performed by charging a mode 2 droplet adiabatically at constant pressure  $\Delta p_1 = \text{const}$  until the maximal electrical field is reached that can be found from the contour plot in Figure 3.24. Reducing the electrical field again, causes the droplet by chance

---

reveal cusp like shapes as those in [Forbes, 1997]. These situations are not studied here.

<sup>18</sup>Experimentally, some kind of perturbation might render the droplet unstable during the conversion setting the droplet into motion. At  $\Pi_3 = \Pi_3^{\text{max}}$  this should happen most easily.

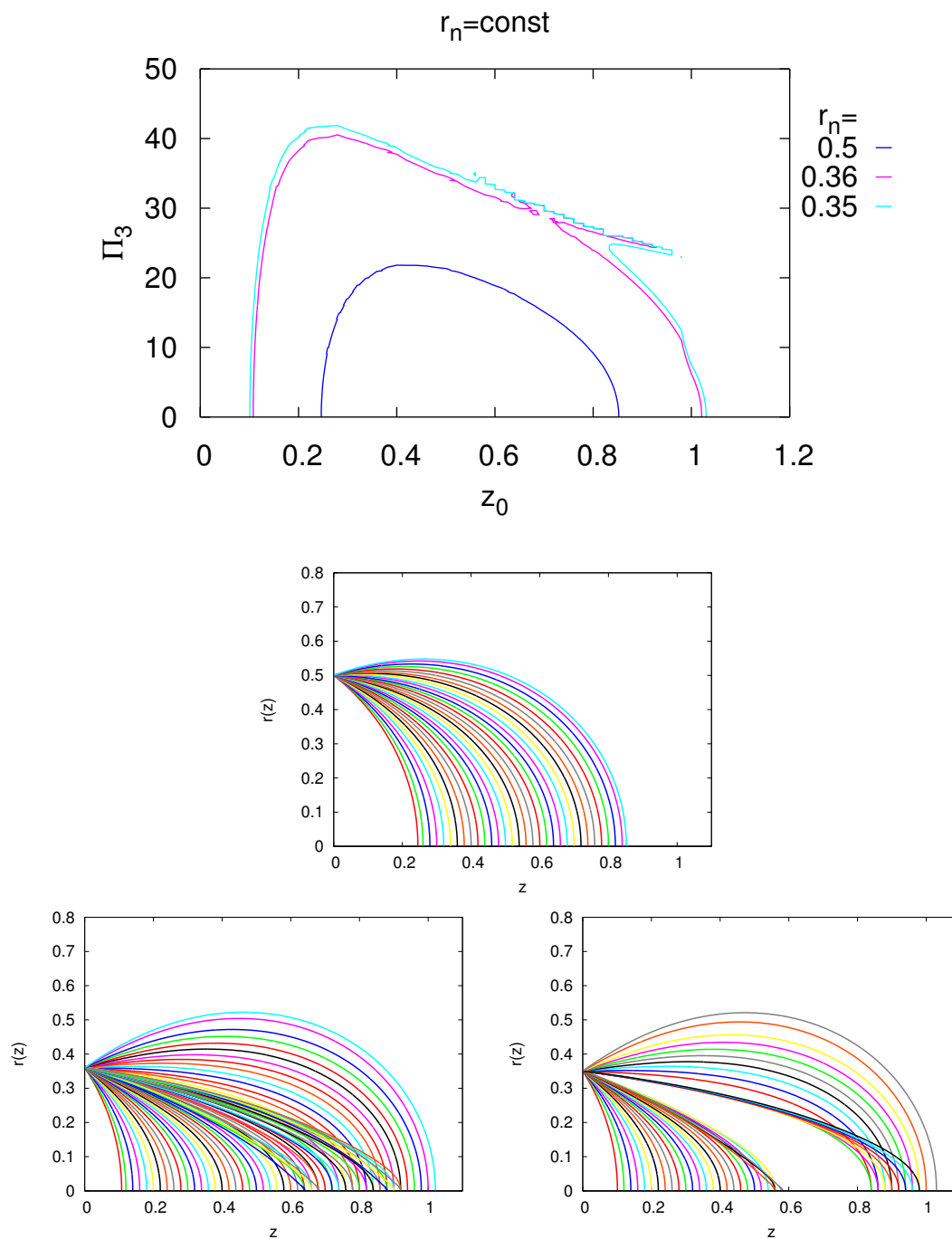


**Figure 3.24:** From top to bottom: A contour plot of the nozzle radius  $r_n = \text{const}$  as a function of the parameter space  $z_0$  and the electrical field  $\Pi_3$  at constant pressure  $\Delta p_1 = 3.0$ . All numerically obtained droplets for the three different nozzle radii  $r_n = 0.5$ ,  $r_n = 0.36$  and  $r_n = 0.35$  of the contour plot are shown, respectively. For radius  $r_n = 0.35$  there is a gap in  $z_0$ , where no solutions exist for this nozzle radius. This goes along with the artificial ripples of the cyan curve visible in the contour plot. Figure 3.27 supplements the contour plot with additional color coded information about the convergence of the algorithm.

to uncharge along the mode 1 branch of the contour plot.

For the smaller nozzle radius  $r_n = 0.36$  there exist three qualitatively different droplets. The contour plot and the droplet survey of Figure 3.24 are complemented by the more detailed Figure 3.25 that distinguishes between these three types of charged droplets. The first kind of droplets are rounded mode 1 and mode 2 droplets as for the large nozzle radius before. The  $\Pi_3(z_0)$  graph of Figure 3.25 shows that they can also be converted theoretically into one another by charging and uncharging them appropriately. The other two kinds of droplets encountered for this nozzle radius are intermediate and conical droplets as displayed in Figure 3.25. These droplets differ from the rounded droplets as their curvature is larger, their volume, surface, dipole moment and energy of state is smaller. This means that the thermodynamically open system of a droplet hanging from a nozzle may prefer intermediate or conical droplets, when charging a mode 2 droplet in the region of the parameter space close to the critical point at  $\Pi_3 \approx 30$ ,  $z_0 \approx 0.7$  for the chosen nozzle radius of  $r_n = 0.36$  at  $\Delta p_1 = 3$ .

Decreasing the nozzle radius even further to  $r_n = 0.35$  reveals some artificial ripples in the contour plot of Figure 3.24 that appear for  $z_0 \in [0.60, 0.82]$  because the numerical algorithm displayed in Figure 3.15 does not converge there anymore for larger electrical fields  $\Pi_3$ . Figure 3.27 shows supplementary color coded information about  $r_n$  and indicates lack of convergence in black. For these electrical fields the condition of convergence  $\|\phi(z)\|_2 < \epsilon$  to solutions of simultaneous mechanical and electrical equilibrium is no longer found to be satisfied, although  $\|\phi(z)\|_2$  is still small. The most probable reason for this vanishing of convergence is that no more electrohydrostatical solutions exist for these large electrical fields, due to a possible bifurcation in parameter  $\Pi_3$ . This interpretation is in agreement with previous theories of critical electrical fields [Taylor, 1964].

The details for the solutions found for the smallest nozzle radius considered  $r_n = 0.35$  are displayed in Figure 3.26. As before, rounded and conical droplets have been found, but there is a gap in  $z_0$  where no solutions seem to exist at all. Consequently, mode 1 and mode 2 droplets cannot be converted into one another anymore via adiabatic charging and uncharging of the droplet for this nozzle radius at the given pressure  $\Delta p_1 = 3$ .

From the experimental or engineering point of view, the nozzle radius becomes an important control parameter that has to be chosen carefully with respect to the desired behavior of the droplet in the isobar case  $\Delta p_1 = \text{const}$  described here. As the contour plots of Figures 3.24 and 3.27 are just two-dimensional slices in the three-dimensional parameter space, it is easy to understand that the choice of the nozzle radii selects isosurfaces of constant nozzle radii in the parameter space  $(\Delta p_1, z_0, \Pi_3)$ . The interpenetration of some of these isosurfaces with the boundary of existing solutions to the electrohydrostatical solution yields surfaces in parameter space representing borders to be crossed in order to trigger the onset of fluid motion.

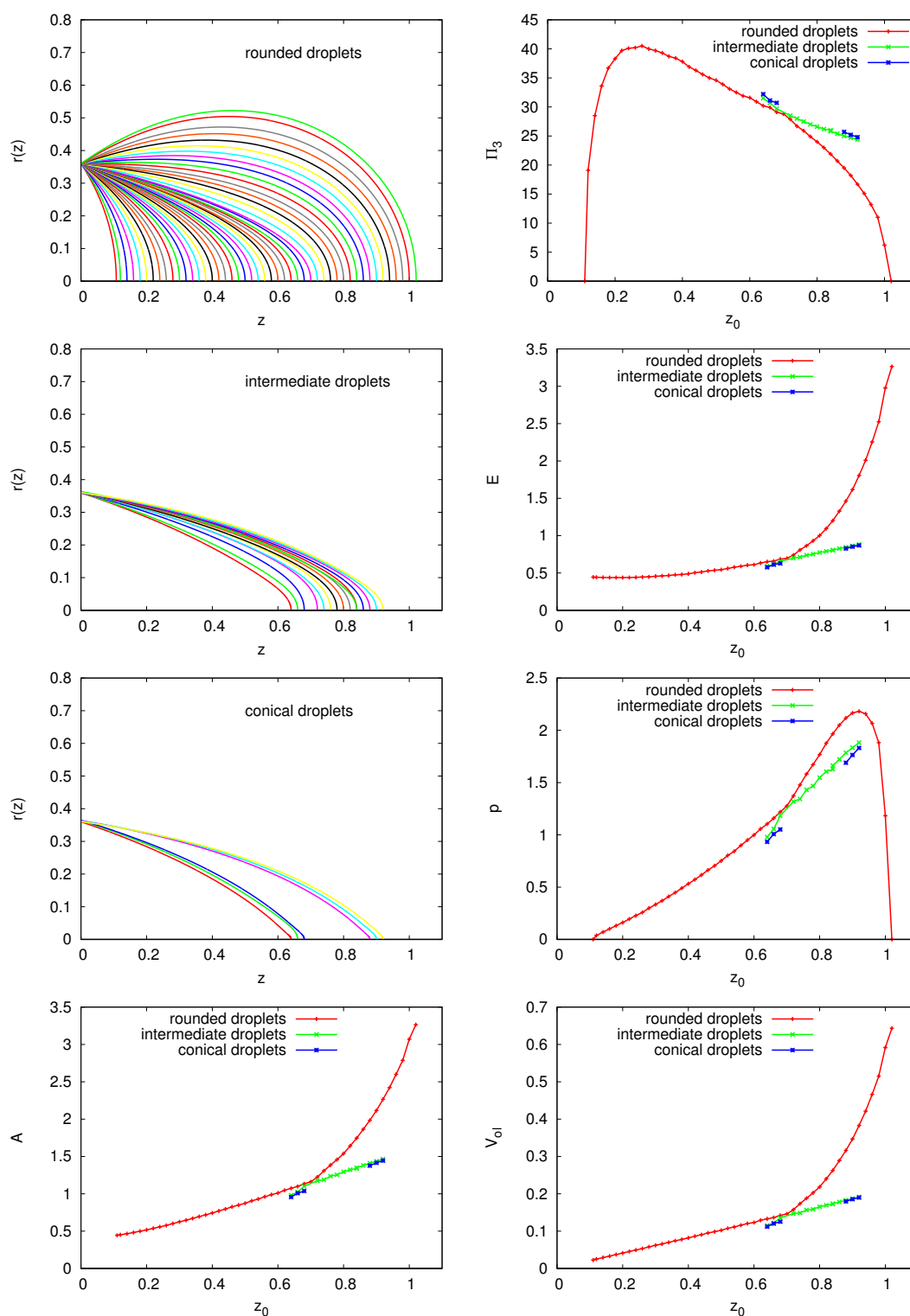


**Figure 3.25:** There exist three types of solutions for the nozzle radius  $r_n = 0.36$  displayed in the left column: rounded, intermediate and conical droplets  $r(z)$ . The properties like electrical field  $\Pi_3$ , energy of state  $E$ , dipole moment  $p$ , surface  $A$  and volume  $V_{ol}$  are color coded in these plots: rounded droplets (red), intermediate droplets (green) and conical droplets (blue).

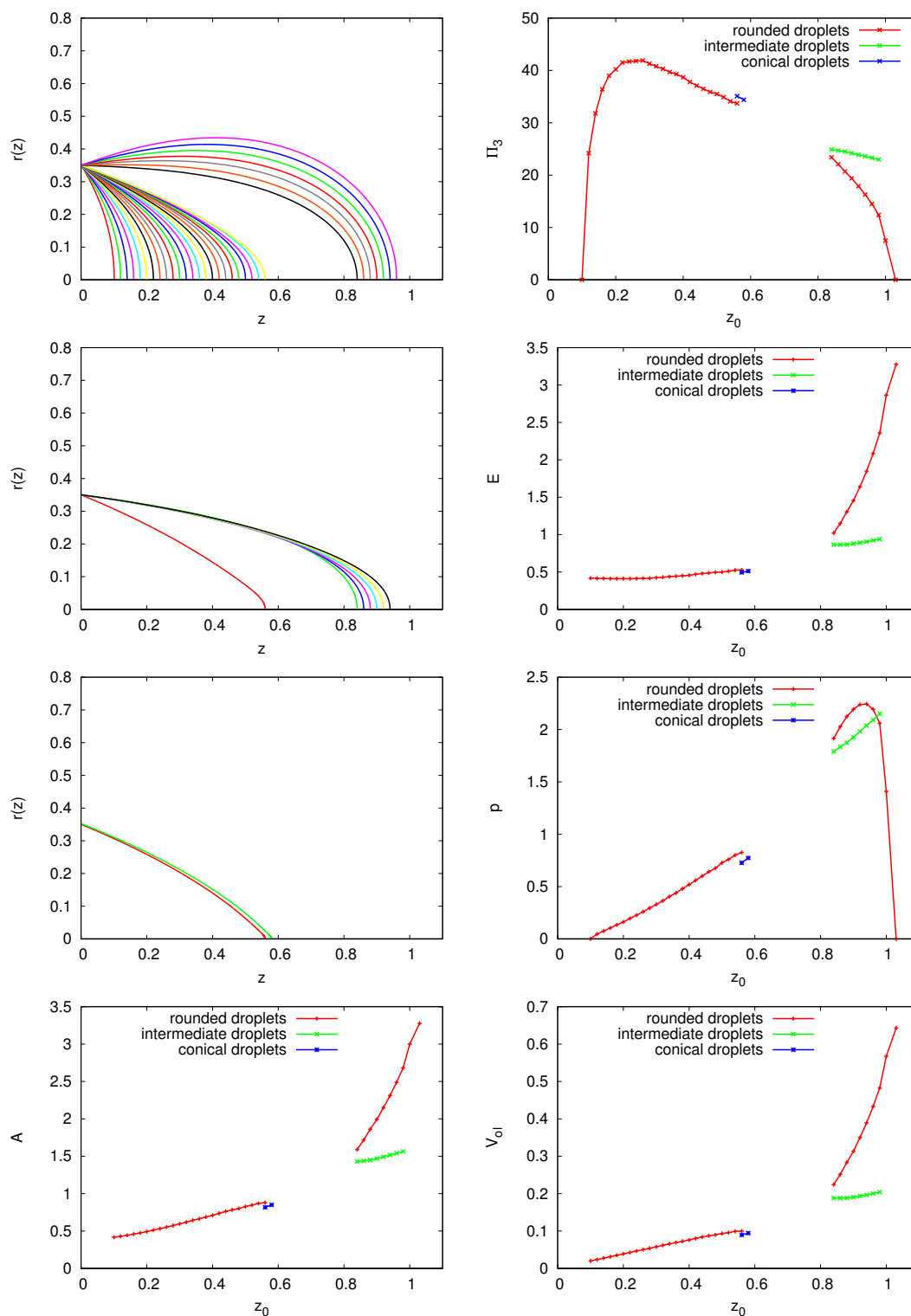


**Figure 3.26:** There exist three types of solutions for the nozzle radius  $r_n = 0.35$ , which are related to the different branches of the contour plot in Figure 3.24 that are color coded in this plot: rounded droplets (red), intermediate droplets (green) and conical droplets (blue).

This means that by the selection of the nozzle radius and the imposition of a specific curve in parameter space  $\mathcal{K}(t) = (\Delta p_1(t), \Pi_3(t))$  a droplet may be charged adiabatically towards the border of existing electrohydrostatical solutions in a precisely controlled way leading to a well defined onset of fluid motion from a deliberately chosen type of droplet.

Unfortunately, the necessary amount of numerical computation to scan large parts of the relevant parameter space is huge. Nevertheless, the method of solution has been demonstrated to work properly and reveals first insights into the structures defined on the parameter space.

### 3.3.2 Charged mode 3 solutions

The charged mode 1 and charged mode 2 solutions corresponding to the left and right branch of the contour plot in Figure 3.24 are not the only solutions existing for a given nozzle. Extending the domain to larger values of  $z_0$  reveals that there are corresponding branches for charged mode 3 and charged mode 4 indicated by the new contour lines emerging at  $z \approx 1.50$  in Figure 3.28a. As the uncharged mode 3 solution is already unstable [Fuchikami et al., 1999], this branch of solutions might be less interesting than those discussed before.

Nevertheless, it is interesting that there exist charged mode 3 and charged mode 4 solutions that are monotonous in  $r(z)$  again. An example is illustrated in Figure 3.28c. By charging the droplet, the curvature at the apex is increased such that it becomes conical as already seen before for the charged mode 1 and charged mode 2 solutions. The reason for this is that the additional pressure on the mode  $n$  droplet with  $n > 2$  due to surface charges changes the curvature on the entire droplet and especially at the apex due to the equipotential condition. In this way, indentations in the shape  $r(z)$  of the uncharged mode  $n$  droplet are less deep and sometimes removed for the charged mode  $n$  droplet. The resulting solutions sometimes are elongated droplets that look like launching jets. However, these solutions are electrohydrostatical solutions, whether they are stable or not.

As the uncharged droplets discussed in Section 3.1.2 possess an indefinite number of modes, the abscissa in the contour plot of Figure 3.28 possesses an indefinite number of points corresponding to solution of these uncharged modes for appropriate nozzle radii. Each pair of an odd and the next even mode will give rise to structures similar to those observed in Figure 3.28a.

The solutions to the electrohydrostatical equations are fixed points for the electrohydrodynamical equations. From the picture of dynamical systems the dynamics of a dynamical system happens in phase space, which is structured by fixed points. In this context, the corresponding elongated droplets at equipotential may explain, why charged one-dimensional jets are regularly found in case free charged liquid surfaces are studied. The existence of these structuring solutions might be related to the dynamics observed.

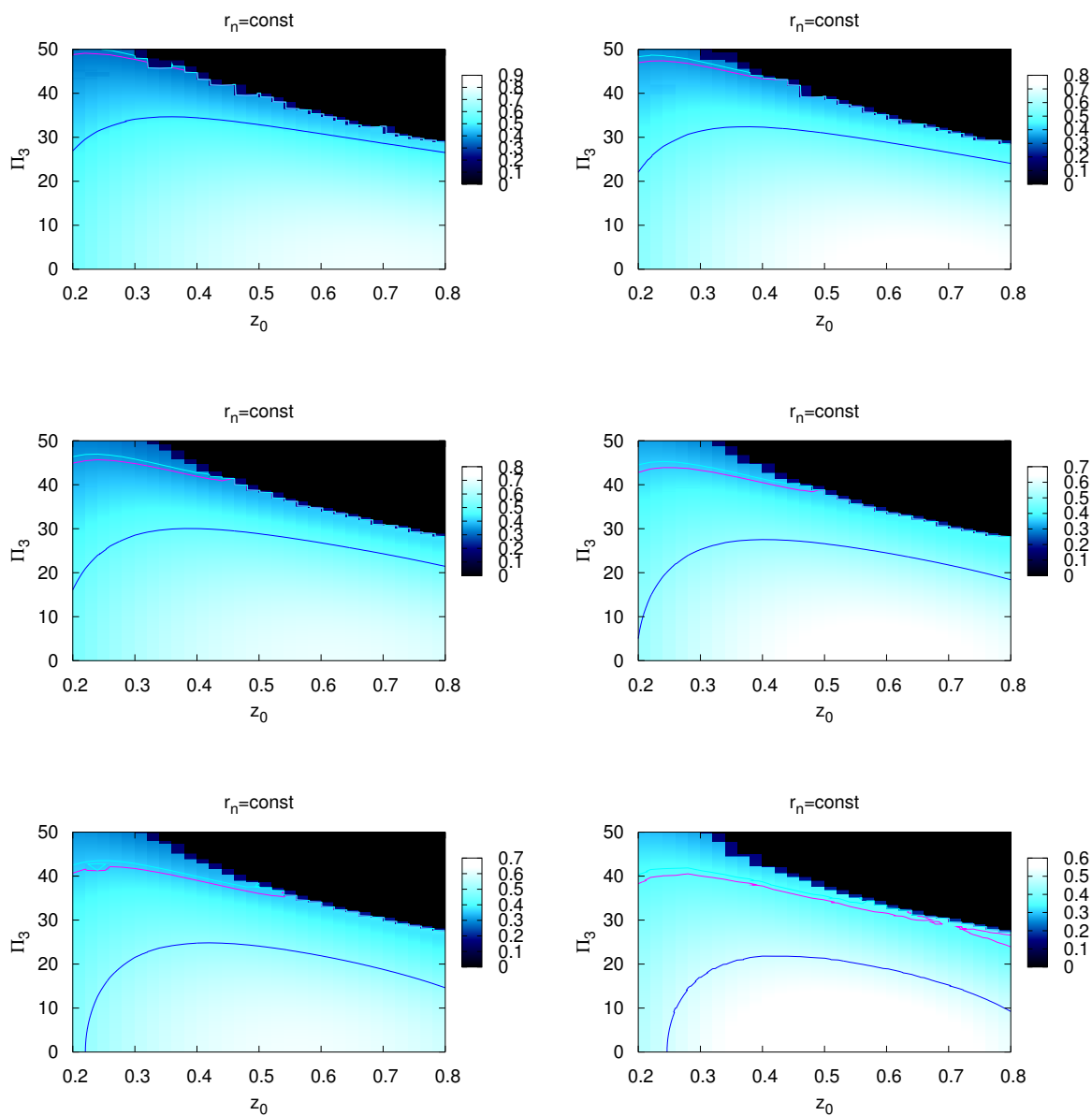
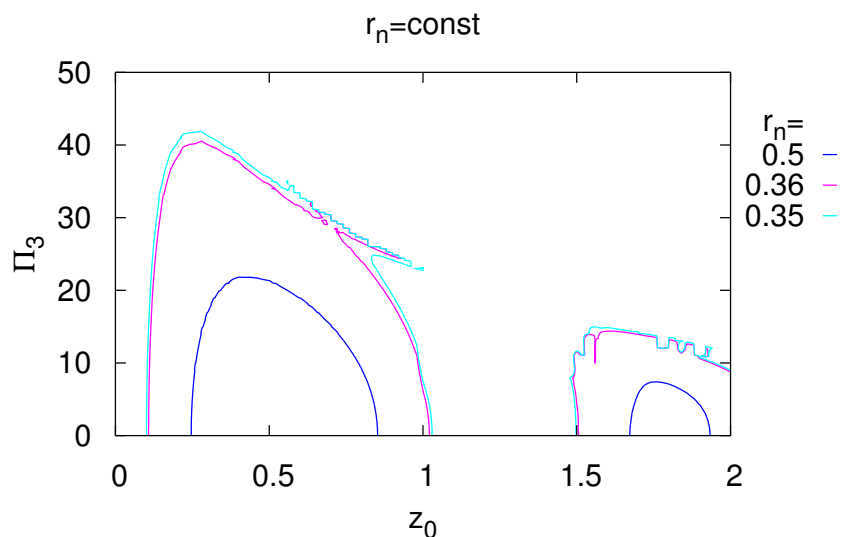


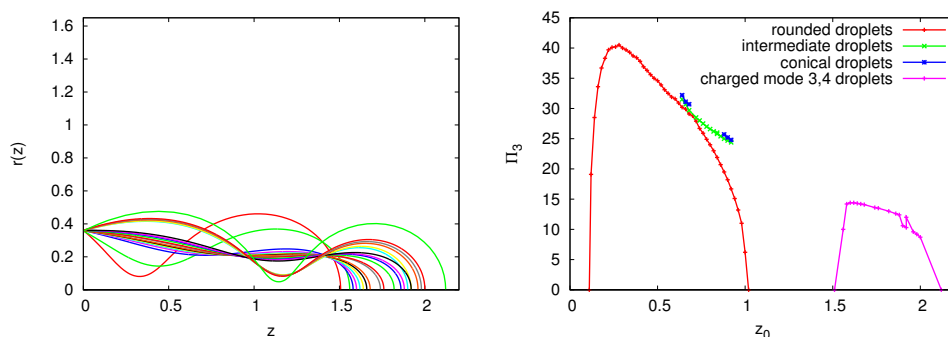
**Figure 3.27:** The color coded contour plots of the nozzle radii  $r_n \in \{0.5, 0.36, 0.35\}$  as in Figure 3.24 for several pressures  $\Delta p_1 \in \{2.0, 2.2, 2.4, 2.6, 2.8, 3.0\}$ , respectively. The black area marks the region, where the numerical algorithm failed to converge. It can be seen that the increase in pressure  $\Delta p_1$  bends down the contour lines towards the abscissa. For the larger pressures solutions for the small nozzles come into existence at the border to the black region. These plots give a hint about the isosurfaces  $r_n = \text{const}$  in the three-dimensional parameter space spanned by  $(\Delta p_1, z_0, \Pi_3)$ .



a)



b)



c)

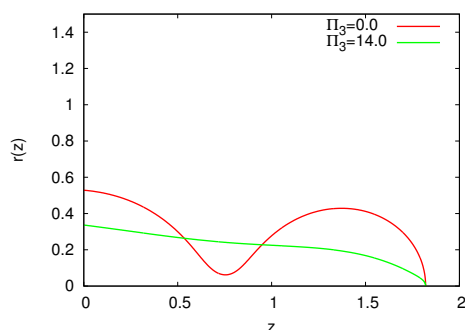


**Figure 3.28:** a) Extending the contour plot of Figure 3.24 to larger values of  $z_0$  reveals the existence of charged mode 3 solutions and charged mode 4 solutions. b) The droplets that are realizable at a nozzle of radius  $r_n = 0.36$  correspond to the magenta contour line. Droplets for  $z_0 \leq 1.02$  are not shown for lucidity as they are shown in Figure 3.25 already. The electrical field  $\Pi_3$  associated to the solutions is displayed. c) An example of an uncharged mode 3 droplet  $\Delta p_1 = 3.0$ ,  $z_0 = 1.82$  that becomes monotonous in  $r(z)$  with a conical apex in case it is charged from  $\Pi_3 = 0.0$  to  $\Pi_3 = 14.0$ .

### 3.3.3 About stability analysis

Performing a stability analysis for numerically obtained electrohydrostatical solutions of droplets in mechanical and electrical equilibrium unfortunately is a nontrivial problem. The reason for this is that the modified Fuchikami equations 3.19 by construction solve a hydrostatical problem, but in order to investigate the stability of solutions, dynamical equations have to be analyzed. Classical studies of hydrodynamical stability of electrified liquid jets always start from special cases where analytical solutions are available [Saville, 1971a, Mestel, 1995]. Fuchikami et al. [Fuchikami et al., 1999] investigated their obtained solutions using Lagrangian dynamics, which is not easily adapted to the electrohydrodynamical problem.

Once, dynamics sets in fluid motion is described by the Navier Stokes equation

$$\rho_l \left( \frac{\partial \vec{u}}{\partial t} + (\vec{u} \cdot \nabla) \vec{u} \right) = -\nabla \cdot \mathbf{\Pi} \quad (3.72)$$

where  $\rho_l$  is the density of the liquid and the right hand side of the equation is given by the divergence of the total stress tensor

$$\mathbf{\Pi} = \underbrace{\eta (\nabla \vec{u} + (\nabla \vec{u})^T)}_{\text{Hydrodynamics}} + \underbrace{\rho_l z \vec{e}_z \cdot \vec{g} + p_1 \mathbf{\mathbb{1}}}_{\text{Electrostatics}} + \underbrace{\epsilon \epsilon_0 \left( \vec{E} \vec{E} - \frac{1}{2} \vec{E} \cdot \vec{E} \mathbf{\mathbb{1}} \right)}_{\text{Free surface}} - \underbrace{\gamma (\mathbf{\mathbb{1}} - \vec{n} \vec{n}) \mathbb{1}_S(\vec{x})}_{\text{Free surface}} \quad (3.73)$$

which consists of the rate of strain tensor plus hydrostatic contributions to the total stress tensor, the Maxwell stress tensor and the Lafaerie tensor [Scardovelli and Zaleski, 1999], respectively. The unit normal of the surface is denoted by  $\vec{n}$  and  $\mathbb{1}_S(\vec{x})$  is the indicator function as defined in Appendix A.3 with  $S$  the set of points belonging to the free surface. It should be noted that the Maxwell stress tensor also includes magnetical contributions, which have been neglected in equation 3.73 because the negligibility of the magnetical field for the liquids used is generally agreed upon [Saville, 1997].

In general, the electrical field

$$\vec{E}(\tilde{r}, z) = - \left( \nabla \phi \left[ r(z) + \delta r(z), \sigma(z) + \delta \sigma(z) \right] \right) (\tilde{r}, z) \quad z, \rho \in \mathbb{R}_0^+ \quad (3.74)$$

to be used in the evaluation of the stress tensor is a complicated functional of the perturbations  $\delta r(z)$  and  $\delta \sigma(z)$  with  $\tilde{r}$  the radial coordinate. The problem of analyzing the stability of the obtained solutions of the electrohydrostatical problem is the transport of charge by advection and conduction simultaneously on very different timescales

$$\frac{\partial \rho_{el}}{\partial t} + \text{div}(\rho_{el} \vec{u} + \vec{j}) = 0 \quad (3.75)$$

with the current density  $\vec{j}(\vec{x}) = K\vec{E}(\rho_{el}, z)$  and charge density  $\rho_{el}(\vec{x})$ . The many degrees of freedom and the lack of satisfactory numerical methods for the treatment of the discontinuous pressure field at the free surface of the flow makes a numerical treatment very difficult. For these reasons, standard methods of stability analysis [Drazin and Reid, 2004, Chandrasekhar, 1981] are inapplicable<sup>19</sup> without a carefully designed numerical method, which demands a study on its own. The development of a more exact stability analysis based on equations 3.72, 3.73 and functional 3.74 for the solutions obtained lies beyond the scope of this work and is left for future studies.

The task for example is to develop a dynamical simulation that starts from the electrohydrostatical solution and shows that *all infinitesimal*<sup>20</sup> perturbation  $\delta r(z)$  and  $\delta\sigma(z)$  result in a restoring fluid motion  $\vec{u}$ . The different timescales of charge relaxation and fluid motion make the problem a hard task.

Alternatively, the stability analysis of electrohydrostatical solutions could be investigated in a similar way as Basaran and Scriven did by using a method of solution based on Galerkin's method with finite element basis functions [Basaran and Scriven, 1990].

### 3.3.4 Gilbert-Taylor cone angles

The carefully designed experiments of Taylor [Taylor, 1964] were designed in order to validate his theory about the balance between the Maxwell and the Laplace pressure at conical fluid interfaces, which lead him to the Taylor cone angle  $\vartheta_T = 130.7^\circ$  or the complementary Taylor cone opening angle  $\vartheta_c = 49.3^\circ$  as reviewed in Section 2.1.

Taylor's analytical result is based on the asymptotical limit of an infinitely extended cone under the neglect of all other pressures such as hydrostatic pressure due to gravity and an additionally applied constant nozzle pressure. The electrodes of his experiments were designed such that the very large nozzle electrode already had the shape of a cone of appropriate opening angle  $\vartheta_c = 49.3^\circ$ . This makes the Taylor cone in the experiment appear much larger than it actually is in order to satisfy the assumption of an infinitely extended cone that is taken for granted by his theory. The experiments successfully validated the theoretical explanation.

In the literature Gilbert-Taylor cones with smaller opening angles have been reported [Yarin et al., 2001, Giglio et al., 2008]. The opening angles of the conical liquid interfaces

---

<sup>19</sup>Although the book by Chandrasekhar is titled *Hydrodynamic and Hydromagnetic Stability* the hydro-magnetical part is limited to the forcing of the flows due to a constant and externally applied magnetic field without dynamical feedback of the flow to the magnetic field.

<sup>20</sup>Numerically, *infinitesimal* perturbations are small but finite perturbations, of course. *All* perturbations are limited to a finite set of representative perturbations.

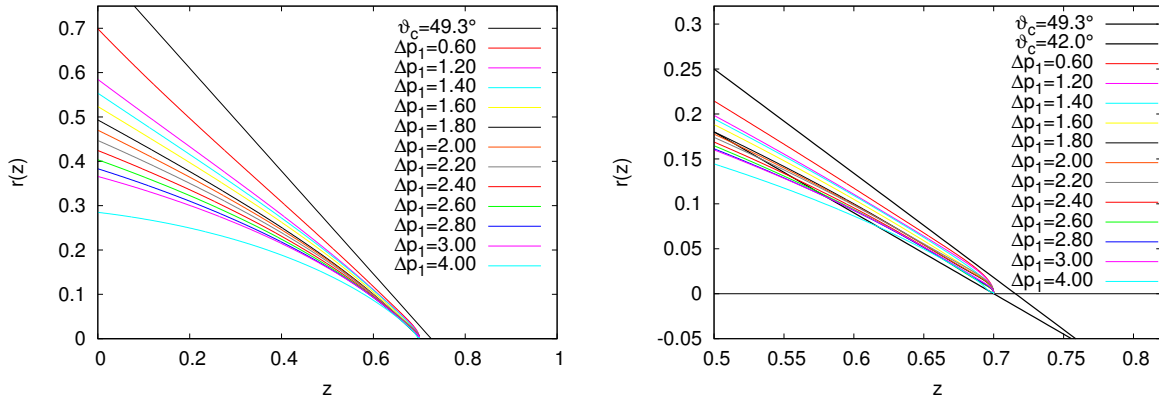


**Figure 3.29:** A sequence of highly charged droplets with  $z_0 = 0.7$  under the variation of the nozzle pressure  $\Delta p_1$  in survey and detail. The black lines indicate the Taylor cone angle  $\vartheta_c = 49.3^\circ$  and the asymptotic opening angle of  $\vartheta = 42^\circ$  for the solutions obtained. As the pressure  $\Delta p_1$  increases, the curvature of the droplet increases as well and continues the conical apex to an uncharged fluid interface at  $z \rightarrow 0$ .

range from  $\vartheta_o = 37.5^\circ$  found by Yarin<sup>21</sup> et al. using a nozzle droplet to  $\vartheta_o = 39^\circ$  found by Giglio et al. using a closed droplet.

The modified Fuchikami equations 3.19 have been derived without the neglect of an additional hydrostatic pressure applied from the nozzle such that droplets can be charged using different nozzle pressures. Figure 3.29 shows the obtained conical droplets for the parameter  $z_0 = 0.7$  for various pressures  $\Delta p_1$ . The corresponding electrical fields  $\Pi_3^{max}$  are the largest electrical fields that allowed a convergence of the numerical algorithm of solution for parameters  $z_0 = 0.7$  and  $\Delta p_1$ , given by

$\Delta p_1$	0.60	1.20	1.40	1.60	1.80	2.00	2.20	2.40	2.60	2.80	3.0	4.0
$\Pi_3^{max}$	35.1	33.6	33.1	32.8	32.4	32.2	31.5	31.5	31.2	30.6	30.4	28.9

As the numerical algorithm encounters difficulties converging<sup>22</sup> for small pressures  $\Delta p_1 \rightarrow 0$  the smallest pressure used is  $\Delta p_1 = 0.6$ , which results in a conical droplet whose opening angle  $\vartheta_o$  is slightly smaller than the opening angle  $\vartheta_c = 49.3^\circ$  of the ideal Taylor cone. For larger pressures the conical liquid surface is more and more curved for smaller values of  $z$ . In the detail of Figure 3.29 it can be seen that the rounded conical tips of these droplets provide an opening angle of  $\vartheta_o \approx 42^\circ$ . The interpretation of this result is quite simple. At the apex of the droplet the hydrostatic and the Maxwell pressure are balanced by the

<sup>21</sup>Refer to Figure 7 a in [Yarin et al., 2001]

<sup>22</sup>The charge density  $\sigma(z)$  is altered a lot during the iteration of the algorithm. For small pressures  $\Delta p_1 < 1$  the fluctuating Maxwell pressure severely impacts on the curvature with too little a stabilization arising from small pressures to ensure a convergence of the iteration.

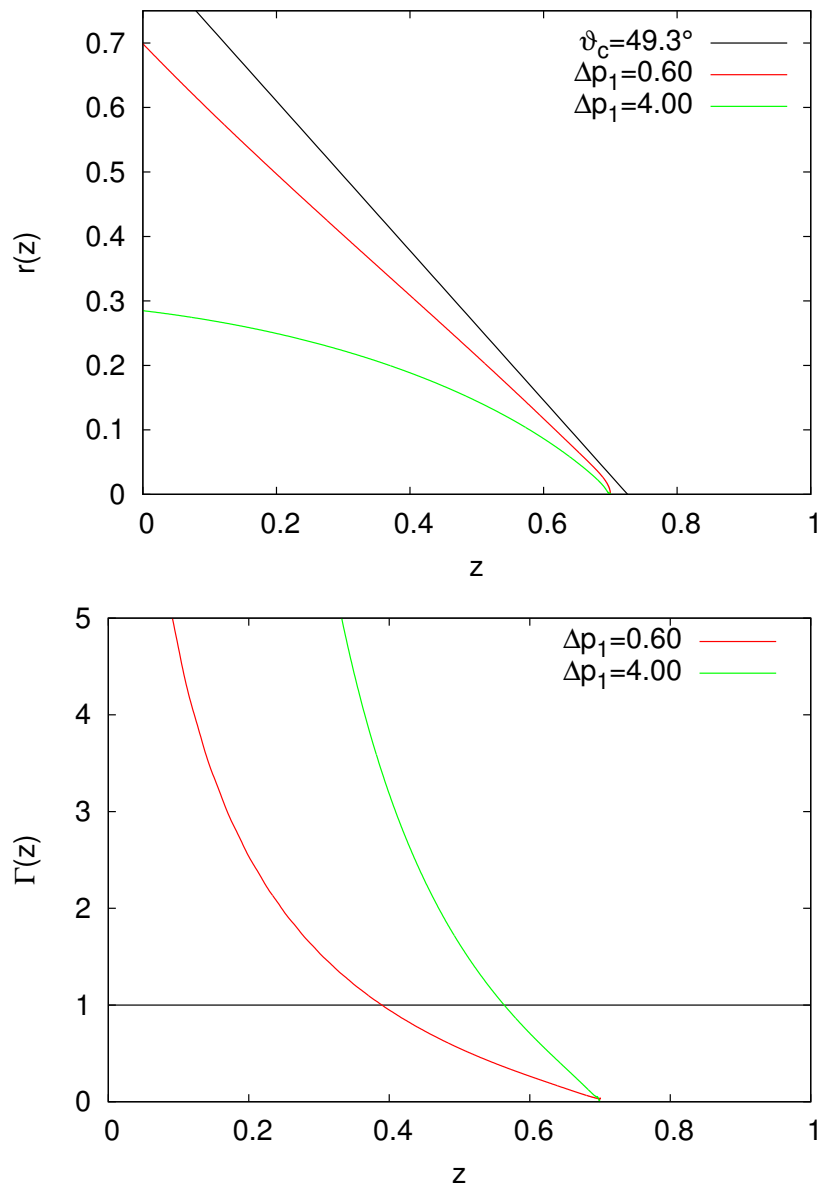


**Figure 3.30:** The two extremal droplets at equipotential taken from Figure 3.29 in comparison to Taylor's asymptotic solution. The ratio  $\Gamma(z) = 2(\Delta p_1 + z)/(\sigma(z))^2$  measures the relative significance of the hydrostatic pressure with respect to the Maxwell pressure from the terms of the right hand side of the Fuchikami equations 3.19. Clearly the hydrostatic pressure dominates for smaller values of  $z$ , where  $\Gamma(z) > 1$ . The asymptotics of the conical ends of the droplets differ from Taylor's, as the droplets smoothly connect the conical regions to the hydrostatical parts of the droplets. This connection is imposed by the non-local equipotential boundary condition.

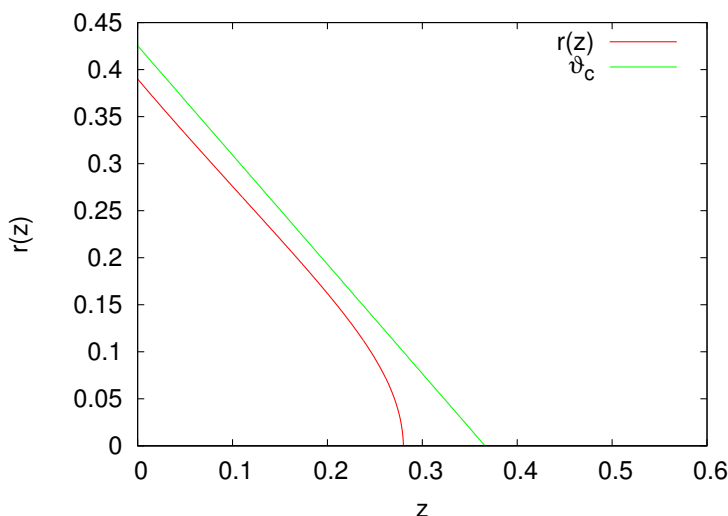


**Figure 3.31:** In the absence of gravity a low nozzle pressure makes charged equipotential droplets approach Taylor’s cone, which is an asymptotical solution with the characteristic opening angle  $\vartheta_c = 49.3$ . Taylor’s asymptotical solution is indicated by the green line for comparison. This solution has been obtained from parameters  $\Delta p_1 = 1.0$ ,  $z_0 = 0.28$  at the electrical field  $\Pi_3 = 54.1$ .

Laplace pressure, where the hydrostatic pressure is almost negligible with respect to the magnitude of the Maxwell and Laplace pressures. At small values  $z \rightarrow 0$  the Maxwell pressure vanishes due to the vanishing of the surface charge density  $\sigma(z)$ , which is an odd function because of its continuous continuation to the image charge of the conical droplet. Hence, at smaller values of  $z$  the Laplace pressure is essentially balanced by the hydrostatic pressure alone, as is the case in uncharged droplets. This fact demonstrates that the charged conical tips of the charged nozzle droplets are continued for decreasing  $z < z_0$  into a droplet that is essentially uncharged close to the nozzle exit at  $z = 0$ . The angle of the conical tip of the charged droplet is apparently dependent on the continuation of the cone towards a rounded droplet. Figure 3.30 shows the transition between the domination of the Maxwell pressure and the hydrostatic pressure for two of the conical droplets displayed in Figure 3.29. The ratio  $\Gamma(z)$  is evaluated directly from the pressure terms of the right hand side of the Fuchikami equations 3.19. In essence this means that the presence of a non-vanishing hydrostatical pressure chooses the angle of the cone in order to continue the conical tip to the droplet that satisfies mechanical and electrical equilibrium simultaneously.

In the absence of gravity the charged droplet visualized in Figure 3.31 reproduces Taylor’s opening angle  $\vartheta_c = 49.3^\circ$  almost perfectly.

In conclusion, Figure 3.29 shows droplets hanging from a nozzle, whose opening angles are decreased at their apices by the non-vanishing hydrostatic pressure. There are two reasons for the deviation from Taylor’s theoretical explanation. At first, his assumption of

a vanishing hydrostatic pressure is not satisfied in many experimental situations. Secondly, the cone of finite size in front of the plate capacitor causes the charge density  $\sigma(z)$  to be an odd function such that Maxwell's pressure vanishes at  $z = 0$ .

### 3.3.5 Overcharged droplets

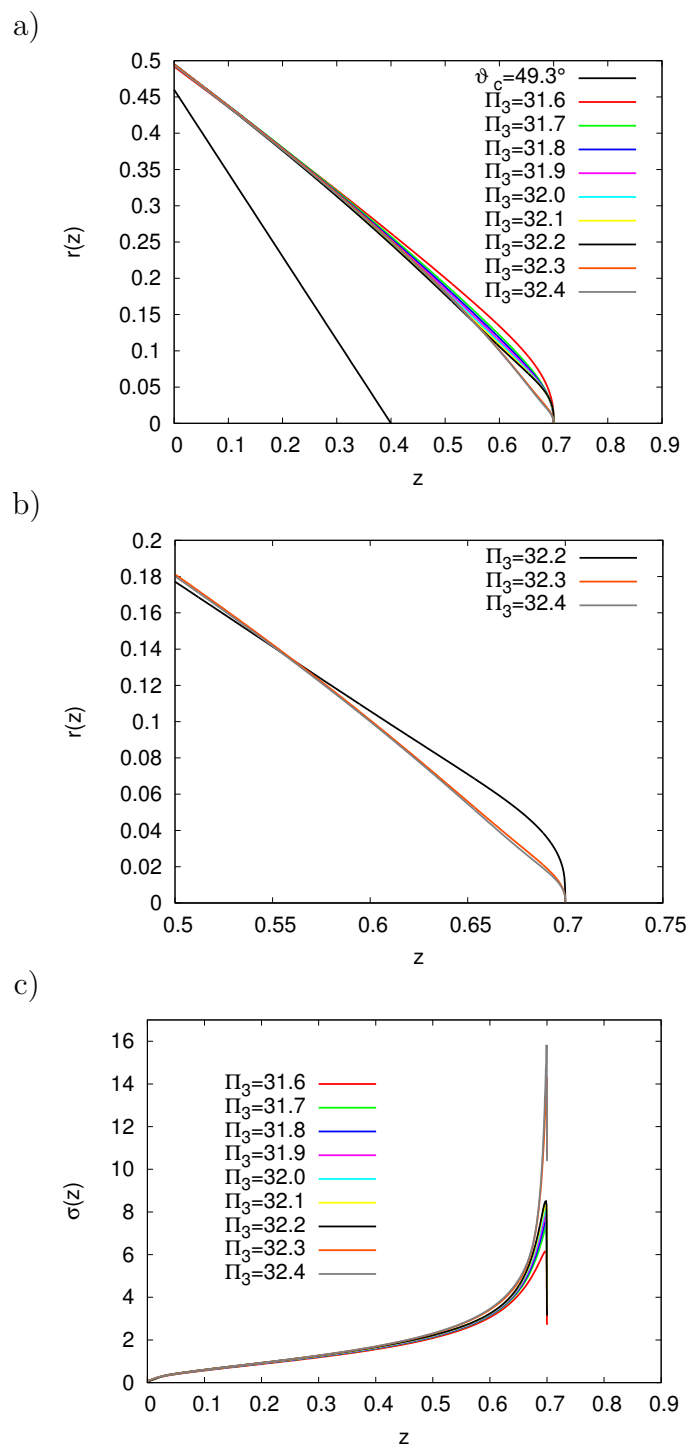
Charging a droplet of given parameters  $\Delta p_1$  and  $z_0$  as displayed in Figure 3.23 on page 69 results in rounded droplets, intermediate droplets or conical droplets independent to the choice of  $z_0$ . It turned out that it is the nozzle radius used in the experiment that restricts the appearance of conical solutions to certain parameters  $\Delta p_1$ ,  $z_0$  and  $\Pi_3$  as discussed in Section 3.3.1. After a conical solution has been obtained the algorithm typically fails to converge in case the electrical field  $\Pi_3$  is increased any further. Nevertheless, sometimes the algorithm converges even for electrical fields beyond those corresponding to conical solutions. In the following these droplets are denominated overcharged droplets and show the onset of necking at the conical fluid interface.

Figure 3.32 a) shows a sequence of shapes of an adiabatically charged nozzle droplet corresponding to a sequence of electrical fields  $\Pi_3$ . In this case the small stepsize in the electrical field  $\Delta\Pi_3 = 0.1$  is still too large to resolve the conical droplet. Instead beautiful overcharged droplets have been found showing the onset of necking.

The detail of the shapes  $r(z)$  illustrated in Figure 3.32 b) shows that there are two kinds of necks to be observed. The first concave indentation is seen for a droplet found for the electrical field  $\Pi_3 = 32.2$  at approximately  $z_{neck} = 0.6$ . This droplet is identified as overcharged intermediate droplet. The next concave indentations are observed for droplets belonging to the category of overcharged conical droplets at electrical fields  $\Pi_3 = 32.3$  and  $\Pi_3 = 32.4$ , whose indentations are located at  $z_{neck} \approx 0.67$ . It has to be kept in mind that all these solutions are solutions of simultaneous mechanical and electrical equilibrium. Exact judgements about the stability of these droplets are very difficult to obtain. Most probably the necked solutions are unstable, which makes sense in view of the experimental observations that overcharged Gilbert-Taylor cones emit jets of a finite radius, whose order of magnitude originates from the equations solved. The difference in  $r(z_{neck})$  of the intermediate droplet and the conical droplet suggests that the initial radius of an eventually emitted jet will also differ by this order of magnitude. In the context of the production of nano-fibers, jet emission from a conical droplet might be more desirable than jet emission from an intermediate droplet.

### 3.3.6 Controlling the directed Coulomb instability

The initiation of jet emission from Gilbert-Taylor cones is observed, when increasing the electrical field beyond a certain critical value. The onset of jet emission typically results in the cone-jet mode, where the dynamical remnant of the Gilbert-Taylor cone emits a jet from its apex. In the following the solution of a highly charged conical droplet is the



**Figure 3.32:** Charged droplets for the parameters  $\Delta p_1 = 1.80$ ,  $z_0 = 0.7$  and a sequence of electrical fields  $\Pi_3$  in survey (a), detail (b) and the associated surface charge density  $\sigma(z)$  (c). a) The single black line indicates the shape of an ideal Taylor cone for comparison. Solutions for electrical fields smaller than  $\Pi_3 = 32.2$  are convex intermediate droplets. b) The overcharged intermediate droplet for  $\Pi_3 = 32.2$  reveals a concave indentation as a consequence of overcharging. The solutions for the larger electrical fields  $\Pi_3 = 32.3$  and  $\Pi_3 = 32.4$  are overcharged conical droplets that also reveal a concave indentation, which occurs at a considerably smaller radius  $r(z_{neck})$  than for the overcharged intermediate droplet.



starting point for an investigation of the behavior of the electrical Weber number  $W_{eE}(z)$  in case the electrical field  $\Pi_3$  of the plate capacitor is switched to larger values instantly.

In this case the droplet is no longer an equipotential and charge carriers are attracted from the nozzle towards the liquid's surface relaxing with the leaky dielectric time scale  $\tau_\epsilon$ , while the fluid is inert and keeps its shape  $r(z)$ . This follows from the time scales already introduced in Section 2.3

$$\tau_\nu = \frac{l_\nu^2}{\nu} \quad \tau_i = \sqrt{\frac{l_i^3 \rho}{2\gamma}} \quad \tau_\epsilon = \frac{\epsilon \epsilon_0}{K} \quad (3.76)$$

which are the time scales of viscous effects, the time scale of inertia and the leaky dielectric time scale, respectively, as already introduced by equation 2.27. For large dimensions of the fluid's surface, the inertial and the viscous time scale are considerably larger than the electrical time scale. This implies that the charges adapt fast to the change in the electrical field. Only close to the apex, the lengths  $l_\nu$  and  $l_i$  are small, such that the fluid sets into motion faster than the charges may relax. The critical lengths have been computed in Section 2.3 as well and typically range below the  $10^{-3}$  capillary lengths regime, which is very small for all solutions presented so far.

Hence, it may be assumed that the droplet provides an inert shape  $r(z)$  and that the charge density  $\sigma(z)$  increases proportionally with the electrical field. This essentially is a separation of time scales, which holds on the entire droplet, wherever the dimensions of the droplet i.e. the radius is larger than  $l_\nu^{crit}$  and  $l_i^{crit}$ . Only at the apex, these small dimensions may be exceeded.

From Lemma 4 the electrical Weber number is given by

$$W_{eE}(z) = \frac{\sigma(z)^2}{\kappa(z)} = \frac{\sigma(z)^2}{z + \Delta p_1 + \frac{1}{2}\sigma(z)^2} \quad (3.77)$$

where the numerator is the surface charge density  $\sigma(z)$  and the denominator represents the curvature  $\kappa(z)$  of the droplet. Following the arguments above, an instantaneous perturbation in the electrical field  $\Pi_3 \rightarrow \chi \Pi_3$  only changes the surface charge  $\sigma(z) \rightarrow \chi \sigma(z)$ , while the shape and thus the curvature  $\kappa(z)$  stays constant. Consequently the electrical Weber is scaled up by  $\chi^2$

$$W_{eE}(z) = \chi^2 \frac{\sigma(z)^2}{z + \Delta p_1 + \frac{1}{2}\sigma(z)^2} \quad (3.78)$$

as the perturbation only applies to  $\sigma(z)$  in the numerator. Applying perturbations of the electrical field of several per cent to the droplet of mechanical and electrical equilibrium obtained from parameters  $\Delta p_1 = 3$ ,  $z_0 = 0.7$  and  $\Pi_3 = 30$  results in the electrical Weber numbers shown in Figure 3.33. The factor  $\chi^2$  allows the electrical Weber number to transcend the critical electrical Weber number  $W_{eE}^{crit} = 2$ . In the electrohydrostatic approach

this turned out to be impossible, as the critical electrical Weber number is only reached in the limit  $\sigma(z_c) \rightarrow \infty$  as discussed in Subsection 3.2.7. Figure 3.33 also points out, at which values of  $z = z_t$  the critical electrical Weber number is transcended. The lower plot emphasizes the associated radius of the droplet  $r(z_t)$ . As discussed in Section 2.2 the Laplace pressure is not capable of compensating the Maxwell pressure for Weber numbers larger than the critical Weber number  $W_{eE}^{crit} = 2$ . This means that the fluid's surface will ultimately be set into motion undergoing a Coulomb explosion. Due to the axisymmetry of the problem, the Coulomb explosion will be directed along the axis of symmetry of the droplet resulting in the onset of jet emission.

The conclusion of this consideration is that the onset of jetting may be controlled by the preparation of a conical droplet and a precisely tuned perturbation in the electrical field. For the experiments of Taylor at voltages of approximately  $U = 7kV$  the perturbation will be in the region of  $\Delta U = 70V$  to  $350V$  for 1 and 5 per cent, respectively, to be applied within the submicrosecond regime in order to satisfy  $\tau^{switch} < \tau_\epsilon$  according to Table 2.1 on page 18. Experimentally this might be a bit challenging, but tractable as high voltage switches in the nanosecond regime are state of the art [Bishop and Barker, 2006].

Alternatively it might be worthwhile to consider an outer highly viscous fluid different from air, which increases the viscous time scale in the outside of the conical apex, such that the fluid interface moves more slowly, while charge relaxation is still fast. This way, the demand on the switching of voltages might be lowered. Such a procedure has already been used by Taylor [Taylor, 1964] (Figure 8) for the study of an electrified oil/water interface and more recently by Marin et al. when studying the whipping instability of electrified liquid jets [Marin et al., 2008].

### 3.4 Closed droplets

In the previous section the properties of droplets hanging from a nozzle have been studied using the modified Fuchikami equations 3.19 in combination to the algorithm to compute the shapes of nozzle droplets at equipotential. From the thermodynamics point of view these droplets are open systems, because the nozzle supplies the droplet with any amount of fluid and charge that is needed to satisfy mechanical and electrical equilibrium on the free surface of the liquid simultaneously.

In this section the same equations and the same algorithm are used to study closed droplets in the absence of gravity. An experimental realization of this situation is for example given by a droplet within a spacecraft experiment similar to the experiments on electrified liquid capillary bridges [Burcham and Saville, 2000].

Although the same equations are used, the physical situation is totally different as no nozzle is present. The closed droplet represents a closed thermodynamical system, as mass

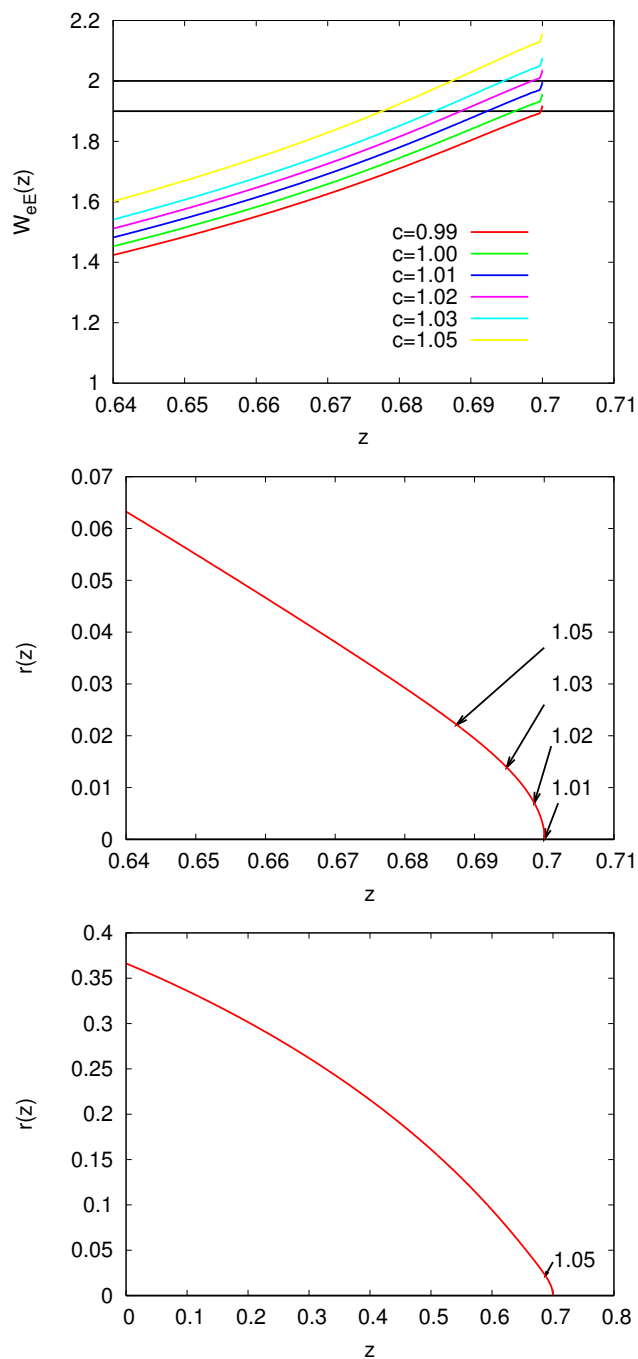


**Figure 3.33:** The influence of an instantaneous increase of the electrical field  $\Pi_3 = 30$  by  $p \in \{-1, 0, 1, 2, 3, 5\}$  per cent on the electrical Weber number  $W_{eE}$  for an inert droplet and fast charge relaxation  $\tau_\epsilon \ll \tau_\nu, \tau_i$ . It can be seen that the critical Weber number  $W_{eE}^{crit} = 2$  is exceeded at the apex of the droplet, which is expected to cause a directed Coulomb explosion and will hence give rise to the onset of jet emission. Perturbations of more than  $p = 1\%$  are sufficient to trigger this directed Coulomb explosion in this case.

and charge are conserved. As already outlined in Table 3.3 on page 42 the experimental situation is determined completely by the selection of a droplet of volume  $V_{ol}$  and the application of an electrical field  $\Pi_3$ . In contrast to the previous section the solution set is found to be either empty, to contain a single element or up to three elements, not more. Despite the differences in the physical situations there exists a strong relationship with the results of the previous section.

The consideration of closed droplets imposes another boundary condition to the droplet, which hung from a nozzle in the previous section. This droplet is now a semi-droplet that is smoothly continued to its image droplet  $r(-z) = r(z)$  by the condition  $r'(z = 0) = 0$ , which is a selection rule for the validity of a computed solution.

All other physical variables like the pressure  $\Delta p_1$  and the radius at the center  $r(z = 0)$  are dependent variables and follow from the solution obtained. The monopole charge  $Q \stackrel{\text{def}}{=} 0$  on the droplet is conserved and is assumed to be zero for all cases considered in the following. Furthermore, the droplet is assumed to consist of a liquid of finite conductivity  $K$ , which implies that the liquid is an electrolyte. Electrolytes provide free ions such that the droplet is polarizable in case it is exposed to an electrical field. The resulting amount of monopole charge located on a semi-droplet due to polarization is denominated by variable  $q$ , where the charge  $+q$  is located on the semi-droplet defined on the interval  $[0, z_0]$  and the monopole charge  $-q$  is located on the opposing semi-droplet defined on  $[-z_0, 0[$ .

The symmetry of the Fuchikami equations 3.19 is broken by gravity as they are not invariant under the transformation  $z \rightarrow -z$ . This means if Figure 3.1 on page 21 is put upside down the gravity still points down and alters the sign of the explicit  $z$  terms in the equations, which originate from the hydrostatic pressure due to gravity. The absence of gravity is equivalent to the dropping of these explicit  $z$  terms and hence symmetrizes the Fuchikami equations such that  $r(-z) = r(z)$  is ensured. Consequently the solution  $\tilde{r}(z)$ ,  $\tilde{\sigma}(z)$  for  $z \in [0, z_0]$  of a droplet in mechanical and electrical equilibrium obtained from the Fuchikami equations and the equipotential boundary condition may be continued to a closed droplet given by

$$r(z) \stackrel{\text{def}}{=} \begin{cases} \tilde{r}(z) & z > 0 \\ \tilde{r}(-z) & z < 0 \end{cases} \quad (3.79)$$

$$\sigma(z) \stackrel{\text{def}}{=} \begin{cases} \tilde{\sigma}(z) & z > 0 \\ -\tilde{\sigma}(-z) & z < 0 \end{cases} \quad (3.80)$$

which is a valid droplet in case  $r'(z = 0) = 0$  is satisfied. This way, the semi-droplet is smoothly connected to its mirror image such that the resulting droplet is closed.

In the following, all closed droplets are uncharged  $Q \stackrel{\text{def}}{=} 0$ , which results in symmetric droplets. For the sake of completeness, it should be noted that the symmetry of a closed droplet will be broken in case it carries a net charge  $Q \neq 0$ . The surface charges due to an

applied electrical field consist of contributions arising from a distribution of the monopole charge  $Q$ , polarized by the electrical field, plus a contribution from the induced charges due to polarization  $+q$  and  $-q$ . Hence, one semi-droplet is stressed by more surface charge than the other such that the symmetry of the droplet is broken by the presence of the net charge  $Q$ . This explains the occurrence of droplets that undergo a directed axisymmetric Coulomb explosion, where a charged droplet develops a single Taylor cone at one side of the droplet while the other side remains more or less spherical. This axisymmetric Coulomb explosion has been studied experimentally using charged and uncharged methanol droplets [Grimm and Beauchamp, 2005].

### 3.4.1 Charged droplets of constant volume

A previous numerical study [Basaran and Scriven, 1990] on a charged sessile droplet of constant volume attached to a plate of a plate capacitor has been performed by Basaran and Scriven, which is one of the very few numerical studies<sup>23</sup> available on the problem of free electrified liquid surfaces.

Basaran and Scriven solved the Young-Laplace equation under the restriction to an equipotential and the conservation of volume using an approach based on Galerkin's method with finite element basis functions. The arising algebraic equations are solved using Newton's method. The parameterization of the physical situation of Basaran and Scriven is different from the following study, as their droplet is a sessile droplet, which sticks to the plate capacitor. Although their equations include gravitational forces they restrict themselves to a vanishingly small gravitational bond number, which is equivalent to the absence of gravity. The solutions they found, are supported by nice experiments using charged bubbles attached to a plate capacitor plate.

In contrast, this study emphasizes a closed droplet, which is allowed to be deformed axisymmetrically along the longitudinal axis in both directions as it is found in experiments [Giglio et al., 2008, Grimm and Beauchamp, 2005]. In the following a free closed droplet of constant volume is charged in the presence of a locally homogeneous electrical field in the absence of gravity by the method developed in Section 3.2.

Figure 3.34 shows a droplet of volume  $V_{ol} = 0.236 \pm 1.5 \times 10^{-3}$  in mechanical and electrical equilibrium for several electrical fields  $\Pi_3$ . It is easily seen that for low electrical fields there exists only a single solution for each electrical field. In case the electrical field is large enough, there exist two or even three solutions. For too large an electrical field there no more exists an electrohydrostatical solution for a closed droplet of this volume. This assertion is based on the scan of the parameter space and will be made clear in the

---

<sup>23</sup>Similar works [Harris and Basaran, 1995, Collins et al., 2007] are all connected to Osman Basaran and are always based on finite element methods.

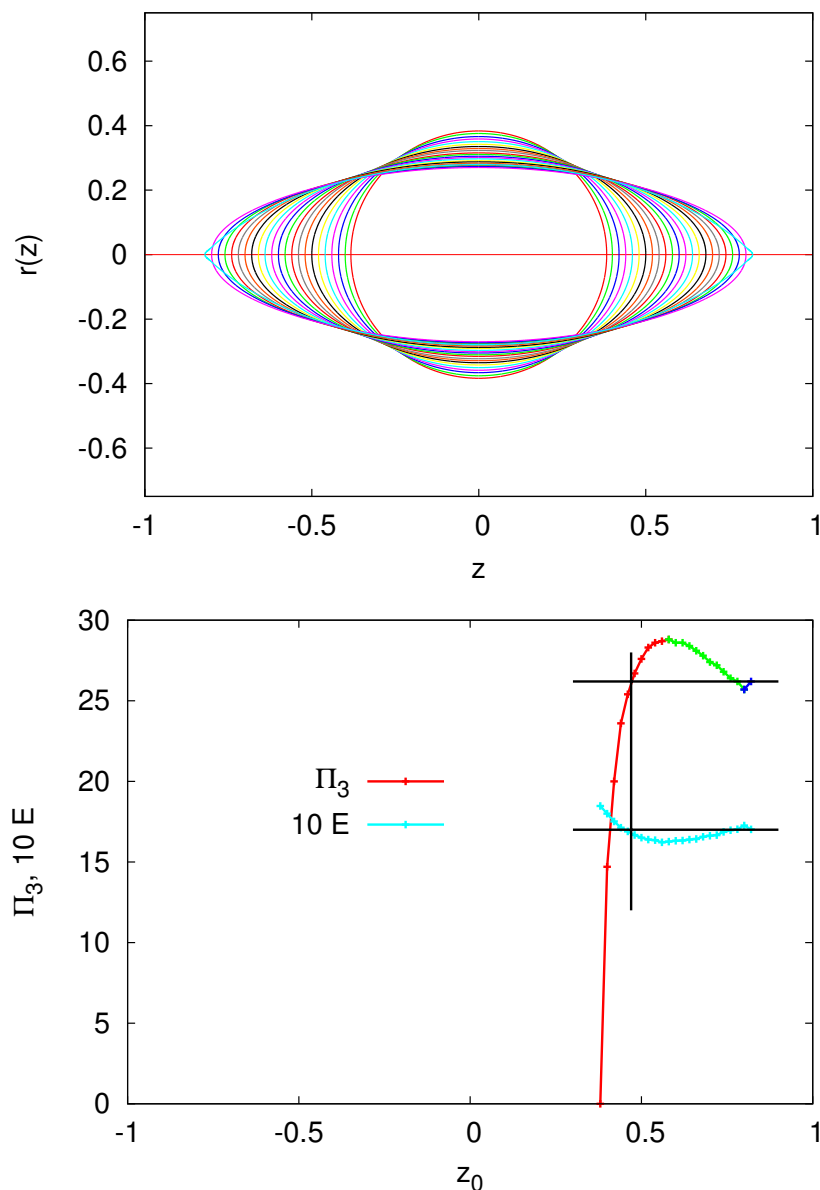


**Figure 3.34:** A conducting equipotential droplet of constant volume in mechanical and electrical equilibrium for several electrical fields  $\Pi_3$ . In the lower plot the data points correspond to the tips of the droplets in the upper plot. It can be seen that for sufficiently large electrical fields there exists more than one solution indicated by the red, green and blue branches. The solution for the largest electrical field is still a rounded droplet and the conical solution appears at a considerably smaller electrical field. Furthermore, the energy of state of the elongated conical droplet is only slightly larger than for the rounded droplet at the same electrical field. The black lines are drawn to illustrate that three solutions exist for the chosen electrical field and that the energy of these droplets is almost the same. The red and green branches of  $\Pi_3(z_0)$  are denominated *charged mode 1 branch* and *charged mode 2 branch* respectively.

following. The Fuchikami equations are integrated from the numerical parameters  $\Delta p_1$ ,  $z_0$  and  $\Pi_3$  resulting in solutions with the dependent variables  $V_{ol}(\Delta p_1, z_0, \Pi_3)$ ,  $q(\Delta p_1, z_0, \Pi_3)$ ,  $p(\Delta p_1, z_0, \Pi_3)$ ,  $r_{z=0}(\Delta p_1, z_0, \Pi_3)$ ,  $E(\Delta p_1, z_0, \Pi_3)$  and  $r'_{z=0}(\Delta p_1, z_0, \Pi_3)$ . The scan of the parameter space is performed in the same way as described in Subsection 3.3.1. The zeros of function  $f(\Pi_3) = r'_{z=0}(\Delta p_1 \stackrel{\text{def}}{=} \text{const}, z_0 \stackrel{\text{def}}{=} \text{const}, \Pi_3)$  indicate solutions of closed droplets, which of course feature a volume  $V_{ol}(\Delta p_1, z_0, \Pi_3)$ . Among these solutions are droplets satisfying  $|V_{ol} - 0.236| < \epsilon$  that are the subject of this study. As the resolution of the scan of the parameter space described in Section 3.3.1 has turned out to be insufficient it has been increased in areas of interest, which practically is equivalent to manually shoot for solutions in  $\Delta p_1$  at fixed values of  $z_0$  satisfying

$$\left| V_{ol}(\Delta p_1, z_0, \Pi_3) \Big|_{r'(z=0)} - 0.236 \right| < \epsilon \quad (3.81)$$

with  $\epsilon = 1.5 \times 10^{-3}$ . Higher precision had dramatically increased the numerical effort without any significant improvement of the results. By shooting in  $\Delta p_1$  it is meant that a droplet is charged for chosen parameters  $\Delta p_1$ ,  $z_0 = \text{const}$  such that solutions  $r(z)$ ,  $\sigma(z)$  are obtained for a sequence of electrical fields  $\Pi_3$ . Among these solutions are droplets satisfying  $r'(z=0) = 0$  which provide the volume  $V_{ol}$  of a closed droplet. If condition 3.81 is not satisfied, the pressure  $\Delta p_1$  is changed and the procedure is repeated until condition 3.81 is satisfied. Function  $f(\Pi_3) = r'_{z=0}(\Delta p_1 \stackrel{\text{def}}{=} \text{const}, z_0 \stackrel{\text{def}}{=} \text{const}, \Pi_3)$  typically possesses only a single root  $f(\Pi_3) = 0$  in the relevant parameter subspace that has been scanned. However, for large  $z_0$  more roots may be found, corresponding to very long droplets as those shown in Figure 3.35. The large  $z_0$  goes along with a large volume of the droplet such that condition 3.81 is obviously violated. The volumes of the example are too large by a factor of  $\approx 5$ .

The solutions computed in large regions of the parameter space showed that for increasing electrical fields the boundary condition  $f(\Pi_3) = 0$  and condition 3.81 are not satisfied simultaneously anymore. This evidence results in the conclusion that there exist no electrohydrostatical solutions for droplets of volume  $V_{ol} = \text{const}$  anymore beyond a maximal electrical field  $\Pi_3$ . Hence, larger electrical fields will ultimately set the fluid into motion and most probably tear the droplet apart.

The lower part of Figure 3.34 looks quite similar to the left part of the function  $\Pi_3(z_0)$  displayed in Figure 3.26 on page 74. Apart from the fact that different boundary conditions and a different parameterization have been used to obtain the results displayed in Figure 3.34 it also shows the existence of a *charged mode 1 branch* and a *charged mode 2 branch*, which are color coded by *red* and *green*, respectively. It is very interesting that the concept of the Fuchikami modes applies to a single closed droplet. Naturally it is expected to exist as the limiting case, where the pressure  $\Delta p_1$  is tuned such that the mode 1 droplet and the mode 2 droplet collapse to the degenerated spherical solution that satisfies  $r'(z=0) = 0$ . If charged, this degeneracy is removed and the closed droplet reveals the existence of a *charged mode 1 branch* and a *charged mode 2 branch* that possesses similarities to the one

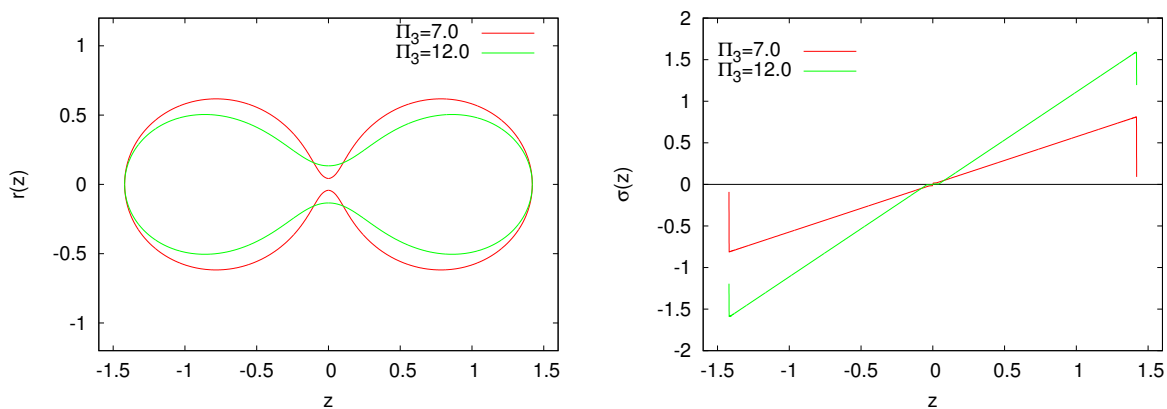


**Figure 3.35:** Two closed charged droplets satisfying  $r'(z = 0) = 0$  and their charge density  $\sigma(z)$  obtained from parameters  $\Delta p_1 = 3.0$ ,  $z_0 = 1.42$  and the electrical fields  $\Pi_3 = 7.0$  and  $\Pi_3 = 12.0$ , respectively. These droplets obviously are the closed and charged equivalents of the critical droplet occurring between mode 2 and mode 3 in the uncharged case.

already encountered in Figure 3.26.

The dependent variables of the charged droplets are visualized in Figure 3.36. They represent important properties of the droplets that is color coded according to the *charged mode 1 branch* in red and the *charged mode 2 branch* in green according to the lower part of Figure 3.34. Interestingly, the energy of state decreases monotonically with the electrical field for both modes. This means that a decrease in the electrical field causes the droplet to take up energy. From equation 3.60 on page 66 it is clear that this behavior is due to the induced dipole aligned with the electrical field. The pressure  $\Delta p_1$  decreases almost monotonically with the electrical field. Just at the point, where the charged mode 1 collapses with the charged mode 2, the monotonicity is not satisfied. The dipole moment  $p$  and the induced charge on a semi-droplet  $q$  increase on the *charged mode 1 branch* and decrease on the *charged mode 2 branch* with the electrical field  $\Pi_3$ , while  $p$  and  $q$  increase monotonically for both branches if they are considered as a function of  $z_0$  instead. In the same parameterization, the central radius  $r_c = r(z = 0)$  of the droplet is seen to decrease monotonically with  $z_0$ . This means that both  $r_c$  and  $z_0$  are measures for the induced dipole moment  $p$  and the charge located on the semi-droplet  $q$ .

Additionally, a conical solution exists that is color coded in blue in the lower part of Figure 3.34. This droplet with a conical end is displayed separately in Figure 3.37 and reveals that it features an opening angle of  $\vartheta = 41^\circ$ , which is considerably smaller than  $\vartheta_c = 49.3^\circ$  as predicted by Taylor for ideal Taylor cones. Once more, the presence of the hydrostatic pressure  $\Delta p_1 = 4.20 \neq 0$  modifies the asymptotics of the conical solution as has already been discussed in Section 3.3.4.



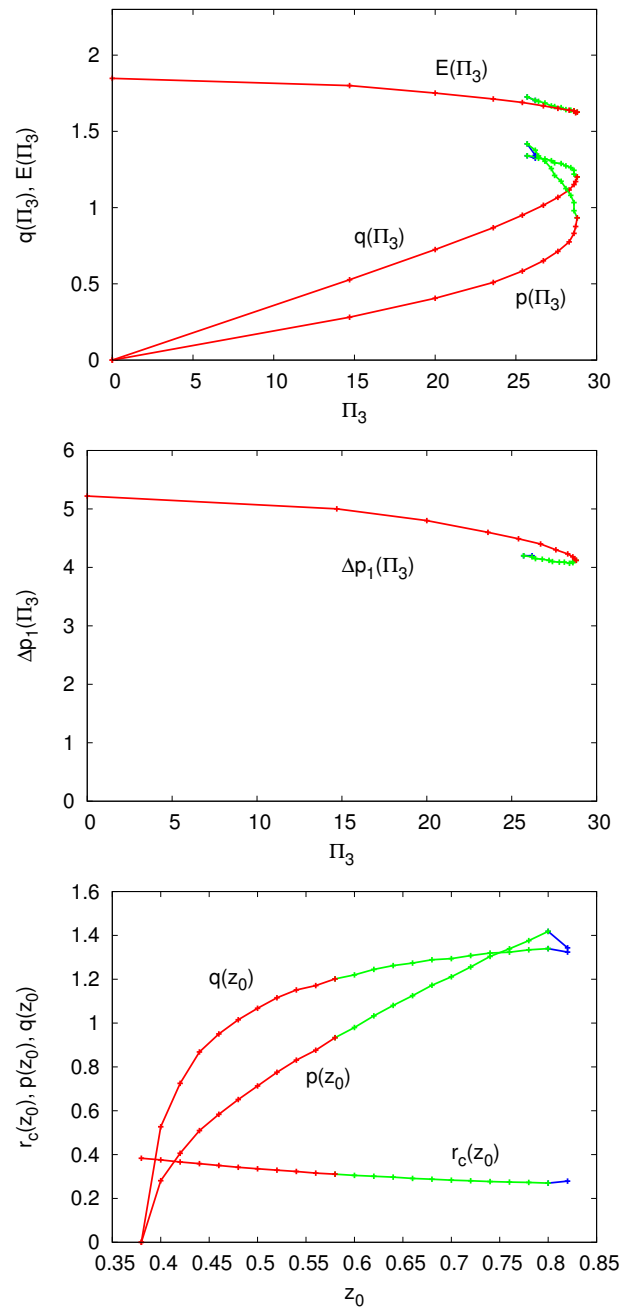
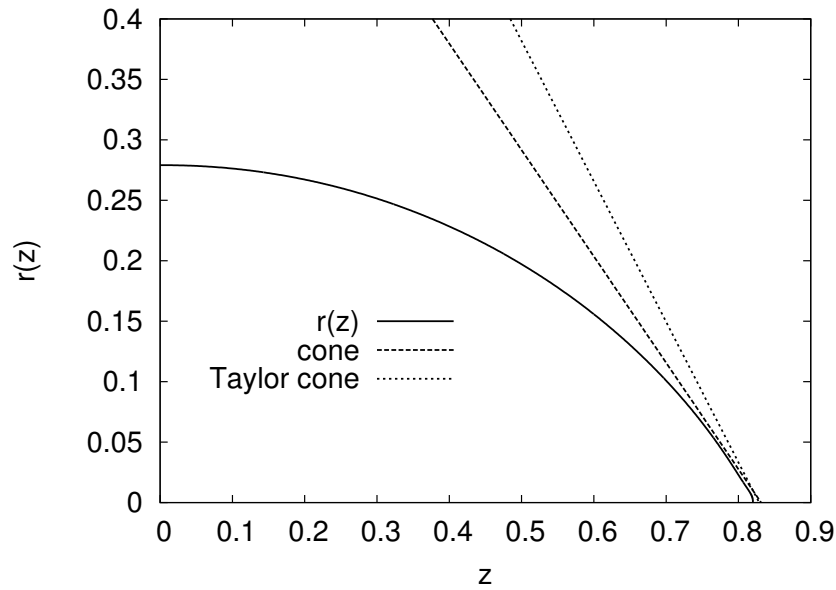


**Figure 3.36:** The dependent physical variables like Energy of state  $E$ , dipole moment  $p$ , induced charge on the semi-droplet  $q$ , pressure difference  $\Delta p_1$  and  $r_c = r(z = 0)$  are displayed as function of the electrical field  $\Pi_3$  and  $z_0$ , respectively. The color coding is in accordance with that of the branches of the electrical field  $\Pi_3(z_0)$  in Figure 3.34. The energy of state  $E$  is seen to decrease monotonically with the electrical field in general and it is almost the same for both branches. The dipole moment  $p$  and the monopole charge on the semi-droplet  $q$  increase on the red branch and decrease on the green branch with the electrical field. Further, it can be seen that  $p$  and  $q$  increase monotonically with the length of the droplet, while  $r_c = r(z = 0)$  decreases monotonically except for the conical solution (blue). Hence,  $r_c$  and  $z_0$  are measures of the dipole moment  $p$  and the charge on the semi-droplet  $q$ .

a)



b)

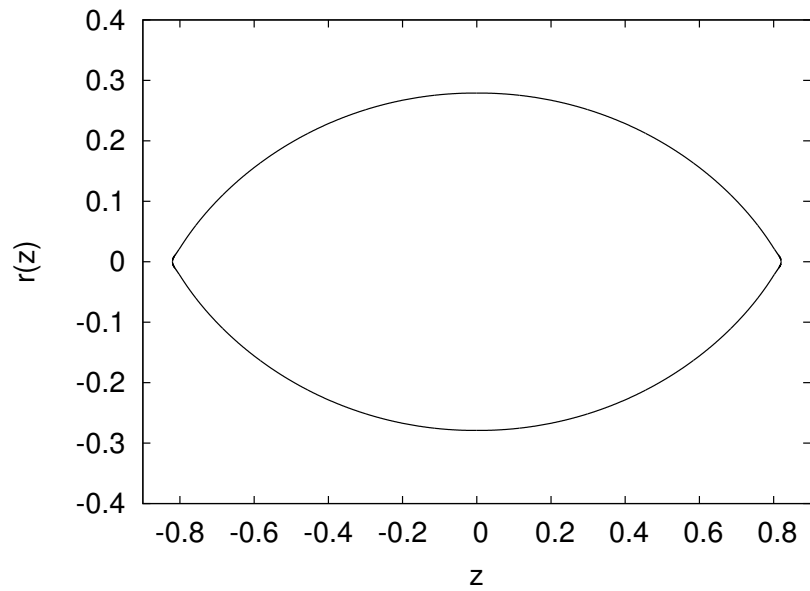
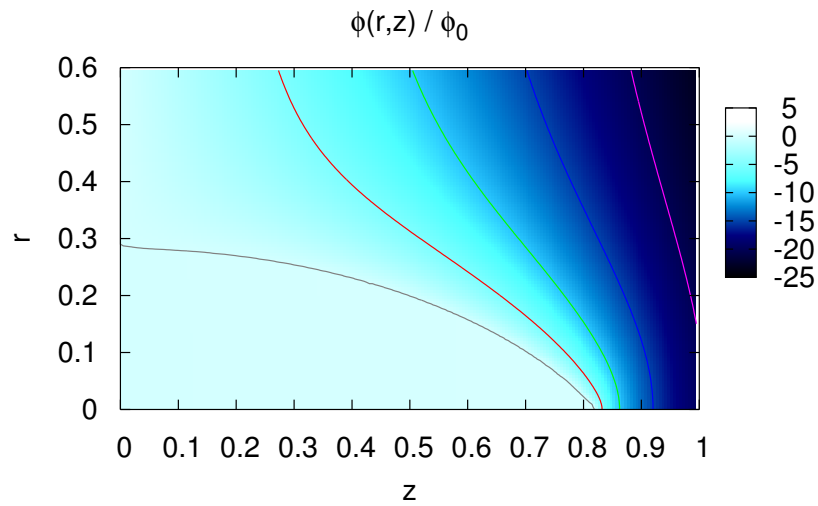


**Figure 3.37:** a) The droplet of constant volume displayed in Figure 3.34 developed a conical tip for the electrical field  $\Pi_3 = 26.2$ . The asymptotic cone opening angle is determined to  $\vartheta = 41^\circ$ . The Taylor cone opening angle  $\vartheta_c = 49.3^\circ$  is displayed for comparison. b) The same solution displayed as closed droplet as it might be observed in an experiment.

a)



b)

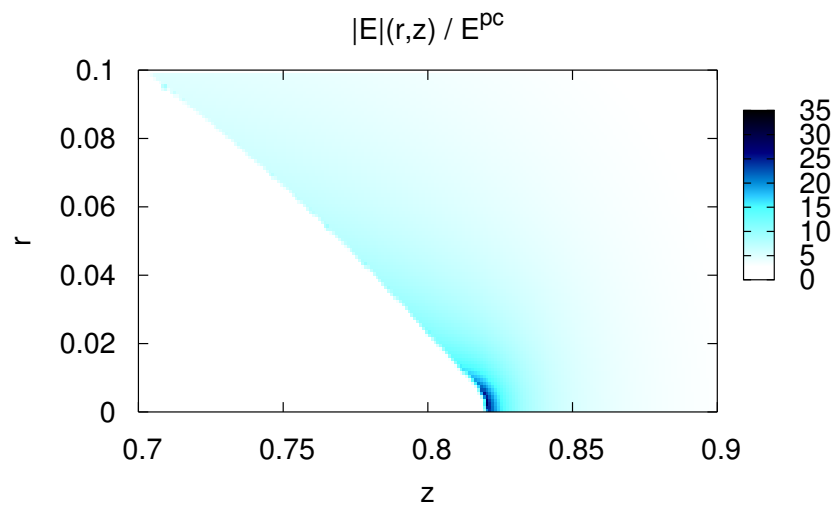


**Figure 3.38:** a) The potential in the vicinity of the conical droplet visualized by a color coding and by contour lines of equipotential. It is nicely seen that the contour line of equipotential  $\phi = 0$  reproduces the shape of the droplet. b) The corresponding value of the enhancement  $|E(r,z)|/\Pi_3$  of the electrical field in the vicinity of the highly charged conical droplet is color coded for the homogeneous plate capacitor electrical field  $\Pi_3 = 26.2$ .

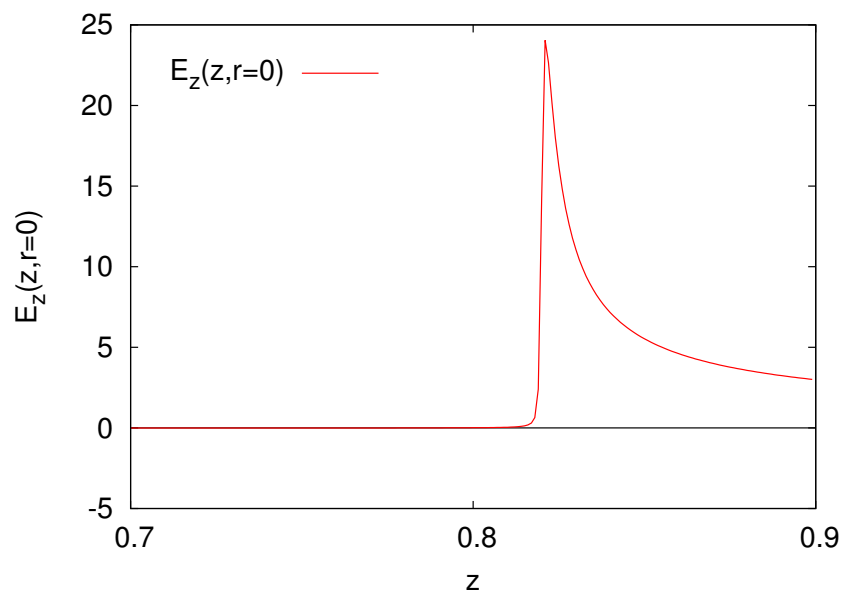


**Figure 3.39:** Enhancement of the axial electrical field at the apex of the highly charged droplet is approximately given by  $E_z/\Pi_3 \approx 25$ .

Figure 3.38 shows a color coded plot of the potential in the vicinity of the same conical droplet. The contour lines of equipotential illustrate the perturbation of the electrostatic potential due to the presence of the polarized droplet. The contour lines are drawn for the potentials  $\phi \in \{0, -5, -10, -15, -20\}$  from left to right in Figure 3.38. Thereby the contour line  $\phi(r, z) = 0$  reproduces almost exactly the shape of the droplet. In the lower part, the value of the enhancement of the electrical field is color coded and easily seen to provide the largest values at the apex of the cone, as expected. Furthermore, it is verified that the inside of the droplet indeed provides a vanishing electrical field and thus indeed satisfies the equipotential condition. Figure 3.39 shows the enhancement  $E_z(r = 0, z)/\Pi_3$  of the axial electrical field along the axis of symmetry addressed by  $r = 0$ . This field enhancement at liquid droplets exposed to electrical fields is interesting in the context of research on lightning discharges in thunderstorms [Ebert, 2008].

### 3.4.2 Emission of tiny droplets

The highly charged conical droplet displayed in Figure 3.37 is the subject of further investigations. In Figure 3.40a this droplet is shown again together with a detail of its apex. The conical part of the apex may be seen to be very slightly indented at  $z \approx 0.805$  as occurs for overcharged droplets. The properties of overcharged droplets have already been studied for the nozzle droplets in Section 3.3.5. An example of a more strongly developed overcharged nozzle droplet is illustrated in Figure 3.32 on page 84 for comparison.

The droplet under discussion here has been integrated from the parameters  $\Delta p_1 = 4.2$ ,  $z_0 = 0.82$  and has been charged to the highest electrical field  $\Pi_3$  possible for these parameters as the numerical algorithm does not converge for larger fields anymore. For electrical fields, beyond an expected upper bond of the electrical field, a solution of mechanical and electrical equilibrium is not expected to exist anymore as has been motivated in Section 2.2 according to Taylor [Taylor, 1964].

The concave indentation due to overcharging indicates that this droplet is most probably not stable anymore, such that the droplet might undergo a directed Coulomb explosion as those observed experimentally [Grimm and Beauchamp, 2005, Giglio et al., 2008]. Jet emission due to a directed Coulomb explosion leads to the formation of tiny droplets in case the fluid is a sufficiently Newtonian fluid that rather undergoes electrospraying than electrospinning.

It is interesting to know about the properties of such an emitted tiny droplet. The properties of such emitted tiny droplets can be estimated from the slightly overcharged droplet simply by considering the extensive quantities charge  $q$  and Volume  $V_{ol}$  according to

$$q(z_1) = -2\pi \int_{z=z_0}^{z_1} \sigma(z) r(z) \sqrt{1 + r'^2(z)} dz \quad (3.82)$$

$$V_{ol}(z_1) = -\pi \int_{z=z_0}^{z_1} r(z)^2 dz \quad (3.83)$$

These quantities are integrated from the apex at  $z_0$  to a cut off position  $z_1 < z_0$ . At this cut off position, the conical tip is cut sharply in order to isolate all extensive quantities on the conical tip, which is used then to form a tiny spherical droplet separated from the large droplet.

The cutting is an idealized form of the electrohydrodynamical jet formation that is followed by the necking of a droplet [Eggers and Dupont, 1994], which is a highly dynamical process<sup>24</sup>. Due to the additional pressure originating from the surface charge the process of necking is much more complicated in this electrohydrodynamical case than in the uncharged hydrodynamical case considered by Eggers and Dupont. This justifies the idealized droplet pinch off by an instantaneous cut at position  $z = z_1$  as an educated guess.

Figure 3.40 shows the charge  $q(z_1)$ , the volume  $V_{ol}(z_1)$  as well as the Rayleigh limiting charge  $q_{RL}(z_1)$  for the tiny droplet cut off from the apex at position  $z_1$ . It is clearly seen that  $q(z_1) < q_{RL}(z_1)$  is satisfied almost everywhere. Only for  $z_1 \rightarrow z_0$  the volume  $V_{ol}(z_1)$  vanishes faster than  $q(z_1)$ , which corresponds to the situation of a disk of charged fluid

---

<sup>24</sup>Even the uncharged necking is already a very complicated process that results in a finite time singularity.

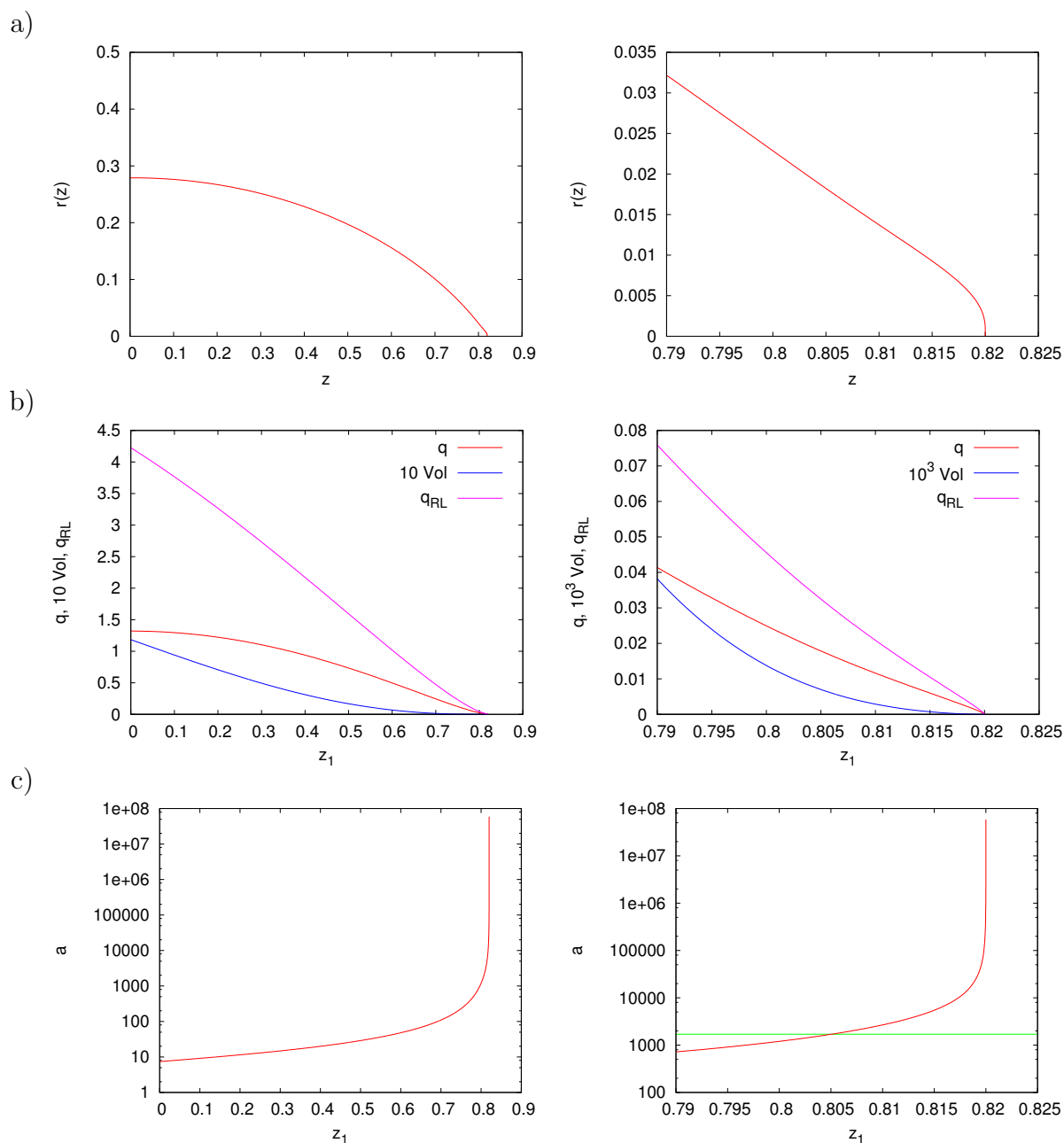


**Figure 3.40:** Survey and details of expected extensive variables of tiny droplets emitted from a large droplet exposed to a strong electrical field on the left and right, respectively. a) A highly charged droplet with conical ends. The detail reveals a slight indentation due to overcharging. b) The charge  $q$ , volume  $V_{ol}$ , surface  $A$  of the conical apex of the droplet cut at  $z_1$  from the droplet. The volume is magnified by factors 10 and  $10^3$ , respectively. The Rayleigh limit  $q_{RL}$  is the maximal charge a droplet of volume  $V_{ol}$  may carry before disintegration. c) The acceleration  $a$  the plate capacitor field imposes on a droplet of volume  $V_{ol}$  and charge  $q$ .

that is cut from the rounded apex in the case of a vanishing thickness as is revealed by the detail of Figure 3.40a for  $z_1 \rightarrow z_0$ . Thus, the situation  $z_1 \rightarrow z_0$  is a limiting case that is not interesting, such that it can be asserted that the Rayleigh limit is always respected by  $q(z_1) < q_{RL}(z_1)$  for any situation of interest.

A tiny droplet of volume  $V_{ol}$  carrying charge  $q$  cut from the large droplet is subject to an acceleration of

$$a = \frac{q}{m} E^{pc} \quad (3.84)$$

in dimensional variables due to electrical fields from Newton's second theorem. Non-dimensionalizing this equation by using the scales from appendix A.2 results in the acceleration

$$a = \frac{1}{4\pi^2} \frac{q}{V_{ol}} \Pi_3 \quad (3.85)$$

in non-dimensional variables. Because the volume and the charge of the emitted tiny droplet are functions of the cutting position  $z_1$ , the acceleration of the droplet drastically depends on the cut, which is illustrated in Figure 3.40(c). If the droplet is cut at the indentation  $z_1 = 0.805$ , the resulting droplet is subjected to an acceleration of  $a \approx 1700g$ . Conservation of volume results in a spherical radius of the emitted droplet of  $r \approx 0.011$ , which in dimensional units is  $r \approx 31\mu m$  in the case of a tiny droplet of water in air.

Accelerating this droplet by the electrical field of the plate capacitor constantly from rest over the typical electrospray or electrospinning distance  $s = 0.2m$ , the time of flight  $t = \sqrt{2s/a} = 4.9ms$  is obtained with a speed of impact  $v = \sqrt{2sa} = 81m/s$ . The order of magnitude of this impact velocity is in agreement with experimental findings [Greiner and Wendorff, 2007].

Summarizing this approach, the charging of closed droplets has shown, that these droplets can be overcharged at their apices due to polarization charges in the same way as nozzle droplets. This overcharging can trigger the onset of jet emission. The jet then removes large amounts of the polarization charge but very little mass from the precursor droplet [Giglio et al., 2008]. The jet emission is not steady due to the finite size of the precursor droplet, such that jet emission is supposed to stop shortly after it has started. The emitted jet gives rise to highly charged tiny droplets that feature a large ratio of charge to mass such that they are subject to a very large acceleration in the surrounding electrical field.

This way, the method developed in Section 3.2 to compute electrohydrostatical solutions of droplets in mechanical and electrical equilibrium have allowed to estimate the physical properties of the tiny droplets by an educated guess.





# Chapter 4

## Modelling of multi-phase Electrospinning

Multi-phase electrospinning is a variation of the classical electrospinning, where the liquid is a colloidal dispersion. As outlined in the introduction, core shell fibers are of special technological interest for material science as it is possible to encapsulate substances within fibers or to tune the properties of composite nano-fibers by the selection of the core and shell materials. Controlling the production of core shell nano-fibers featuring well defined properties using coaxial electrospinning is a challenging problem as the entrainment of the inner fluid can not be controlled easily [Reznik et al., 2006]. An alternative method of production of core shell nano-fibers is multi-phase electrospinning, which has turned out to be quite controllable [Stoiljkovic et al., 2007, Stoiljkovic, 2007].

The colloidal dispersion consists of kinetically stabilized monodisperse colloids dissolved in an aqueous polymeric solution. In case the colloids consist of a soft material, the spherical colloids have been observed to undergo morphological transitions forming a homogeneous core fiber during the electrospinning process. Hard particles like spherical latex colloids maintain their spherical morphology and arrange themselves in amorphous structures. These structures are clusters of colloids, which are indefinitely extended in one dimension and therefore form core fibers covered by a shell of residual polymers.

After the removal of the residual polymer shell by a chemical process, the colloidal nano-fibers have been observed to be mechanically stable, although very brittle. Figure 4.1 shows such a colloidal nano-fiber. In the following it will turn out that the colloids are mainly bound due to the attractive London force, which is a very short ranged van der Waals force. For the colloids used in the experiments this force is a contact binding force.

Using multi-phase electrospinning water insoluble colloidal nano-fibers have been produced from an aqueous solution without the use organic solvents. This is a technological advantage, because the production of water insoluble fibers commonly demands the use of organic solvents, which typically are inflammable, toxic, hazardous and expensive. This

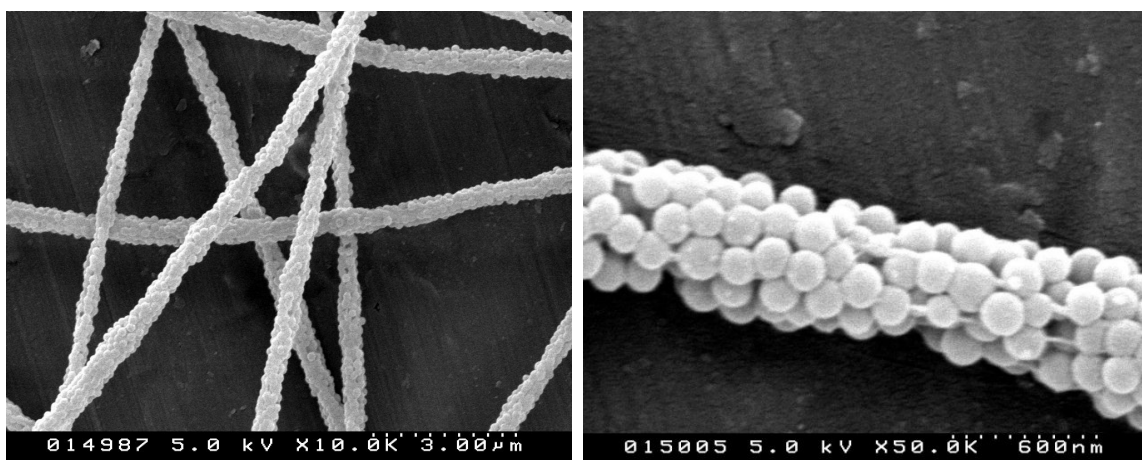


**Figure 4.1:** Extended colloidal nano-fibers covered by the residual polymer as produced by multi-phase electrospinning and a colloidal core nano-fiber after the removal of the residual polymer, respectively. The experimental images have been contributed by Aleksandar Stoiljkovic [Stoiljkovic, 2007].

makes multi-phase electrospinning an interesting method of production for water insoluble colloidal nano-fibers.

At first sight, the arrangement of the colloids within the nano-fiber displayed in Figure 4.1 is disordered as translational invariance is not satisfied. A closer look reveals that the placement of colloids is not of entirely random origin for two reasons. The colloidal nano-fiber does not feature single add-on particles at all. Instead, more or less closed layers of particles are found, which provide a lot of defects like void defects. Furthermore, there are particles arranged in hexagons on the surface of the fiber. The explanation for the lack of add-on particles is that the colloids are under a strong forcing during the electrospinning process, such that any add-on particle is pushed into the outer layer of particles and then maximizes its number of neighbors there. The occasionally discernable hexagonal arrangements of particles on the surface of the colloidal nano-fiber is a finite size effect, as the hexagonal arrangements of particles is the densest packing in two dimensions. Wrapping layer by layer of a highly defected two-dimensional densest packing around a central axis, the resulting amorphous colloidal fiber is reminiscent of the previous prevalence of order.

The facts that colloids consisting of soft materials lose their spherical morphology that no add-on particles are present and that layers of particles seem to be wrapped around the axis of symmetry are an indication for a strong forcing of the particles during the electrospinning process. Hence, the strong forcing arising from the electrospinning of colloidal dispersions is the basis for a theoretical model set up in order to investigate the possible arrangements of particles quantitatively. It will be demonstrated that a weak forcing is not compatible with the colloidal nano-fibers observed in the experiments. This modelling

approach is justified due to the problems outlined in Chapter 1 that make any first principle approach on multi-phase electrospinning a very difficult task.

The relevant physical situation of multi-phase electrospinning is discussed in Section 4.1, which serves as a basis for an appropriate and tractable model for the multi-phase electrospinning developed in Section 4.2. In Section 4.3 the numerical method to solve the model is presented. Finally, the results obtained from these simulations are presented in Section 4.4. This chapter is closed by conclusions drawn from the numerically and experimentally obtained results in Section 4.5.

## 4.1 Electrified colloidal dispersions

In this section the interplay between the electrospinning jet, the aqueous polymeric solution and the particles as well as the interaction between the particles themselves will be discussed in order to develop a simple model that takes into account the relevant physical effects.

Electrospinning is started by feeding a droplet from the nozzle by a volume flow rate  $\dot{Q}$  in the presence of a strong electrical field until jet emission starts. This jet thins in the electrospinning process and may be considered an uniaxial elongational flow. This flow separates neighbored points on the centerline exponentially in time [Morrison, 2001]. The particles in the dispersion are expected to swim with the flow along the streamlines that are quickly converging to the centerline.

Considering the aqueous polymeric solutions used in the experiments, the final fiber consists of only 10 to 25 mass percent of the initial dispersion as the water almost completely evaporates during the electrospinning process. Since the colloidal particles are not subjected to evaporation their number density increases continuously by about one order of magnitude from approximately  $1.4 \cdot 10^{13} \text{ 1/cm}^3$  to  $1.4 \cdot 10^{14} \text{ 1/cm}^3$ . Hence, the evaporation of solvent increases the colloid concentration. The uniaxial elongational flow is a volume conserving flow that causes the particles to approach the centerline where they separate exponentially in time. Due to the conservation of volume the mean distance between particles is not affected by this flow. The concentration of the particles rises due to evaporation of the solvent. This effectively decreases the mean distance between the particles.

The volume flow rates used in the experiments are of the order of  $\dot{Q} \sim 1 \text{ ml/h} \sim 10^{-9} \text{ m}^3/\text{s}$  and the final fiber radius is of the order  $r_{fin} \sim 10^{-6} \text{ m}$ . This allows to estimate the final velocity

$$v_{fin} = \lambda \frac{\dot{Q}}{\pi r_{fin}^2} \sim 32 \frac{\text{m}}{\text{s}} \quad (4.1)$$

where  $\lambda \approx 0.05 \dots 0.1$  is the volume fraction that remains after the evaporation of the solvent. The order of magnitude of the velocity estimated here is in agreement with

experimental findings [Greiner and Wendorff, 2007]. Under the assumption that the final velocity is the result of a constant acceleration over the gap distance  $d \approx 0.2m$ , the duration of the electrospinning process may be estimated to be

$$t_{fin} = \frac{2d}{v_{fin}} = 13ms$$

which is the timescale of the electrospinning process. As colloidal particles are subjected to Brownian motion, a timescale of diffusion follows from the Einstein relation [Einstein, 1905]

$$D = \frac{k_B T}{6\pi\eta r_p} \quad (4.2)$$

where  $r_p \approx 50nm$  is the radius of the colloids and  $\eta \sim 0.1Pas$  the viscosity of the colloidal dispersion. The time it takes for a particle to diffuse a length equal to its radius follows from  $r_p = \sqrt{2Dt_D}$  and is estimated to

$$t_D = 3\pi\eta r_p^2 / k_B T = 28ms. \quad (4.3)$$

Comparing the timescales  $t_{fin}$  and  $t_D$  it becomes obvious that Brownian motion is a subdominant process compared to the strong electrohydrodynamical flow.

The forces of interaction between the particles in a polymeric solution arises from different origins. First of all, there are steric forces acting on the particles that are due to the presence of the polymer in the solution. For example, there are polymers that bind a head group to the surfaces of the particles and prevent the particles from touching due to their overlapping polymer shells, which results in a repulsive force. In poor solvents on the other hand, the intersegment attraction between the polymer chains dominates and causes a net attractive force [Hiemenz and Rajagopalan, 1997]. Other polymers like the Polyvinylalcohol used in the experiments bind with their backbone to the particles and glue them together once they are close enough. The colloidal dispersions used in the experiments showed coagulation and resulted in colloidal crystals such that the dispersions had to be kinetically stabilized by using a nonanionic surfactant, which prevents the Polyvinylalcohol from attaching the particles to each other [Stoiljkovic, 2007].

The most important force acting on the particles is the attraction due to the London van der Waals force. This interaction is described by using the short range interaction potential for spherical colloids [Israelachvili, 1997]

$$V(d) = \begin{cases} -\frac{Ar_p}{12d} & d \ll r_p \\ +\infty & d \leq 0 \end{cases} \quad (4.4)$$

where  $A = 1.4 \cdot 10^{-20}J$  is the Hamaker constant for latex<sup>1</sup> [Israelachvili, 1997],  $r_p$  is the particle radius and  $d$  is the shortest distance between the surfaces of the spherical colloidal

---

<sup>1</sup>Latex is equivalent to polystyrene.

particles. This potential is singular for touching particles with  $d = 0$ . Common practice [Israelachvili, 1997] to overcome this singularity is to use a lower bond  $d > d_{min} \stackrel{\text{def}}{=} 0.2nm$ , which is of the order of atomic diameters. Consequently, the binding energy of two latex colloids of radius  $r_p = 50nm$  is determined to  $E_b = -2.9 \cdot 10^{-19} J = -1.8eV$ . For electrified liquid jets the charges are expected to be located at the surface of the liquid jet [Hohman et al., 2001a]. As it cannot be ruled out that colloids are charged, the limiting case of Coulomb repulsion balancing van der Waals attraction is found via

$$|E_b| = V(2r_p) = \frac{n_1 n_2 e^2}{8\pi\epsilon\epsilon_0 r_p} \quad (4.5)$$

with  $n_1, n_2$  the number of elementary charges carried by particle 1 and particle 2, respectively. Assuming  $n_1 = n_2 = n_{limit}$  and  $\epsilon \approx 80$  for the aqueous solution, the limiting number of elementary charges is found to  $n_{limit} \approx 100$ . Therefore, two colloids carrying approximately 100 elementary charges each are kinetically stabilized by inhibiting the van der Waals attraction via Coulomb repulsion.

Summarizing the physical situation of the colloidal particles in the aqueous polymeric solution subjected to the electrohydrodynamical flow, it can be said that the particles swim with the flow. Evaporation increases the number density of the colloidal particles. Van der Waals forces bind the particles together once they are close enough. The residual polymer encapsulates the colloidal core fiber. Due to the experimental evidence that the particles cluster to colloidal nano-fiber structures, the particles either cannot be charged beyond the Coulomb stabilization limit or dynamical effects overcome the repulsion and last long enough for the charges to volatilize. This allows the model to disregard the Coulomb repulsion in general. Steric repulsive forces are inhibited by the nonanionic surfactant, such that they do not demand an extra representation in the model. The attraction due to attractive steric forces such as the depletion force is qualitatively covered by the attractive van der Waals force.

## 4.2 The model

Based on the physical reasoning in the previous section, a simple model is set up that allows to study the structures found in colloidal nano-fibers. This model replaces the true electrohydrodynamics problem by gradient dynamics in a potential landscape. The potential landscape consists of contributions from the particle - particle interaction and a cylindrical confining potential that models the uniaxial elongational flow in the presence of evaporation. The model consists of a functional

$$f : \mathbb{R}^{3N} \rightarrow \mathbb{R} \quad (4.6)$$

which assigns a real number to a given configuration of  $N$  particles with  $3N$  coordinates, which will be called a *vector of state* or for simplicity a *state*

$$\vec{p}_N = (x_1, y_1, z_1, \dots, x_N, y_N, z_N) \quad (4.7)$$

of the system. The position of particle  $i$  is given by  $\vec{r}_i = (x_i, y_i, z_i)$  in cartesian coordinates.

The functional  $f$  is designed to map a given state to a real number, which essentially has the meaning of a potential energy associated to that state. Hence, there are no kinetic terms involved. The motivation to design the functional like this, is to minimize it for an ensemble of random initial states analogous to any real dynamics in the formation process, which will by Fick's law tend to evolve to states of lower energy. As dissipation is present in the real system, any real dynamics leads to states of the system, where the thermodynamical force and equivalently the gradient of the functional vanishes. If the state locally minimizes the functional, the state is considered stable. If there are still unstable directions present, the system is considered unstable, but it might be frustrated in the real dynamics. By replacing the intractable equations of motion of the full electrohydrodynamics problem of multi-phase electrospinning by the energy functional, the dynamics are not modelled at all. However, the final states of the real dynamics are at states of mechanical equilibrium. As this model takes into account all relevant effects of statical particle particle interaction, the states of mechanical equilibrium found by solving the model are expected to be a subset<sup>2</sup> of the states of mechanical equilibrium originating from the equilibration of the true dynamics.

The functional consists of 2 contributions

$$f_{\gamma L}[\vec{p}_N] = V_{\gamma}^{jet}[\vec{p}_N] + V_L^{pp}[\vec{p}_N] \quad (4.8)$$

where

$$V_{\gamma}^{jet}[\vec{p}_N] = \gamma \sum_{i=1}^N (x_i^2 + y_i^2) \quad (4.9)$$

models the uniaxial elongational flow. Particles located on the centerline do not contribute to the functional via  $V_{\gamma}^{jet}$ , while off-centerline particles contribute to the functional quadratically with respect to their distance to the centerline. Of course, a minimization of  $f_{\gamma L}$  under the neglect of  $V_L^{pp}$  will cause the particles to move towards the centerline where they no longer feel any radial force, as is the case for the uniaxial elongational flow. The parameter  $\gamma$  controls the strength of the thinning of the jet in the uniaxial elongational flow under evaporation. This means, a larger  $\gamma$  presses the particles together more strongly. The second term in equation (4.8) represents the energy related to particle-particle interaction

$$V_L^{pp}[\vec{p}_N] = \sum_{i,j,n} V^{ia}(r_{ijn}) \quad (4.10)$$

---

<sup>2</sup>Additionally, there might be a large set of frustrated states in the real dynamics, where the residual gradient is too small to drive discernable dynamics of moving particles within the very viscous residual polymer.

where  $V^{ia}(r_{ijn})$  describes the interaction energy between two particles with distance

$$r_{ijn} = \sqrt{(x_i - x_j)^2 + (y_i - y_j)^2 + (z_i - z_j + nL)^2}. \quad (4.11)$$

The parameter  $L$  represents the length of the domain, which is illustrated in Figure (4.2). In the real uniaxial elongational flow, a piece of the jet thins and causes the particles to form a colloidal nano-fiber at the centerline. This fiber reaches a final length  $L$  where all particles have settled and the shell fiber, consisting of the residual polymer, is solidified. The model on the contrary is parameterized with a given final length  $L$  of the domain and a given number of particles  $N$  inside the domain. The lower the particle concentration in the real jet or the more it is elongated, the smaller the particle density  $\rho = \frac{N}{L}$  is chosen for the numerics to be equivalent to the experiment. The index  $n$  corresponds to the quasi periodic boundary conditions illustrated in Figure (4.2). With  $n \in \{-1, 0, 1\}$  the domain is periodically continued by one period above and below the jet in order to avoid boundary effects in axial direction at the boundary of the domain. As the van der Waals force is very short-ranged, the quasi periodic boundary condition is practically equivalent to a full periodic boundary condition.

Physically the particle-particle interaction potential  $V^{ia}$  is given by the short ranged attraction by the van der Waals force and the hard sphere behavior provided by the latex particles. Figure (4.3) shows a plot of the ideal hard sphere colloid potential, which is given by equation (4.4) with  $d = d_{ijn} = r_{ijn} - 2r_p + d_{min}$ . As discussed before,  $d_{min}$  is of the order of an atomic diameter. For comparison, Figure (4.3) also shows Lennard-Jones- $(\mu, \nu)$ -potentials

$$V_{\mu\nu}^{LJ}(r) = -E_b \left[ \left( \frac{2r_p}{r} \right)^\mu - 2 \left( \frac{2r_p}{r} \right)^\nu \right] \quad (4.12)$$

where  $(\mu, \nu) \in \{(12, 1), (12, 6), (24, 12)\}$ . As the real potential (4.4) vanishes with  $V(d) \sim d^{-1} \sim r^{-1}$ , the potential is long-ranged compared to the Lennard-Jones-(12,6)-potential. However, the singularity at  $d = 0$  and the ratio  $r_p/d_{min}$ , which determines the binding energy, scale the potential such that its absolute value vanishes very fast with the inter particle distance as illustrated in Figure 4.3. Consequently, it gets the character of a contact potential, which significantly contributes to the energy functional in case the particles are very close to each other, only. For distant particles, fluctuations will dominate the attractive forces originating from the contact potential. Using the contact potential  $V^{ia}(r_{ijn}) = V(r_{ijn} - 2r_p + d_{min})$  is physically correct, but introduces numerical problems, as it is discontinuous at  $r = 2r_p$ . A Lennard-Jones- $(\mu, \nu)$ -potential is a better choice, since it is continuous, differentiable and reproduces the binding energy correctly. The different interaction potential between the particles changed the system dramatically if for example Lagrangian dynamics would be considered. This modelling approach emphasizes the study of states of force equilibria, where the shape of the potential is not important as long as the energy contribution of neighbored particles is reproduced correctly. From Figure 4.3 it can be seen, that the real potential 4.4 causes only touching particles to contribute significantly

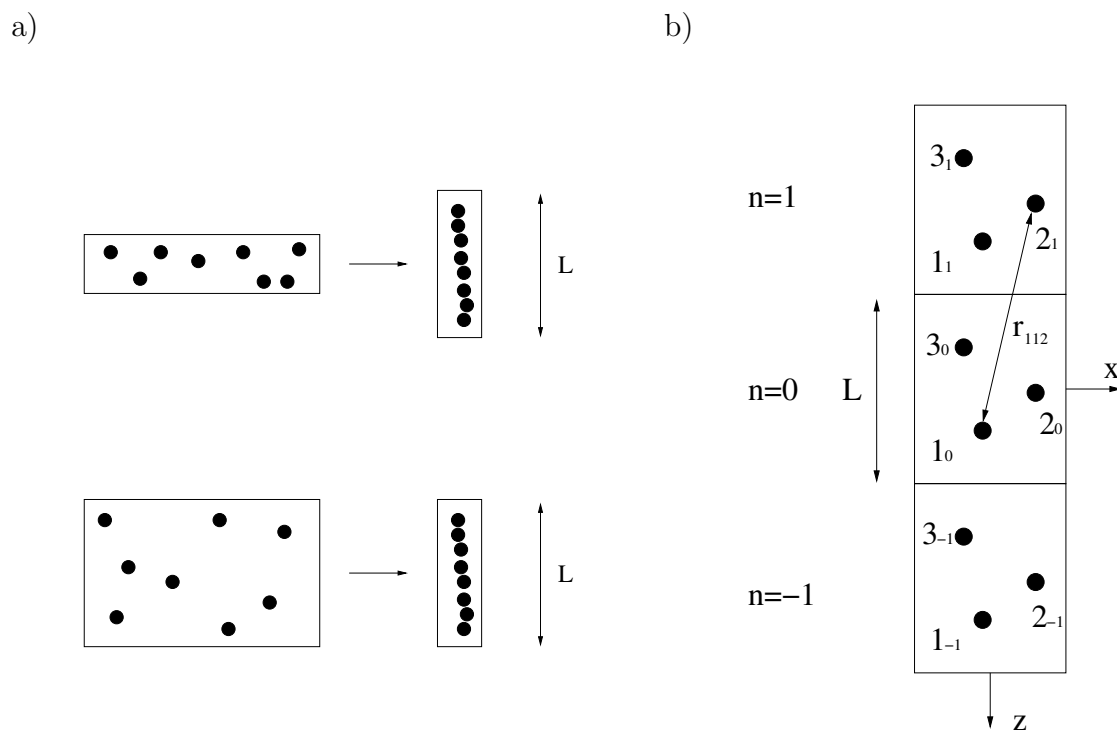


**Figure 4.2:** a) A piece of jet assembles a colloidal nano-fiber via the true electrohydrodynamics of multi-phase electrospinning (above) by the uniaxial elongational flow of a piece of jet and the gradient dynamics of the model system (below) with a domain of constant length  $L$ . b) The domain of length  $L$  is periodically continued by one period in each direction along the axis of symmetry.

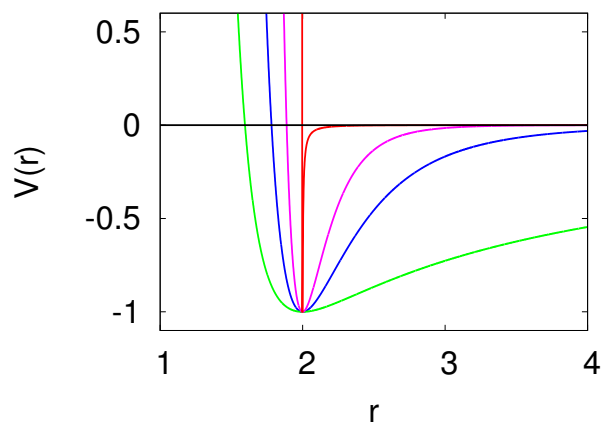


**Figure 4.3:** Comparison between the true hard sphere - van der Waals potential, which is the function that is discontinuous at  $r = 2$  (red) and the Lennard-Jones- $(\mu, \nu)$ -potentials: (12,1) in green, (12,6) in blue and (24,12) in magenta.



to the energy, while second neighbors almost do not contribute. Therefore, the real potential may be replaced by any potential that features the appropriate binding energy and vanishes sufficiently fast in such a way that second neighboring particles do not contribute to the energy significantly. In this modelling approach, a Lennard-Jones-(12,6)-potential has been chosen, as its contribution at  $r = 3r_p$  is 16% of the binding energy and just 3.1% at  $r = 4r_p$ , which is considered to be small enough. Note that the Lennard Jones potential is well behaved for  $r_{ijn} \leq 2r_p$  and therefore increases the performance of the numerics in comparison to the true interaction potential of the colloids.

The binding length of two colloids is slightly modified by the introduction of the Lennard-Jones-(12,6)-potential depending on the environmental conditions, because the Lennard-Jones-potential introduces a finite compressibility, which is equivalent to some sparse elasticity of the particles in case they are pressed together by the confining potential  $V_\gamma^{jet}$  modelling the uniaxial elongational flow of the jet.

### 4.3 Solving the model

In the previous section the physical basis of multi-phase electrospinning has been discussed providing a basis for a theoretical model. In the following, the numerical method is presented, which has been used to minimize the energy functional in order to find true roots of the gradient of the functional. Furthermore, the method to investigate the stability of the corresponding state of force equilibrium is discussed. Using the length scale  $r_0 = r_p$  and the energy scale  $E_0 = |E_b|$ , the non-dimensional energy functional is given by

$$f_{\gamma,L}[\vec{p}_N] = \gamma \sum_{i=1}^N (x_i^2 + y_i^2) + \frac{1}{2} \sum_{n=-1}^1 \sum_{i=1}^N \sum_{\substack{j=1 \\ i \neq j}}^N \left[ \left( \frac{2}{r_{nij}} \right)^{12} - 2 \left( \frac{2}{r_{nij}} \right)^6 \right] \quad (4.13)$$

with  $r_{nij}$  given by equation 4.11. In order to study states of minimal energy of the family of quasi periodic systems displayed in Figure 4.2, reasonable numbers have to be chosen for the numerical parameters  $\gamma$ ,  $L$  and  $N$ . Parameters  $L$  and  $N$  are not independent of each other from a physical point of view, because of their relationship to the particle density  $\rho = \frac{N}{L}$ . This particle density is a physical parameter that counts the number of particles per length of the colloidal nano-fiber and hence is a measure for the average thickness of the resulting nano-fiber. In the following, the particle density  $\rho$  is tuned by  $N \in \mathbb{N}$  with a fixed length  $L = 10$  that automatically leads to a discretization of  $\rho$ . As the system is studied for a set of parameters with  $\rho \in [0.7, 5]$  the only free parameter is  $\gamma$ . The study of force equilibria starts from an initial state of randomly distributed particles located at

$$\vec{r}_i = (x_i, y_i, z_i) \in [-M, +M] \times [-M, +M] \times [-L/2, +L/2] \quad (4.14)$$

with an appropriately chosen  $M \approx 10$ . Consequently, the initial vector of state of the system is given by

$$\vec{p}_N^{(0)} = (x_1, y_1, z_1, \dots, x_N, y_N, z_N). \quad (4.15)$$

The energy functional 4.13 is analytical as long as the vector of state  $\vec{p}_N$  provides  $(x_i, y_i, z_i) \neq (x_j, y_j, z_j) \quad \forall i \neq j$ . This means, two or more particles may not be located at exactly the same coordinates. As the functional is known analytically, its gradient  $\vec{g}_N = (\text{grad } f_{\gamma,L})(\vec{p}_N)$  is readily evaluated for the given vector of state from its analytical representation. The minimization of the functional is started using a very simple method of straight descent in the direction of the gradient, which is given by the iteration

$$\vec{p}_N^{(\nu+1)} = \vec{p}_N^{(\nu)} + \lambda_\nu \vec{g}_N^{(\nu)} \quad (4.16)$$

where  $\lambda_\nu$  is chosen such that  $0 < \lambda_\nu \|\vec{g}_N^{(\nu)}\|_\infty \ll 1$ . This method is capable of minimizing the gradient of the functional reliably for a given initial condition  $\vec{p}_N^{(0)}$ . The advantage of this method with respect to the method of steepest descent or the method of conjugated gradients is its property to cavort within the configuration space prior to getting trapped to a minimum. The other methods mentioned are designed to preferentially find the minimum closest to the initial condition instead. By the use of this gradient method an ensemble of initial states is iterated and settles each one quite fast to some minimum. In this way, the gradient method is expected to preferentially find the minima with large basins of attraction that are of interest for statistical assertions.

The convergence of the iteration is measured by the vanishing of  $\|\vec{g}_N^{(\nu)}\|_\infty$ . Consequently, the number of iterations to be performed in order to satisfy

$$\|\vec{g}_N^{(\nu)}\|_\infty = \|(\text{grad } f_{\gamma,L})[\vec{p}_N^{(\nu)}]\|_\infty < \epsilon \quad (4.17)$$

with  $\epsilon$  close to machine precision, diverges. The minimization via the gradient method is stopped, if  $\|\vec{g}_N^{(\nu)}\|_\infty < \epsilon$  where  $\epsilon = \frac{\gamma}{100}$  has been chosen. This choice is reasonable, as  $\gamma$  is the energy of a particle located at the distance of one radius from the centerline. Hence,  $\epsilon$  is a small limit for the maximal component of the force occurring for the given vector of state  $\vec{g}_N^{(\nu)}$  with respect to the underlying functional  $f_{\gamma,L}$ . After the initial state  $\vec{p}_N^{(0)}$  has been minimized to  $\vec{p}_N^{(\nu)}$  using the gradient method, the Newton-Raphson method [Press et al., 1992] is utilized to determine the root of the gradient up to machine precision. As double precision is used with a typical  $\gamma \lesssim \mathcal{O}(100)$ , the root finding is stopped in case  $\|\vec{g}_N^{(\mu)}\|_\infty \leq \epsilon_M = 10^{-10}$  is satisfied. The Newton-Raphson method takes advantage of the multi-dimensional Taylor expansion of the gradient of the energy functional

$$(\text{grad } f_{\gamma,L})[\vec{p} + \delta\vec{p}] = (\text{grad } f_{\gamma,L})[\vec{p}] + \mathbf{J}\delta\vec{p} + \mathcal{O}(\delta\vec{p}^2) \quad (4.18)$$

where

$$\mathbf{J} = \left( \frac{\partial}{\partial x_j} (\text{grad } f_{\gamma,L}) \Big|_i \right) = \left( \frac{\partial^2 f_{\gamma,L}}{\partial x_j \partial x_i} \right) = \mathbf{H} \quad (4.19)$$

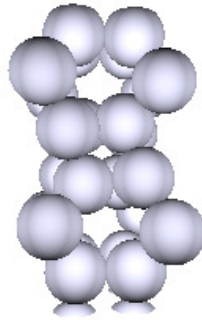


**Figure 4.4:** An unphysical state of vanishing gradient found by the Newton-Raphson method without previous minimization by the gradient method. This finding demonstrates that it is necessary to minimize the functional prior to root finding in order to find the physically relevant arrangements of mechanical equilibrium.

is the Jacobi matrix of the gradient of the functional, which is equivalent to the Hesse matrix  $\mathbf{H}$  of the energy functional. If the root is already in the vicinity of the vector of state  $\vec{p}_N$  the idea behind the Newton-Raphson method is to set  $(\text{grad } f_{\gamma,L})(\vec{p} + \delta\vec{p}) = \vec{0}$  in order to obtain

$$\mathbf{J}\delta\vec{p}_N^{(\mu)} = -(\text{grad } f_{\gamma,L})[\vec{p}_N^{(\mu)}]. \quad (4.20)$$

This is then solved for  $\delta\vec{p}_N^{(\mu)}$ , giving a new estimate

$$\vec{p}_N^{(\mu+1)} = \vec{p}_N^{(\mu)} + \delta\vec{p}_N^{(\mu)} \quad (4.21)$$

for the root of the gradient. By simply using the Newton-Raphson method without previous minimization, unphysical states are found most often if the method converges at all. The resulting states provide at least a vanishing gradient like the example shown in Figure 4.4. These states are very often not states of minimal energy. To emphasize the study to physically relevant states, the initial state is previously minimized to the limit discussed above using the gradient method. After the minimization the Newton-Raphson method converges most often either to a state of minimal energy or a frustrated state, where the norm of the gradient falls below the  $\epsilon$  specified above without being close to an exact root and still features unstable directions. These states are both of physical interest and are denominated states of force equilibrium in the following.

The stability of the obtained solutions is investigated by evaluating the Hesse matrix

$$\mathbf{H} = \left( \frac{\partial^2 f}{\partial x_i \partial x_j} [\vec{p}_N] \right) \quad (4.22)$$

of the energy functional for the given state. Due to the two continuous symmetries of the functional with respect to rotation around and translation along the  $z$  axis, the Hesse

matrix of the vector of state possesses two vanishing eigenvalues such that it is not easily detected, whether non-positive eigenvalues occur. To remedy this defect, the functional is extended  $f \rightarrow \tilde{f}$  which is given by

$$\tilde{f}_{\gamma,L}[\vec{p}_N] = f_{\gamma,L}[\vec{p}_N] + \gamma(y_s - y_{s0})^2 + \gamma(z_s - z_{s0})^2. \quad (4.23)$$

The purpose of the modified functional is the resulting change to the Hesse matrix  $\mathbf{H} \rightarrow \tilde{\mathbf{H}}$  in 2 elements which eliminates the two continuous symmetries and their associated vanishing eigenvalues. Prior to the evaluation of the modified Hesse matrix, the vector of state is rotated around the  $z$  axis in such a way that the  $x_s$  component of the off centerline particle  $s$  vanishes. After minimization and root finding, the state is supposed to be a state of minimal energy, which allows to set  $y_{s0} = y_s$  and  $z_{s0} = z_s$ . A state is considered a state of minimal energy, if the the modified Hesse matrix is positive definite i.e. the eigenvalues  $E_i$  satisfy  $E_i > 0 \quad \forall i$ .

After minimization and root finding procedures and the judgement about the stability for an ensemble of initial conditions, the resulting solutions have to be compared in order to find out whether the final states are equal or not. States  $\vec{p}_N$  and  $\vec{p}'_N$  that are equal up to isometries are identified by comparing the multisets

$$\begin{aligned} M(\vec{p}_N) &= \{r_{ijn} | 1 \leq i < j \leq N, n = 0\} \\ &= \{m_1, \dots, m_{\frac{N^2-N}{2}}\} \end{aligned} \quad (4.24)$$

of the inter-particle distances  $r_{ij0}$  with  $m_i \leq m_{i+1}$ . Equal multisets of inter-particle distances correspond to equal states except for isometries like rotation around the  $z$  axis, translation along the  $z$  axis, chirality and permutations of particles [Welker, 2007]. Hence, the equality of states  $\vec{p}_N$  and  $\vec{p}'_N$  is declared in case

$$|m_i - m'_i| < \epsilon \quad (4.25)$$

is satisfied. A reasonable choice for the system under study is  $\epsilon = 10^{-3}$  because very small differences, arising from the lack of perfect convergence of the numerical root finding, are not distinguished. It has to be pointed out that there might exist different exact roots of the gradient of the functional that differ by less than  $\epsilon$  in the elements of their multisets of inter particle distances, but these differences are small enough to consider these states equal, as they certainly show the same morphology.

## 4.4 Numerical results

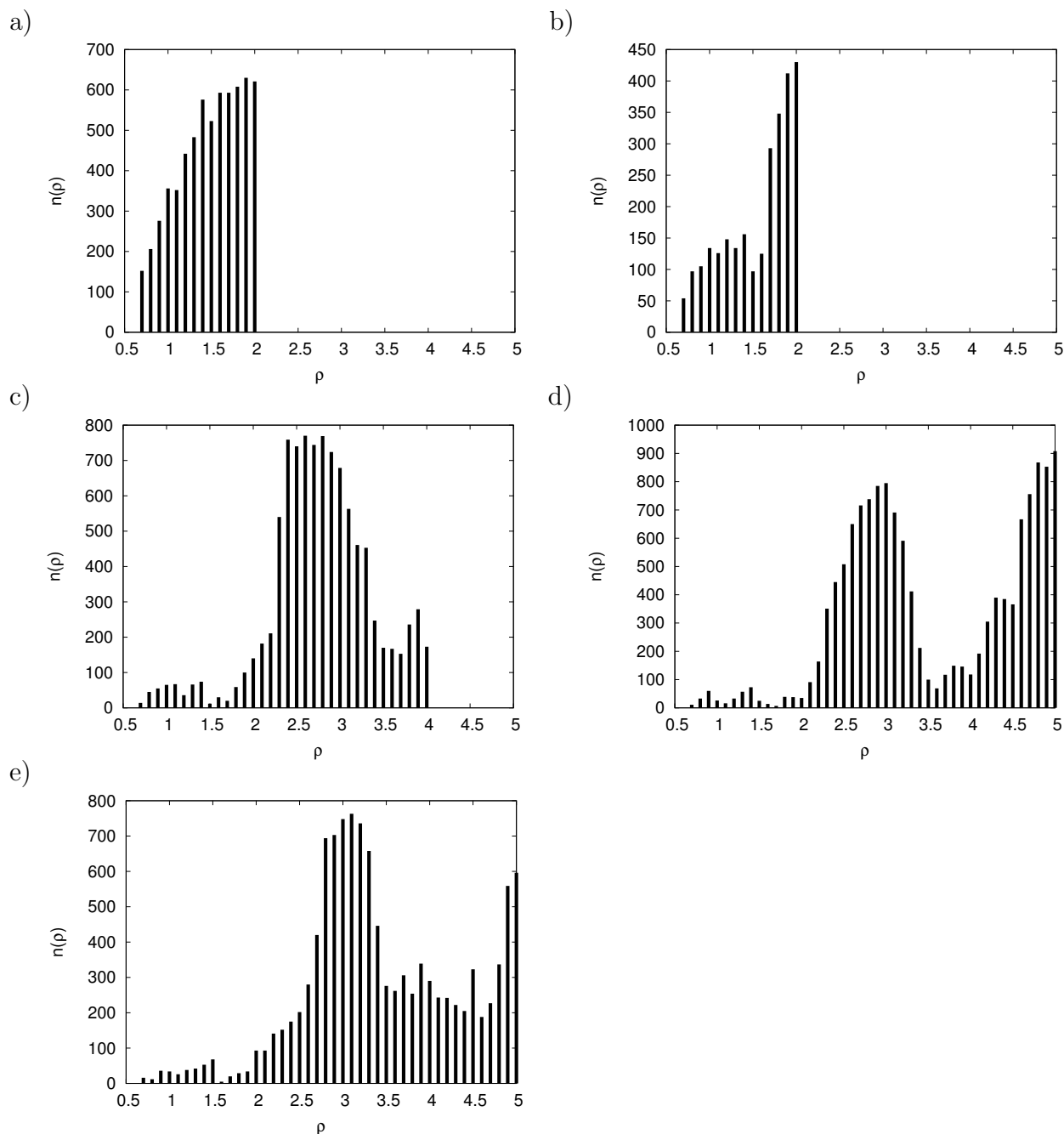
The model presented in the previous section is used to investigate the resulting states of mechanical equilibrium for large ensembles of initial states of randomly distributed particles. As already outlined these initial states are subjected to minimization of the energy functional, root finding of its gradient and the investigation of stability, respectively. After

each of these states has lead to a state of mechanical equilibrium these states are compared pairwise in order to count the number of occurrences of a specific vector of state. Furthermore, the number of different states obtained from a large ensemble of initial states for identical numerical parameters  $\gamma$ ,  $L$  and  $N$  is of special interest.

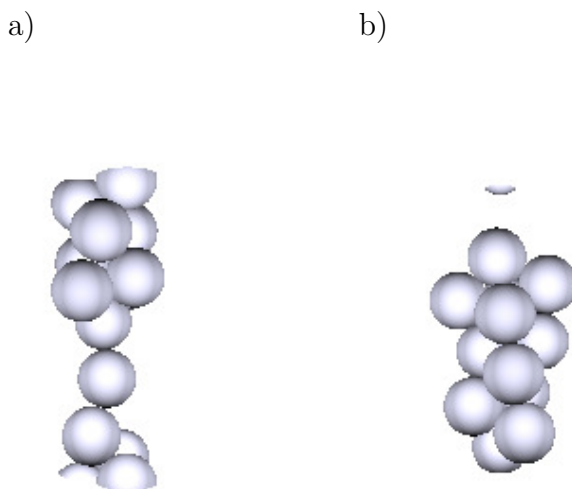
The parameters of the energy functional  $f_{\gamma L}$  are chosen such that  $L = 10 = \text{const}$ ,  $\gamma \in \{1, 3.1, 10, 31, 100\}$  with  $N \in \{7, 8, 9, \dots, 50\}$ . In addition the three numerical parameters the model system consists of two physical parameters  $\rho$  and  $\gamma$ , only. The choice of  $L$  and  $N$  fixes the particle density  $\rho$ . The only free parameter is  $\gamma$ , which models the strength of the thinning process. A large  $\gamma \gg E_b = 1$  models a jet, which is strongly stretched by the electrospinning of the fluid, associated with a strong forcing on the particles due to the relatively large viscosity of the colloidal dispersion. A small  $\gamma \approx E_b$  describes a situation where the interaction between individual particles begins to dominate over the forcing by the electrohydrodynamical flow. It will become obvious that a weak forcing by the flow results in clustering of particles, while a strong forcing causes the particles to align in cylindrical fibers.

Figure 4.5 shows the number  $n(\rho)$  of different states of mechanical equilibrium that have been found as a function of the particle density for an ensemble of 1000 initial states of randomly distributed particles for each  $\rho$ . In Figure 4.5a the thinning is described by  $\gamma = 1$  i.e. the inter particle interaction starts to dominate over the thinning imposed by the uniaxial elongational flow. The weak forcing by the flow causes the gradient of the potential landscape to possess a lot of roots, which are readily found. For  $\gamma = 1$  and  $\gamma = 3.1$  the uniaxial elongational flow is no longer strong enough to prevent a topological transition of the forming colloidal nano-fiber. The particles start to cluster instead of swimming with the flow to the centerline of the jet. Consequently, the fiber tends to break into clusters as illustrated in Figure 4.6. This behavior is found in experiments if the particle concentration is too low or the viscosity of the polymer solution used for the dispersion is not sufficiently large. A low viscosity results in a reduced forcing on the particles.

In Figure 4.5 c), d), e) the forcing of the flow is stronger due to a successively larger  $\gamma$ . As the convergence properties of the numerics improve for larger  $\gamma$ , larger particle densities are accessible. Because of the stronger forcing by the electrospinning jet in Figure 4.5d there obviously exist some particle densities e.g.  $\rho = 1.7$  and  $\rho = 3.6$ , which result in a reduced number of different states found. Figure 4.7 illustrates representative states for these densities as well as for  $\rho = 3.0$ , which features a lot more different states. In case of a perfectly ordered crystal structure the multiset of occurring distances between individual particles does not include certain prohibited distances, while selected distances occur very often. Hence, the first and the third state are considered to be ordered, while the second state is amorphous. The number of occurrences of these states are  $n_1(1.7) = 994$ ,  $n_2(3.0) = 8$  and  $n_3(3.6) = 873$  in the ensemble of 1000 simulations each. Apparently the landscape of the energy functional features fewer roots of its gradient if perfectly ordered states exist for a given set of parameters.



**Figure 4.5:** Displayed are the numbers of different states  $n(\rho)$  found for ensembles of 1000 initial conditions for each  $\rho$ . The states are solutions obtained for different parameters of the flow: a)  $\gamma = 1$ , b)  $\gamma = 3.1$ , c)  $\gamma = 10$ , d)  $\gamma = 31$  and e)  $\gamma = 100$ , respectively. It can be seen that strong flows with larger  $\gamma$  show characteristic minima in  $n(\rho)$ . For the smaller  $\gamma$ , the convergence behavior deteriorates such that larger particle densities  $\rho$  result in very large computational effort. Thus, the calculations have been cut off at  $\rho = 2$  and  $\rho = 4$ , respectively.



**Figure 4.6:** Two topologically different states of mechanical equilibrium obtained from the weak forcing of the flow  $\gamma = 1$ . a) The quasi periodic colloidal nano-fiber is infinitely extended in one dimension. b) The colloidal nano-fiber is broken into clusters, as the inter-particle interaction starts to dominate over the forcing of the flow.

This example also indicates that perfectly ordered structures only exist in case the state provides an exact cylindrical symmetry featuring closed shells consisting of particle layers. In case the outer shell is not completely filled, which for example is the case for  $\rho = 3.0$ , the landscape of the energy functional features a lot of roots of its gradient. The explanation for this is very simple. The first void defect introduced to a highly symmetric ideal crystal possesses only a small amount of degeneration resulting in a slight increase of the number of states found. The introduction of the second void defect to this less symmetrical state possesses a large amount of degeneration. In case the particle density  $\rho$  is too small to match a crystal featuring closed shells, such void defects are unavoidable. The more of these defects occur the smaller is the resemblance to a crystal. Only in cases where the particle density is very close to that of an ideal crystal featuring closed shells, the number of states found becomes small.

The fact that ordered structures exist for selected particle densities in combination with the evidence that these ordered states are preferentially found in the simulations for the reasons outlined, allows to expect the real system to favorize certain particle densities as well. If the particle density in a piece of jet is not close to a particle density of an ideal crystal, the thinning of the jet will change the length  $L$  over which the particle density  $\rho$  is considered during the dynamical process. This rearrangement will happen in such a way that the particles are driven into place by the underlying flow until the particle density matches a favorable particle density or the solidification of the shell fiber freezes

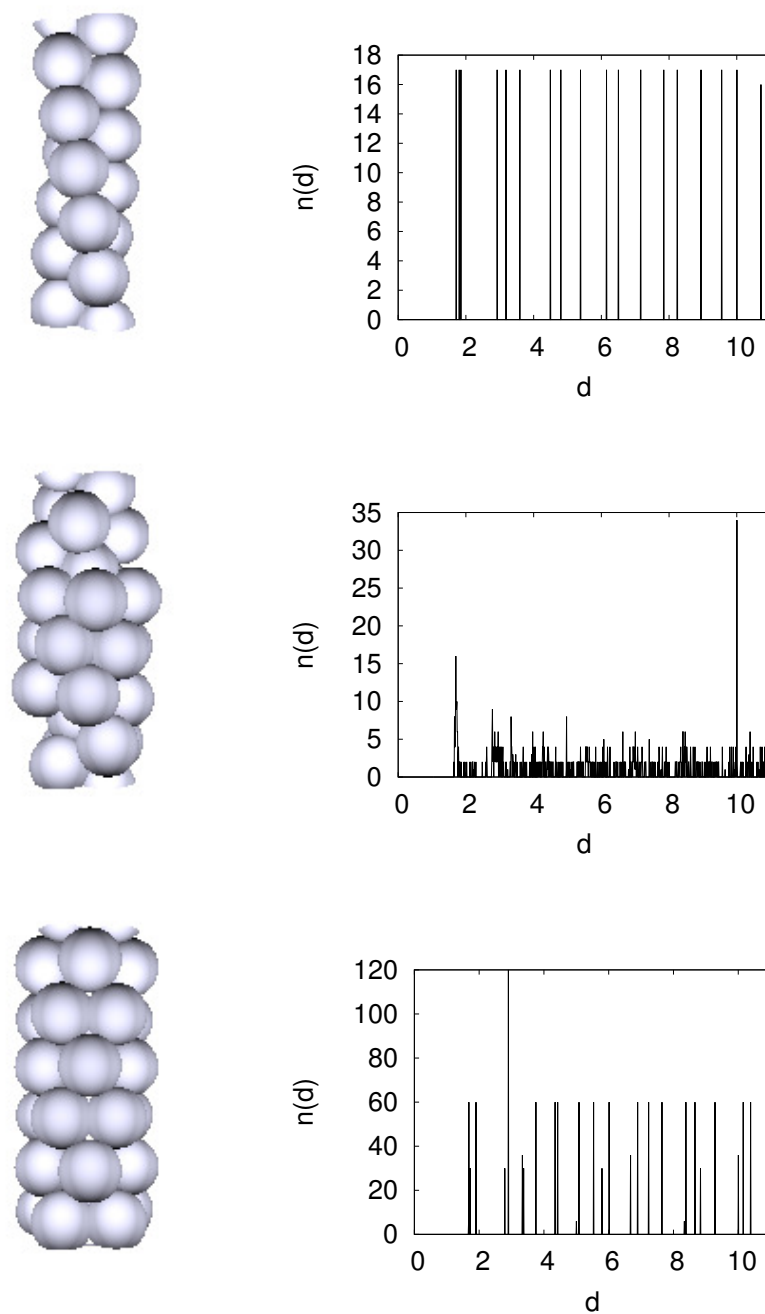


**Figure 4.7:** Selected states with histograms  $n(d)$  of their multisets of inter-particle distances  $d$  illustrate almost perfect order, amorphous behavior and almost perfect order for particle densities  $\rho = 1.7$ ,  $\rho = 3.0$  and  $\rho = 3.6$ , respectively, according to prominent particle densities  $\rho$  of Figure 4.5d under relatively strong forcing  $\gamma = 31$  by the flow.



the particles into place.

Once a colloid possesses a large number of neighbors it will preferentially stick to them, as the contact potential binds them by  $E_b$  for each colloid. Hence, it is energetically favorable that a colloid settles to a position with a large number of touching neighbors, which is largest for crystals featuring closed shells. By this line of argument it is not surprising that most of the fibers found in the experiments are smooth and typically provide a more or less filled outer shell and no add-on particles.

Regarding the stability properties of different states of mechanical equilibrium displayed in Figure 4.8a provides additional information to Figure 4.5d with  $\gamma = 31$ . For low particle densities  $\rho < 2.0$ , there are very few states of mechanical equilibrium that are stable, while the unstable and indefinite states dominate. For densities  $\rho \geq 2.0$  the stable states of mechanical equilibrium dominate and qualitatively reproduce Figure 4.5d. Figure 4.8b refers to the same data, but only displays states that have been found at least three times. The broad maximum between  $\rho = 2.0$  and  $\rho = 3.5$  gets dramatically smaller and splits into two peaks located at  $\rho = 2.3$  and  $\rho = 3.2$ . The fact that there are so many different and disordered states found for densities  $\rho \in [2.3, 3.2]$ , which do scarcely occur more than once, is an indication that there might not exist an attractive ordered state for these particle densities at all.

The situation may be understood in the following way. From Figure 4.9 it is easily verified that up to four particles are easily arranged in a cylinder symmetrical configuration within a two-dimensional slice of the nano-fiber at constant  $z$ , yielding  $\rho(N = 4) = \frac{N}{2r_p} = 2$ . The first four states displayed in Figure 4.9 are examples for these states and are denominated *single-layer fibers*, while the states for  $\rho = 3.6$  and  $\rho = 4.2$  are denominated *second-layer fibers*. This name has been chosen because the *second-layer fibers* might be looked at as a layer of particles wrapped around an inner *single-layer fiber*. Adding another additional particle to the slice of a single-layer fibers breaks the cylindrical symmetry and hence introduces a lot more conceivable configurations of mechanical equilibrium. As a consequence, the absolute number  $a(\rho)$  of states of mechanical equilibrium grows rapidly with the particle density  $\rho$ . Figure 4.9 illustrates the threshold behavior at  $\rho_{crit} = 2$  as transition from a colloidal single-layer nano-fiber to a colloidal second-layer nano-fiber using the example of Figure 4.5d with  $\gamma = 31$ .

The final question of how to control the diameter of the colloidal nano-fiber experimentally is an intriguing theoretical problem if the full equations of multi-phase electrospinning are considered as already outlined in Chapter 1. However, assuming in error that the particles lack any feedback to the electrohydrodynamical flow of the jet, the electrospinning would be independent of the amount of particles swimming with the flow. In this case, the jet will thin to its final diameter and freeze the particles within the residual polymer. Twice the particle concentration would result in twice the cross section of the colloidal nano-fibers.

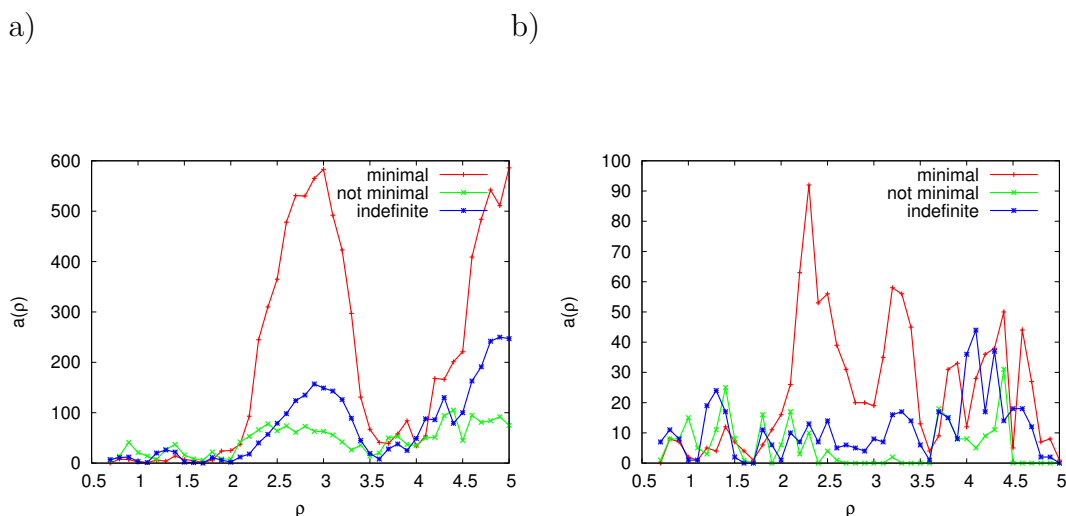


**Figure 4.8:** The number of different states of mechanical equilibrium for  $\gamma = 31$  that are considered minimal, not minimal and those that are probably indefinite as a function of the particle density  $\rho$ . a) The stability properties of all states. b) The stability of states that occur at least three times. This is an indication that no ordered state seems to exist at  $\rho \approx 3$ .

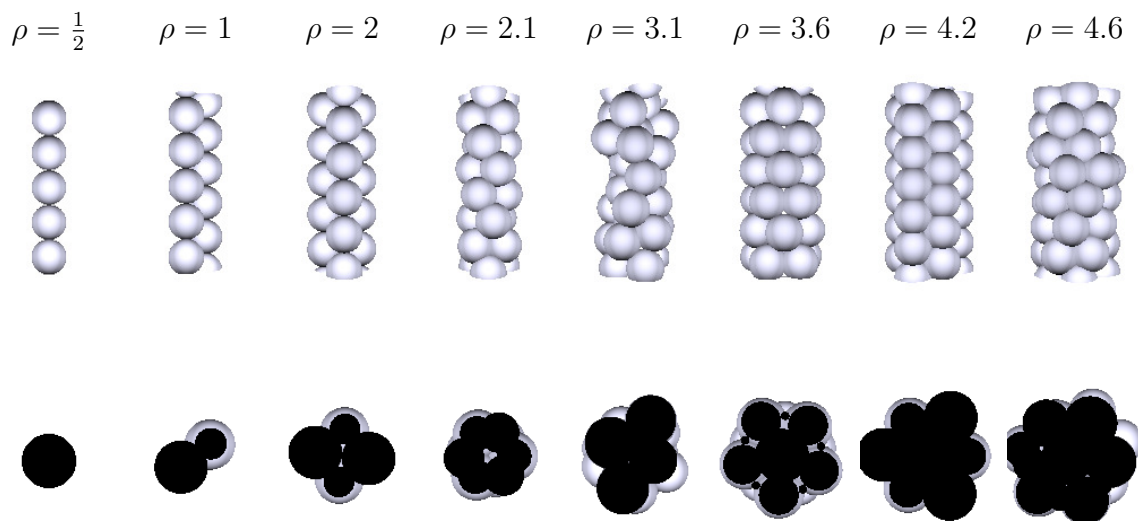


**Figure 4.9:** Different ordered states of mechanical equilibrium for various particle densities  $\rho$  and their cross sections taken from a cut at the center of the nano-fiber are displayed. At  $\rho = 3.1$  no ordered state seems to exist, resulting in a large amount of amorphous arrangements. At  $\rho = 3.6$  and  $\rho = 4.2$  the second layer of particles forms a closed shell around an inner colloidal structure. At  $\rho = 4.6$ , the third layer of particles does not form a closed shell yet, again resulting in a large amount of amorphous arrangements.

If the feedback of the particles on the flow is indeed negligible, the above line of argument holds at least on a qualitative basis. Based on this reasoning a monotonic increase of the diameter of the colloidal nano-fiber could be found experimentally simply by controlling the initial particle concentration of the colloidal dispersion.

Examples of experimentally obtained colloidal nano-fibers in comparison with theoretical results are illustrated in Figure 4.10. The concentrations of the colloidal dispersions are given in the figure caption by e.g. 5% S100:PVA=70:30, which means that 5 per cent by weight of polymer is dispersed in 95 per cent by weight of water. The total amount of polymer added to the water consists of 70 per cent by weight of solid colloidal particles of diameter  $d_p = 100nm$  and 30 per cent by weight of water soluble PVA polymer [Stoiljkovic, 2007]. The material of the colloidal particles is Latex i.e. Polystyrene for all experimental images in this work.

From the images the ratios  $\frac{d_f}{d_p} = \frac{r_f}{r_p}$  can be estimated to 1.5, 2.5 and 4.0 respectively, where  $d_f$  is the diameter of the fiber,  $d_p$  the diameter of a representative particle and  $r_f$  as well as  $r_p$  are the corresponding radii. The particle density of the experimentally obtained colloidal nano-fibers can be estimated from the images via the diameters  $d_f$  and  $d_p$  by

$$\rho_{exp} = \frac{\pi}{4\sqrt{3}} \left( \frac{d_f}{d_p} \right)^2. \quad (4.26)$$

A derivation of this formula is found in appendix<sup>3</sup> A.8 on page 138. Figure 4.10 shows the comparison between the experimentally obtained colloidal nano-fibers and theoretical results for approximately the same particle densities. Qualitatively, the same kind of structures are found in theory and experiment as the double stranded helical fiber has been found in the first place as well as a relatively disordered state at  $\rho \approx 2.9$  where the theory expects no ordered states and a slightly more regular state at  $\rho = 4.1$ , where the theory predicts more regular arrangements according to the structure of  $n(\rho)$  displayed in Figure 4.5d.

## 4.5 Conclusions on multi-phase electrospinning

Mutual feedback between experiments and the theoretical modelling approach has lead to reasonable theoretical assumptions imposed on the model developed for the numerical study of multi-phase electrospinning. The quantitative numerical results lead to reasonable interpretations that are in agreement with experimental observations.

In this way, it has been found that the thickness of the colloidal core nano-fibers can at least to some extend be controlled by the concentration of the colloidal dispersion. The experimental finding that add-on particles do not occur on a regular basis together with

---

<sup>3</sup>It has to be kept in mind that  $r_p = 1$  in the non-dimensional formulation given by equation 4.26.

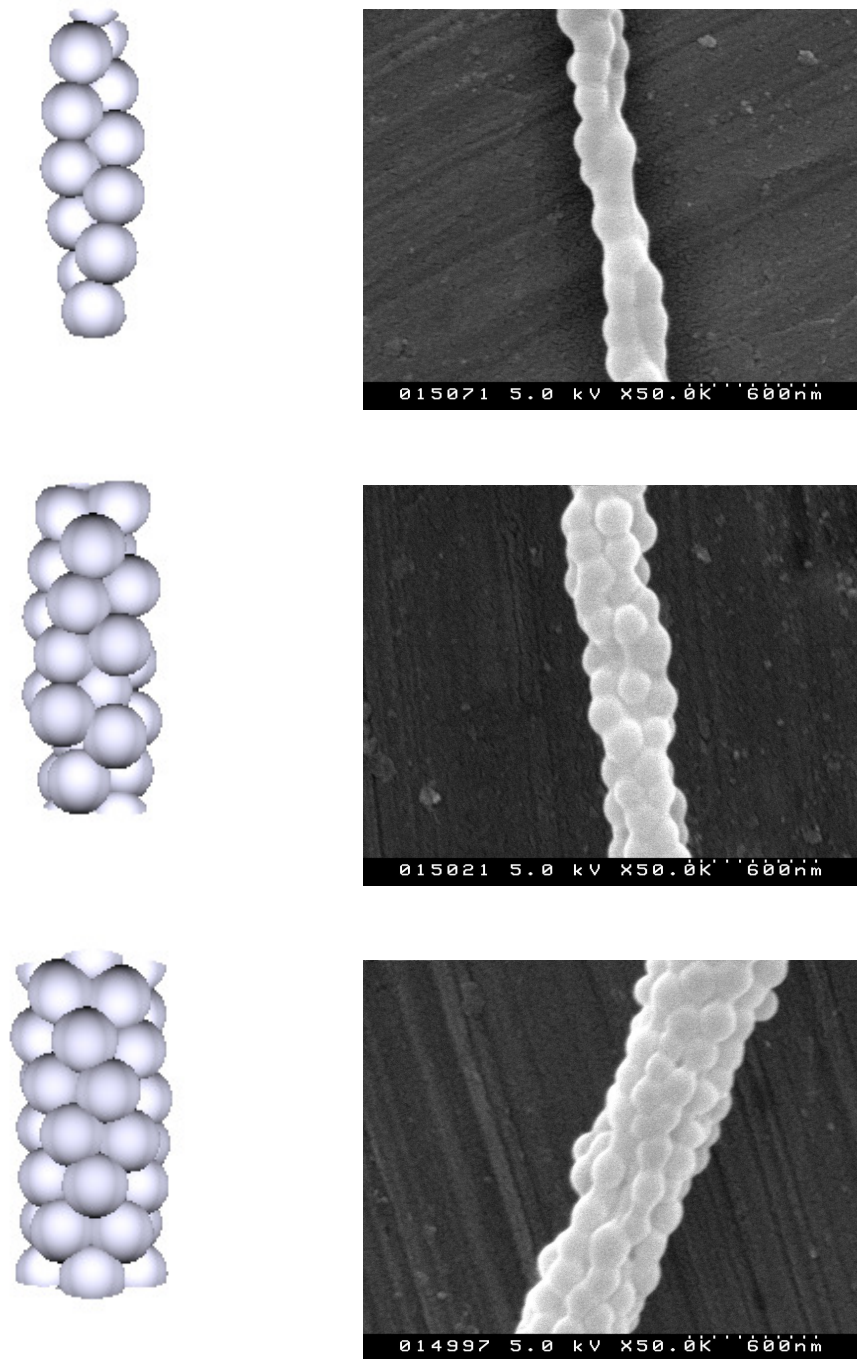


**Figure 4.10:** Comparison between numerical results and corresponding experimental data. The exact theoretical particle densities are  $\rho_{th} = 1.1$ ,  $\rho_{th} = 2.8$  and  $\rho_{th} = 4.1$ , respectively, from top to bottom corresponding to the concentrations of the colloidal dispersion 5% S100:PVA=50 : 50 with  $\rho_{exp} \approx 0.97$ , 5% S100:PVA=70 : 30 with  $\rho_{exp} \approx 2.9$  and 5% S100:PVA=80 : 20 with  $\rho_{exp} \approx 4.1$ . The experimental part has been contributed by Aleksandar Stoiljkovic.

the experimental fact that soft colloids lose their morphology, suggest that the electrohydrodynamical flow of an evaporating jet forces the colloids very strongly. The theoretical findings for weak and strong forcing i.e. a small and a large  $\gamma$  approve these arguments on a quantitative basis that is illustrated in Figure 4.5. Qualitatively this finding is supported by examples for weak forcing displayed in Figure 4.6, which is in contrast to examples for strong forcing shown in Figure 4.7. Furthermore, the numerical results obtained from the theoretical model suggest that ordered structures do not seem to exist for certain particle densities.

The existence of one-dimensional ideal crystals for certain particle densities has been found to have an ordering effect on the numerically obtained solutions and reduces the number of states found for these particle densities. Experimentally this finding is not easily verified as the tiny colloidal nano-fibers can not be analyzed by quantitative measurements apart from the SEM imaging already performed. Nevertheless, the existence of ideal crystals, where the colloidal particles maximize the number of neighboring particles, allows to interpret the structures of the experimentally obtained colloidal nano-fibers as amorphous arrangements that are attracted towards ideal crystals during the formation process of the nano-fiber for thermodynamical reasons. Constructively, the amorphous arrangements may as well be contemplated as one-dimensional crystals that have been decrystallized by the introduction of void defects and the subsequent relaxation of the induced tension.

Multi-phase electrospinning has turned out to be a stable electrospinning process that allows to produce core-shell nano-fibers in a very controllable way. The colloidal dispersions can be tuned by the polymers and the particles used, which makes multi-phase electrospinning a promising technique for the production of composite materials consisting of colloidal nano-fibers.

The author is very grateful to Aleksandar Stoiljkovic for the experimental contribution to this chapter, the stimulating cooperation and friendship.



# Chapter 5

## Conclusion & outlook

The motivation behind this thesis has been to improve the understanding of the relevant mechanisms underlying the formation of jets from electrified liquid interfaces. Jets are emitted from Gilbert-Taylor cones, which are static electrified liquid interfaces in simultaneous mechanical and electrical equilibrium. The mechanism of jet formation is of interest from the point of fundamental research, whereas the technological interest lies in the precise control of jet emission in order to produce nano-fibers from electrified polymeric solutions via the electrospinning process. A control of the jet emission process beyond trial and error demands a fundamental understanding of the involved processes. This study has focussed on electrohydrostatic solutions of electrified liquid interfaces prior to jet emission.

### 5.1 Conclusion

In this thesis a numerical method has been developed in order to compute the shapes and properties of electrified droplets. This method has been used to study electrified droplets hanging from a nozzle as well as closed droplets in a homogeneous electrical field. The numerical solutions obtained include rounded droplets, intermediate droplets, conical droplets and overcharged droplets in the order of increasing electrical field.

In Taylor's classical asymptotical explanation the opening angle of the Gilbert-Taylor cones is  $\vartheta_c = 49.3^\circ$ , while electrified droplets have been observed to show considerably smaller opening angles [Giglio et al., 2008, Yarin et al., 2001]. The numerical results have asymptotically reproduced Taylor's classical opening angle  $\vartheta_c$  in the limit of vanishing hydrostatic pressure. Larger hydrostatic pressures have been observed to result in smaller opening angles of Gilbert-Taylor cones.

After revising elementary definitions and insights of Taylor, Chapter 2 closes with a short treatise on jet emission from ideal Taylor cones. It has been shown that the liquid's surface of the Taylor cone is destabilized on the entire surface. Furthermore, jet emission from

infinitely extended ideal Taylor cones has to be distinguished from jet emission from finite sized Taylor cones. Jet emission from ideal Taylor cones can be considered as directed Coulomb explosion.

In Chapter 3 a method has been developed allowing to compute the shapes of droplets that hang from a nozzle located at the upper plate of a plate capacitor. The solutions to the equations derived, describe droplets in mechanical and electrical equilibrium at the same time. Given an electrical field the solution of such a droplet consists of the surface charge density  $\sigma(z)$  on the droplet's surface and the shape  $r(z)$  of the droplet. The differential equations describing the mechanical equilibrium of the interface are an extension of the Fuchikami equations [Fuchikami et al., 1999]. The constraint of electrical equilibrium demands the droplet to be at an equipotential. The resulting additional equation is a highly nonlinear integral equation that can be cast into the shape of a Fredholm integral equation of the first kind, whose kernel is implicitly dependent on its solution. Solving such a nonlinear integral equation of the first kind is considered a true challenge in the literature on integral equations [Wing and Zahrt, 1991], as the theory on these equations is scarcely developed.

Despite this fact, an iterative algorithm has successfully been developed that solves the Fuchikami equations under the restriction to an equipotential. The solution satisfies the Fuchikami equations and the integral equations of the equipotential boundary condition simultaneously. Obtained solutions of the limiting case of vanishing nozzle pressure have been demonstrated to approach the opening angle  $\vartheta_c = 49.3^\circ$  of Taylor's analytical solution in the absence of gravity. In order to characterize the droplet a very simple exact analytical expression for the energy of state of an electrified droplet has been derived. The electrical Weber number has been obtained numerically and is available, spatially resolved for any droplet computed. The solutions of droplets hanging from a nozzle depend on three physical parameters namely the electrical field, the nozzle pressure and the nozzle radius. The algorithm converges for a large fraction of the parameter space and stops converging after a rounded droplet has deformed into a conical droplet. After the conical solution the algorithm sometimes still finds overcharged droplets for further increased electrical fields. These overcharged droplets are static solutions that are considered precursors of jet emission. For even larger electrical fields the algorithm does not converge anymore, which is in agreement with theoretical predictions and experimental findings [Taylor, 1964, Taylor, 1969].

A fraction of the parameter space has been investigated numerically. It has revealed that uncharged nozzle droplets of Fuchikami mode 1 and Fuchikami mode 2 approach each other in case they are exposed to the homogeneous electrical field of the plate capacitor at constant nozzle pressure. Apart from these solutions intermediate droplets and conical droplets have been found, too. The ensemble of obtained solutions gives rise to isosurfaces of constant nozzle radius in parameter space. The choice of the nozzle radius selects one of these surfaces in parameter space, such that the nozzle radius determines whether in-



intermediate or conical droplets can be found or not.

Jet emission from Gilbert-Taylor cones i.e. conical fluid interfaces of finite size is different from jet emission from ideal Taylor cones. The explanation of jet emission from non-ideal Taylor cones is based on overcharged droplets. They could be found for large electrical fields just prior to the vanishing of convergence of the numerical method of solution. These overcharged droplets show a cone, rounded at the tip, which shows the onset of necking at a certain distance from the apex of the cone. This onset of necking is inherent to the solution of the equations for mechanical and electrical equilibrium.

With applications in technology in mind an instantaneous perturbation in the electrical field has been shown to result in a directed Coulomb explosion of the apex of a Taylor cone. The magnitude of the perturbation of the electrical field determines the size of the destabilized region. It is concluded that such a perturbation is a candidate for a control variable to be used to control the onset of jet emission. A detailed experimental investigation is desirable.

In the absence of gravity the method of solution has been used to compute the shapes of closed droplets in a homogeneous electrical field. In this case only two physical parameters determine the solution, which are the electrical field and the volume of the droplet. Additionally, a smoothness condition has to be satisfied in order to connect two semi-droplets continuously differentiable to form a closed droplet. Similarities to the nozzle droplets have been found in the structure of the ensemble of obtained solutions in parameter space. Charged Fuchikami mode 2 droplets exist for closed droplets in case appropriate electrical fields are applied. A study on the properties of the slightly overcharged conical tip of a charged closed droplet has allowed to estimate the mass, charge and the acceleration of a tiny droplet emitted from the apex of the conical droplet into the homogeneous electrical field. The acceleration has been estimated to be of the order of approximately 1700 multiples of  $g$ . These tiny droplets are interesting in connection with research on lightning discharges [Ebert, 2008].

The field of numerics on electrohydrostatical free surface problems is not extensively developed such that the results of this thesis are complementary to those of Basaran and Scriven [Basaran and Scriven, 1990].

In Chapter 4 a multi-phase electrospinning has been studied. The fully developed electrohydrodynamical flow of an evaporating jet of a colloidal dispersion is so complicated that a treatment from first principles has been considered intractable. After the relevant physical effects have been identified, a reasonable model has been set up allowing to study the structures of colloidal nano-fibers quantitatively. It has been shown that it is the evaporative flow that pushes the particles together very strongly. This forcing orders the arrangements of the colloids to some extent. The numerical results obtained from the

theoretical model made clear that the system favors particle densities, which lie close to theoretical values of ideal one-dimensional crystals. For thermodynamical reasons these ideal crystals are favored as each colloid maximizes the number of binding partners, and hence minimizes the free energy. The process of multi-phase electrospinning happens so fast that the colloids typically are frozen in a frustrated state or a state of local energetical minimum more or less close to an ideal one-dimensional crystal. Experiment and theory have mutually contributed to the development of a model for the study of multi-phase electrospinning, whose predictions are in agreement with experimentally verified dependencies.

## 5.2 Outlook

Suggesting further research, the development of a numerical stability analysis of the electrohydrostatical solutions is recommended. First ideas to this subject have been discussed in Section 3.3.3.

Furthermore, the author is interested in an experimental investigation of the computed structures in the parameter space of the nozzle droplets that are shown in Figures 3.25 and 3.26 on pages 73 and 74, respectively. Additionally, the controlled launching of jets from electrohydrostatic solutions as discussed in Subsection 3.3.6 on page 83 is a very interesting approach to the control of the onset of jet emission. In case these results are found to be sustainable, they will have an impact on the controllability of jet emission for electrospinning applications. Appropriately chosen curves in parameter space  $\mathcal{K}(\Delta p_1(t), \Pi_3(t))$  would allow to prepare nozzle droplets in states like intermediate droplets or conical droplets. In case these droplets are deliberately destabilized by driving them into parameter regimes, where no electrohydrostatic solutions exist anymore the onset of jetting starts from precisely controlled initial conditions. This way, the initial radius of the jet might be controlled much more precise as well. Hence, the controllability of the electrospinning process will be improved.

# Appendix A

## Definitions, supplements and derivations

### A.1 List of symbols

$\rho$	density
$\gamma$	surface tension
$K$	conductivity
$R$	Radius (as a geometrical property)
$r$	radius (as an independent variable)
$\kappa$	mean curvature
$\sigma$	surface charge
$\Pi_i$	non-dimensional parameter no. $i$
$\phi$	electrostatic potential
$\vartheta_T = 130.7^\circ$	Taylor cone angle
$\vartheta_c = 49.3^\circ$	Taylor cone opening angle
$L^2$	space of square integrable functions
$\mathbf{1}$	unit tensor
$\mathbf{T}_k(s)$	Fredholm integral operator with kernel $k(s, z)$
$\mathbf{D} = \frac{\eta}{2} (\nabla \vec{u} + (\nabla \vec{u})^T)$	rate of strain tensor
$\mathbf{p}^M = \epsilon \epsilon_0 \left( \vec{E} \vec{E} - \frac{1}{2} \vec{E} \cdot \vec{E} \mathbf{1} \right)$	Maxwell stress tensor
$\mathbf{L} = \gamma (\mathbf{1} - \vec{n} \vec{n}) \mathbb{1}_S(x)$	Lafaurie tensor

## A.2 List of scales

$W_{eE}$	$= \frac{\epsilon\epsilon_0 E^2}{\gamma\kappa}$	the electrical Weber number
$\Pi_1$	$= \frac{\gamma_1}{\gamma_2}$	ratio of surface tensions
$\Pi_2$	$= \frac{\rho_2 - \rho_1}{\rho_1 - \rho_0}$	ratio of densities
$\Pi_3$	$= \frac{4\pi^2 \epsilon\epsilon_0}{\sigma_0} E^{pc}$	non-dimensional electrical field
$l_0$	$= \sqrt{\frac{\gamma_1}{(\rho_1 - \rho_0)g}}$	capillary length
$P_0$	$= \sqrt{\gamma_1(\rho_1 - \rho_0)g} = \frac{\gamma_1}{l_0}$	capillary pressure
$m_0$	$= \rho_1 l_0^3$	scale for mass
$a_0$	$= g$	scale for acceleration
$\sigma_0$	$= \sqrt{\frac{\gamma_1 \epsilon\epsilon_0}{l_0}}$	scale for charge density
$A_0$	$= l_0^2$	scale for surface
$V_0$	$= l_0^3$	scale for volume
$q_0$	$= \sigma_0 l_0^2$	scale for charge
$p_0$	$= \sigma_0 l_0^3$	scale for dipole moment
$E_0$	$= \gamma_1 l_0^2$	scale for energy
$\phi_0$	$= E^{pc} l_0$	scale for electrostatic potential

## A.3 Definition of functions

Sign function

$$\text{sign}(x) \stackrel{\text{def}}{=} \begin{cases} 1 & x > 0 \\ 0 & x = 0 \\ -1 & x < 0 \end{cases} \quad (\text{A.1})$$

Heaviside function

$$\Theta(x) \stackrel{\text{def}}{=} \begin{cases} 1 & x > 0 \\ \frac{1}{2} & x = 0 \\ 0 & x < 0 \end{cases} \quad (\text{A.2})$$

Indicator function

$$\mathbb{1}_A(x) \stackrel{\text{def}}{=} \begin{cases} 1 & x \in A \\ 0 & x \notin A \end{cases} \quad (\text{A.3})$$

The Pochhammer-symbol [Lebedev, 1972]

$$(\lambda)_k = \lambda(\lambda + 1) \dots (\lambda + k - 1) \quad (\lambda)_0 = 1, \quad k \in \mathbb{N} \quad (\text{A.4})$$

The hypergeometric series [Andrews et al., 2000]

$${}_2F_1(\alpha, \beta; \gamma; z) = \sum_{k=0}^{\infty} \frac{(\alpha)_k (\beta)_k}{k! (\gamma)_k} z^k \quad (\text{A.5})$$

Legendre function of the first kind [Lebedev, 1972]

$$\begin{aligned} P_\nu(z) &= \frac{\Gamma(\frac{\nu}{2} + \frac{1}{2})}{\sqrt{\pi}\Gamma(\frac{\nu}{2} + 1)} \cos \frac{\nu\pi}{2} {}_2F_1\left(\frac{\nu}{2} + \frac{1}{2}, -\frac{\nu}{2}; \frac{1}{2}; z^2\right) \\ &\quad + \frac{2\Gamma(\frac{\nu}{2} + 1)}{\sqrt{\pi}\Gamma(\frac{\nu}{2} + \frac{1}{2})} \sin \frac{\nu\pi}{2} z {}_2F_1\left(\frac{1}{2} - \frac{\nu}{2}; \frac{\nu}{2} + 1; \frac{3}{2}; z^2\right) \\ &z, \nu \in \mathbb{C}, \quad |z| < 1 \end{aligned} \quad (\text{A.6})$$

Legendre function of the second kind [Lebedev, 1972]

$$\begin{aligned} Q_\nu(z) &= e^{\mp\nu\pi i/2} \left[ \frac{\Gamma(\frac{\nu}{2} + 1)\sqrt{\pi}}{\Gamma(\frac{\nu}{2} + \frac{1}{2})} z {}_2F_1\left(\frac{1}{2} - \frac{\nu}{2}, \frac{\nu}{2} + 1; \frac{3}{2}; z^2\right) \right. \\ &\quad \left. + \frac{\Gamma(\frac{\nu}{2} + \frac{1}{2})\sqrt{\pi}}{2\Gamma(\frac{\nu}{2} + 1)} {}_2F_1\left(\frac{\nu}{2} + \frac{1}{2} - \frac{\nu}{2}; \frac{1}{2}; z^2\right) \right] \\ &\nu, z \in \mathbb{C}, \quad \nu \neq -1, -2, -3, \dots \end{aligned} \quad (\text{A.7})$$

Complete elliptic integral of the first kind [Lebedev, 1972]

$$K(k) = \int_{\vartheta=0}^{\frac{\pi}{2}} \frac{1}{\sqrt{1 - k^2 \sin^2 \vartheta}} d\vartheta \quad (\text{A.8})$$

Complete elliptic integral of the second kind [Lebedev, 1972]

$$E(k) = \int_{\vartheta=0}^{\frac{\pi}{2}} \sqrt{1 - k^2 \sin^2 \vartheta} d\vartheta \quad (\text{A.9})$$

with

$$\frac{d}{dk} K(k) = \frac{1}{k} \left[ \frac{E(k)}{1 - k^2} - K(k) \right] \quad (\text{A.10})$$

$$\frac{d}{dk} E(k) = \frac{E(k) - K(k)}{k} \quad (\text{A.11})$$

## A.4 Singular value decomposition and condition

**Singular value decomposition** is a very valuable tool that is used throughout this work. This appendix points out its definition and some properties that are important in the context of this thesis.

Any  $m \times n$  matrix  $\mathbf{M}$  possesses a singular value decomposition of the form

$$\mathbf{M} \stackrel{\text{def}}{=} \mathbf{U}\mathbf{\Sigma}\mathbf{V}^* \quad (\text{A.12})$$

with  $\mathbf{U}$  an unitary  $m \times m$  matrix,  $\mathbf{\Sigma} = s_i \delta_{ij}$  a *diagonal*  $m \times n$  matrix and  $\mathbf{V}^*$  a unitary  $n \times n$  matrix [Stoer and Burlisch, 2005]. The singular values  $s_i$  satisfy  $s_i \in \mathbb{R}_0^+$  and  $s_i \geq s_{i+1} \forall i$ . The column vectors of  $\mathbf{U}$  are the left singular vectors and the column vectors of  $\mathbf{V}$  i.e. the row vectors of  $\mathbf{V}^*$  are the right singular vectors of matrix  $\mathbf{M}$ . The left singular vectors are the eigenvectors of the matrix  $\mathbf{M}\mathbf{M}^*$  and the right singular vectors are the eigenvectors of matrix  $\mathbf{M}^*\mathbf{M}$ . Consequently, the left and right singular vectors are identical if  $\mathbf{M}$  is hermitian. In this case, there exists a unitary matrix  $\mathbf{Q}$  such that

$$\mathbf{M} = \mathbf{Q}\mathbf{D}\mathbf{Q}^* \quad (\text{A.13})$$

with  $\mathbf{D}$  a diagonal matrix, whose elements are real. The hermitian matrix  $\mathbf{M}$  gives rise to

$$\mathbf{M}\mathbf{M}^* = \mathbf{Q}\mathbf{D}\mathbf{Q}^*\mathbf{Q}\mathbf{D}\mathbf{Q}^* = \mathbf{Q}\mathbf{D}^2\mathbf{Q}^* \quad (\text{A.14})$$

in comparison to the general problem

$$\mathbf{M}\mathbf{M}^* = \mathbf{U}\mathbf{\Sigma}\mathbf{V}^*\mathbf{V}\mathbf{\Sigma}^*\mathbf{U}^* = \mathbf{U}\mathbf{\Sigma}^2\mathbf{U}^* \quad (\text{A.15})$$

reveals the identity  $\mathbf{Q} = \mathbf{U} = \mathbf{V}$  for hermitian matrices and the singular values on the diagonal of  $\mathbf{\Sigma} = +\sqrt{\mathbf{D}^2}$ . The positive sign of the root is chosen according to convention. This identity follows from the uniqueness of the singular value decomposition based on the non-degenerate singular values  $s_i > s_{i+1} \forall i$ . In case  $\mathbf{\Sigma}^{-1}$  exists, the inverse matrix is obviously given by  $\mathbf{M}^{-1} = \mathbf{V}\mathbf{\Sigma}^{-1}\mathbf{U}^*$ , because

$$\mathbf{M}^{-1}\mathbf{M} = \mathbf{V}\mathbf{\Sigma}^{-1}\mathbf{U}^*\mathbf{U}\mathbf{\Sigma}\mathbf{V}^* = \mathbf{1}. \quad (\text{A.16})$$

Since  $\mathbf{\Sigma} = s_i \delta_{ij}$  is a diagonal matrix with  $s_i \in \mathbb{R}_0^+$  the matrix  $\mathbf{M}$  is singular in case  $s_j = 0$  for all  $j > k$ . The corresponding right singular vectors  $\vec{v}_j$  of matrix  $\mathbf{V} = (\vec{v}_1, \dots, \vec{v}_n)$  span the null space

$$\mathcal{N}(\mathbf{M}) = \left\{ \left\{ \sum_j \lambda_j \vec{v}_j \right\} \middle| s_j = 0, \lambda_j \in \mathbb{C} \right\} \quad (\text{A.17})$$

of matrix  $\mathbf{M}$ .

In case matrix  $\mathbf{M}$  is non-singular i.e.  $s_i \neq 0 \quad \forall i$ , but provides a large condition number  $\text{cond}(\mathbf{M})$ , which is defined below, the matrix is close to being singular and is termed an ill-conditioned matrix. A numerical inversion or solution approach of such an ill-conditioned matrix results in very large relative errors for the vector of solution. In these cases a truncated singular value decomposition TSVD gives rise to a rank  $k$  approximation

$$\mathbf{M}_k = \mathbf{U}\mathbf{\Sigma}_k\mathbf{V}^* \quad \text{with} \quad \mathbf{\Sigma}_k = \begin{cases} s_i & i \leq k \\ 0 & i > k \end{cases} \quad (\text{A.18})$$

of an ill-conditioned matrix  $\mathbf{M}$ , where  $k$  has to be chosen carefully. The matrix

$$\mathbf{S}_k = a_i\delta_{ij} \quad \text{with} \quad a_i = \begin{cases} \frac{1}{s_i} & i \leq k \\ 0 & i > k \end{cases} \quad (\text{A.19})$$

gives rise to the *pseudoinverse*<sup>1</sup>

$$\mathbf{M}_k^{-1} = \mathbf{V}\mathbf{S}_k\mathbf{U}^* \quad (\text{A.20})$$

of the rank  $k$  approximation  $\mathbf{M}_k$  of matrix  $\mathbf{M}$  [Golub and Kahan, 1965]. If matrix  $\mathbf{M}$  is truly singular there exists a  $k$  such that  $s_j = 0 \quad \forall j > k$ . In this case a singular matrix is identical to its rank  $k$  approximation.

The *pseudoinverse* matrix inverts the mapping performed by matrix  $\mathbf{M}_k$  apart from the loss of information due to projection on the null space of matrix  $\mathbf{M}_k$ . This means that the mapping

$$\vec{b} = \mathbf{M}_k\vec{x} = \mathbf{M}_k(\vec{x}_{\bar{n}} + \vec{x}_n) = \mathbf{M}_k\vec{x}_{\bar{n}} + \underbrace{\mathbf{M}_k\vec{x}_n}_{=0} = \mathbf{M}_k\vec{x}_{\bar{n}} \quad (\text{A.21})$$

with  $x_n \in \mathcal{N}(\mathbf{M}_k)$  and  $\vec{x}_{\bar{n}} \cdot \vec{y} = 0 \quad \forall \vec{y} \in \mathcal{N}(\mathbf{M}_k)$  can be inverted partially in order to obtain the *fixed solution*

$$\vec{x}_{\bar{n}} = \mathbf{M}_k^{-1}\vec{b}. \quad (\text{A.22})$$

The general solution then is non-uniquely given by

$$\vec{x} = \vec{x}_{\bar{n}} + \vec{y} \quad (\text{A.23})$$

with  $\vec{y} \in \mathcal{N}(\mathbf{M}_k)$  an arbitrary null space element. If the condition of a matrix is large and results in large errors for the vector of solution the neglect of the smallest singular values results in the rank  $k$  approximation

$$\mathbf{M}\vec{x} = \vec{b} \quad \implies \quad \mathbf{M}_k\vec{x}_{\bar{n}} = \vec{b} \quad \implies \quad \vec{x} = \vec{x}_{\bar{n}} + \vec{y} \quad (\text{A.24})$$

that determines the *fixed solution* and explicitly shows the freedom of choice of the null space element  $\vec{y}$ . Additional knowledge about the problem is needed then in order to choose an adequate  $\vec{y} \in \mathcal{N}(\mathbf{M}_k)$  to a specific mathematical or physical problem. The main idea about the pseudoinverse is that  $\vec{y}$  is not chosen automatically due to round off errors in the numerical solution process but with great care afterwards, regarding the nature of the problem.

---

<sup>1</sup>As matrix  $\mathbf{M}_k$  is truly singular by construction, matrix  $\mathbf{M}_k^{-1}$  is not the inverse matrix of  $\mathbf{M}_k$ .

**The condition of a matrix** is defined by the fraction of the largest and smallest singular value

$$\text{cond}(\mathbf{M}) \stackrel{\text{def}}{=} \frac{s_1}{s_n} \quad (\text{A.25})$$

[Press et al., 1992] and is a measure for the deformation of an  $n$  sphere after being mapped by matrix  $\mathbf{M}$ . In case  $s_n = 0$  the matrix is singular with  $\text{cond}(\mathbf{M}) \stackrel{\text{def}}{=} \infty$ , which corresponds to a loss of information due to the mapping of an  $n$  sphere to an  $n-1$  dimensional manifold. If the condition of a matrix satisfies  $\text{cond}(\mathbf{M}) \gtrsim 10^\nu$  with  $\nu$  the number of trustworthy digits of the machine numbers<sup>2</sup>, an  $n$  sphere is deformed by the mapping of the matrix so much that the precision of the numbers is not sufficient to prevent the build up of considerable errors during the numerical process of solution of the matrix equation. This means that the  $n$  sphere cannot be reconstructed from its strongly deformed image without a dramatical build up of rounding errors due to the finite precision of the numbers used.

Equivalently, the condition describes the worst case amplification of relative errors in the inhomogeneity  $\vec{b}$  by

$$\frac{\|\Delta\vec{x}\|}{\|\vec{x}\|} \leq \text{cond}(\mathbf{M}) \frac{\|\Delta\vec{b}\|}{\|\vec{b}\|} \quad (\text{A.26})$$

or the impact of an error-prone matrix  $\mathbf{M} \rightarrow \mathbf{M} + \Delta\mathbf{M}$

$$\frac{\|\Delta\vec{x}\|}{\|\vec{x}\|} \leq \text{cond}(\mathbf{M}) \frac{\|\Delta\mathbf{M}\|}{\|\mathbf{M}\|} (1 + \mathcal{O}(\|\mathbf{M}\|)) \quad (\text{A.27})$$

on the relative error of the vector of solution  $\vec{x}$  [Ciarlet et al., 1989].

## A.5 Discretized integral equations

In the following the discretization of the Fredholm integral equations 3.40 and 3.42 are given, which have been used for solving the inverse source problem numerically. For convenience the continuous functions are discretized into vectors

$$\begin{aligned} z &\longrightarrow \vec{z} &&= (z_0, z_1, \dots, z_{n-1}) \\ \sigma(z) &\longrightarrow \vec{\sigma} &&= (\sigma_0, \sigma_1, \dots, \sigma_{n-1}) \\ r(z) &\longrightarrow \vec{r} &&= (r_0, r_1, \dots, r_{n-1}) \\ W_{eE}(z) &\longrightarrow \vec{W}_{eE} &&= (W_{eE0}, W_{eE1}, \dots, W_{eEn-1}) \\ &\vdots &&\ddots \end{aligned}$$

The general form of the Fredholm integral equation of the first kind with inhomogeneity  $f(z)$  is given by

$$0 = f(z) + (\mathbf{T}_k \sigma)(z) \quad (\text{A.28})$$

---

<sup>2</sup>For *double* precision float point numbers on standard PC's it is  $\nu \approx 12$  [Press et al., 1992].



with

$$\mathbf{T}_k(z) = \int_{\tilde{z}=a}^b k(z, \tilde{z}) \cdot d\tilde{z} \quad (\text{A.29})$$

the infinite dimensional Fredholm integral operator with kernel  $k(z, \tilde{z})$  [Werner, 2002]. Discretizing the integral equation 3.40 results in the linear algebraic equation

$$\mathbf{M}\vec{\sigma} = \Pi_3\vec{z} \quad (\text{A.30})$$

with matrix

$$\mathbf{M} = \left( M_{\mu\nu}(z_\mu, z_\nu) - M_{\mu\nu}(z_\mu, -z_\nu) \right). \quad (\text{A.31})$$

Matrix  $\mathbf{M}$  is the discretized Fredholm operator of equation 3.40 that follows directly from the discretization of the kernel  $f_r(z, \tilde{z})$  of equation 3.29 which is given by

$$M_{\mu\nu}(z_\mu, z_\nu) = \frac{2A_\nu}{\sqrt{(z_\mu - z_\nu)^2 + (r_\mu + r_\nu)^2}} K(k_{\mu\nu}) \quad (\text{A.32})$$

where  $K(x)$  is the complete elliptic integral of the first kind with coefficient

$$k_{\mu\nu} = 2\sqrt{\frac{r_\mu r_\nu}{(z_\mu - z_\nu)^2 + (r_\mu + r_\nu)^2}} \quad (\text{A.33})$$

and surface element

$$A_\nu = \frac{\pi}{4} \left[ \begin{aligned} &(1 - \delta_{\nu,0}) (3r_\nu + r_{\nu-1}) \sqrt{(z_\nu - z_{\nu-1})^2 + (r_\nu - r_{\nu-1})^2} \\ &+ (1 - \delta_{\nu,n-1}) (3r_\nu + r_{\nu+1}) \sqrt{(z_{\nu+1} - z_\nu)^2 + (r_{\nu+1} - r_\nu)^2} \\ &+ \delta_{0,\nu} 4r_\nu^2 \end{aligned} \right] \quad (\text{A.34})$$

associated to ring  $\nu$  with  $\nu \in \{0, 1, 2, \dots, n-1\}$ . Discretizing the Fredholm integral operator of the modified Fredholm integral equation 3.42 results in

$$\mathbf{M}_\lambda^{mod} = \left( M_{\mu\nu}(z_\mu, z_\nu) - M_{\mu\nu}(z_\mu, -z_\nu) + \lambda M_{\mu\nu}^{mod}(z_\mu, z_\nu) - \lambda M_{\mu\nu}^{mod}(z_\mu, -z_\nu) \right) \quad (\text{A.35})$$

where  $M_{\mu\nu}$  is defined as before and

$$M_{\mu\nu}^{mod}(z_\mu, z_\nu) = 2A_\nu \left[ \frac{r'_\nu + (z_\mu - z_\nu + (r_\mu + r_\nu)r'_\mu) \frac{k_{\mu\nu}^2}{4r_\mu}}{2r_\mu \sqrt{(z_\mu - z_\nu)^2 + (r_\mu + r_\nu)^2}} \left( \frac{E(k_{\mu\nu})}{1 - k_{\mu\nu}^2} - K(k_{\mu\nu}) \right) - \frac{z_\mu - z_\nu + (r_\mu + r_\nu)r'_\mu}{(z_\mu - z_\nu)^2 + (r_\mu - r_\nu)^2} K(k_{\mu\nu}) \right] \quad (\text{A.36})$$

with  $k_{\mu\nu}$  and  $K(x)$  as before.  $E(x)$  is the complete elliptic integral of the second kind. Furthermore, the derivative  $r'(z)$  of radius  $r(z)$  is given without proof by the second order

finite difference scheme

$$r'_\mu = \begin{cases} \frac{(\lambda_\mu+1)r_\mu - \lambda_\mu r_{\mu+1} - r_{\mu+2}}{(\lambda_\mu+1)z_\mu - \lambda_\mu z_{\mu+1} - z_{\mu+2}} + \mathcal{O}(\Delta z^2) & \lambda_\mu = - \left( \frac{z_{\mu+2} - z_\mu}{z_{\mu+1} - z_\mu} \right)^2 \quad \mu = 0 \\ \frac{(\lambda_\mu+1)r_\mu - \lambda_\mu r_{\mu+1} - r_{\mu-1}}{(\lambda_\mu+1)z_\mu - \lambda_\mu z_{\mu+1} - z_{\mu-1}} + \mathcal{O}(\Delta z^2) & \lambda_\mu = - \left( \frac{z_\mu - z_{\mu-1}}{z_{\mu+1} - z_\mu} \right)^2 \quad 0 < \mu < n-1 \\ \frac{(\lambda_\mu+1)r_\mu - \lambda_\mu r_{\mu-1} - r_{\mu-2}}{(\lambda_\mu+1)z_\mu - \lambda_\mu z_{\mu-1} - z_{\mu-2}} + \mathcal{O}(\Delta z^2) & \lambda_\mu = - \left( \frac{z_{\mu-2} - z_\mu}{z_{\mu-1} - z_\mu} \right)^2 \quad \mu = n-1 \end{cases} \quad (\text{A.37})$$

for a non equidistant mesh  $\{z_\mu\}$  in forward, central and backward differences respectively. These formulas can be derived straight forward from the Taylor expansion of function  $r(z)$  by methods described in [Tannehill et al., 1997].

The discretization of the modified Fredholm integral equation of the first kind 3.42 is given by the linear algebraic equation

$$\mathbf{M}_\lambda^{mod} \vec{\sigma} = \Pi_3(\vec{z} + \lambda \vec{u}) \quad (\text{A.38})$$

with  $\vec{u} \stackrel{\text{def}}{=} (1, 1, \dots, 1)$ .

## A.6 The potential of a charged ring

**Lemma 5.** *The electrostatic potential of a charged ring of radius  $R$  and line charge density  $\tau$ , which is located at  $z'$  is given by*

$$\phi(\rho, z, z') = \frac{\tau}{2\pi\epsilon\epsilon_0} \sqrt{\frac{R}{\rho}} k(\rho, z, z') K(k(\rho, z, z')) \quad (\text{A.39})$$

where

$$k(\rho, z, z') = 2 \sqrt{\frac{\rho R}{(z - z')^2 + (\rho + R)^2}} \quad (\text{A.40})$$

and  $K(x)$  is the complete elliptic integral of the first kind as defined in equation A.8 [Zhu, 2005].

*Proof.* The variables  $R$ ,  $r$ ,  $s$ ,  $\rho$ ,  $z$ ,  $z'$ ,  $\alpha$  and  $\vartheta$  are referred to as illustrated in figure A.1. From  $r^2 = s^2 + z^2$  and  $s^2 = \rho^2 + R^2 - 2\rho R \cos(\alpha' - \vartheta)$  follows

$$r^2 = z^2 + (\rho + R)^2 - 2\rho R [1 + \cos(\alpha - \vartheta)]. \quad (\text{A.41})$$

The potential of the ring then is found from the integral

$$\begin{aligned} \phi(\rho, z, z') &= \int \frac{dq}{4\pi\epsilon\epsilon_0 r} \\ &= \frac{\tau R}{4\pi\epsilon\epsilon_0} \int_{\alpha'=0}^{\alpha} \frac{d\alpha'}{\sqrt{z^2 + (\rho + R)^2 - 2\rho R [1 + \cos(\alpha' - \vartheta)]}} \end{aligned} \quad (\text{A.42})$$

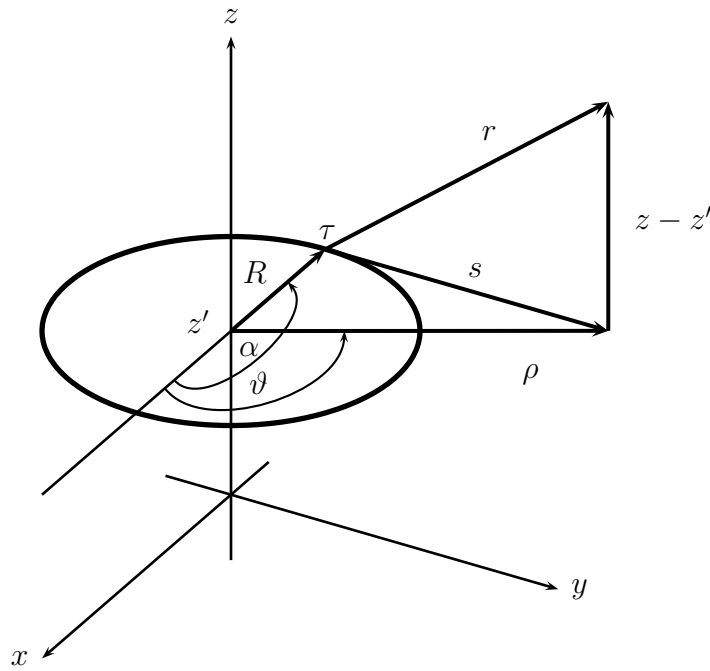


**Figure A.1:** Variables used in the derivation of the potential of a ring.

with the differential  $dq = \tau dl = \tau R d\alpha'$ . Making use of the abbreviation A.40 results in

$$\phi(\rho, z, z') = \frac{\tau R k}{4\pi\epsilon\epsilon_0 \sqrt{4\rho R}} \int \frac{d\alpha'}{\sqrt{1 - \frac{k^2}{2} [1 + \cos(\alpha' - \vartheta)]}}. \quad (\text{A.43})$$

Substituting  $\alpha' - \vartheta = \pi - 2\beta$  and using the identity  $1 + \cos(\alpha' - \vartheta) = 2 \sin^2(\beta)$  gives way to

$$\phi(\rho, z, z') = \frac{\tau k}{4\pi\epsilon\epsilon_0} \sqrt{\frac{R}{\rho}} \int_{\beta=\frac{\pi+\vartheta-\alpha}{2}}^{\frac{\pi+\vartheta}{2}} \frac{d\beta}{\sqrt{1 - k^2 \sin^2 \beta}}. \quad (\text{A.44})$$

Integrating over the complete ring defines  $\alpha = 2\pi$ . Setting  $\vartheta = 0$  by rotating the coordinate system appropriately yields

$$\phi(\rho, z, z') = \frac{\tau k}{4\pi\epsilon\epsilon_0} \sqrt{\frac{R}{\rho}} \left[ \underbrace{\int_{\beta=0}^{\frac{\pi}{2}} \frac{d\beta}{\sqrt{1 - k^2 \sin^2 \beta}}}_{=K(k)} + \underbrace{\int_{\beta=-\frac{\pi}{2}}^0 \frac{d\beta}{\sqrt{1 - k^2 \sin^2 \beta}}}_{=K(k)} \right]. \quad (\text{A.45})$$

The second term is equal to the complete elliptic integral of the first kind  $K(k)$ , which is obvious by the transition  $\beta \rightarrow -\beta$  and the swap of the integral boundaries. The final

result is

$$\phi(\rho, z, z') = \frac{\tau}{2\pi\epsilon\epsilon_0} \sqrt{\frac{R}{\rho}} k(\rho, z, z') K(k(\rho, z, z')) \quad (\text{A.46})$$

which is the assertion.  $\square$

## A.7 Ideal conducting sphere in a homogeneous field

In the following an expression for the surface charge on an ideally conducting sphere will be derived [Fliessbach, 2000]. An appropriate scaling will be used to express the surface charge density in the same non-dimensional variables as those used for the droplets in the plate capacitor field. In this way, the software developed and used in chapter 3 is tested against an analytically known reference.

**Lemma 6.** *The surface charge  $\sigma(z)$  of an ideal conducting sphere of radius  $R$  in a homogeneous electrical field  $\vec{E} = E_0\vec{e}_z$  is given by*

$$\sigma(z) = 3\epsilon\epsilon_0 E_0 \frac{z}{R} \quad z \in [-R, +R]. \quad (\text{A.47})$$

*Proof.* The general solution of Laplace's equation  $\Delta\phi(r, \vartheta) = 0$  for problems of cylindrical symmetry

$$\phi(r, \vartheta) = \sum_{nu=0}^{\infty} \left( a_\nu r^\nu + \frac{b_\nu}{r^{\nu+1}} \right) P_\nu(\cos \vartheta) \quad (\text{A.48})$$

is satisfied outside of the sphere. At the sphere radius  $\phi(R, \vartheta) = \phi_0 = \text{const}$  is satisfied and such that

$$\phi_0 \underbrace{P_0(\cos \vartheta)}_{=1} = \sum_{nu=0}^{\infty} \left( a_\nu R^\nu + \frac{b_\nu}{R^{\nu+1}} \right) P_\nu(\cos \vartheta). \quad (\text{A.49})$$

Multiplying the above equation by  $P_\mu(\cos \vartheta)$  and integrating over  $\vartheta$  results in the following conditions

$$\begin{aligned} b_0 &= R(\phi_0 - a_0) & n &= 0 \\ b_n &= -a_n R^{2n+1} & n &\neq 0 \end{aligned} \quad (\text{A.50})$$

due to the orthogonality of the Legendre Polynomials  $\int_{x=-1}^1 P_\nu(x) P_\mu(x) dx = \frac{1}{2n+1} \delta_{\nu\mu}$ . Far from the sphere, the solution is expected to be undisturbed by the presence of the sphere itself and hence  $\phi(r, \vartheta) = \phi_1 - E_0 z$  where  $z = r \cos \vartheta = r P_1(\cos \vartheta)$  for  $r \rightarrow \infty$  and hence

$$\phi_1 - E_0 r P_1(\cos \vartheta) = \sum_{\nu=0}^{\infty} \left( a_\nu r^\nu + \frac{b_\nu}{r^{\nu+1}} \right) P_\nu(\cos \vartheta). \quad (\text{A.51})$$

Again using the orthogonality of the Legendre polynomials in the limit  $r \rightarrow \infty$  results in

$$\begin{aligned} a_0 &= \phi_1 & n &= 0 \\ a_1 &= -E_0 & n &= 1 \\ a_n &= 0 & n &> 1 \end{aligned} \quad (\text{A.52})$$

and consequently in

$$\begin{aligned} b_0 &= R(\phi_0 - \phi_1) & n &= 0 \\ b_1 &= E_0 R^3 & n &= 1 \\ b_n &= 0 & n &> 1. \end{aligned} \quad (\text{A.53})$$

The potential of an ideally conducting sphere in a homogeneous electrical field then is given by

$$\phi(r, \vartheta) = \phi_1 + (\phi_0 - \phi_1) \frac{R}{r} - E_0 \left( r - \frac{R^3}{r^2} \right) \cos \vartheta \quad r \geq R. \quad (\text{A.54})$$

The first term depends on the choice of the point of reference, the second belongs to a monopole charge on the sphere and is not of interest here such that we set  $\phi_0 = \phi_1$  corresponding to a vanishing monopole charge on the sphere. The third term describes the corrections to the potential due to polarization of the sphere. The surface charge density now follows from the potential

$$\sigma(z) = -\epsilon\epsilon_0 (\vec{n} \cdot \nabla \phi(r, \vartheta)) \Big|_{r=R} = -\epsilon\epsilon_0 \frac{\partial \phi}{\partial r} \Big|_{r=R} \quad (\text{A.55})$$

with  $z = R \cos \vartheta$  on the sphere follows

$$\sigma(z) = 3\epsilon\epsilon_0 E_0 \frac{z}{R} \quad (\text{A.56})$$

□

**Corollary 7.** *Using the scalings  $\sigma_0$ ,  $l_0$  and  $\Pi_3 = \frac{4\pi^2 \epsilon\epsilon_0}{\sigma_0} E_0$  for non-dimensionalizing the charge density it follows*

$$\sigma(z) = \frac{3}{4\pi^2} \Pi_3 \frac{z}{R} \quad (\text{A.57})$$

*in non-dimensional variables with the non-dimensional electrical field  $\Pi_3$ .*

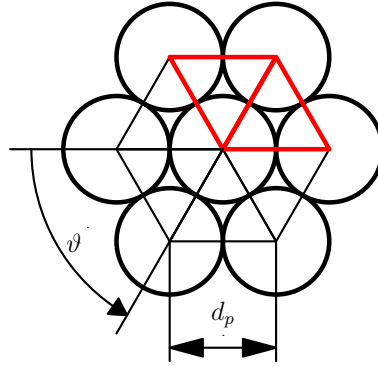


**Figure A.2:** A slice of the fiber may be assumed to consist of a two dimensional densest packing of colloidal particles. Obviously,  $\vartheta = 60^\circ$  and  $d_p = 2r_p$  is satisfied. In the limit of an infinitely extended layer, the lattice is composed of circles shown or equivalently by cells like the red rhombus.

## A.8 Experimental determination of the particle density

**Lemma 8.** *The particle density of colloidal nano-fibers is estimated from experimental data by*

$$\rho_{exp} = \frac{\pi}{4\sqrt{3}r_p} \left(\frac{d_f}{d_p}\right)^2 \quad (\text{A.58})$$

where  $d_f$  and  $d_p$  are the measured diameters of the fiber and the particles, respectively.

*Proof.* A slice of a colloidal nano-fiber of thickness  $L = 2r_p$  is approximated by a two dimensional densest packing as shown in figure A.2, where  $d_f = 2r_f$  and  $d_p = 2r_p$  are the diameters and radii of the fiber and the particles respectively. The particle density is defined by

$$\rho = \frac{N}{L} = \frac{N}{2r_p}. \quad (\text{A.59})$$

The area of a triangle in figure A.2 is given by

$$A_{tr} = \frac{1}{2} (2r_p) (2r_p) \underbrace{\sin 60^\circ}_{=\frac{\sqrt{3}}{2}} = \sqrt{3} r_p^2 \quad (\text{A.60})$$

and the area of a single void between 3 particles is found by

$$A_{void} = A_{tr} - \frac{1}{2}A_{circle} = \left(\sqrt{3} - \frac{\pi}{2}\right) r_p^2. \quad (\text{A.61})$$

Each circle in figure A.2 is equivalent to a rhombus like the one illustrated in red, such that it is clear that each particle contributes two voids resulting in

$$A_f = N(A_{circle} + 2A_{void}) = 2N\sqrt{3}r_p^2 \quad (\text{A.62})$$

which is identified to  $A_f = \pi r_f^2$  resulting in

$$N = \frac{\pi}{2\sqrt{3}} \left( \frac{r_f}{r_p} \right)^2 \quad (\text{A.63})$$

such that the particle density becomes

$$\rho_{exp} = \frac{\pi}{4\sqrt{3}r_p} \left( \frac{d_f}{d_p} \right)^2 \quad (\text{A.64})$$

and therewith proves the assertion. □





# Bibliography

- [Abramowitz and Stegun, 1972] Abramowitz and Stegun (1972). *Handbook of mathematical functions (online version)*. National Bureau of Standards: [http://www.iopb.res.in/somen/abramowitz\\_and\\_stegun/toc.htm](http://www.iopb.res.in/somen/abramowitz_and_stegun/toc.htm).
- [Achtzehn et al., 2005] Achtzehn, T., Müller, R., Duft, D., and Leisner, T. (2005). The Coulomb instability of charged microdroplets: dynamics and scaling. *The European Physical Journal D*, 34:311–313.
- [Adams, 2001] Adams, D. (2001). A fine set of threads. *Nature*, 411:236.
- [Andrews et al., 2000] Andrews, G. E., Askey, R., and Roy, R. (2000). *Special Functions*. Cambridge University Press.
- [Barrero et al., 1998] Barrero, A., Ganan-Calvo, A. M., Davila, J., Palacio, A., and Gomez-Gonzalez, E. (1998). Low and high Reynolds number flow inside Taylor cones. *Phys. Rev. E*, 58:7309.
- [Bartoli et al., 1984] Bartoli, C., von Rhoden, H., Thompson, S. P., and Blommers, J. (1984). Recent developments in high current liquid metal ion sources. *Vacuum*, 34:43–46.
- [Basaran and Scriven, 1990] Basaran, O. A. and Scriven, L. E. (1990). Axisymmetric shapes and stability of pendant and sessile drops in an electrical field. *Journal of Colloid and Interface Science*, 140:10–30.
- [Batchelor, 2002] Batchelor, G. K. (2002). *An introduction to fluid dynamics*. Cambridge mathematical library.
- [Bishop and Barker, 2006] Bishop, A. I. and Barker, P. (2006). Subnanosecond pockels cell switching using avalanche transistors. *Rev. Sci. Instrum.*, 77:044701.
- [Boudriot et al., 2006] Boudriot, U., Dersch, R., Greiner, A., and Wendorff, J. H. (2006). Electrospinning approaches towards scaffold engineering - a brief overview. *Artificial Organs*, 30:785–792.
- [Bronstein et al., 1999] Bronstein, Semendjajew, Musiol, and Mühlig (1999). *Taschenbuch der Mathematik*. Harri Deutsch Verlag.

- [Burcham and Saville, 2000] Burcham, C. L. and Saville, D. A. (2000). The electrohydrodynamic stability of a liquid bridge: microgravity experiments on a bridge suspended in a dielectric gas. *J. Fluid Mech.*, 405:37.
- [Burger et al., 2006] Burger, C., Hsiao, B. S., and Chu, B. (2006). Nanofibrous materials and their applications. *Annu. Rev. Mater Res.*, 36:333–368.
- [Carretero-Benignos, 2005] Carretero-Benignos, J. A. (2005). *Numerical simulation of a single emitter colloid thruster in pure droplet cone-jet mode*. PhD thesis, MIT.
- [Castro and Bocanegra, 2006] Castro, S. and Bocanegra, R. (2006). Water-based compound Taylor cones held in vacuum: Feasibility and application to colloidal propulsion. *Appl. Phys. Lett.*, 88:123105–1.
- [Chandrasekhar, 1981] Chandrasekhar, S. (1981). *Hydrodynamic and Hydromagnetic stability*. Dover.
- [Cherney, 1999] Cherney, L. T. (1999). Structure of Taylor cone-jets: Limit of low flow rates. *J. Fluid Mech.*, 378:167–196.
- [Ciarlet et al., 1989] Ciarlet, P. G., Miara, B., Thomas, J.-M., and Buttigieg, A. (1989). *Introduction to numerical linear algebra and optimisation*. Cambridge University Press.
- [Clasen et al., 2005] Clasen, C., Eggers, J., Fontelos, M. A., Li, J., and McKinley, G. H. (2005). The beads-on-string structure of viscoelastic threads. *J. Fluid Mech.*, 556:283–308.
- [Cohen et al., 2001] Cohen, I., Li, H., Houglund, J. L., Mrksich, M., and Nagel, S. R. (2001). Using selective withdrawal to coat microparticles. *Science*, 218:133.
- [Collins et al., 2007] Collins, R. T., Harris, M. T., and Basaran, O. A. (2007). Breakup of electrified jets. *J. Fluid Mech.*, 588:75–129.
- [Couillet et al., 2005] Couillet, P., Mahadevan, L., and Riera, C. S. (2005). Hydrodynamical models for the chaotic dripping faucet. *J. Fluid Mech.*, 526:1–17.
- [Dante Alighieri, 1307] Dante Alighieri (1307). *The Divine Comedy*. Transl. Henry Wadsworth Longfellow, ILT’s Digital Dante Project.
- [de la Mora, 1992] de la Mora, J. F. (1992). The effect of charge emission from electrified liquid cones. *J. Fluid Mech.*, 243:561–574.
- [de la Mora, 2007] de la Mora, J. F. (2007). Fluid dynamics of Taylor cones. *Annu. Rev. Fluid Mech.*, 39:217–244.
- [Doshi and Reneker, 1995] Doshi, J. and Reneker, D. H. (1995). Electrospinning process and applications of electrospun fibers. *Journal of electrostatics*, 35:151–160.

- [Drazin and Reid, 2004] Drazin, P. G. and Reid, W. H. (2004). *Hydrodynamic stability*. Cambridge University Press.
- [Dror et al., 2007] Dror, Y., Salalha, W., Avrahami, R., Zussmann, E., Yarin, A. L., Dersch, R., Greiner, A., and Wendorff, J. H. (2007). One-step production of polymeric microtubes by co-electrospinning. *Small*, 3:1064–1073.
- [Ebert, 2008] Ebert, U. (2008). Personal communication. 13th Fall seminar on Nonlinear Dynamics in Bayreuth.
- [Eggers, 1997] Eggers, J. (1997). Nonlinear dynamics and breakup of free-surface flows. *Rev. Mod. Phys.*, 69:865.
- [Eggers and Dupont, 1994] Eggers, J. and Dupont, T. F. (1994). Drop formation in a one-dimensional approximation of the Navier-Stokes equation. *J. Fluid Mech.*, 262:205.
- [Eggleton et al., 2001] Eggleton, C. D., Tsai, T.-M., and Stebe, K. J. (2001). Tip streaming from a droplet in the presence of surfactants. *PRL*, 87:048302–1.
- [Einstein, 1905] Einstein, A. (1905). Über die von der molekularkinetischen theorie der wärme geforderte bewegung von in ruhenden flüssigkeiten suspendierten teilchen. *Annu. Rev. Fluid Mech*, 17:549–560.
- [Feng, 2002] Feng, J. J. (2002). The stretching of an electrified non-newtonian jet: A model for electrospinning. *Phys. Fluids*, 14:3912.
- [Fenn et al., 1989] Fenn, J. B., Mann, M., Meng, C. K., Wong, S. F., and Whitehouse, C. M. (1989). Electrospray ionization for mass-spectrometry of large biomolecules. *Science*, 246:64–71.
- [Fliessbach, 2000] Fliessbach, T. (2000). *Elektrodynamik*. Spektrum Verlag.
- [Forbes, 1997] Forbes, R. G. (1997). Understanding how the liquid ion source works. *Vacuum*, 48:85–97.
- [Formhals, 1934] Formhals, A. (1934). Process and apparatus for preparing artificial threads. *US Patent No. 1,975,504*.
- [Fuchikami et al., 1999] Fuchikami, N., Ishioka, S., and Kiyono, K. (1999). Simulation of a dripping faucet. *JPSJ*, 68:1185–1196.
- [Ganan-Calvo, 1997] Ganan-Calvo, A. M. (1997). Cone-jet analytical extension of Taylors electrostatic solution and the asymptotic universal scaling laws in electrospinning. *PRL*, 79:217.
- [Ganan-Calvo, 2004] Ganan-Calvo, A. M. (2004). On the general scaling theory for electrospinning. *J. Fluid Mech.*, 507:203–212a.

- [Giglio et al., 2008] Giglio, E., Gervais, B., Rangama, J., Manil, B., Huber, B. A., Duft, D., Müller, R., and Leisner, T. (2008). Shape deformations of surface-charged microdroplets. *PR E*, 77:036319.
- [Gilbert, 1600] Gilbert, S. W. (1600). *De Magnete*. Transl. P.F. Mottelay. Dover.
- [Golub and Kahan, 1965] Golub, G. and Kahan, W. (1965). Calculating the singular values and pseude-inverse of a matrix. *J. SIAM Numer. Anal. Ser. B.*, 2:205–224.
- [Grafe and Graham, 2003] Grafe, T. H. and Graham, K. M. (2003). Nanofiber webs from electrospinning. *Nonwovens in Filtration - fifth International Conferences, Stuttgart, Germany*.
- [Greiner and Wendorff, 2007] Greiner, A. and Wendorff, J. H. (2007). Electrospinning: A fascinating method for the preparation of ultrathin fibers. *Angewandte Chemie int. Ed.*, 46:5670–5703.
- [Grimm and Beauchamp, 2005] Grimm, R. L. and Beauchamp, J. L. (2005). Dynamics of field induced droplet ionization: Time-resolved studies of distortion, jetting, and progeny formation from charged and neutral methanol droplets exposed to strong electric fields. *J. Phys. Chem. B*, 109:8244–8250. axisymmetric coulomb explosions of droplets due to net charge.
- [Harris and Basaran, 1995] Harris, M. T. and Basaran, O. A. (1995). Equilibrium shapes and stability of nonconducting pendant drops surrounded by a conducting fluid in an electric field. *Journal of Colloid and Interface Science*, 170:308–319.
- [Herbert Goldstein and Safko, 2006] Herbert Goldstein, Charles P. Poole, J. and Safko, J. L. (2006). *Klassische Mechanik*. Wiley-VCH.
- [Heuser, 2004] Heuser, H. (2004). *Lehrbuch der Analysis 2*. Teubner.
- [Hiemenz and Rajagopalan, 1997] Hiemenz, P. C. and Rajagopalan, R. (1997). *Principles of Colloid and Surface Chemistry*. Marcel Dekker.
- [Higuera, 2003] Higuera, F. J. (2003). Flow rate and electric current emitted by a Taylor cone. *J. Fluid Mech.*, 484:303–327.
- [Hohman et al., 2001a] Hohman, M. M., Shin, M., Rutledge, G., and Brenner, M. P. (2001a). Electrospinning and electrically forced jets. i. stability theory. *Phys. Fluids*, 13:2201.
- [Hohman et al., 2001b] Hohman, M. M., Shin, M., Rutledge, G., and Brenner, M. P. (2001b). Electrospinning and electrically forced jets. ii. applications. *Phys. Fluids*, 13:2221.

- [Israelachvili, 1997] Israelachvili, J. N. (1997). *Intermolecular and surface forces*. Academic Press.
- [Jackson, 1998] Jackson, J. D. (1998). *Classical Electrodynamics*. Wiley and Sons.
- [Johnson and Sadhal, 1985] Johnson, R. E. and Sadhal, S. S. (1985). Fluid mechanics of compound multiphase drops and bubbles. *Ann. Rev. Fluid Mech.*, 17:289–320.
- [Kaipio and Erkki, 2005] Kaipio, J. K. and Erkki, S. (2005). *Statistical and computational inverse source problems*. Springer.
- [Kirsch, 1996] Kirsch, A. (1996). *An Introduction to the Mathematical Theory of Inverse Problems*. Springer.
- [Larrondo and Manlay, 1981] Larrondo, L. and Manlay, R. S. J. (1981). Electrostatic fiber spinning from polymer melts. i. experimental observations on fiber formation and properties. *Journal of Polymer sciences*, 19:909–920.
- [Larsen et al., 2003] Larsen, G., Velarde-Ortiz, R., Minchow, K., Barrero, A., and Loscertales, I. G. (2003). A method for making inorganic and hybrid (organic/inorganic) fibers and vesicles with diameters in the submicrometer and micrometer range via sol-gel chemistry and electrically forced liquid jets. *J. Am. Chem.*, 125:1154.
- [Lebedev, 1972] Lebedev, N. N. (1972). *Special Functions & their Applications*. Dover.
- [Lopez-Herrera et al., 2003] Lopez-Herrera, J., Barrero, A., Lopez, A., Loscertales, I., and Marquez, M. (2003). Coaxial jets generated from electrified Taylor cones. scaling laws. *Journal of Aerosol Science*, 34:535–552.
- [Loscertales et al., 2002] Loscertales, I. G., Barrero, A., Guerrero, I., Cortijo, R., Marquez, M., and Ganan-Calvo, A. M. (2002). Micro/nano encapsulation via electrified coaxial jets. *Science*, 295:1695.
- [Marangoni, 1871] Marangoni, C. (1871). Über die ausbreitung der tropfen einer flüssigkeit auf der oberfläche einer anderen. *Ann. Phys.*, 143:337–354.
- [Marin et al., 2008] Marin, A. G., Riboux, G., Loscertales, I. G., and Barrero, A. (2008). Whipping instabilities in electrified liquid jets. *arXiv:0810.0155v1 [physics.flu-dyn]*.
- [Melcher and Taylor, 1969] Melcher, J. and Taylor, G. (1969). Electrohydrodynamics: A review of the role of interfacial shear stress. *Annu. Rev. Fluid Mech.*, 1:111–146.
- [Mestel, 1994] Mestel, A. J. (1994). Electrohydrodynamic stability of a slightly viscous jet. *J. Fluid Mech.*, 274:93–113.
- [Mestel, 1995] Mestel, A. J. (1995). Electrohydrodynamic stability of a highly viscous jet. *J. Fluid Mech.*, 312:311–326.

- [Morrison, 2001] Morrison, F. A. (2001). *Understanding Rheology*. Oxford University Press.
- [Phillips, 1962] Phillips, D. L. (1962). A technique for the numerical solution of certain integral equations of the first kind. *Journal of the ACM*, 19:84.
- [Press et al., 1992] Press, Teukolsky, Vetterling, and Flannery (1992). *Numerical recipes in C*. Cambridge.
- [Reithmeier et al., 2001] Reithmeier, H., Herrmann, J., and Göpferich, A. (2001). Development and characterization of lipid microparticles as a drug carrier for somatostatin. *International Journal of Pharmaceutics*, 218:133.
- [Reznik et al., 2006] Reznik, S. N., Yarin, A. L., Zussmann, E., and Basaran, O. A. (2006). Evolution of a compound droplet attached to a core shell nozzle under action of a strong electric field. *Phys. Fluids*, 18:062101.
- [Saville, 1970] Saville, D. A. (1970). Electrohydrodynamic stability: Fluid cylinders in longitudinal electric fields. *The physics of fluids*, 13:2987–2994.
- [Saville, 1971a] Saville, D. A. (1971a). Electrodynamic stability: effects of charge relaxation at the interface of a liquid jet. *J. Fluid Mech.*, 48:815–827.
- [Saville, 1971b] Saville, D. A. (1971b). Stability of electrically charged viscous cylinders. *The physics of fluids*, 14:1095–1099.
- [Saville, 1997] Saville, D. A. (1997). Electrohydrodynamics: The Taylor - Melcher leaky dielectric model. *Annu. Rev. Fluid Mech.*, 29:27.
- [Scardovelli and Zaleski, 1999] Scardovelli, R. and Zaleski, S. (1999). Direct numerical simulation of free-surface and interfacial flow. *Annu. Rev. Fluid Mech.*, 31:567–603.
- [Shepherd and Sturtevant, 1982] Shepherd, J. E. and Sturtevant, B. (1982). Rapid evaporation at the superheat limit. *J. Fluid Mech.*, 121:379.
- [Stoer and Burlisch, 2005] Stoer and Burlisch (2005). *Mathematische Numerik 2*. Springer.
- [Stoiljkovic, 2007] Stoiljkovic, A. (2007). *Preparation of water-insoluble fibers from aqueous colloidal dispersions by electrospinning*. PhD thesis, Philipps-Universität Marburg.
- [Stoiljkovic et al., 2007] Stoiljkovic, A., Ishaque, M., Justus, U., Hamel, L., Klimov, E., Heckmann, W., Eckhardt, B., Wendorff, J. H., and Greiner, A. (2007). Preparation of water-stable submicron fibers from aqueous latex dispersion of water-insoluble polymers by electrospinning. *Polymer*, 48:3974–3981.
- [Stone et al., 1999] Stone, H. A., Lister, J. R., and Brenner, M. P. (1999). Drops with conical ends in electric and magnetic fields. *Proc. R. Soc. Lond. A*, 455:329–347.

- [Sun et al., 2006] Sun, D., Chang, C., Li, S., and Lin, L. (2006). Near-field electrospinning. *Nano Letters*, 6:839–842.
- [Suvorov and Zubarev, 2004] Suvorov, V. G. and Zubarev, N. M. (2004). Formation of the Taylor cone on the surface of liquid metal in the presence of an electric field. *J. Phys. D. Appl. Phys.*, 37:289–297.
- [Tannehill et al., 1997] Tannehill, J. C., Anderson, D. A., and Pletcher, R. H. (1997). *Computational Fluid Mechanics and Heat Transfer*. Taylor and Francis.
- [Taylor, 1964] Taylor, S. G. (1964). Disintegration of water drops in an electric field. *Proc. Roy. Soc. A*, 280:383.
- [Taylor, 1969] Taylor, S. G. (1969). Electrically driven jets. *Proc. Roy. Soc. A*, 313:453–475.
- [Tonks, 1935] Tonks, L. (1935). A theory of liquid surface rupture by a uniform electric field. *Phys. Rev.*, 15:562–568.
- [Torza and Mason, 1970] Torza, S. and Mason, S. G. (1970). Three-phase interactions in shear and electrical fields. *J. Colloid Interface Sci.*, 33:67–83.
- [Utada et al., 2005] Utada, A. S., Loreneau, E., Link, D. R., Kaplan, P. D., Stone, H. A., and Weitz, D. A. (2005). Monodisperse double emulsions generated from a microcapillary device. *Science*, 308:537.
- [V.K. Ivanov and Tanana, 2002] V.K. Ivanov, V. V. and Tanana, V. (2002). *Theory of ill-posed problems and its applications*. de Gruyter.
- [Wan et al., 2006] Wan, Y. Q., He, J. H., Yu, J. Y., and Wu, Y. (2006). Electrospinning of high-molecule peo solution. *Journal of Applied Polymer Science*, 103:3840–3843.
- [Wazwaz, 1997] Wazwaz, A.-M. (1997). *A first course in integral equations*. World scientific.
- [Welker, 2007] Welker, V. (2007). Personal communication.
- [Werner, 2002] Werner (2002). *Funktionalanalysis*. Springer.
- [Wing and Zahrt, 1991] Wing, G. M. and Zahrt, J. D. (1991). *A Primer on Integral Equations of the First Kind*. Siam.
- [Yarin et al., 2001] Yarin, A., Koombhongse, S., and Reneker, D. H. (2001). Taylor cone and jetting from liquid droplets in electrospinning of nanofibers. *J. Appl. Phys.*, 90:4836–4846.
- [Zeleny, 1917] Zeleny, J. (1917). Instability of electrified liquid surfaces. *Phys. Rev.*, 10:1–7.

- [Zeng, 2003] Zeng, J. (2003). *Meso- and nano-scaled polymer fibers and tubes*. PhD thesis, Philipps-Universität Marburg.
- [Zhu, 2005] Zhu, P. (2005). Field distribution of a uniformly charged circular arc. *Journal of Electrostatics*, 63:1035.



# Acknowledgements

I am deeply indebted to my doctoral adviser Prof. Bruno Eckhardt for putting faith in me, when I was in a precarious situation prior to my studies in Marburg.

I thank my friend Aleksandar Stoiljkovic for his experimental contribution to this work and the stimulating cooperation we shared.

I am grateful to my close friends Annette Kohnen and Mischa Schmidt, who did a lot of proofreading and consequently helped me very much.

I appreciate the willingness of Prof. Stöckmann to examine this thesis.

Furthermore, I enjoyed the cooperations with Prof. Greiner, Prof. Wendorff and their groups from the chemistry department. Especially, Mathias Becker, Roland Dersch, Martin Gräser and Thorsten Röcker helped me continuously with fruitful discussions.

I hold in high regard the helpful discussions with Prof. Welker from the math department and Prof. Ebert from the CWI and the University of Eindhoven.

I am indebted to Jürgen Vollmer for all the committed advises. The intense professional friendship with Tobias Schneider was helpful all the time with respect to great many topics. Furthermore, I thank all my colleagues of the AG KoSy for the friendly atmosphere during my stay, especially Prof. Großmann, Prof. Lenz, Prof. Schumacher, Thomas Niedermayer, Tobias Bischoff and Michael Grau.

I thank Johannes Brauckmann for his collaboration while doing his Bachelor Thesis in our group on particles interacting in a shear flow.

Many of the numerical results contained in this work would not have been accessible without the Marburg Linux Cluster MARC. I am obligated to the IT-support of Dr. Thomas Gebhardt on the MARC.

This work has financially been supported by the German Science Foundation DFG under the Schwerpunktprogramm SPP1165.

# Wissenschaftlicher Werdegang

Name	Großmann
Vorname	Florian
Geburtstag	1976-11-30
Geburtsort	Hamburg
Staatsangehörigkeit	deutsch
Familienstand	ledig
Berufliche Bildung	Kommunikationselektroniker (Funktechnik) Dipl.-Ing. (FH) Physikalische Technik Dipl.-Phys.
1983-08 bis 1987-07	Besuch der <b>Grundschule</b> Nahe.
1987-08 bis 1993-08	Besuch der <b>Realschule</b> im Schulzentrum Süd Norderstedt.
1993-08 bis 1997-01	<b>Ausbildung</b> zum Kommunikationselektroniker (Funktechnik) bei der Deutschen Lufthansa Technik AG.
1997-01 bis 1997-08	<b>Berufstätigkeit</b> bei der Deutschen Lufthansa Technik AG in der Starkstromabteilung.
1997-08 bis 1998-07	Besuch der <b>Fachoberschule</b> (FOS) der Kreisberufsschule Norderstedt.
1998-10 bis 2002-09	<b>Studium</b> der Physikalischen Technik an der privaten Fachhochschule Wedel mit Schwerpunkt Technische Optik.
2001-09 bis 2002-02	<b>Praktikum</b> im Rahmen des Studiums am Laser - Zentrum Hannover e.V.
2002-03 bis 2002-08	<b>Diplomarbeit</b> am Laser - Zentrum Hannover e.V.: 'Charakterisierung laser-induzierter Fluoreszenz optischer Komponenten'. Die Diplomarbeit wurde mit dem <b>Hamburger VDI Preis 2003</b> gewürdigt (1. Platz).
2002-10 bis 2004-07	<b>Ergänzungsstudium</b> Physik an der Technischen Universität Clausthal.
2003-10 bis 2004-07	<b>Diplomarbeit</b> am Institut für statistische Physik und nichtlineare Dynamik der TU-Clausthal: 'Investigation of non-standard period-doubling in a piecewise continuous dynamical system'.
2004-10 bis 2005-01	<b>Doktorand</b> am Institut für Energietechnik / Professur für Kernenergietechnik der Technische Universität Dresden. Das Projekt war unterfinanziert.
2005-04 bis 2009-07	<b>Doktorand</b> am Fachbereich Physik der Philipps - Universität Marburg in der Arbeitsgruppe Komplexe Systeme bei Prof. Bruno Eckhardt.